TECHNISCHE UNIVERSITÄT MÜNCHEN

Fakultät für Chemie

Porphyrinic MOF: Film Preparation and Properties of Electrochemical sensing/catalysis

Zhenyu Zhou

Porphyrinic MOF: Film Preparation and Properties of Electrochemical sensing/ catalysis
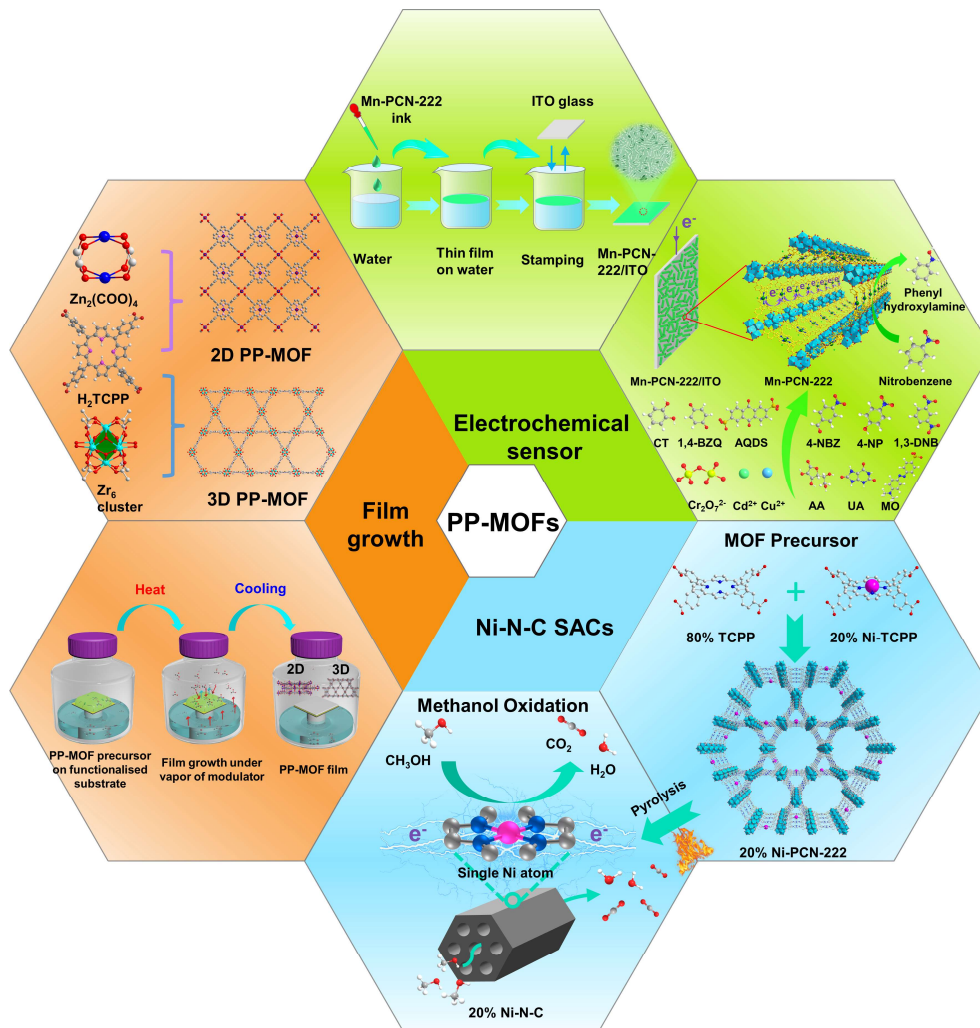
DISSERTATION
Submitted by

Zhenyu Zhou

October 2021

Acknowledgement

During my PhD study, I experienced an enjoyable and unforgettable time in Germany. I received lots of kind help and advices from many individuals, and thanks to these, I was able to complete my thesis successfully. This memory is an invaluable asset for me and I will remember it for the rest of my life.

First of all, I would like to sincerely thank my PhD supervisor, **Prof. Dr. Roland A. Fischer**, for giving me the opportunity to work in such a united and supportive group on this interesting topic. I am very grateful for his tremendous and helpful guidance, suggestion, support and encouragement over the past four years, as well as for his numerous efforts put into my work. I really appreciate his tolerance of my mistakes and his encouragement of my progress. His valuable guidance enriches my knowledge and helps me to improve scientific skills and thinking.

I acknowledge to China Scholarship Council (CSC) for providing the scholarship to support my PhD study in Germany. I also thank the Chair of Inorganic and Metal-Organic Chemistry (AMC) in Technical University of Munich for the laboratory facilities and chemicals for my PhD study. I appreciate Graduate School of Technical University of Munich for the financial support to international conference in New Zealand.

I would like to address my special thanks to **Prof. Dr. Martin Elsner** for accepting to be the chairman of my doctoral dissertation defence. I would like to express my special thanks and appreciation to **Prof. Dr. Roland A. Fischer** and **Prof. Dr. Aliaksandr S. Bandarenka** for accepting to be the examiners of my doctoral dissertation defence.

I would like to express my special thanks to **Prof. Dr. Christof Wöll** for his kindness as my mentor and all the help in my PhD study.

I also would like to express my thanks to **Dr. Wei-jin Li** for lots of valuable discussions and supports during the whole time of my PhD period. Thank you very much for all your warm help in not only my study but also my life in Germany.

Many thanks also to **Dr. Soumya Mukherjee** for his fruitful discussions and kind help in my paper work. It is a pleasure to work with you.

you being on my side and understanding me. Wish you healthy, happy and beautiful every day! 亲爱的老婆，谢谢你一直以来的陪伴，和你在一起的每一天都很快乐！祝你永远的健康，开心，漂亮！愿我们今后的每一天都幸福快乐！❤

To my dear wife (梁会敏)

既然选择了远方 便只顾风雨兼程

汪国真《热爱生命》

Table of Content

VIII

Abbreviations

IUPAC	International Union of Pure and Applied Chemistry
PCPs	Porous coordination polymers
SBUs	Second building units
MOFs	Metal–organic frameworks
BDC	Terephthalate
PIZA	Porphyrinic Illinois zeolite analogue
PP	Porphyrin
VAC	Vapor-assisted conversion
2D	2-Dimensional
3D	3-Dimensional
LBL	Layer-by-layer
ITO	Indium tin oxide
LB	Langmuir–Blodgett
LPE	Liquid phase epitaxy
SURMOF	Surface mounted metal-organic framework
MA	Modular assembly
PCs	Porous carbons
TCPP	Tetrakis(4-carboxyphenyl)-porphyrin
PCN	Porous coordination network
DMF	N,N-dimethylformamide
SAM	Self-assembled monolayer
$Zn(OAC)_2$	Zinc acetate
PXRD	Powder X-ray diffraction
GIXRD	Grazing incidence X-ray diffraction
ATR-IR	Attenuated total reflection infrared spectroscopy
UV-Vis	Ultraviolet–visible spectroscopy
SEM	Scanning electron microscopy
$Zn_2(ZnTCPP)$	$[Zn_2(COO)_4]_2(Zn\text{-}TCPP)$

PCN-222	$[Zr_6O_4(OH)_4](TCPP)_2$
PCN-224	$[Zr_6O_4(OH)_4]_2(TCPP)_3$
MOF-525	$[Zr_6O_4(OH)_4](TCPP)_3$
IUPAC	International Union of Pure and Applied Chemistry
QCM	Quartz crystal microbalance
EtOH	Ethanol
MeOH	Methanol
CV	Cyclic voltammetry
NPs	Nanoparticles
EDX	Energy-dispersive X-ray spectroscopy
RSD	Relative standard deviation
BET	Brunauer-Emmett-Teller
MOF	Metal-organic frameworks
MOF-2	Cubdc
MOF-5	$Zn_4O(BDC)_3$
MTV-MOF	Multivariate metal-organic framework
MUD	11-mercaptoundecanol
MHDA	16-mercaptohexadecanoic acid
NMR	Nuclear magnetic resonance
NP	Nanoparticles
NB	Nitrobenzene
EDA	Electron donor-acceptor
HER	Hydrogen evolution reaction
USEPA	United States of Environmental Protection Agency
LOD	Limit of detection
NACs	Nitroaromatic compounds
4-NBZ	4-nitrobenzaldehyde
4-NP	4-nitrophenol
1,3-DNB	1,3-dinitrobenzene
CT	Catechol

1,4-BZQ	1,4-benzoquinone
AQDS	Anthraquinone-2,6-disulfonate
AA	Ascorbic acid
UA	Uric acid
MO	Methyl orange
MOR	Methanol oxidation reaction
DFT	Density functional theory
DMFCs	Direct methanol fuel cells
SACs	Single-atom catalysts
JCPDS	Joint committee on powder diffraction standards
HAADF-STEM	High-angle annular darkfield scanning transmission electron microscope
ICP-OES	Inductively coupled plasma optical emission spectrometry
XPS	X-ray photoelectron spectroscopy
XANES	X-ray absorption near edge structure
FT-EXAFS	Fourier transform-extend X-ray absorption fine structure
ECSA	Electrochemically active surface area
RDS	Rate-determining steps

Chapter 1

General introduction and motivations

1.1 Metal-Organic Frameworks (MOFs): a new class of porous materials

1.1.1 Porous materials

Porosity is an important feature in material science and porous materials offer a wide range of desirable applications, *viz.*, gas storage and separation, catalysis, sensing, energy storage and biomedicine. Two intrinsic features of porous materials, pore size and shape, often emerge as the key aspects that drive properties relevant to potential applications. Following the 2013 International Union of Pure and Applied Chemistry (IUPAC) recommendation on nomenclature, porous materials can be classified into three types based on pore sizes: microporous materials (< 2 nm), mesoporous materials (2-50 nm), and macroporous materials (> 50 nm).[1] Moreover, based on the uniformity of pore shapes, porous materials can also be categorized as amorphous (*e.g.*, activated carbon, porous organic polymers) and crystalline (*e.g.*, zeolites).

With intensive research, the last three decades have witnessed a surge like never before, including but not limited to activated carbon, porous polymers, zeolites, mesoporous silica, metal foams, *etc.*. Among these porous materials, activated carbon and zeolites are two traditional adsorbents with widespread commercial use, often as the state-of-the-art. For example, activated carbon is adept to function in water treatment, abatement of volatile organic compounds (VOCs), to filter materials and carbon-support catalysts.[2] However, non-uniform pore sizes and shapes of activated carbon tend to limit some of their applications, such as size-selective sorption and mass transfer. Zeolites, composed of corner- or edge-sharing $[SiO_4]^{4-}$ or $[AlO_4]^{4-}$ tetrahedra, have regular structures with well-defined pore sizes and shapes.[3] In synergy with their high thermal and chemical stability, zeolites are adopted by a miscellany of industrial applications, such as heterogeneous catalysts, adsorbent materials and ion-exchangers,[2b, 3-4] unsurprisingly making the largest contribution to the global purification industry.

Despite their low cost, traditional inorganic porous materials such as zeolites, are often handicapped by one or more of the performance parameters not aligned well with the desired applications. This is even more prominent in targeted

applications that require task-specific functionalities. Due to the limited tetrahedral modules ($[SiO_4]^{4-}$ and $[AlO_4]^{4-}$), it is difficult to enrich the diversity of synthetic zeolites and endow them with desired features. To create a catalogue of tailor-made *i.e., à la carte* structures that paves the way into desired functions, a wide variety of flexible and versatile organic ligands are self-assembled by coordination chemistry with diverse inorganic nodes/metal clusters, leading to the formation of an emerging group of porous hybrid materials with well-defined, periodic, (usually) crystalline networks: metal-organic frameworks (MOFs).

1.1.2 MOFs with diverse network and functionality

MOFs, also known as porous coordination polymers (PCPs), are constructed by stitching metal ions/clusters with organic bridging ligands to form a coordination network containing potential voids.[5] Compared to the traditional porous materials such as activated carbons and zeolites, MOFs exhibit many attractive features, such as ultrahigh surface areas, adjustable pore structures, and tunable functionalities, *etc.*.[6] For example, MOFs can possess a high surface area of 10000 m^2/g, much higher than zeolites (~1000 m^2/g) and active carbons (up to 3500 m^2/g).[7] In the last two decades, the emergence of MOFs has ushered in striking advances. Thanks to the huge diversity offered by the metals/metal clusters and organic ligands that sustain MOFs, >100,000 different MOFs have been deposited to the Cambridge Structural Database (CSD 2020.3 data release) with various compositions, structures and morphologies, and this number keeps growing.[7-8]

Reflecting on the two decades timeline of the changing state of MOF research, structure-property relationships have classified them into three generations: 1st, 2nd and 3rd (Figure 1.1).[9] The 1st generation MOFs (or coordination polymers (CPs)), were developed in the late 1950s.[10] These frameworks fail to feature permanent porosity, because the structures irreversibly collapse upon removing the guest molecules from the pores (**Figure 1.1a**). It was the late 1990s which saw a big change to the status quo, thanks to the emergence of 2nd generation MOFs. Relying on the pioneering contributions from Yaghi *et al.*,[11] Kitagawa *et al.*,[12] and Ferey *et al.*,[13] MOFs could indeed be endowed with permanent porosity, introduced by HKUST-1 and MOF-5 in 1999.[14] With improved stability and robustness, the MOF structures retained porosity after guest removal (**Figure 1.1b**). This was a typical

paradigm shift, laying the foundation of where MOFs stand now in terms of their immediate relevance to several applications. The 3rd generation MOFs (**Figure 1.1c**), known as soft porous crystals with structurally "dynamic" and adaptable frameworks exhibit reversible responses to one or more of external stimuli (such as light, heat, electric field or specific guest molecules).[9]
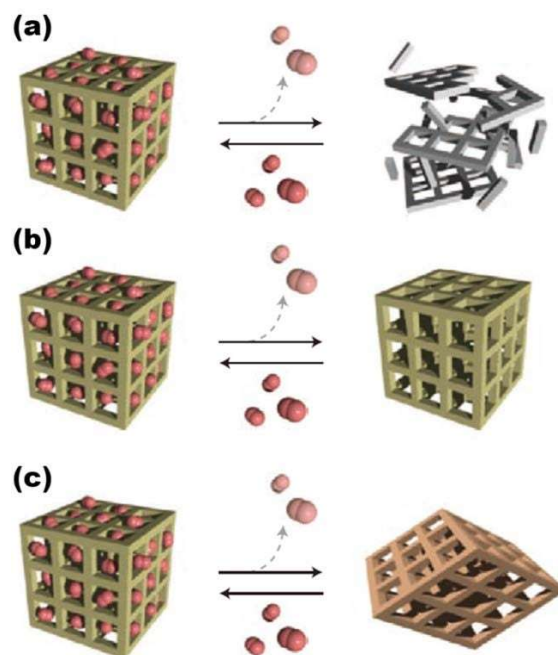
Figure 1.1 Classification of MOFs in three generations. [Reprinted with permission from ref.[9]. Copyright 2009 Macmillan Publishers Limited]

To describe the structure of MOFs, it is important to understand the function of metal clusters, also known as secondary building units (SBUs) in the MOFs design and formation.[15] Bonding of the metal ions to the bridging oxygen or nitrogen atoms of the ligands are known to afford SBUs. Formation of a certain SBU establishes the geometry and connectivity of the metal-organic network, thereby directing the custom-built Lego® approach in compositionally modular MOFs.[15-16] To date, more than 100 SBUs with different geometries and connectivities are known, and some widely used examples are presented in **Figure 1.2a**.[6a, 17] Indeed, the diversity of SBUs contribute to the structural richness of emerging MOFs. Besides the roles in structural diversity and predesigned topology, SBUs also play an important role in the structural stability of MOFs. Normally, MOFs constructed by SBUs with high-valence metal ions show relatively high stability. For example, the Zr_6O_4 cluster composed of Zr(IV) reveals high corrosion-resistance and high oxophilicity, *i.e.*, the affinity to hard oxygen donor ligands (such as, benzene-1,4-dicarboxylate (BDC)).

These contribute to the superior thermal and chemical stability of UiO-66.[18] In addition, SBUs affect or can even dominate several MOF properties, including catalysis,[19] gas adsorption and separation[20].
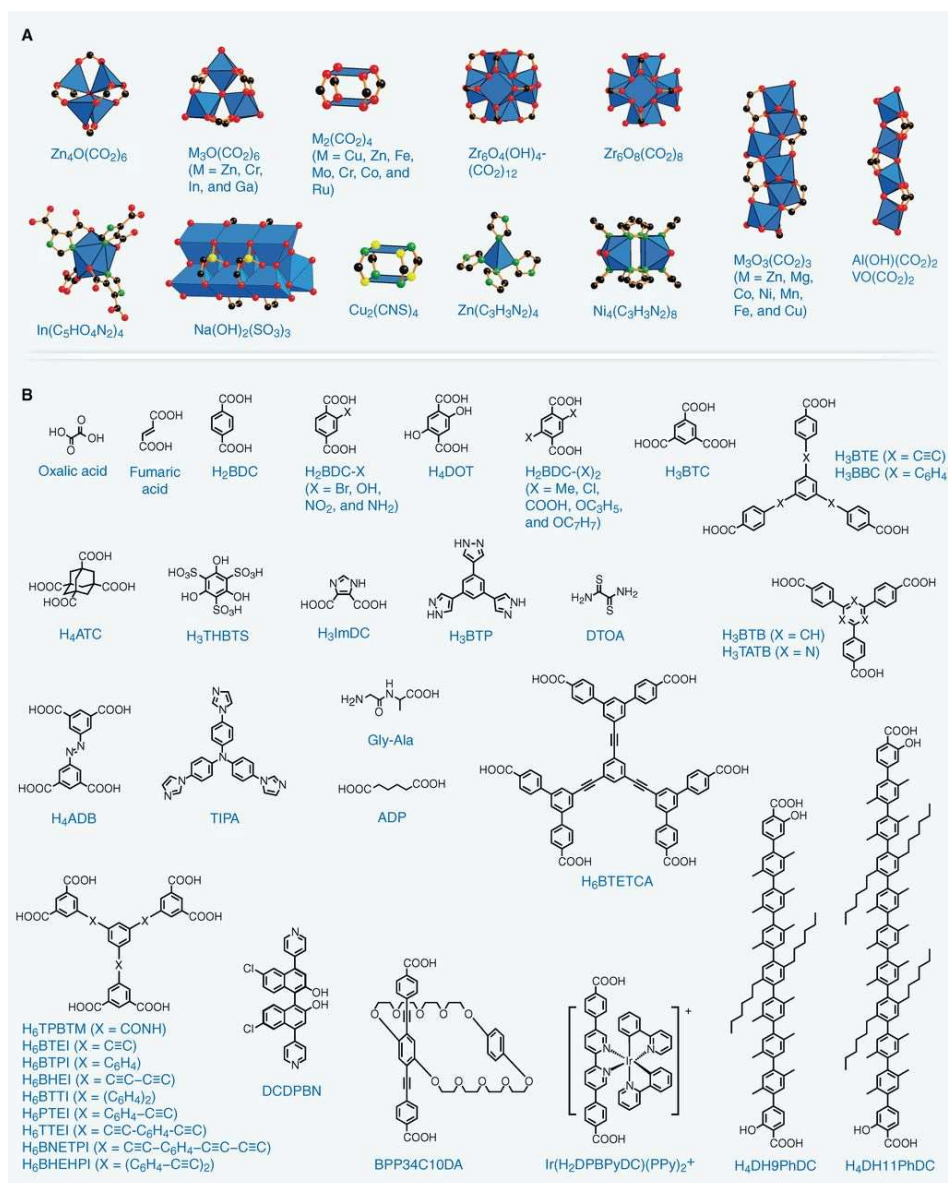
Figure 1.2 Representative inorganic SBUs (A) and organic ligands (B) as MOF building blocks. [Reprinted with permission from ref.[6a]. Copyright 2013 American Association for the Advancement of Science]

Compared to these SBUs, organic ligands benefit from a much higher diversity, with more than 1000 reported in the context of MOFs **(Figure 1.2b)**. Such an abundance of organic ligands enrich the MOF library and enable MOFs with custom-designed structures and properties.[7] The pore apertures of MOFs can be rationally adjusted from 3 to 98 Å by using linkers of different lengths **(Figure**

1.3a).[21] By judicious incorporation of intrinsically functional organic linkers or pre-functionalized linkers with reactive pendant groups, for example, -X (X = F, Cl, Br), -NH$_2$, -NO$_2$ and alkoxy groups, their properties can be regulated **(Figure 1.3b)**.[22]
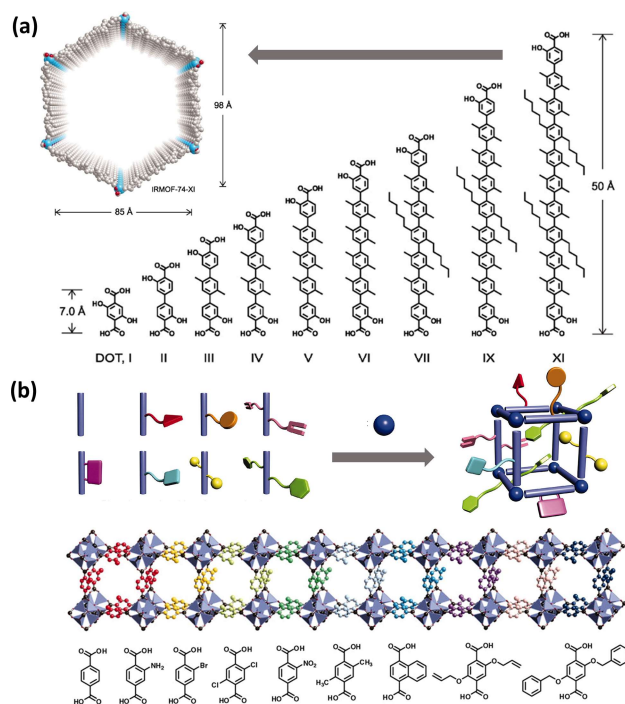
Figure 1.3 (a) Enlargement of the pore sizes of IRMOFs based on the length of organic ligands; (b) Multivariate MOF-5 with eight distinctly functionalized ligands. [Reprinted with permissions from ref.[21a] (a) and [22] (b). Copyrights 2012 and 2010 American Association for the Advancement of Science, respectively]

Over the years, quite a few synthetic methods have been developed to synthesize MOFs. The most common is the solvothermal method, in which metal salts and organic ligands, sometimes accompanied by a modulator, are all directly dissolved in water or organic solvent and heated at certain temperature(s) for several hours or days. This culminates in the synthesis of MOF crystals, sometimes suitable for single crystal X-ray diffraction. Whereas this approach can more often yield high-quality crystals, it tends to suffer from long reaction time, high energy consumption, and solvent waste.[23] To overcome those handicaps, some new methods have come to the fore. For example, microwave-assisted heating shows an accelerated synthesis process, enabling the growth of high-quality uniform crystals over one to several minutes.[24] Synthesis of MOFs with reduced reaction times is also achieved by sonochemical strategy.[25] In addition, mechanochemical synthesis, as a solvent-free approach has found use in producing MOFs with no to

little solvent.[26] Apart from the aforementioned techniques, other methods, such as electrochemical synthesis, catenation control, post-modification synthesis have also been established to synthesize bulk MOFs.[23]

Combining the diversity of both SBUs and organic ligands, MOFs feature plentiful structural possibilities and their chemical/physical properties can be pre-designed and adjusted.[15, 22, 27] MOFs feature high porosity and surface area, great thermal/chemical stability, magnetism, luminescence, chirality, electron/proton conductivity, redox activity, which makes them promising for many applications, *e.g.*, gas storage and separation,[2b] water harvesting,[28] drug delivery,[29] sensing,[30] and catalysis[31].

1.2 Porphyrinic MOFs

1.2.1 Porphyrin
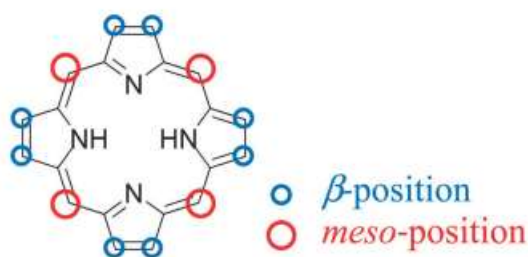
Figure 1.4 The unsubstituted porphyrin macrocycle with four *meso*- and the eight *β*-positions [Reprinted with permission from ref.[32]. Copyright 2013 The Royal Society of Chemistry]

Porphyrins are widely present in nature and are closely related to life sciences, such as chlorophyll, cytochromes, hemoglobins, myoglobins, vitamin B12 and so on.[33] Those Porphyrin compounds play an indispensable role in the metabolism of organisms, such as hemoglobin for the transmission of oxygen, chlorophyll for photosynthesis, *etc.*. The simplest porphyrin, named porphin, is a macrocycle connected to four pyrrole subunits and methylene (=CH-) bridges (**Figure 1.4**).[32] Porphyrin's structure supports a very stable arrangement of aromatic single and double bonds, leading to a highly conjugated molecule with 18 π-electrons. There are two major sites in the porphyrin macrocycle, *meso* and *β*-pyrrole positions, where can be substituted by various substituents. Moreover, at the centre of a porphyrin ring, two protons coordinate to the pyrrole nitrogen, which can be removed. This affords two negative charges to bind with a range of metal ions (*e.g.*,

Mg, Ti, Cr, Mn, Cu, Co, Fe, Ni, Zn, Mo, Ru, Pd, Pt, Au, Tm, Yb, and Lu) to form metalloporphyrins. Therefore, the properties and functions of such metalloporphyrins are tuneable by introducing targeted functional groups on the substitution positions and specific metals embedded in the porphyrin centres.

As typical planar conjugated macrocyclic compounds, porphyrins not only play an important role in nature, but also induce growing research interests in terms of exploiting their potentials in various applications. Thanks to their structural robustness, strong aromaticity, optical/electrical properties, as well as rich metal coordination chemistry, porphyrin derivatives are widely used in biocatalysis,[34] organic solar cells,[32] chemical sensing,[35] semiconductors,[36] molecular electronic devices,[37] photodynamic therapy,[38] and many functional materials such as DNA-binding or fragmentation reagents,[38] light-emitting materials[39] and magnetic materials.[40]

1.2.2 Porphyrinic MOFs (PP-MOFs)

Multifunctional porphyrins with rigid and robust structures can serve as promising linkers for the construction of porphyrinic MOFs. Owing to the ease of modifications, the porphyrins show wide-ranging diversity (**Figure 1.5a**). For example, linker connectivity can be precisely tuned from 2 to 8, and ligand size can be enlarged by introducing longer arms on the tetrapyrrole ring.[41] By coupling ingeniously designed porphyrin ligands and different metal clusters, various PP-MOFs with different topologies and functionalities have been designed and developed, constituting a highly interesting branch of MOFs (**Figure 1.5b**). Even though in their infancy, PP-MOFs received much attention and the number of papers devoted to PP-MOFs presents a stable increase over the last decade.
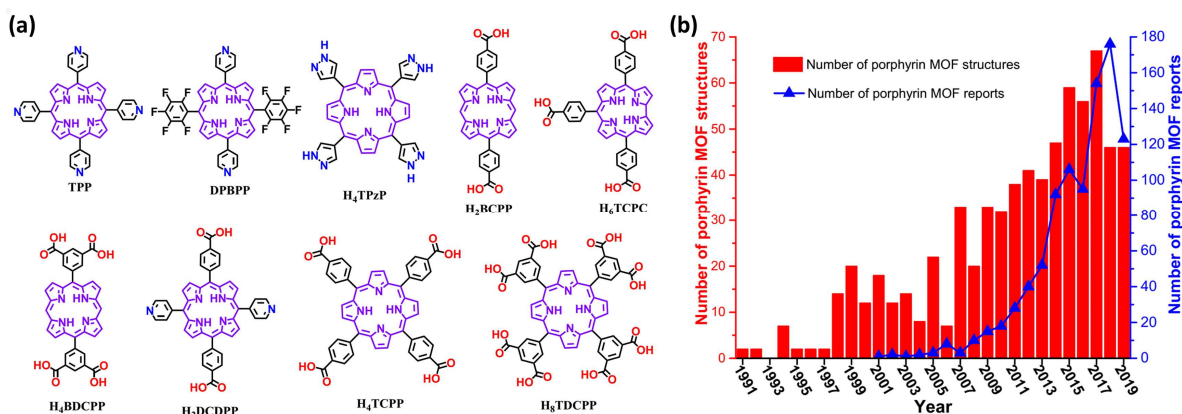
Figure 1.5 (a) Representatives of porphyrin-based ligands for PP-MOFs synthesis. (b)The development of PP-MOFs over decades. [Reprinted with permission from ref.[41a]. Copyright 2020 Elsevier]

The first porphyrin-based coordination polymer was reported in 1991 by Robson *et al.*,[42] with the infinite 3-dimensional structure sustained by Cd^{2+} whereas the 4-connected palladium porphyrins appeared promising for constructing the frameworks with metal ions.

In 1999, Lin *et al.* introduced the first porphyrin-based stable MOF structure after removing guest molecules. This comprised of Co(II)/Mn(II) ions and tetra(4-pyridyl)porphyrin, resulting in a 3D network with large voids.[43] The structural stability stems from the axial coordination of pyridyl arms of a porphyrin with the metal centres of adjacent porphyrins, resulting in an inter-connected framework.

In 2002, Suslick and coworkers developed a microporous porphyrin-based framework, PIZA-1 (PIZA = porphyrinic Illinois zeolite analogue), formed by linear trinuclear Co-based nodes and tetra-(4-carboxyphenyl)porphyrin (TCPP) ligands via strong metal-charged carboxylateporphyrin bonds. PIZA-1 exhibited high structural stability (decomposition at 375 °C).[44] Following this work, several other structurally similar frameworks of the PIZA family were also developed with excellent stability and high microporosity.[45] For example, PIZA-4 possessed excellent thermal stability (400 °C) with a high Langmuir surface area of 800 m^2/g.[46]

These works present the feasibility of porphyrins for the rational construction of PP-MOFs. Since then, PP-MOF structures have increased exponentially, particularly with the emergence of serval typical classes of PP-MOFs, such as the paddle-wheel type two-dimensional (2D) PP-MOFs, three-dimensional (3D) pillared PP-MOFs, Zr-based PP-MOFs.

1.2.2.1 Two-dimensional and three-dimensional pillared PP-MOFs

In the construction of PP-MOFs, porphyrin ligands can easily form the two-dimensional (2D) MOFs nanosheets when coordinating to paddle-wheel subunits (SBUs). Choe group was the first to report a 2D "checkerboard" pattern in PP-MOFs back in 2009, named this as PPF-1. In PPF-1, 4-connected metallated tetra-(4-carboxyphenyl)porphyrins (M-TCPPs) ligand is linked by paddle-wheel SBUs $M_2(COO)_4$ (M = Zn, Co) in a 1:1 ratio (**Figure 1.6a**).[47] Following this work, similar

2D PP-MOFs were also developed by Kitagawa and coworkers in 2010, with subunits of $Cu_2(COO)_4$.[48] Moreover, a typical 2D PP-MOF isostructural to MOF-2 was reported by Christof Wöll and coworkers, the former composed of 2-connected 5,15-(di-4-carboxyphenyl)-10,20-(diphenyl)porphyrin (DCPP) ligands and paddle-wheel $Zn_2(COO)_4$ in a 2:1 ratio.[36] Those 2D PP-MOF possess features, such as excellent photophysics and accessible active sites, beneficial overall to a plethora of photovoltaic, catalytic, electrochemical, phototherapy and sensing applications.[36, 49]

On top of this, the obtained 2D PP-MOFs can be extended to 3D pillared PP-MOFs with the use of additional ditopic ligands (*e.g.*, bipyridyl molecules) as pillars to connect the adjoining 2D layers (**Figure 1.6b**).[50] In the 2D PP-MOFs, there are two vacancies on the axial sites of the paddle-wheel SBUs, available to coordinate with bipyridyl pillars via metal-nitrogen bonds. These pillars extend 2D PP-MOFs along the crystallographic *c* direction to develop 3D connectivity. In addition, the existence of embedded metal ions in metalloporphyrin centres offers a likelihood of associating second ligating sites. However, due to different coordination geometries, the metal ions elicit different coordination environments. For example, three metalloporphyrins M-TCPP (M =Co, Zn, and Pd) exhibit six- (octahedral geometry), five- (square-pyramidal geometry), and four- (square-planar geometry) coordination environments respectively, which means the Co-TCPP can offer two additional pillaring sites, one site from Zn-TCPP, and Pd-TCPP does not participate in coordination with pillars.[50a] Thus by selecting metalloporphyrin ligands, the 2D PP-MOF layers can be pillared in multiple stacking modes, mainly along three classes of patterns, *viz.* AA, AB and ABBA types (**Figure 1.6b**).
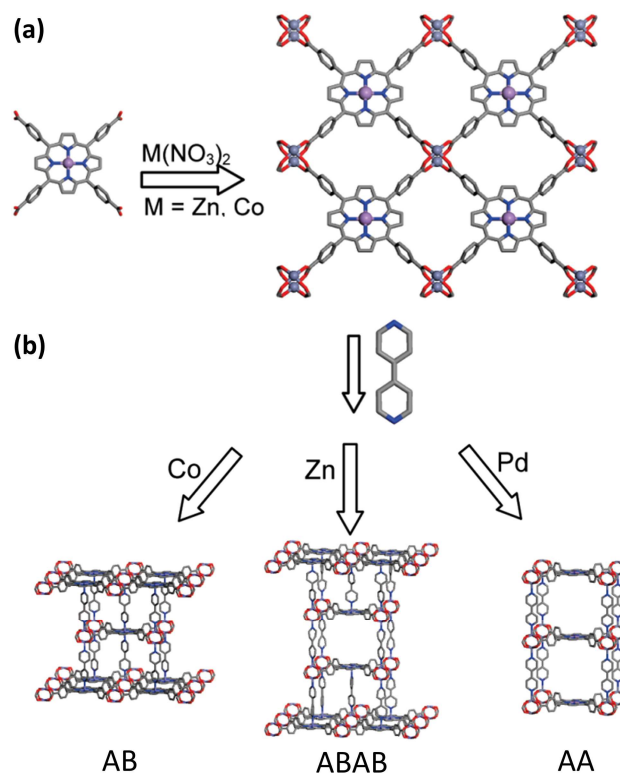
Figure 1.6 (a) 2D pattern PP-MOFs formed with TCPP and paddle-wheel SBUs. (b) The construction of 3D pillared PP-MOFs by connecting the 2D PP-MOF layers by pillar ligands (4,4′-bipyridine, bpy). [Reprinted with permission from ref.[50a]. Copyright 2009 American Chemical Society]

When both the axial sites of the metalloporphyrin and paddle-wheel SBU are valid for coordination, the pillars, in general, cannot identify the available coordinative sites belonging to metal centres of paddle-wheel SBUs or metalloporphyrins. To retain accessible metal centres in PP-MOFs for some target applications, a controlled strategy was developed, for example, by using the pillar of 2,2′-dimethyl-4,4′-bipyridine (DMBPY) instead of 4,4′-bipyridine (bpy).[50c, 51] Owing to steric repulsion from the methyl group, DMBPY features a preferential coordination to paddle-wheel SBU, largely preserving the porphyrin metal centres. This strategy to distinguish the specific metals for framework assembly, directs the synthesis of functional PP-MOFs.

Porphyrins play a role not only as ligands coordinating to paddle-wheel SBUs, but also as a pillar, such as dipyridyl porphyrins. Hupp *et al.* synthesized a highly porous ZnPO-MOF with free-base dipyridyl porphyrins and a tetratopic carboxylate ligand as subunits, in which dipyridyl porphyrins serve as pillars.[52] As an extension of this work, Hupp's group subsequently developed a family of PP-MOFs, named robust porphyrinic materials (RPMs), by incorporating metalloporphyrins (M-TCPP)

and M-bipyridyl porphyrins as struts, in which the 2D layered networks are assembled by the M-TCPPs and paddle-wheel SBUs and then pillared by dipyridyl porphyrin.[53] RPMs possess large pore channels and abundant active metal sites, even two different metal sites by incorporating two distinct metalloporphyrins in a single material, highly intriguing as multi-functional catalysts.

1.2.2.2 Zr-based PP-MOFs

In the steadily evolving family of PP-MOFs, Zr-based PP-MOFs arguably attract the most attention because of their robust structure and excellent thermal/chemical stability.[54] Due to the high charge density, zirconium (IV) cation features high affinity towards oxygen donor ligands and polarizes the oxygen to form highly stable Zr_6-oxo-clusters (e.g. Zr_6O_8 cluster) via the strong Zr—O bonds, thus resulting in the high stability of frameworks.[54] In addition, the connectivity of Zr_6O_8 clusters can be tuned to 6, 8, and 12, contributing to the diverse topologies (such as *she*, *csq* and *ftw*) of Zr-based PP-MOFs (**Figure 1.7**).[41b]
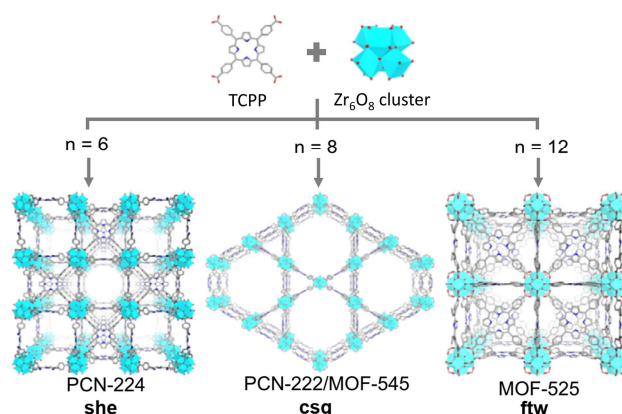
Figure 1.7 Zr-based PP-MOFs formed with 4-connected TCPP and different connected (6, 8, 12) Zr_6O_8 clusters, resulting in diverse topologies. [Reprinted with permission from ref.[41b]. Copyright 2020 Elsevier]

Zhou's group developed a series of Zr-based PP-MOFs employing the symmetric tetrakis(4-carboxyphenyl)porphyrin (TCPP), named porous coordination networks (PCN). The first example as PCN-222 was reported in 2012, combined by M-TCPP (M = H_2, Mn, Fe, Co, Ni, Cu, Zn) with varying central metal ions with the Zr_6 clusters as nodes to construct 3D PP-MOFs.[55] The PCN-222 features highly stable, mesoporous structure with high density of catalytic centres, endowing it superior activity for the catalytic oxidation of various substrates. Subsequently,

several Zr-based PP-MOFs in the PCN family, such as PCN-223/224/225/228, are constructed by the same building units of Zr_6 clusters and TCPP ligands.[56] Due to the intrinsic differences in the connectivity of the Zr_6 cluster and rotation angles of the phenyl arms of the TCPP ligands, these PP-MOFs, including PCN-222, exhibited highly different topologies and pore architectures.[41a] For example, PCN-224 is bridged by 6-connected Zr_6 clusters, constructing the cubic networks (*she*) with ~2 nm micropores;[56b] while, PCN-222 (*csq*) with 8-connected Zr_6 clusters possesses large hexagonal mesochannels of ~3 nm and small trigonal microchannels of 1.3 nm;[55] PCN-223, consisted of 12-connected Zr_6 clusters, feature a *shp-a* network with uniform triangular 1D microchannels of 1.2 nm.[56a] Besides, another typical PP-MOFs, MOF-525, reported by Morris and coworkers, is also linked by 12-connected Zr_6 clusters and TCPP, same with PCN-223, but shows the *ftw* topology with ~2 nm micropores.[57] It is worth mentioning that the TCPP ligand can be further extended, and coordinating to the 12-connected Zr_6 clusters, can lead to the formation of *ftw* topology networks PCN-228, PCN-229, and PCN-230 with higher pore sizes.[56d] These Zr-based PP-MOFs with same subunits and various crystal topologies were realized by varying the synthetic condition (such as ligand/metal ratio, precursor concentration, solvent, pH, and most importantly the modulator and reaction temperature) to form either kinetic or thermodynamic products.[58]

Besides the prototypical Zr_6O_8 node, some other Zr-oxo-clusters also lead to the formation of PP-MOFs. For example, PCN-221 consists of porphyrinic ligands (TCPP) and 12-connected Zr_8O_6 clusters to afford a 3D MOF with *ftw* topology. PCN-221 features two types of polyhedral cages (~1.1 and ~2.0 nm).[59] Another example is the PCN-226, with 3D framework constructed by bridging infinite zigzag ZrO_7 chains with metalloporphyrin molecules (M-TCPP), showing a pore aperture distribution of 0.53−0.78 nm.[60]

All these Zr-based PP-MOFs possess chemical and thermal stability, high density of catalytic centres and excellent photophysical properties, therefore qualifying as excellent candidates to serve a variety of applications, for instance, gas adsorption and separation, biomimetic catalysis, photocatalysis, photodynamic therapy, electrochemical catalysis and catalytic sensing.[41a] Besides the previously mentioned PP-MOFs (paddle-wheel type, pillared, Zr-based), there are still some

typical ones of research hotspots, for example, the 3D PP-MOFs based on the infinite metal china SBUs (Al, Pb, Cd, *etc.*),[61] 6-connected $Fe_3O(COO)_6$ SBUs (PCN-600),[62] and 4-connected $In(COO)_4$ SBUs[63] with the TCPP linkers. Moreover, besides the commonly used carboxylate-based porphyrin (*e.g.*, TCPP), PP-MOFs based on metal-azolate bonds have been proposed by combining the 12-connected Ni_8 clusters and pyrazolate-based porphyrin (PCN-601/602), which can withstand strong basic conditions (*e.g.*, 10 M NaOH).[64] Furthermore, PP-MOFs with mixed metal clusters (ZJU-18)[65] or organic ligands (*e.g.*, PCN-134,[66] PCN-900[67] and UPF-1[68]) have also been reported. All of these suggest the enrichment of PP-MOFs library.

1.2.3 Porphyrinic MOF thin films

MOF thin films are a fast-developing field, which endows various potential applications, including membrane separations, sensing, energy production, electronic devices and optical applications.[69] On this point, PP-MOFs with high porosity and excellent photophysical properties films are one of the most promising candidates for the integration into film-based devices for such applications. Recently, PP-MOF thin films have triggered an upsurge in research interest as regards developing effective film fabrication methods, aimed at the integration of PP-MOFs into specific substrates and devices.

Thus far, several methods have been developed to enable the growth of PP-MOF thin films, *viz.*, direct solvothermal growth,[70] liquid-phase epitaxy (LPE),[36] Langmuir–Blodgett layer-by-layer (LB-LBL) assembly,[48] modular assembly (MA),[71] inkjet printing methods[72].

Direct solvothermal growth: the substrate is immersed into the precursor solutions (metal salts and organic ligands); and during the solvothermal conditions, PP-MOF thin films grow on the substrate surface in an intergrown and continuous mode. To facilitate the nucleation and crystallization of PP-MOFs, substrates are preferably functionalised prior the use. The surface modification on substrate is normally accomplished by depositing self-assembly monolayers (SAMs) with specific functional terminal groups (*e.g.*, carboxyl, hydroxyl, pyridyl groups). For instance, the gold substrate can be modified by 11- mercaptoundecanol (MUD), 16-mercaptohexadecanoic acid (MHDA) and (4,(4-pyridyl)phenyl)-methanethiol (PPMT)

to form hydroxyl, carboxyl and pyridyl groups on surface, respectively.[36, 73] Beside the SAMs, other strategies, such as UV Ozone or O_2 plasma treatment have been utilized to generate the hydroxyl group on surface of oxide substrates, like silicon or glass substrates. These terminal functional groups can coordinate with the metal nodes or organic ligands, contributing to the anchor and nucleation of MOF films.

With the aid of terminal functional groups, solvothermal method provides a facile way to fabricate strongly adhering, homogeneous, and crystalline PP-MOF films, even oriented ones. For example, Bartosz A. Grzybowski and coworkers achieved the growth of PCN-221, PCN-222, and PCN-223 films on a diverse range of substrates, including aluminium/zirconium/zinc/copper foil, glass, FTO, ITO, silicon, polymer.[70] Oriented films were prepared on the Cu foil pretreated with benzoic acid. Lots of other PP-MOFs, such as MOF-525, Al-TCPP-Co, PCN-223, PCN-224, PPF-11 are also successfully integrated into films via this approach for applications in electrochemical sensing, CO_2 reduction, oxygen reduction reaction (ORR), water oxidation, solar cells, *etc*.[74]

Although the method is efficient and versatile, it tolerates some intrinsic drawbacks, including time and energy consumption, as well as a weak control over film thickness and surface morphology (*e.g.*, roughness, grain size and distribution).

Liquid-phase epitaxy (LPE): this method allows the growth of PP-MOF film at relatively low temperatures in a layer-by-layer (LBL) mode, involving alternately immersing the functionalized substrates in metal salt/cluster or organic ligand solutions. The two reactive steps are alternated with rinsing step to remove excess and/or weakly physisorbed reactants.

LPE-LBL can yield highly smooth, homogeneous, oriented and crystalline PP-MOF thin films with controllable thickness by changing the growth cycles, named surface mounted MOFs (SURMOFs). For example, Christof Wöll *et al.* prepared the 2D porphyrin SURMOF 2 on different supports via the LPE-LBL method (**Figure1.8a**).[36] The obtained oriented and crystalline PP-MOF films exhibit superior photophysical properties, enabling fabrication of photovoltaic device. A pillar-layered PP-MOF film was also fabricated on silicon substrate using the efficient LPE-LBL technique **(Figure1.8b),** allowing the potential application of PP-MOF films as solar energy conversion devices with efficient light-harvesting and

energy transport.[75] Besides, benefit from this method, other reported 2D PP-MOF films also show high quality and possess excellent properties, such as photoconductivity, high photocarrier generation efficiency.

The LPE-LBL method is a useful and efficient tool for the PP-MOFs film growth, especially the 2D and 3D pillar-layered PP-MOF (mainly paddlewheel SBU-based networks), but shows low feasibility in film growth of 3D PP-MOF with complex topologies, *e.g.*, the Zr-based PP-MOFs. Moreover, a special deposition set-up, such as pump or spray systems are needed. And normally the pre-prepared SBUs normally is imperative for the nucleation and growth of PP-SURMOFs.
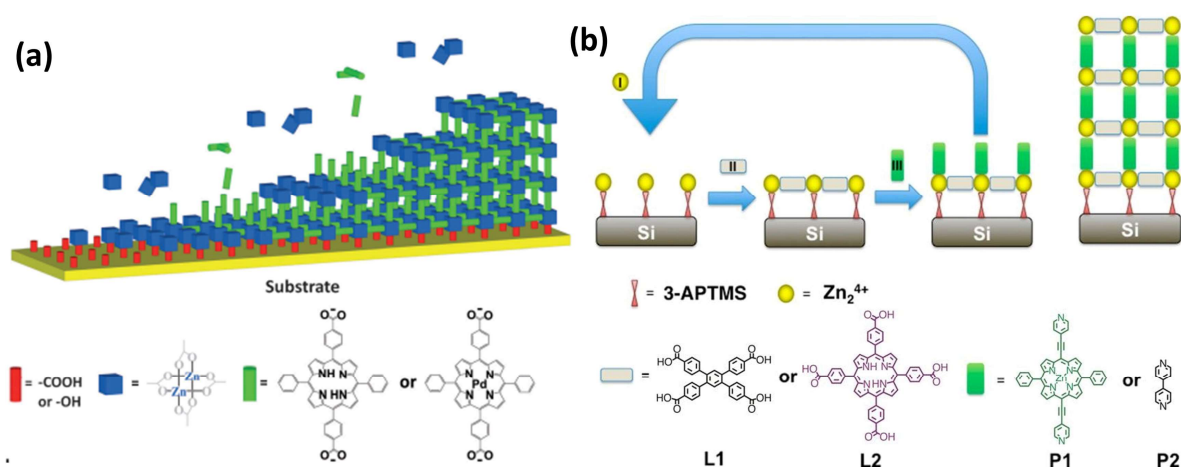
Figure 1.8 Preparation of (a) 2D porphyrin SURMOF 2 and (b) 3D pillared PP-SURMOFs via LPE-LBL method [Reprinted with permission from ref.[36] (a) and [75] (b). Copyright 2015 Wiley-VCH Verlag GmbH & Co. KGaA and 2013 American Chemical Society, respectively]

Langmuir–Blodgett layer-by-layer (LB-LBL) assembly: The LB-LBL approach was proposed by H. Kitagawa and co-workers for the growth of PP-MOF thin film.[48, 76] It is a facile bottom-up method to fabricate oriented and crystalline film on support at room temperature. Simply put, through a spread of the solution of H_2TCPP onto the $CuCl_2$ aqueous solution, seed layer can be formed after compressing the molecules on the surface (the LB technique), 2D PP-MOF layers (H_2TCPP-Cu) are formed on the solution surface (**Figure 1.9**). After that, thin layers are transferred on substrates in the layer-by-layer fashion via a simple dipping process, leading to the sequential growth of PP-MOF films, such as NAFS-1 and NAFS-2.
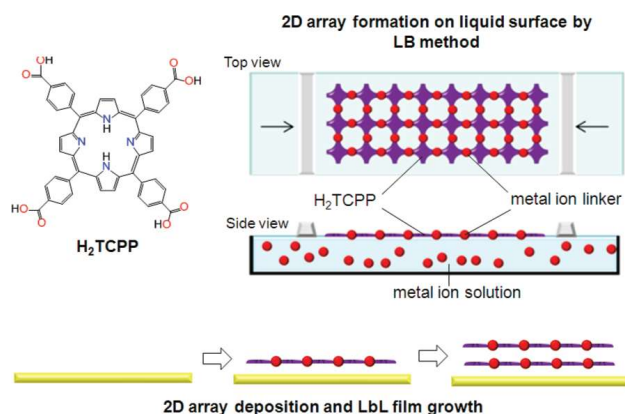
Figure 1.9 Preparation of 2D PP-MOFs via LB-LBL method [Reprinted with permission from ref.[76]. Copyright 2011 American Chemical Society]

Modular assembly (MA): The MA strategy, also developed by H. Kitagawa's group, shows a similar film growth process to LB-LBL approach with a difference in the source of 2D PP-MOF layers.[71] Differing from the Langmuir–Blodgett base formation in LB-LBL, 2D PP-MOFs are solvothermally synthesized and dissolved in ethanol and dispersed by sonication, serving as precursors of well-ordered seed layer. After a spread of the layers on water and a similar stamping transfer, ordered, homogenous and crystalline PP-MOF films are formed (**Figure 1.10**). The feasibility of MA technique is confirmed by the successful deposition of Cu-TCPP thin films, and the high-quality film showed excellent proton transport.[71, 77]
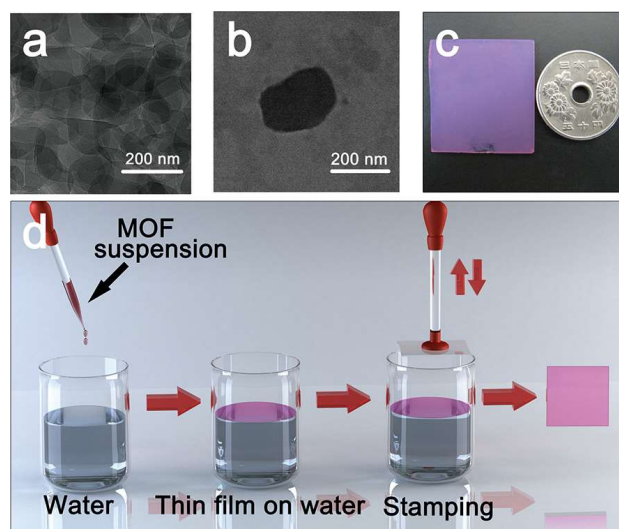
Figure 1.10 (a, b) TEM images of the solvothermally synthesized Cu−TCPP nanosheets. (c) Photograph of the Cu−TCPP thin film of 15 cycles. (d) Modular assembly for the fabrication of Cu−TCPP thin film. [Reprinted with permission from ref.[71]. Copyright 2012 American Chemical Society]

Apart from the feasibility in 2D PP-MOF films fabrication, solvothermally

synthesized precursors allow its perspective in facile and straightforward film growth of complex 3D PP-MOFs (*e.g.*, Zr-based PP-MOFs), which cannot be achieved in the LB-LBL process.

Inkjet printing: This technique for PP-MOF film fabrication involves the preparation of a well-dispersed suspension of the as-synthesized PP-MOF crystals and using it as the ink for inkjet printing directly. Liao *et al.* prepared uniform MOF-525 film patterns on conductive ITO glass using this method for electrochemical sensing;[72] while this approach cannot avoid particle sedimentation of ink and nozzle clogging due to the big particle size and particle aggregation, which hindering the application of inkjet printing. On top of it, a special set-up is necessary for printing process.

Although several methods have been established to prepare PP-MOF thin films, each one features limited feasibility. Hence, the efforts to develop facile and effective approaches for the growth of PP-MOF film with high quality (homogenous, oriented, crystalline, thickness-controllable) have never been ceased, offering the cornerstone for their further specific applications.

1.2.4 Porphyrinic MOF derived porous M-N-C matrix

Most MOFs suffer from limited charge transfer, despite the recent advances on strategic improvements, such as integration as thin films with improved interfacial contact, introduction of guest molecules in pores, composites with carbon material.[36, 78] Recently, a novel strategy based on the conversion of MOFs into more conductive materials such as porous carbons (PCs) has emerged, attractive in applications (*e.g.*, electrocatalysts) where high charge mobility and improved flexibility are of priority.[79] By judiciously selecting specific MOFs and carbonization conditions, MOF-derived PCs enable a facile and straightforward control on the pore and shape, as well as heteroatomic (*e.g.*, nitrogen, oxygen, sulfur, phosphorus, *etc.*) loading. Therefore, with extended surface areas and hierarchical pores, the MOF-derived PCs possess intrinsic merit on the diffusion of substrates. Moreover, the periodic MOF structures show congenital superiority for homogeneous distribution of specific atoms, even throughout the PCs after pyrolysis. Moreover, the high degree level of graphitized carbon endows the materials an excellent electrical conductivity as well as chemical and thermal stabilities.
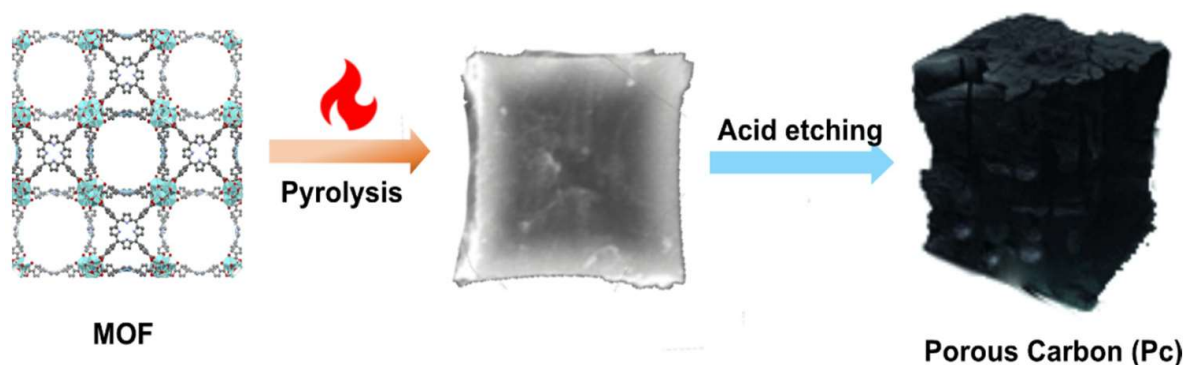
Figure 1.11 Preparation of MOF derived PCs with PP-MOFs as precursors. [Reprinted with permission from ref.[79]. Copyright 2021 Multidisciplinary Digital Publishing Institute]

Increased researchers' attention is observed on the transformation of PP-MOFs as PCs (**Figure 1.11**). Due to their rich nitrogen atoms and various possibility of metal centres (*e.g.*, Ni, Fe, Co, Cu) in porphyrin ligands, PP-MOFs offer the opportunity to prepare a range of M–N–C type materials with highly stable and catalytically active M–N_4 moieties.[79] Combining the excellent electrical conductivity, the M–N–C materials, thus, are promising candidates for the application in various electrocatalysis, such as oxygen-reduction reaction (ORR), water splitting (hydrogen evolution reactions (HER) and oxygen evolution reaction (OER)), carbon dioxide reduction reaction (CO_2RR), nitrogen reduction reaction (NRR), nitrophenol reduction, *etc*..[79]

On top of this, catalytic properties of M-N-C can be regulated simply by adjusting the incorporation of metal elements of different mass ratios, species, kinds (single or bimetallic). By adapting a mixed-ligand strategy by using both metal-free porphyrin and metalloporphyrin, the metal ratio in M-N-C can be changed. When dwindling the incorporation ratio of metalloporphyrin, the distance of adjacent metalloporphyrin ligands is expanded; thus, aggregation of metal species can be effectively suppressed at an atomic level, resulting in formation of single atom metal site implanted porous N-doped carbon.[80] This type of single atom catalysis (SACs) achieve the utmost utilization of metal sites, therefore greatly enhancing the catalytic efficiency.

The metal species in M-N-C materials significantly affect the catalytic performance in specific applications. For example, Ni-N-C exhibits a superior CO Faradaic efficiency (FE) of 96.8%, much better than Fe-, Co- and Cu-N-C in

electrocatalytic CO_2 reduction.[81] While, Fe-N-C shows a high FE of 4.51% and an ammonia yield rate of 1.56 ×10^{-11} mol cm^{-2} s^{-1} in NRR, surpassing Co- and Ni-N-C.[82]

Besides the single metal species, bimetallic M-N-C materials also are proposed for synergetic effect in electrochemical applications. For example, Jiang and coworkers prepared a bimetallic Fe/Co-N-C from the pyrolysis of PCN-224-FeCo.[83] The FeN_x sites provide superior catalytic activity and CoN_x sites boost a high-level graphitization, synergetically resulting in the outstanding ORR performance on the bimetallic Fe/Co-N-C catalyst.

1.3 Motivation and outlines

As discussed above, PP-MOFs serve as promising candidates for various specific applications, especially after the integration as thin film or conversion to active M-N-C PCs. However, in the field of thin films and derived M-N-C materials, there still are several unmet challenges: 1: although several film fabrication techniques have been developed, it is still challenging to grow PP-MOF thin films, especially 3D PP-MOFs, of high quality, combining good crystallinity, controllable orientation, adjustable morphology and thickness, all in one; Moreover, in-depth understanding of the PP-MOF film's nucleation and growth processes is an uncharted territory; 2: a systematical exploration unveiling original impetus of PP-MOF films and fully leveraging their potentials into specific real-world applications is unsatisfactory, e.g. sensing; 3: for the M-N-C catalysts originating from PP-MOFs, how to optimize the materials with desired functionalities and enhanced specific catalytic properties is still an unresolved matter. Surrounded by these issues, this thesis mainly aims at 1: developing a facile and versatile strategy to integrate PP-MOFs as high-quality thin films, and systematically the nucleation and growth processes after rational comparison with various other useful methods; 2: exploring the maximal potential of PP-MOF thin film as an electrochemical sensor for a variety of substances; 3: precisely regulating the catalytic sites in M-N-C matrix at the atom level, and further exploiting the potential in electrocatalytic methanol oxidation. A detailed description of each chapter is as follows:

Chapter 2 introduces and develops a vapor-assisted conversion (VAC) method to grow PP-MOF thin films on various substrates (*viz.*, Au, silicon wafer, ITO glass).

To further explore the nucleation and growth mechanism of PP-MOF films, a variety of other useful methods (*viz.*, solvothermal, modular assembly, LPE-LBL) also were used to prepare them by using PP-MOFs of varying dimensionalities: 2D and 3D. Our studies demonstrate that PP-MOF films are likely to feature different nucleation and growth processes under different deposition strategies. This study comprehensively analyses the pros and cons of different fabrication methods that have led to functional PP-MOF films. In addition to the first utilization of VAC method to fabricate PP-MOF films, this inclusive study is primed to serve as a reference point in the future, intimately linked with the topical research advances on MOF films preparation and their controlled growth.

Chapter 3 describes a well-known PP-MOF, Mn-PCN-222, integrated as a thin film on the conductive indium tin oxide (ITO) surface. The resulting Mn-PCN-222/ITO demonstrates multifaceted voltammetric sensing of several inorganic ions, organic hazardous substances and pollutants, *viz.*, nitroaromatics, phenolic and quinone-hydroquinone toxins, heavy metal ions, biological species, as well as azo dyes. The nitrobenzene (NB) was chosen as a model toxin to optimize the critical parameters, *e.g.*, scan rate, pH, accumulation time based on the cyclic voltammetry (CV). It also offers to study selectivity, stability, recyclability and reproducibility of the sensor. All our studied toxin detections are marked with wide linear ranges and low limits of detection, ideal for transitioning to higher technological readiness levels. The high sensing efficiencies are sustained beyond just single substrates, binary and tertiary systems of increased complexity also register performances likewise. The periodic and porous PP-MOF platform with ordered and accessible metalloporphyrin redox sites offers the right features of high-density active sites, large surface area, 1D mesochannels to facilitate rapid analyte aggregation and mass transport, key factors to enable sensitive sensing. An optimal combination of selectivity, long-term stability, and reproducibility of Mn-PCN-222/ITO is discovered, unparalleled among the current MOF-based electrochemical sensors. In essence, Mn-PCN-222/ITO is primed to serve as a reference point while designing the next-generation versatile electrochemical sensors.

Chapter 4. Here we synthesize Ni-PCN-222 and convert it into Ni sites incorporated porous N-doped carbon via pyrolysis, named as Ni-N-C. The catalytic Ni sites are highly dispersed in a single atom level by a mixed ligand strategy. By

incorporating 20% Ni-TCPP and 80% free-metal H_2TCPP as organic ligands, the obtained 20% Ni-PCN-222 is transformed under pyrolysis. We achieve single Ni atoms distribution in N-doped PCs, named 20% Ni-N-C. The derived 20% Ni-N-C catalysts exhibit electrocatalytic properties towards methanol oxidation reaction (MOR). Benefiting from the single-atom Ni sites, hierarchical pores, oriented mesochannels, excellent conductivity and stable Ni-N_4 moieties, the derived 20% Ni-N-C registers high electrocatalytic activity towards methanol oxidation reaction (MOR) alongside long-time stability.

Chapter 5 demonstrates the experimental details and characterizations in Chapters 2-4. The details, including porphyrin ligands synthesis and PP-MOFs powder preparation and thin film fabrication by various strategies, as well as the transformation process of porous Ni-N-C matrixs, are all described. A variety of characterization details (such as XRD, ATR-IR, sorption isotherms, SEM, TEM, UV-Vis, NMR, cyclic voltammetry (CV) and Raman) are included. Moreover, part of the supplementary data of Chapters 3 and 4 is presented here in this chapter, to avoid repetition.

Chapter 6 summarizes the thesis findings and summarize the future perspectives along this research field. This thesis aims at the preparation of high-quality PP-MOF films and single-atom Ni-N-C catalysts derived from PP-MOFs, further exploring their potential applications in voltammetric sensing and electrocatalytic MOR.

1.4 References

[1]   J. Rouquerol, D. Avnir, C. Fairbridge, D. Everett, J. Haynes, N. Pernicone, J. Ramsay, K. Sing, K. Unger, *Pure Appl. Chem.* **1994**, *66*, 1739.

[2]   a) M. Danish, T. Ahmad, *Renew. Sustain. Energy Rev.* **2018**, *87*, 1-21; b) L. Zhu, D. Shen, K. H. Luo, *J. Hazard. Mater.* **2020**, *389*, 122102.

[3]   B. M. Weckhuysen, J. Yu, *Chem. Soc. Rev.* **2015**, *44*, 7022-7024.

[4]   V. J. Inglezakis, *J. Colloid Interface Sci.* **2005**, *281*, 68-79.

[5]   a) H. C. Zhou, J. R. Long, O. M. Yaghi, *Chem. Rev.* **2012**, *112*, 673-674; b) S. Kitagawa, R. Kitaura, S. i. Noro, *Angew. Chem. Int. Ed.* **2004**, *43*, 2334-2375.

[6]   a) H. Furukawa, K. E. Cordova, M. O'Keeffe, O. M. Yaghi, *Science* **2013**, *341*, 1230444; b) X. Zhang, Z. Chen, X. Liu, S. L. Hanna, X. Wang, R. Taheri-Ledari, A. Maleki, P. Li, O. K. Farha, *Chem. Soc. Rev.* **2020**, *49*, 7406-7427.

[7]   P. Z. Moghadam, A. Li, S. B. Wiggin, A. Tao, A. G. P. Maloney, P. A. Wood, S. C. Ward, D. Fairen-Jimenez, *Chem. Mater.* **2017**, *29*, 2618-2625.

[8]   P. Z. Moghadam, A. Li, X. W. Liu, R. Bueno-Perez, S. D. Wang, S. B. Wiggin, P. A. Wood, D. Fairen-Jimenez, *Chem. Sci.* **2020**, *11*, 8373-8387.

[9]   S. Horike, S. Shimomura, S. Kitagawa, *Nat. Chem.* **2009**, *1*, 695-704.

[10]   Y. Kinoshita, I. Matsubara, T. Higuchi, Y. Saito, *Bull. Chem. Soc. Jpn.* **1959**, *32*, 1221-1226.

[11]   O. M. Yaghi, G. Li, H. Li, *Nature* **1995**, *378*, 703-706.

[12]   M. Kondo, T. Yoshitomi, H. Matsuzaka, S. Kitagawa, K. Seki, *Angew. Chem. Int. Ed.* **1997**, *36*, 1725-1727.

[13]   D. Riou, G. Férey, *J. Mater. Chem.* **1998**, *8*, 2733-2735.

[14]   a) S. S.-Y. Chui, S. M.-F. Lo, J. P. H. Charmant, A. G. Orpen, I. D. Williams, *Science* **1999**, *283*, 1148-1150; b) H. Li, M. Eddaoudi, M. O'Keeffe, O. M. Yaghi, *nature* **1999**, *402*, 276-279.

[15]   M. J. Kalmutzki, N. Hanikel, O. M. Yaghi, *Sci. Adv.* **2018**, *4*, eaat9180.

[16]   U. Schubert, *Chem. Soc. Rev.* **2011**, *40*, 575-582.

[17]   D. J. Tranchemontagne, J. L. Mendoza-Cortes, M. O'Keeffe, O. M. Yaghi, *Chem. Soc. Rev.* **2009**, *38*, 1257-1283.

[18]   M. Kandiah, M. H. Nilsen, S. Usseglio, S. Jakobsen, U. Olsbye, M. Tilset, C. Larabi, E. A. Quadrelli, F. Bonino, K. P. Lillerud, *Chem. Mater.* **2010**, *22*, 6632-6640.

[19] a) E. D. Metzger, C. K. Brozek, R. J. Comito, M. Dinca, *ACS Cent. Sci.* **2016**, *2*, 148-153; b) J. Jiang, F. Gandara, Y. B. Zhang, K. Na, O. M. Yaghi, W. G. Klemperer, *J. Am. Chem. Soc.* **2014**, *136*, 12844-12847.

[20] a) P. D. Dietzel, R. E. Johnsen, H. Fjellvag, S. Bordiga, E. Groppo, S. Chavan, R. Blom, *Chem. Commun.* **2008**, 5125-5127; b) E. D. Bloch, W. L. Queen, R. Krishna, J. M. Zadrozny, C. M. Brown, J. R. Long, *science* **2012**, *335*, 1606-1610.

[21] a) H. Deng, S. Grunder, K. E. Cordova, C. Valente, H. Furukawa, M. Hmadeh, F. Gándara, A. C. Whalley, Z. Liu, S. Asahina, *science* **2012**, *336*, 1018-1023; b) L. Chen, J. W. Ye, H. P. Wang, M. Pan, S. Y. Yin, Z. W. Wei, L. Y. Zhang, K. Wu, Y. N. Fan, C. Y. Su, *Nat. Commun.* **2017**, *8*, 15985.

[22] H. Deng, C. J. Doonan, H. Furukawa, R. B. Ferreira, J. Towne, C. B. Knobler, B. Wang, O. M. Yaghi, *Science* **2010**, *327*, 846-850.

[23] S. T. Meek, J. A. Greathouse, M. D. Allendorf, *Adv. Mater.* **2011**, *23*, 249-267.

[24] Z. Ni, R. I. Masel, *J. Am. Chem. Soc.* **2006**, *128*, 12394-12395.

[25] W. J. Son, J. Kim, J. Kim, W. S. Ahn, *Chem. Commun.* **2008**, 6336-6338.

[26] A. Pichon, A. Lazuen-Garay, S. L. James, *CrystEngComm* **2006**, *8*, 211.

[27] M. Zhang, M. Bosch, T. Gentle Iii, H.-C. Zhou, *CrystEngComm* **2014**, *16*, 4069-4083.

[28] J. Canivet, A. Fateeva, Y. Guo, B. Coasne, D. Farrusseng, *Chem. Soc. Rev.* **2014**, *43*, 5594-5617.

[29] M. X. Wu, Y. W. Yang, *Adv. Mater.* **2017**, *29*.

[30] L. E. Kreno, K. Leong, O. K. Farha, M. Allendorf, R. P. Van Duyne, J. T. Hupp, *Chem. Rev.* **2011**, *112*, 1105-1125.

[31] J. Lee, O. K. Farha, J. Roberts, K. A. Scheidt, S. T. Nguyen, J. T. Hupp, *Chem. Soc. Rev.* **2009**, *38*, 1450-1459.

[32] L. L. Li, E. W. Diau, *Chem. Soc. Rev.* **2013**, *42*, 291-304.

[33] a) E. Rose, A. Lecas, M. Quelquejeu, A. Kossanyi, B. Boitrel, *Coord. Chem. Rev.* **1998**, *178-180*, 1407-1431; b) T. K. Chandrashekar, S. Venkatraman, *Acc. Chem. Res.* **2003**, *36*, 676-691; c) A. Jasat, D. Dolphin, *Chem. Rev.* **1997**, *97*, 2267-2340; d) C. F. Pereira, M. M. Simoes, J. P. Tome, F. A. Almeida Paz, *Molecules* **2016**, *21*.

[34] J. C. Barona-Castano, C. C. Carmona-Vargas, T. J. Brocksom, K. T. de

Oliveira, *Molecules* **2016**, *21*, 310.

[35] H. Lee, K.-I. Hong, W.-D. Jang, *Coord. Chem. Rev.* **2018**, *354*, 46-73.

[36] J. Liu, W. Zhou, J. Liu, I. Howard, G. Kilibarda, S. Schlabach, D. Coupry, M. Addicoat, S. Yoneda, Y. Tsutsui, T. Sakurai, S. Seki, Z. Wang, P. Lindemann, E. Redel, T. Heine, C. Woll, *Angew. Chem. Int. Ed.* **2015**, *54*, 7441-7445.

[37] M. Jurow, A. E. Schuckman, J. D. Batteas, C. M. Drain, *Coord. Chem. Rev.* **2010**, *254*, 2297-2310.

[38] H. Huang, W. Song, J. Rieffel, J. F. Lovell, *Front. Phys.* **2015**, *3*.

[39] B. Li, J. Li, Y. Fu, Z. Bo, *J. Am. Chem. Soc.* **2004**, *126*, 3430-3431.

[40] H. Wende, M. Bernien, J. Luo, C. Sorg, N. Ponpandian, J. Kurde, J. Miguel, M. Piantek, X. Xu, P. Eckhold, W. Kuch, K. Baberschke, P. M. Panchmatia, B. Sanyal, P. M. Oppeneer, O. Eriksson, *Nat. Mater.* **2007**, *6*, 516-520.

[41] a) X. Zhang, M. C. Wasson, M. Shayan, E. K. Berdichevsky, J. Ricardo-Noordberg, Z. Singh, E. K. Papazyan, A. J. Castro, P. Marino, Z. Ajoyan, Z. Chen, T. Islamoglu, A. J. Howarth, Y. Liu, M. B. Majewski, M. J. Katz, J. E. Mondloch, O. K. Farha, *Coord. Chem. Rev.* **2021**, *429*; b) L. Feng, K.-Y. Wang, E. Joseph, H.-C. Zhou, *Trends Chem.* **2020**, *2*, 555-568; c) W. Y. Gao, M. Chrzanowski, S. Ma, *Chem. Soc. Rev.* **2014**, *43*, 5841-5866.

[42] B. F. Abrahams, B. F. Hoskins, R. Robson, *J. Am. Chem. Soc.* **1991**, *113*, 3606-3607.

[43] K. J. Lin, *Angew. Chem. Int. Ed.* **1999**, *38*, 2730-2732.

[44] M. E. Kosal, J.-H. Chou, S. R. Wilson, K. S. Suslick, *Nat. Mater.* **2002**, *1*, 118-121.

[45] K. S. Suslick, P. Bhyrappa, J.-H. Chou, M. E. Kosal, S. Nakagaki, D. W. Smithenry, S. R. Wilson, *Acc. Chem. Res.* **2005**, *38*, 283-291.

[46] D. W. Smithenry, S. R. Wilson, K. S. Suslick, *Inorg. Chem.* **2003**, *42*, 7719-7721.

[47] M. Laurent, J.-L. Ricard, J.-J. Bahain, P. Voinchet, L. Rousseau, *C. r. Acad. Sci., Ser. 2, Earth Planet. Sci.* **2000**, *330*, 581-583.

[48] R. Makiura, S. Motoyama, Y. Umemura, H. Yamanaka, O. Sakata, H. Kitagawa, *Nat. Mater.* **2010**, *9*, 565-571.

[49] a) M. Zhao, Y. Wang, Q. Ma, Y. Huang, X. Zhang, J. Ping, Z. Zhang, Q. Lu, Y. Yu, H. Xu, Y. Zhao, H. Zhang, *Adv. Mater.* **2015**, *27*, 7372-7378; b) Y. Xiao,

W. Guo, H. Chen, H. Li, X. Xu, P. Wu, Y. Shen, B. Zheng, F. Huo, W. D. Wei, *Mater. Chem. Front.* **2019**, *3*, 1580-1585; c) B. Li, X. Wang, L. Chen, Y. Zhou, W. Dang, J. Chang, C. Wu, *Theranostics* **2018**, *8*, 4086-4096; d) Y. Zhao, L. Jiang, L. Shangguan, L. Mi, A. Liu, S. Liu, *J. Mater. Chem. A* **2018**, *6*, 2828-2833; e) Y. Wang, M. Zhao, J. Ping, B. Chen, X. Cao, Y. Huang, C. Tan, Q. Ma, S. Wu, Y. Yu, Q. Lu, J. Chen, W. Zhao, Y. Ying, H. Zhang, *Adv. Mater.* **2016**, *28*, 4149-4155.

[50] a) E.-Y. Choi, P. M. Barron, R. W. Novotny, H.-T. Son, C. Hu, W. Choe, *Inorg. Chem.* **2009**, *48*, 426-428; b) H. Chung, P. M. Barron, R. W. Novotny, H.-T. Son, C. Hu, W. Choe, *Cryst. Growth Des.* **2009**, *9*, 3327-3332; c) C. Zou, C.-D. Wu, *Dalton Trans.* **2012**, *41*, 3879-3888.

[51] P. M. Barron, C. A. Wray, C. Hu, Z. Guo, W. Choe, *Inorg. Chem.* **2010**, *49*, 10217-10219.

[52] A. M. Shultz, O. K. Farha, J. T. Hupp, S. T. Nguyen, *J. Am. Chem. Soc.* **2009**, *131*, 4204-4205.

[53] O. K. Farha, A. M. Shultz, A. A. Sarjeant, S. T. Nguyen, J. T. Hupp, *J. Am. Chem. Soc.* **2011**, *133*, 5652-5655.

[54] Y. Bai, Y. Dou, L. H. Xie, W. Rutledge, J. R. Li, H. C. Zhou, *Chem. Soc. Rev.* **2016**, *45*, 2327-2367.

[55] D. Feng, Z. Y. Gu, J. R. Li, H. L. Jiang, Z. Wei, H. C. Zhou, *Angew. Chem. Int. Ed.* **2012**, *51*, 10307-10310.

[56] a) D. Feng, Z. Y. Gu, Y. P. Chen, J. Park, Z. Wei, Y. Sun, M. Bosch, S. Yuan, H. C. Zhou, *J. Am. Chem. Soc.* **2014**, *136*, 17714-17717; b) D. Feng, W. C. Chung, Z. Wei, Z. Y. Gu, H. L. Jiang, Y. P. Chen, D. J. Darensbourg, H. C. Zhou, *J. Am. Chem. Soc.* **2013**, *135*, 17105-17110; c) H. L. Jiang, D. Feng, K. Wang, Z. Y. Gu, Z. Wei, Y. P. Chen, H. C. Zhou, *J. Am. Chem. Soc.* **2013**, *135*, 13934-13938; d) T. F. Liu, D. Feng, Y. P. Chen, L. Zou, M. Bosch, S. Yuan, Z. Wei, S. Fordham, K. Wang, H. C. Zhou, *J. Am. Chem. Soc.* **2015**, *137*, 413-419.

[57] W. Morris, B. Volosskiy, S. Demir, F. Gandara, P. L. McGrier, H. Furukawa, D. Cascio, J. F. Stoddart, O. M. Yaghi, *Inorg. Chem.* **2012**, *51*, 6443-6445.

[58] X. Gong, H. Noh, N. C. Gianneschi, O. K. Farha, *J. Am. Chem. Soc.* **2019**, *141*, 6146-6151.

[59] D. Feng, H. L. Jiang, Y. P. Chen, Z. Y. Gu, Z. Wei, H. C. Zhou, *Inorg. Chem.* **2013**, *52*, 12661-12667.

[60] M. O. Cichocka, Z. Liang, D. Feng, S. Back, S. Siahrostami, X. Wang, L. Samperisi, Y. Sun, H. Xu, N. Hedin, H. Zheng, X. Zou, H. C. Zhou, Z. Huang, *J. Am. Chem. Soc.* **2020**, *142*, 15386-15395.

[61] a) M. H. Xie, X. L. Yang, C. D. Wu, *Chem. Commun.* **2011**, *47*, 5521-5523; b) A. Fateeva, P. A. Chater, C. P. Ireland, A. A. Tahir, Y. Z. Khimyak, P. V. Wiper, J. R. Darwent, M. J. Rosseinsky, *Angew. Chem. Int. Ed.* **2012**, *51*, 7440-7444; c) C. Zou, M.-H. Xie, G.-Q. Kong, C.-D. Wu, *CrystEngComm* **2012**, *14*, 4850.

[62] K. Wang, D. Feng, T. F. Liu, J. Su, S. Yuan, Y. P. Chen, M. Bosch, X. Zou, H. C. Zhou, *J. Am. Chem. Soc.* **2014**, *136*, 13983-13986.

[63] Z. Lin, Z. M. Zhang, Y. S. Chen, W. Lin, *Angew. Chem. Int. Ed.* **2016**, *128*, 13943-13947.

[64] a) K. Wang, X. L. Lv, D. Feng, J. Li, S. Chen, J. Sun, L. Song, Y. Xie, J. R. Li, H. C. Zhou, *J. Am. Chem. Soc.* **2016**, *138*, 914-919; b) X. L. Lv, K. Wang, B. Wang, J. Su, X. Zou, Y. Xie, J. R. Li, H. C. Zhou, *J. Am. Chem. Soc.* **2017**, *139*, 211-217.

[65] X. L. Yang, M. H. Xie, C. Zou, Y. He, B. Chen, M. O'Keeffe, C. D. Wu, *J. Am. Chem. Soc.* **2012**, *134*, 10638-10645.

[66] S. Yuan, J. S. Qin, L. Zou, Y. P. Chen, X. Wang, Q. Zhang, H. C. Zhou, *J. Am. Chem. Soc.* **2016**, *138*, 6636-6642.

[67] L. Zhang, S. Yuan, L. Feng, B. Guo, J. S. Qin, B. Xu, C. Lollar, D. Sun, H. C. Zhou, *Angew. Chem. Int. Ed.* **2018**, *57*, 5095-5099.

[68] E. Jin, I. S. Lee, D. Kim, H. Lee, W.-D. Jang, M. S. Lah, S. K. Min, W. Choe, *Sci. Adv.* **2019**, *5*, eaav4119.

[69] J. Liu, C. Woll, *Chem. Soc. Rev.* **2017**, *46*, 5730-5770.

[70] S. M. Yoon, J. H. Park, B. A. Grzybowski, *Angew. Chem. Int. Ed.* **2017**, *56*, 127-132.

[71] G. Xu, T. Yamada, K. Otsubo, S. Sakaida, H. Kitagawa, *J. Am. Chem. Soc.* **2012**, *134*, 16524-16527.

[72] C.-H. Su, C.-W. Kung, T.-H. Chang, H.-C. Lu, K.-C. Ho, Y.-C. Liao, *J. Mater. Chem. A* **2016**, *4*, 11094-11102.

[73] B. Liu, O. Shekhah, H. K. Arslan, J. Liu, C. Woll, R. A. Fischer, *Angew. Chem. Int. Ed.* **2012**, *51*, 807-810.

[74] a) C.-W. Kung, T.-H. Chang, L.-Y. Chou, J. T. Hupp, O. K. Farha, K.-C. Ho, *Electrochem. Commun.* **2015**, *58*, 51-56; b) X. Gao, S. DelaCruz, C. Zhu, S. Cheng, D. Gardner, Y. Xie, C. Carraro, R. Maboudian, *Carbon* **2019**, *148*, 64-71; c) P. M. Usov, B. Huffman, C. C. Epley, M. C. Kessinger, J. Zhu, W. A. Maza, A. J. Morris, *ACS Appl. Mater. Interfaces* **2017**, *9*, 33539-33543; d) P. M. Usov, S. R. Ahrenholtz, W. A. Maza, B. Stratakes, C. C. Epley, M. C. Kessinger, J. Zhu, A. J. Morris, *J. Mater. Chem. A* **2016**, *4*, 16818-16823; e) M. A. Gordillo, D. K. Panda, S. Saha, *ACS Appl. Mater. Interfaces* **2019**, *11*, 3196-3206.

[75] M. C. So, S. Jin, H.-J. Son, G. P. Wiederrecht, O. K. Farha, J. T. Hupp, *J. Am. Chem. Soc.* **2013**, *135*, 15698-15701.

[76] S. Motoyama, R. Makiura, O. Sakata, H. Kitagawa, *J. Am. Chem. Soc.* **2011**, *133*, 5640-5643.

[77] G. Xu, K. Otsubo, T. Yamada, S. Sakaida, H. Kitagawa, *J. Am. Chem. Soc.* **2013**, *135*, 7438-7441.

[78] a) A. A. Talin, A. Centrone, A. C. Ford, M. E. Foster, V. Stavila, P. Haney, R. A. Kinney, V. Szalai, F. El Gabaly, H. P. Yoon, *Science* **2014**, *343*, 66-69; b) X. Liu, M. Kozlowska, T. Okkali, D. Wagner, T. Higashino, G. Brenner-Weiss, S. M. Marschner, Z. Fu, Q. Zhang, H. Imahori, S. Brase, W. Wenzel, C. Woll, L. Heinke, *Angew. Chem. Int. Ed.* **2019**, *58*, 9590-9595.

[79] F. Figueira, F. A. A. Paz, *C.* **2021**, *7*, 47.

[80] L. Jiao, G. Wan, R. Zhang, H. Zhou, S. H. Yu, H. L. Jiang, *Angew. Chem. Int. Ed.* **2018**, *57*, 8525-8529.

[81] L. Jiao, W. Yang, G. Wan, R. Zhang, X. Zheng, H. Zhou, S. H. Yu, H. L. Jiang, *Angew. Chem. Int. Ed.* **2020**, *59*, 20589-20595.

[82] R. Zhang, L. Jiao, W. Yang, G. Wan, H.-L. Jiang, *J. Mater. Chem. A* **2019**, *7*, 26371-26377.

[83] X. Fang, L. Jiao, S. H. Yu, H. L. Jiang, *ChemSusChem* **2017**, *10*, 3019-3024.

Chapter 2

Porphyrin based metal–organic framework films: nucleation and growth*
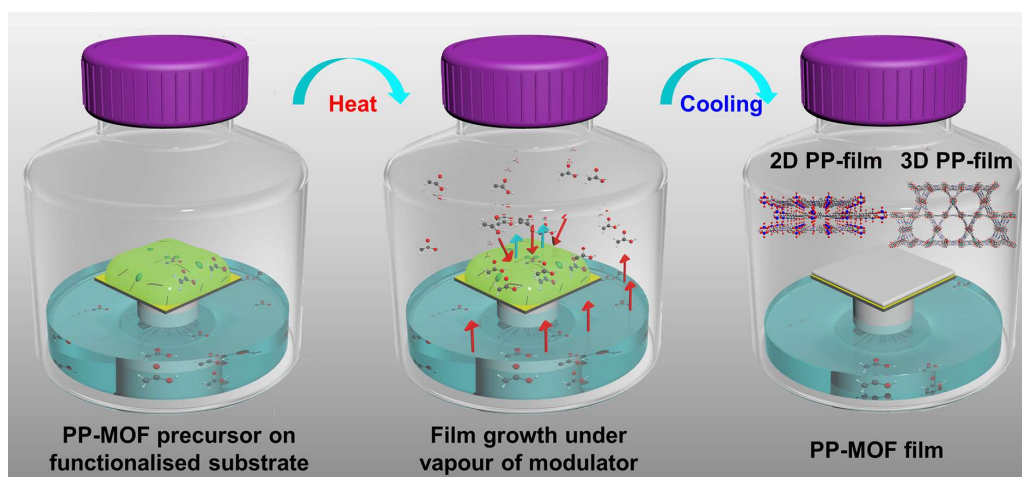
Abstract

Integration of porphyrin based metal-organic frameworks (PP-MOFs) on solid surface has emerged as a key advancement in terms of exploring their promising applications. However, a great challenge remains unmet when it comes to successfully fabricating a PP-MOF film with crystallinity, controllable orientation, adjustable morphology and thickness, all sustained in one. Herein, for the first time, vapor-assisted conversion (VAC) was developed as a facile and versatile technique to fabricate functional PP-MOF films on various substrates that relates to different application requirements. To understand the nucleation and growth mechanism, a number of fabrication methods were leveraged to prepare the PP-MOF films, thanks to an assortment of PP-MOFs varying from two-dimensional (2D) to three-dimensional (3D) scaffolds. The studies show that PP-MOF films are likely to display different nuleation and growth processes following different deposition approaches. This study demonstrates the pros and cons of different methods in the fabrication of functional PP-MOF films, potentially offering critical tools and reference points for the next-generation of functional MOF thin films preparation in general.

2.1 Introduction

Metal-organic frameworks (MOFs) are composed of organic linkers and inorganic metal nodes (or clusters) to afford potentially porous metal-organic nanospace.[1] Thanks to their modular composition amenable to reticular chemistry, good thermal stability and high surface areas, well-defined MOFs with tailored functionalities have drawn enormous attentions in the communities of chemistry and materials science.[2] As a sub-class of MOFs, porphyrin-based MOF (PP-MOF) are known for their specific potentials in catalysis and photoelectric devices, largely favoured because of their conjugated macrocyclic structures.[3] Considering practicality to serve diverse applications, integration of MOFs in the form of films onto solid surface is a desired advance. In fact, the fabrication of PP-MOFs as thin film could exploit the inherited merits of PP-MOFs as films, in order to show their promising applications in photovoltaics,[3a] sensors,[4] (photo)electrocatalysis.[5] To date, a number of MOF film preparation methods, such as seeding growth,[6] dip-coating,[7] electrochemical deposition,[8] layer-by-layer (LBL) deposition,[9] and solvothermal approach,[5b, 10] have been developed for depositing MOFs onto various substrates. However, a systematic study of the pros and cons of these methods into the fabrication of PP-MOF films remains to be addressed.

Of late, a number of reports have surfaced that cover the emerging topic of preparing application-ready PP-MOF films. For instance, methods such as Langmuir-Blodgett layer-by-layer (LB-LBL),[11] modular assembly,[12] and spray liquid-phase epitaxy (SP-LPE)[13] have been developed to prepare crystalline 2D PP-MOF films. However, these either require a special deposition set-up, or need pre-treatments such as the formation of well-ordered seed layer on the surface or heavily rely upon the functional groups of the substrate surface, impeding its potential scale-up and consequent applications. Regarding the fabrication of 3D PP-MOF films, it turns out to be a more complicated challenge. Although LBL[14] and inkjet printing methods[5a] have been reported to prepare 3D PP-MOF films, the crystallinity and orientation of the films are far from satisfactory. Thus far, solvothermal method is the most common approach and using it enables the growth of PP-MOF films.[5b, 10] However, it suffers from downsides: time and energy consumption combined with a weak control of surface morphology (*e.g.*, roughness,

grain size and distribution) and thickness. A great challenge exists as regards the fabrication of a PP-MOF film that synergises good crystallinity, controllable orientation, adjustable morphology and thickness.

Herein, a vapour-assisted conversion (VAC) method was developed to fabricate 2D and 3D PP-MOF films deposited on various substrates, such as gold/silicon/ITO substrates. VAC method is based on the conversion of precursors by casting a solution layer on substrates to form a continuous crystalline film, largely credited to an exposure of precursors to the vapours from specific modulators under moderate temperatures.[15] We demonstrate that, while delivering a high quality thin film, this approach remains straightforward and versatile.

To further understand the nucleation and growth mechanism in PP-MOF films, three other typical methods such as solvothermal, modular assembly and LPE (**Scheme 1**) have been investigated in parallel with the VAC approach. All of these share a common aim: leaning forward towards the fabrication of 2D and 3D PP-MOF films. Grazing incidence X-ray diffraction (GIXRD), scanning electron microscopy (SEM), environment-controlled quartz crystal microbalance (BEL-QCM) were used to study the characteristics such as crystallinity, orientation, morphology, thickness and porosity to evaluate the pros and cons of each method towards nucleation and growth in functional PP-MOF films. This resulted in a unique back-to-back investigation of the mechanisms involved in the nucleation and growth of PP-MOF films. Well-known 2D PP-MOFs such as $Zn_2(ZnTCPP)$ (TCPP, tetrakis(4-carboxyphenyl)-porphyrin) and 3D PP-MOFs such as PCN-222 (PCN, porous coordination network), PCN-224 and MOF-525 have been used as typical examples to investigate the nucleation and growth of porphyrin-based MOF films.
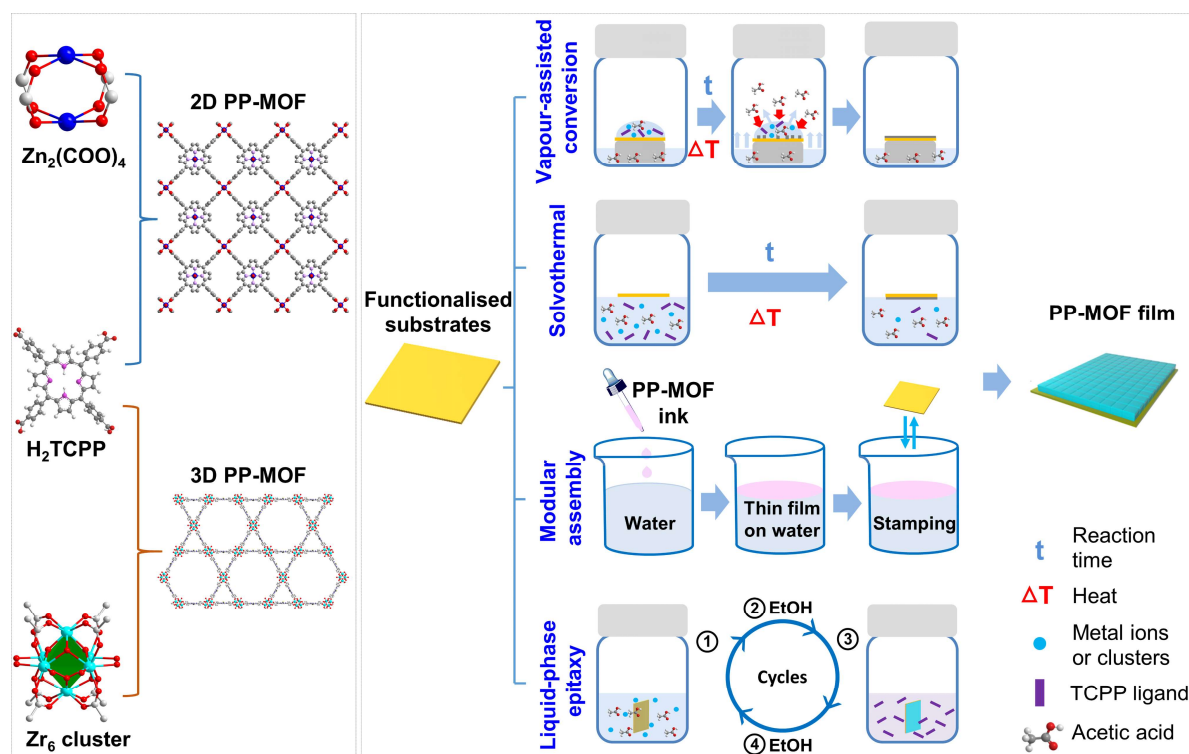
Scheme 1. Schematic representation of 2D and 3D PP-MOF films deposited on carboxylate-terminated gold substrates via diverse methods: a) vapour-assisted conversion; b) solvothermal; c) modular assembly; d) liquid-phase epitaxy. The left side comprises the building units and crystal structures of the 2D $Zn_2(ZnTCPP)$ and 3D PCN-222, on the top and at the bottom respectively.

2.2 Results and Discussion

2.2.1 Preparation and characterisation of 2D PP-MOF film

Until recently, many 2D PP-MOFs have been fabricated as films to explore promising applications.[3a, 4, 16] As a commonly studied 2D PP-MOF with a well-known simple composition, $Zn_2(ZnTCPP)$ was selected as a prototype to investigate the nucleation and growth mechanisms in 2D PP-MOF films. $Zn_2(ZnTCPP)$ comprises Zn(II)-centered TCPP (ZnTCPP) units linking binuclear Zn paddlewheel metal nodes $Zn_2(COO)_4$, affording a 2D "checkerboard" structure (**Figure 2.1a-c**). Along the *ab* plane, Zn(II) residing inside porphyrin units gets coordinated to the zinc atoms in the paddlewheel units. These classical "checkerboard" layers are further stacked in AA packing arrangement, leading to the 2D PP-MOF structure (**Figure 2.1d, Table S1** in Chapter 5). According to the literatures detailing the preparation of paddlewheel structure based MOF films, [11a, 17] the MOF $Zn_2(ZnTCPP)$ could indeed serve as a good candidate to conduct our intended study: that to study nucleation and growth processes in prototypal 2D PP-MOF

films.
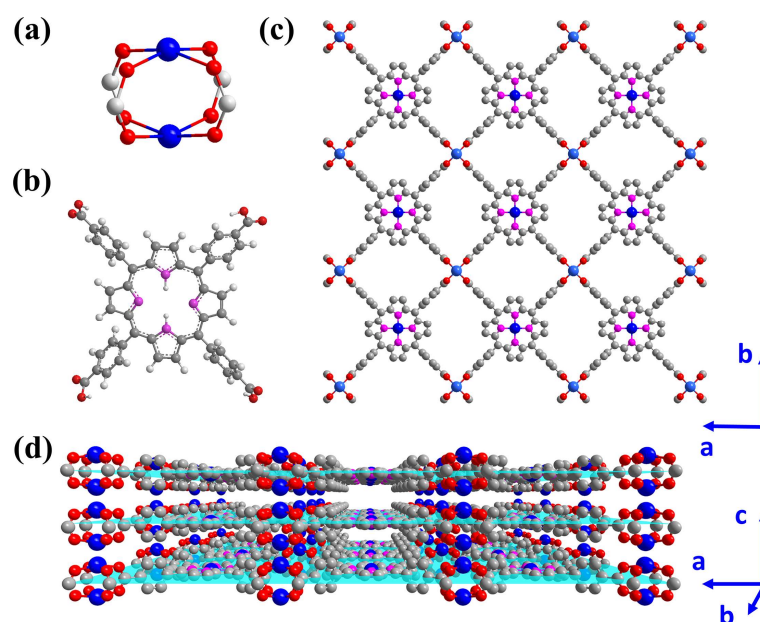
Figure 2.1 Structures of the building units a) $Zn_2(COO)_4$ paddlewheel metal node, b) TCPP ligand for 2D $Zn_2(ZnTCPP)$ nanosheets; 2D "checkerboard" structure of $Zn_2(ZnTCPP)$ nanosheets c) view along [001] direction of one layer of $Zn_2(ZnTCPP)$; d) the layered structure of 2D $Zn_2(ZnTCPP)$ nanosheets stacked in an AA packing pattern, planes were inserted in each layer. H atoms have been omitted for clarity. Colour scheme: C, grey; O, red; N, pink and Zn, blue.

To begin with, VAC was employed to prepare $Zn_2(ZnTCPP)$ MOF films. Subsequently, solvothermal, modular assembly and LPE methods, all were used separately to prepare $Zn_2(ZnTCPP)$ MOF films to draw rational comparisons with VAC. Different substrates are supposed to show different surface behaviours to initiate different nucleation and growth in the resulting MOF films. Meanwhile, considering its practical uses, PP-MOFs need to be deposited on specific substrates. For example, microelectronic devices usually require the PP-MOF to be deposited on gold surface;[3c] whereas electrocatalytic devices or semiconductor devices need depositions on conductive ITO glass and silicon substrate, respectively.[5a, 18] Therefore, a variety of potential substrates with distinct surface functional groups will be examined with respect to their relative suitability towards nucleation and growth of the corresponding PP-MOF films. Unless otherwise mentioned, PP-MOF films in the following discussion refer to films that were deposited on carboxylate-terminated gold surface.

In each of our VAC experiments, a mixture of *N,N*-dimethylformamide (DMF) and acetic acid (v/v: 200:1) was filled as the vapour source and a substrate (1 × 1

cm) was placed on the platform in a glass vial (**Scheme 1**). The reactants $Zn(NO_3)_2 \cdot 6H_2O$, TCPP and modulator acetic acid were dissolved in a binary mixture of DMF and ethanol (v/v: 3/1) as the precursor solution (**Table S2** in Chapter 5). Then, a droplet of this precursor solution was evenly deposited on the substrate. The vial, upon sealing was transferred into a preheated oven to facilitate further film growth. Removal of the $Zn_2(ZnTCPP)$ film from oven was followed by washing with fresh DMF and ethanol. Final step was to dry it under vacuum.
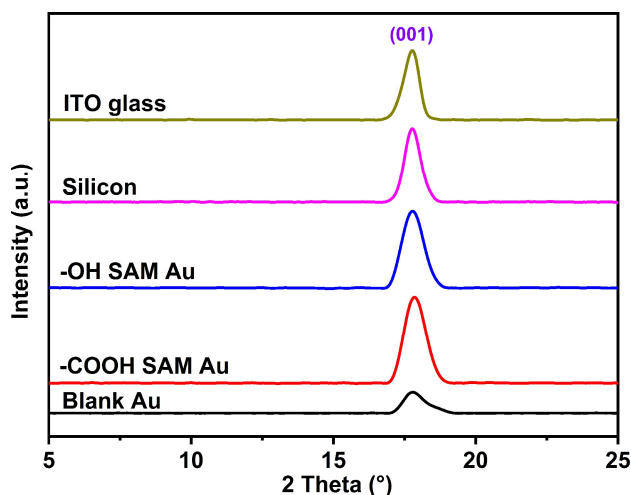
Figure 2.2 GIXRD patterns of $Zn_2(ZnTCPP)$ films grown by VAC method on different substrates: blank gold, –COOH SAM gold, –OH SAM gold, silicon and ITO glass.

GIXRD patterns reveal that $Zn_2(ZnTCPP)$ MOF films could be successfully grown on differently functionalised solid surfaces, *i.e.*, blank substrates, carboxyl-terminated and hydroxyl-terminated self-assembled monolayer (SAM) substrates by adopting the VAC method (**Figure 2.2**). The SAM functionalised substrates were obtained upon immersion of substrates in 1-mercaptoundecanol (MUD) and 16-mercaptohexadecanoic acid (MHDA) for at least 24 h at room temperature. According to the GIXRD patterns, the obtained $Zn_2(ZnTCPP)$ films demonstrated bulk phase purity with high crystallinity for all substrates, after subjecting to a 3 h aging process under 80 °C vapour exposed environment. Under identical conditions, the PP-MOF films deposited on solid substrates functionalised with –COOH and/or –OH groups, exhibit a strong XRD peak intensity when compared with the PXRD pattern of a film cast on an analogous substrate with no functionalisation. The results suggest that PP-MOF films have a better crystallinity on functionalised substrates *versus* the non-functionalised substrates. This can be attributed to the induction ability of functional groups during the nucleation step in

PP-MOFs. Whilst nucleating, the functional groups facilitate Zn(II) ions to be anchored on the surface via coordination bonds. [3a, 19] Thereafter, these coordinated Zn(II) can serve as a metal source during the PP-MOF film growth. On the contrary, in the non-functionalised surfaces, weak interactions like hydrogen bonding and van der Waals interactions between the surface and Zn(II) ions suffer from an equilibrium process during the nucleation step. This hinders the subsequent growth process, resulting in a low crystallinity.[20] In VAC assisted growth process, the resulting PP-MOF films exhibit a preferred orientation [001] which is independent of surface anchored functional groups.
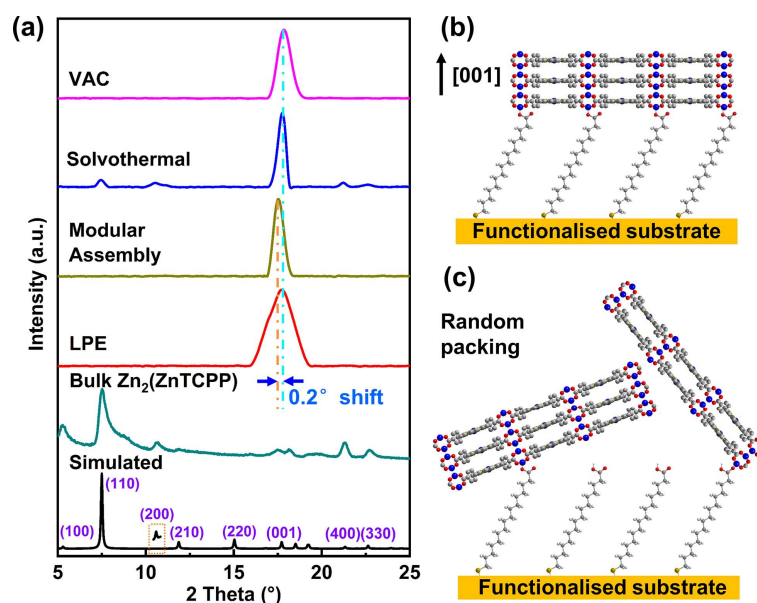
Figure 2.3 (a) Simulated and experimental PXRD patterns of bulk $Zn_2(ZnTCPP)$ and GIXRD patterns of the $Zn_2(ZnTCPP)$ films fabricated by VAC, solvothermal, modular assembly and LPE methods (the inset is the magnified (200) peak); schematic illustration of the $Zn_2(ZnTCPP)$ films grown along the [001] direction by (b) VAC, modular assembly and LPE; (c) solvothermal method leading to random packing. Relevant details: thin films were prepared on –COOH functionalised gold substrates (1 cm x 1 cm) (VAC deposition was conducted using 30 μL freshly prepared MOF precursor solution with acetic acid acting as modulator at 80 °C for 3 h; modular assembly deposition was performed with five stamping cycles; LPE deposition was done over thirty consecutive cycles).

In solvothermal method, the $Zn_2(ZnTCPP)$ film was grown on a typical –COOH functionalised gold substrate in a reactant solution composed of $Zn(NO_3)_2 \cdot 6H_2O$, TCPP and modulator acetic acid, in a binary mixture of DMF and ethanol (v/v, 3/1) at 80 °C for one day. The GIXRD patterns in **Figure 2.3a** suggest a random orientation of the surface-grown $Zn_2(ZnTCPP)$ film. This is evidenced by a predominant reflection along [001] with several weak peaks appearing at (110),

(200) and (400). This is indicative of the high challenges associated with the fabrication of a perfectly oriented 2D PP-MOF film, if solvothermal method is pursued.

Regarding the modular assembly method, $Zn_2(ZnTCPP)$ nanosheets were synthesised first and ultrasonically dispersed in ethanol to get a PP-MOF ink; the ink carefully placed on water exhibited a spontaneous spread-out. This afforded a thin film on top of the water surface due to its hydrophobicity, following which it was transferred to the substrates yielding a thin film via a stamping process. The as-prepared $Zn_2(ZnTCPP)$ film displays a preferably oriented [001] growth at 17.6° with a lattice space of 1.007 nm (calculated from Bragg equation, $n\lambda = 2d \sin\theta$). Only a slight shift (0.2°) appeared, on comparing with the films prepared via VAC, solvothermal and LPE methods (17.8° with a lattice space of 0.996 nm). The peak shift and lattice difference can be ascribed to the different film deposition strategies, each governed by distinct crystallisation equilibrium processes from the other. Modular assembly is a top-down deposition technique, in which the film composed of 2D $Zn_2(ZnTCPP)$ nanosheets are ultrasonically stripped from the bulk $Zn_2(ZnTCPP)$.[12] Ultrasonication is likely to disintegrate the weak interlayer interactions, vis-à-vis to increase the interlayer space between the nanosheets.

For the $Zn_2(ZnTCPP)$ film growth using LPE, the –COOH functionalised substrate was immersed in $Zn(OAC)_2 \cdot 2H_2O$ and TCPP solutions in an alternating manner; an ethanol washing step lying in between two consecutive reactive steps. According to the GIXRD pattern in **Figure 2.3a**, a crystalline $Zn_2(ZnTCPP)$ film with preferred orientation along the [001] direction was obtained. This disclosed the feasibility of LPE to grow 2D $Zn_2(ZnTCPP)$ films on functionalised substrates. Our observation of several strong (hk0) peaks (*viz.*, (100), (110), (200), (400) and (330)) in the in-plane XRD patterns and (001) peaks in the GIXRD patterns confirmed the high crystallinity and perfect orientation of the $Zn_2(ZnTCPP)$ films grown by VAC, modular assembly and LPE methods; whereas, the in-plane XRD and GIXRD pattern of solvothermally prepared $Zn_2(ZnTCPP)$ film included the characteristic (001) peak, suggestive of the random nature of film growth (**Figures 2.3** and **2.4**).[12]
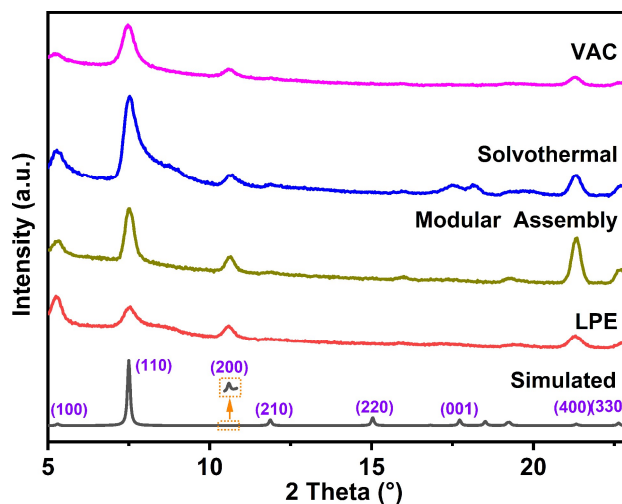
Figure 2.4 In-plane PXRD patterns of $Zn_2(ZnTCPP)$ films fabricated by VAC, solvothermal, modular assembly and LPE methods. The insert was the magnified (200) peak.
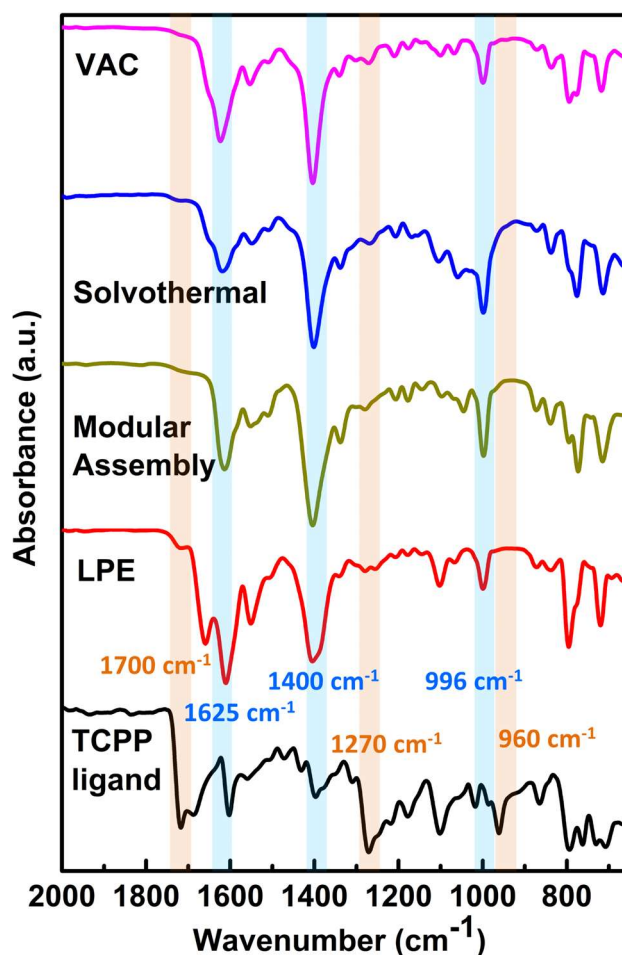
Figure 2.5 ATR-IR spectra of TCPP ligand and $Zn_2(ZnTCPP)$ films fabricated on –COOH terminated gold substrates by different methods.

Attenuated total reflection infrared spectroscopy (ATR-IR) spectra and ultraviolet–visible spectroscopy (UV-Vis) spectra were also carried out to confirm

the compositions of the PP-MOF films, prepared by all four deposition techniques. The free H_2TCPP ligands were metalated during the growth of $Zn_2(ZnTCPP)$ film as evidenced by disappearance of the N–H stretching vibration at 960 cm^{-1} and appearance of a new peak at 996 cm^{-1}. This could be assigned to Zn-N bonds (**Figure 2.5**).[16b, 21] Moreover, compared to the spectrum of H_2TCPP, $Zn_2(ZnTCPP)$ films indicated peaks disappearing around 1700 and 1270 cm^{-1} and two new strong peaks appearing around 1625 cm^{-1} and 1400 cm^{-1}. These synchronous disappearance and emergence of IR stretching signatures indicate coordination of the TCPP carboxylate groups to the Zn(II) atoms.[12, 21]
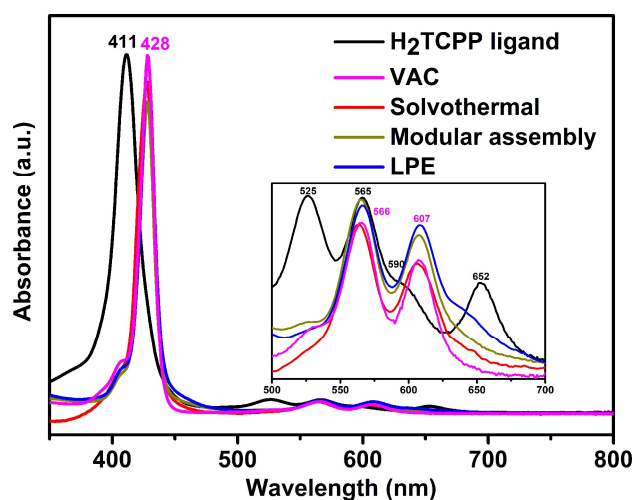
Figure 2.6 UV-Vis spectra of TCPP ligand and $Zn_2(ZnTCPP)$ films fabricated on –COOH terminated gold substrates by different methods: VAC, solvothermal, modular assembly and LPE. Note that enlarged Q-band region is inserted.

The UV-Vis spectrum of H_2TCPP ligand presents a strong Soret band at 411 nm together with four Q-bands at 525, 565, 590, and 652 nm (**Figure 2.6**). The Soret band of $Zn_2(ZnTCPP)$ films was noticed to undergo a red shift to 428 nm, and two weak Q bands red-shifted to 567 and 603 nm respectively. This confirmed the metalation of porphyrin rings by Zn(II) during the reaction process.[16b]

SEM images identified differences in morphologies among the differently prepared PP-MOF films, suggesting variations that must have occurred during the nucleation and growth of the PP-MOF crystallites onto the –COOH terminated gold surface.[22] The $Zn_2(ZnTCPP)$ film prepared by VAC shows a smooth, dense and homogeneous distribution with a grain size of ~ 200 nm (**Figures 2.7a-b**). By controlling the stoichiometry of acetic acid serving as reaction modulator, morphologies in $Zn_2(ZnTCPP)$ film could be fine-tuned. For example, a crystalline

film with a flat and rough layer on the solid surface could be obtained by excluding the use of acetic acid, featuring rectangular nanosheet morphology ~ 500 nm, each (**Figures 2.8** and **2.9**). A Similar phenomenon was observed in the films prepared without acetic acid and DMF (**Figures 2.10** and **2.11**). The carboxylic acid groups in acetic acid are anticipated to selectively coordinate to Zn(II) ions, serving as nucleation modulator during the growth of 2D PP-MOF. [16b, 23] In the initial stage, such a modulator is known to compete with the TCPP ligand while coordinating to Zn(II) ions, leading to a 2D structure along *ab* plane. This competition is supposed to slow down the nucleation of $Zn_2(ZnTCPP)$ nanosheets. Meanwhile, acetic acid easily coordinated to Zn(II), to elicit steric hindrance impeding the isotropic growth of $Zn_2(ZnTCPP)$ along *c* axis. [16b, 24] Thus, the $Zn_2(ZnTCPP)$ film with small nanosheets could be obtained. Besides, the thickness of films grown via VAC could be controlled facilely by using different amounts of the precursor solution for VAC growth (**Figure 2.12**).
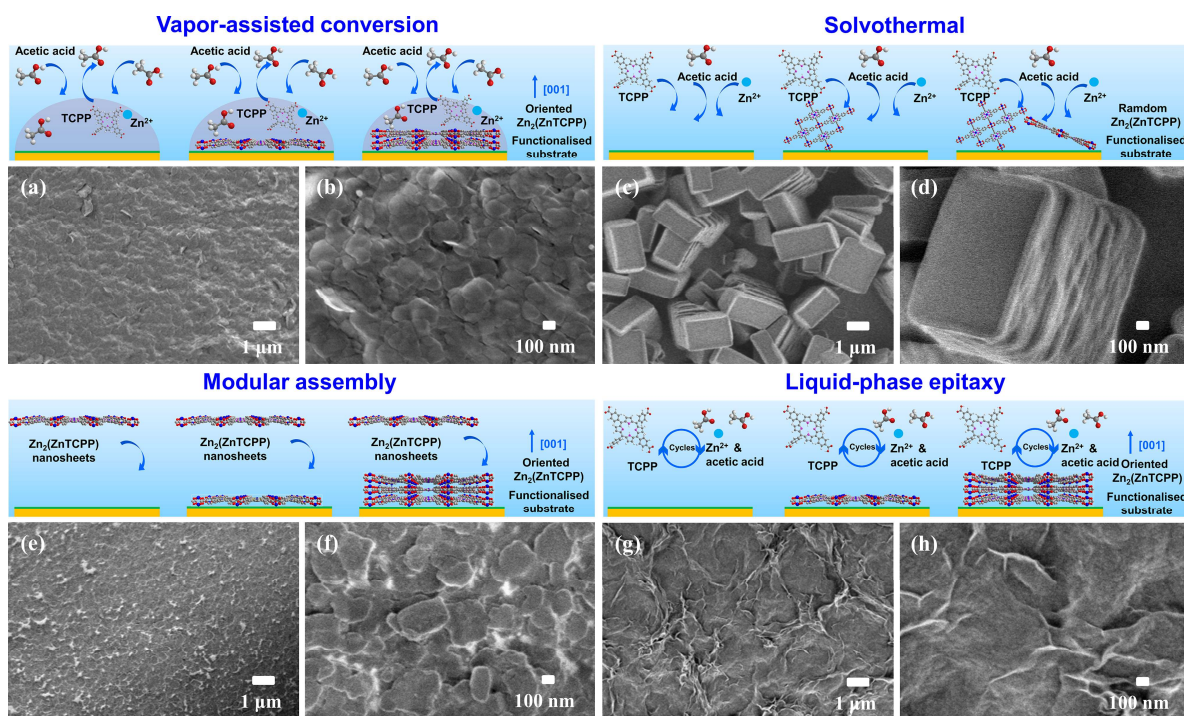
Figure 2.7 SEM images of Zn2(ZnTCPP) films fabricated by (a-b) VAC, (c-d) solvothermal, (e-f) modular assembly and (g-h) LPE methods; the proposed nucleation and growth processes involved in each method are schematically illustrated on top of these SEM images. All films were prepared on the –COOH functionalised gold substrates (1 cm x 1 cm) (relevant details: VAC deposition was performed using 30 µL freshly prepared MOF precursor solution with acetic acid as modulator, at 80 °C for 3 h.; modular assembly deposition was conducted with five consecutive stamping cycles; LPE deposition was done over for thirty consecutive cycles).
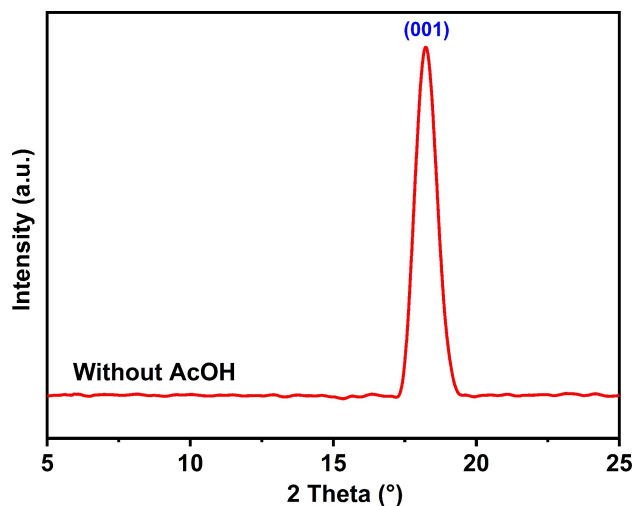
Figure 2.8 GIXRD patterns of Zn$_2$(ZnTCPP) film grown by VAC method on –COOH terminated gold substrate without acetic acid as modulator.
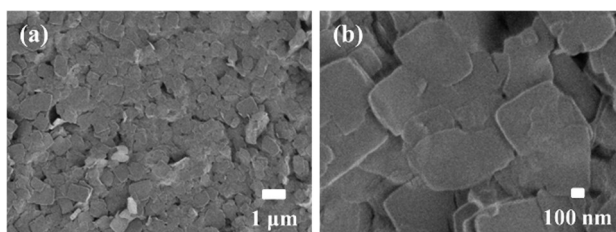
Figure 2.9 SEM images of Zn$_2$(ZnTCPP) film grown by VAC method on –COOH terminated gold substrate without acetic acid as modulator.
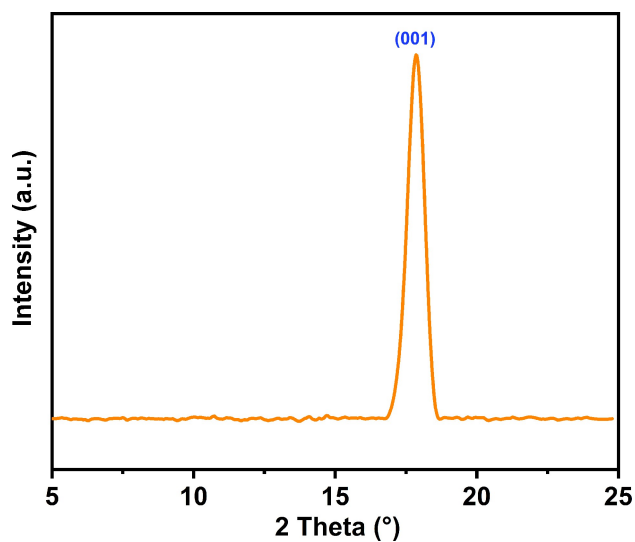
Figure 2.10 GIXRD patterns of Zn$_2$(ZnTCPP) film grown by VAC method on –COOH terminated gold substrate without acetic acid and DMF.
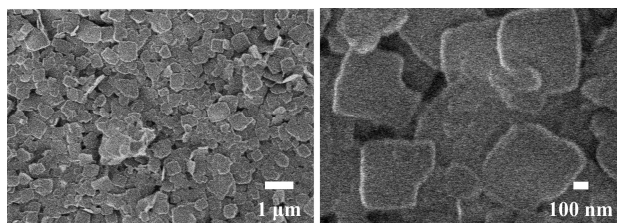
Figure 2.11 SEM images of $Zn_2(ZnTCPP)$ film grown by VAC method on –COOH terminated gold substrate without acetic acid and DMF.
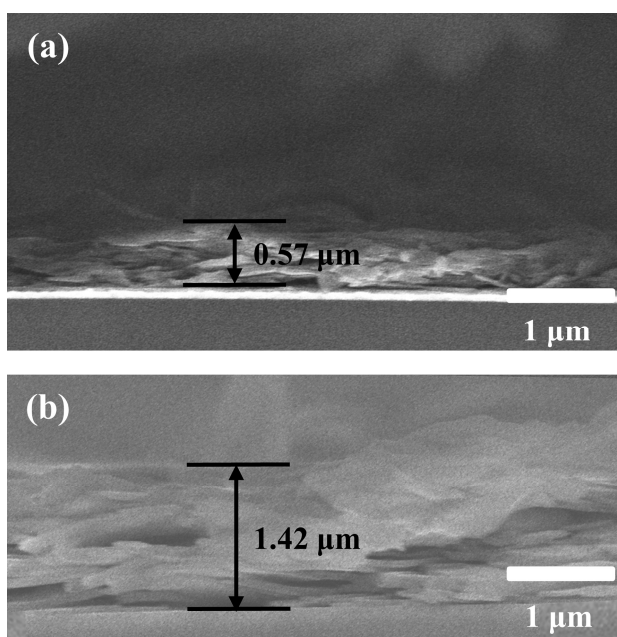
Figure 2.12 Cross-section SEM images of $Zn_2(ZnTCPP)$ films grown by VAC method on –COOH terminated gold substrate with (a) 30 µL and (b) 60 µL of precursor solution.

In contrast, the films solvothermally grown exhibit a random packing behaviour as opposed to being chemically anchored onto the surface (**Figures 2.7c-d**). This is because: $Zn_2(ZnTCPP)$ with a simple 2D "checkerboard" structure can be formed rapidly and the abundant 2D layers in proximity could interact to get aligned. Such alignment could facilitate growth and self-packing along the *c*-axis rather than precise nucleation on the substrate surface. Most of the PP-MOF crystallites could be observed along the *ab* plane ([001] oriented growth) accompanied by a small amount of other faces. This indicates a lack of preference in the orientation of film growth. These results are in agreement with the GIXRD profiles. Thanks to modular assembly, a smooth and homogeneous surface of $Zn_2(ZnTCPP)$ film could be obtained (**Figures 2.7e-f**). Because of ultrasonic stripping of the $Zn_2(ZnTCPP)$ nanosheets from its bulk form, a small size (~300 nm), high-aspect-ratio flaky morphology could be accessed. Such a controlled assembly process enables us to

prepare dense and packed nanofilms (**Figures 2.7e-f**). The film thickness can be manipulated by adjusting the number of deposition cycles.[12] Meanwhile, powered by to our command on the concentrations of precursor solutions and on the number of deposition cycles, LPE offers the advancement to nucleate small sites and grow a uniform film of high topical interest (**Figures 2.7g-h**). Beauty of the LPE method lies with the fact that it allows the MOF films to grow with a precisely controlled nanoscale thickness, guided by a regulated number of deposition cycles. [16c]   In simple terms, VAC, modular assembly and LPE methods feature advantages such as to precisely engineer the nucleation and growth processes of fabricating uniform 2D PP-MOF films with fine-tuned thickness, whereas the solvothermal approach works well for nucleation with difficulties to control their morphology and thickness.

Table 2.1 Surface roughness of $Zn_2(ZnTCPP)$ films fabricated via different methods.

Methods	R_a (nm)	R_q (nm)
VAC	4.5	6.1
Solvothermal	54.1	61.2
Modular assembly	8.1	10.4
LPE	2.9	3.1
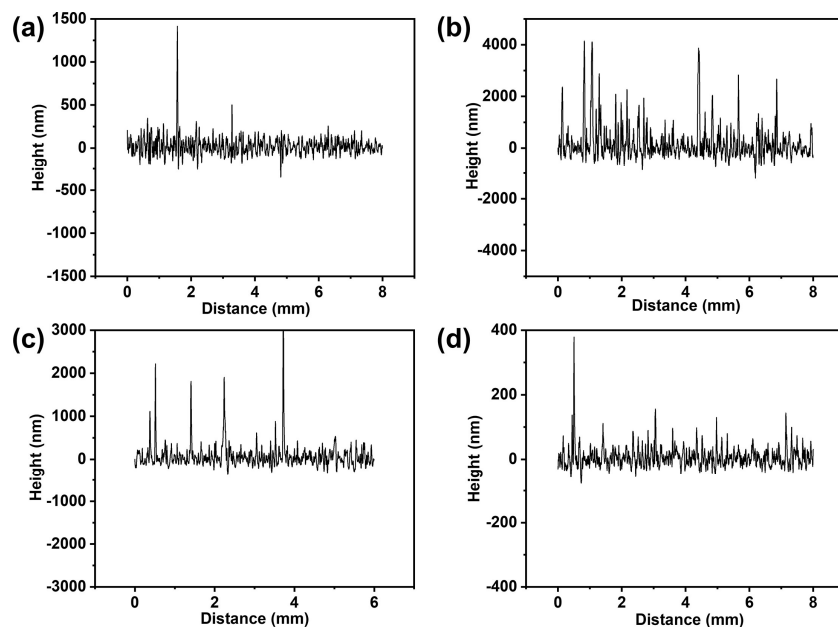
Figure 2.13 Roughness profiles of $Zn_2(ZnTCPP)$ films fabricated on –COOH terminated gold substrates by (a) VAC, (b) solvothermal, (c) modular assembly and (d) LPE methods.

Evaluation of surface roughness by determining the arithmetic average roughness (R_a) and the root mean squared roughness (R_q) (**Table 2.1**) confirmed

flatness of the differently prepared films (**Figure 2.13**).[25] The Zn$_2$(ZnTCPP) films prepared by VAC and LPE exhibit surface roughness profiles (**Figures 2.13a** and **2.13d**) with R$_a$ values of 4.5 nm and 2.9 nm, respectively. In modular assembly, the film is characterised with an acceptable roughness profile, R$_a$ = 8.1 nm (**Figure 2.13c**). Consistent with the SEM image, the film grown via solvothermal method exhibits roughness (**Figure 2.13b**) with a much higher R$_a$ ~ 54.1 nm; a plausible outcome of the random packing of bulk Zn$_2$(ZnTCPP) crystallites.

2.2.2 Preparation and Characterisation of 3D PP-MOF films

Zirconium-based porphyrinic MOFs (Zr-MOFs) are typical representatives of 3D PP-MOFs.[26] They feature extraordinary chemical stability, a wide range of pore sizes, and excellent (photo)electrocatalytic properties, ideally suited for a wide range of applications, such as solar cell, chemical sensor and photo/electrocatalysis.[5, 27] Similar to the studies on 2D PP-MOF films, VAC, solvothermal, modular assembly and LPE methods were implemented to prepare 3D PP-MOF films. PCN-222, PCN-224 and MOF-525 can result from the coordination of TCPP ligand with Zr$_6$ cluster but exhibit different network topologies and pore architectures, an artefact of the intrinsic differences in the metal-organic coordination numbers and symmetries of the Zr$_6$ clusters composing the frameworks (**Figure 2.14**).[26] A set of identical structural connectors *i.e.* links and different framework topologies could afford the distinct 3D structures of PCN-222, PCN-224 and MOF-525, making them comparable examples. A coherent study of such analogues helps us to understand the nucleation and growth processes in prototypal 3D PP-MOF films cast on different solid surfaces, and outcomes of different deposition routes associated therein.
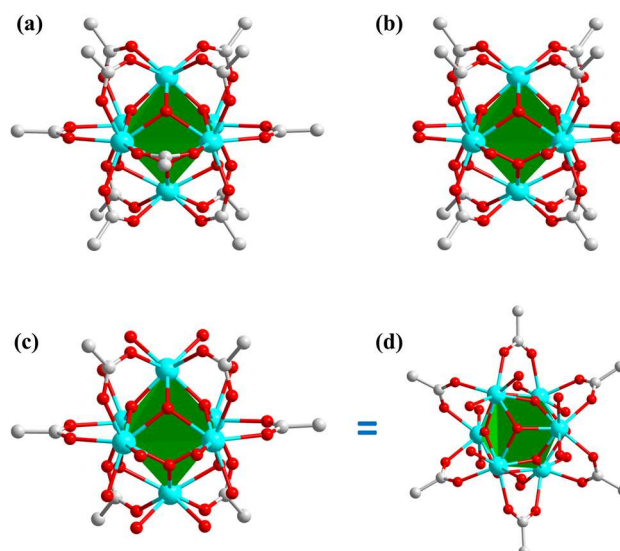
Figure 2.14 Different connectivities of Zr_6 clusters in the structures of Zirconium-based porphyrinic MOFs: (a) 12-connected Zr_6 cluster for MOF-525; (b) 8-connected Zr_6 cluster for PCN-222; (c-d) 6-connected Zr_6 cluster for PCN-224 ((c): side view; (d): top view). Colour scheme: C, grey; O, red, and Zr, aqua. The green polyhedron represent the octahedral geometry of the Zr_6 cluster.

We began to study the VAC assisted growth of PCN-222 films on –COOH functionalised substrates. GIXRD patterns of PCN-222 films confirmed its phase purity and high crystallinity (**Figure 2.15**). Unlike the 2D Zn_2(ZnTCPP) nanosheet, the oriented growth of 3D PCN-222 crystallites favours its formation on the functional group modified substrates. A highly oriented film along [100] direction was obtained on the –COOH functionalised gold surface. However, the PCN-222 films grew upon silicon wafer and ITO glass showed two weak peaks at ~ 6.6° and 8.3°, corresponding to the [211] and [420] orientations respectively. These suggest randomly oriented growth of these films. Growth mechanism of the oriented PCN-222 on –COOH functionalised gold surface is illustrated in **Figure 2.16b**. During reaction, Zr(IV) metal ions nucleate to form the Zr_6 clusters. The carboxylic groups of SAM functionality selectively coordinate to these Zr_6 clusters subsequently, anchoring the metal clusters on the surface. Following this, TCPP linkers coordinate to the Zr_6 clusters inducing the "oriented/layered" growth of PCN-222 along the *bc* plane, parallel to the substrate. This in turn contributes to the further nucleation and growth along the *a* axis (**Figure 2.17**).[10a] The functional organic groups of SAM on the substrate surface offer a few advantages to facilitate selective nucleation and oriented growth of PP-MOF films, whereas a favourable reaction condition is also deemed crucial for film fabrication purposes.
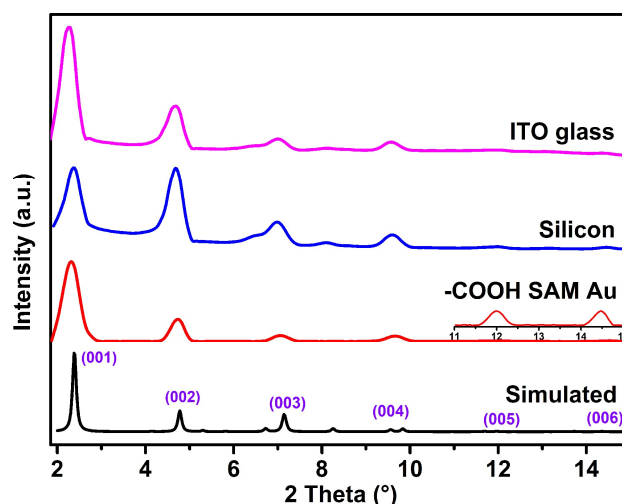
Figure 2.15 GIXRD patterns of PCN-222 films grown by VAC technique on different functionalised substrates: –COOH SAM gold, silicon, ITO glass. Note that VAC deposition was conducted using 30 μL freshly prepared MOF precursor solution with the acetic acid as modulator (r_M = 219) at 100 °C for 3 h.
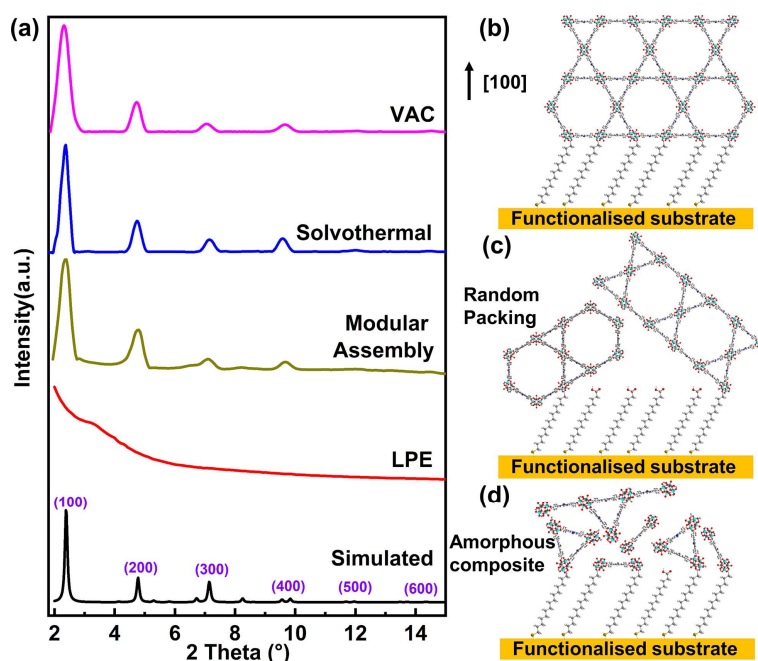
Figure 2.16 (a) Simulated PXRD pattern of bulk PCN-222 and GIXRD patterns of PCN-222 films fabricated by VAC, solvothermal, modular assembly and LPE methods; schematic illustration of the PCN-222 films grown along the [100] direction by (b) VAC and solvothermal methods; (c) modular assembly method leading to random packing and (d) growth of amorphous composite via LPE. Relevant details: thin films were prepared on –COOH functionalised gold substrates (1 cm x 1 cm) (VAC deposition was conducted using 30 μL freshly prepared MOF precursor solution with acetic acid as modulator (r_M = 219) at 100 °C for 3 h; modular assembly deposition was performed with five stamping cycles; LPE deposition was done over thirty consecutive cycles).
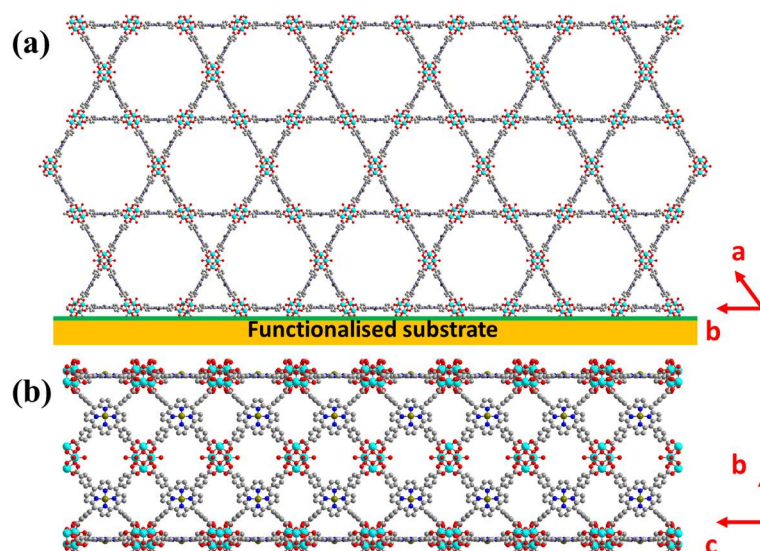
Figure 2.17 (a) Side-view scheme (the *ab* plane) of the PCN-222 film grown upon functionalised substrate along *a* axis ([100] direction), in which the channels are parallel to the plane of the substrate; (b) the *bc* plane of PCN-222 film which nucleated on the substrate surface.

To obtain further insights into the VAC assisted growth of PCN-222 films, we separately investigated the impacts of modulator concentrations, precursor concentrations, reaction times, reaction temperatures, and droplet volumes on the crystallinity, morphology and thickness. This was done by altering the synthetic conditions (**Table S3** in Chapter 5). Even a slight change to the amount of modulator in the form of acetic acid can result in differences in crystallinity, morphology, orientation of the PP-MOF films, reiterating the vital role played by a modulator during the fabrication of a PP-MOF film. As shown in **Figure 2.18**, the obtained PCN-222 films display a relatively poor crystallinity in the form of weak GIXRD peaks when the modulator/metal salt ($ZrOCl_2 \cdot 8H_2O$) concentration ratio (r_M) was below 219. PCN-222 films with a good orientation and crystallinity were formed with the r_M of 219 to 437. By adjusting the modulator and upon further controlling the r_M from 437 to 874, phase transition from PCN-222 to PCN-224 could be noted in the PP-MOF. Mediated by modulator adjustment, grain size in PCN-222 increased from an r_M of 219 to 437 (**Figure 2.19**). This is because low concentration of modulator results in a fast nucleation and crystallisation process, which is in agreement with the literature reports.[5a, 28] High precursor concentration resulted in the randomly oriented growth of PCN-222 film, accessed via VAC (**Figure 2.20**). The plausible reason is attributed to the abundance of reactants that induces vast nucleation in the precursor solution and exacerbates the difficulty to control the

oriented growth followed by nucleation on functionalised substrate surfaces. An adequate reaction time is important to efficiently sustain nucleation and crystalline growth. Herein, we find that a reaction time of only 3 h was sufficient to afford the PCN-222 films and a prolonged reaction time of 12 h did not bring any change: a pure and crystalline phase was retained (**Figure 2.21**). Reaction temperature is also vital behind the nucleation and crystallisation of PP-MOF films. For PCN-222, a highly crystalline and oriented film was obtained at 100 °C, whereas a low temperature of 80 °C resulted in a considerable loss of crystallinity in the PCN-222 film (**Figure 2.22**).
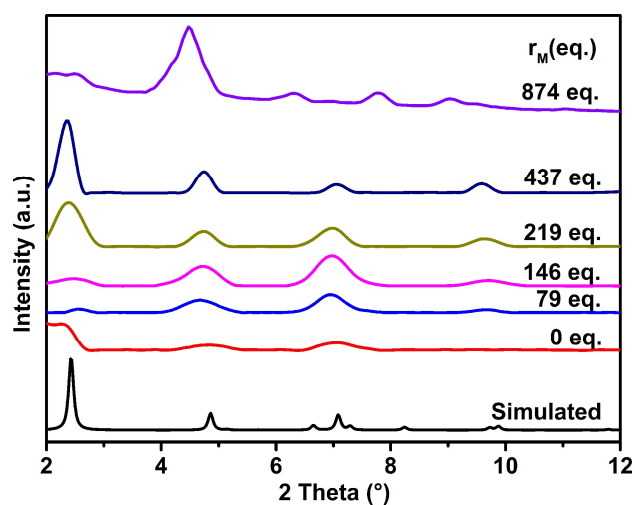
Figure 2.18 GIXRD patterns of PCN-222 films grown on –COOH terminated gold substrates by VAC method with different modulator to metal ratios (r_M).
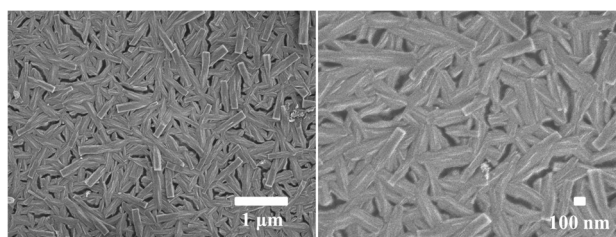
Figure 2.19 SEM images of PCN-222 film grown on –COOH terminated gold substrate by VAC method with r_M at 437.
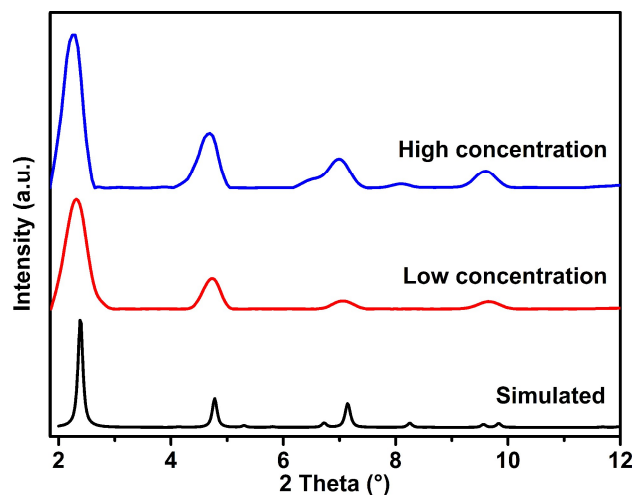
Figure 2.20 GIXRD patterns of PCN-222 films grown by VAC method on –COOH terminated gold substrate with low and high precursor concentrations.
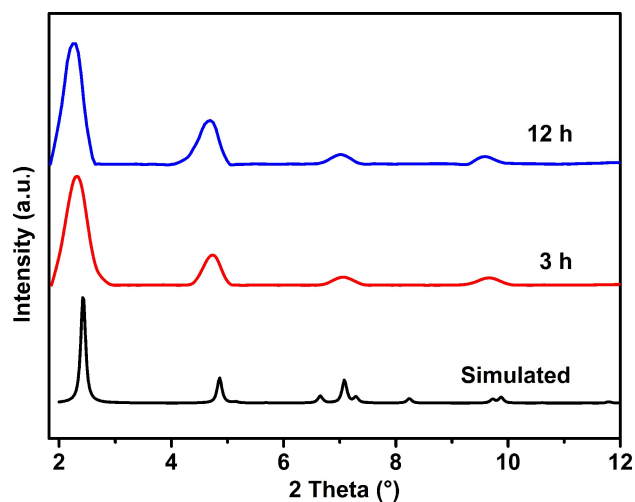
Figure 2.21 GIXRD patterns of PCN-222 films grown on –COOH terminated gold substrates by VAC method using different reaction time.
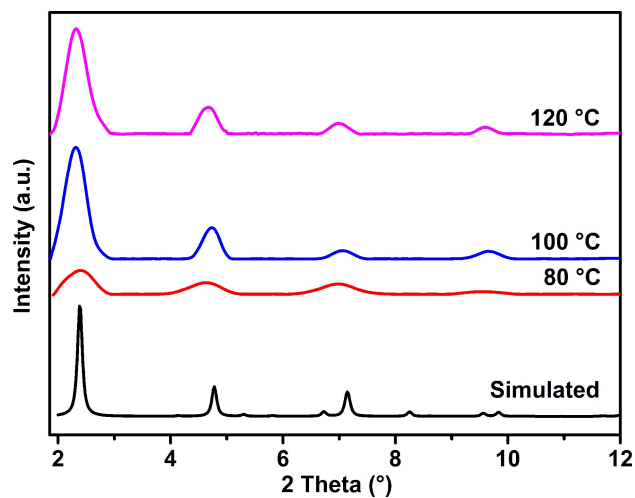
Figure 2.22 GIXRD patterns of PCN-222 films grown on –COOH terminated gold substrates by VAC

method on different reaction temperatures.

To better understand the nucleation and growth processes of the 3D PP-MOF film, similar to our foregoing studies on the 2D analogues, modular assembly, LPE and solvothermal methods were used to fabricate the PCN-222 films to comparatively analyse their crystallinity, morphology and thickness. As shown in **Figure 2.16**, GIXRD patterns confirmed that crystalline PCN-222 film with an oriented growth could be solvothermally prepared. Upon comparing this result to 2D $Zn_2(ZnTCPP)$, it appears that the more complex 3D MOF architecture of PCN-222 and a higher amount of modulator used in its synthetic process could slow down the reaction rate，leveraging opportunities for selective and precise nucleation on the surface-localised functional groups.[23] When deposited by modular assembly, PCN-222 film displays a good crystallinity *versus* those prepared solvothermally. In fact, modular assembly could not achieve an oriented growth in the PCN-222 film, evident from the weak nature of two GIXRD peaks at 6.6° and 8.3°. The random orientation in the 3D PP-MOF film is attributed to the rod-like PCN-222 crystallites (**Figures 2.23e-f).** Compared to the modularity and high-aspect-ratio flaky structure in the 2D PP-MOF congener, in its 3D form, to form an oriented film by controlling the crystallites orientation becomes increasingly difficult.[12, 29] GIXRD pattern of the PCN-222 film fabricated by LPE did not reveal any characteristic peak, thus suggesting the formation of amorphous PCN-222. The plausible explanation might be the high energy barrier of formation in cases of such complicated and symmetric 3D topology structures (**csq** for PCN-222), which lies beyond the reach of LPE operating under a relatively mild condition.[26a, 29-30] To be specific, during the MOF crystallisation process, secondary building units (SBUs) are formed initially. Credited to this direct supply of pre-synthetic SBUs, the nucleation kinetics gets accelerated in order to reduce the energy barrier of MOF crystallisation.[31] However, for 3D PP-MOFs like PCN-222, growth of a crystalline film evidently fails with the introduction of Zr_6 cluster-based SBUs as metal resource, under the mild conditions of LPE. This seems a shortcoming of LPE, considering scopes of growing the 3D films of PCN-222.
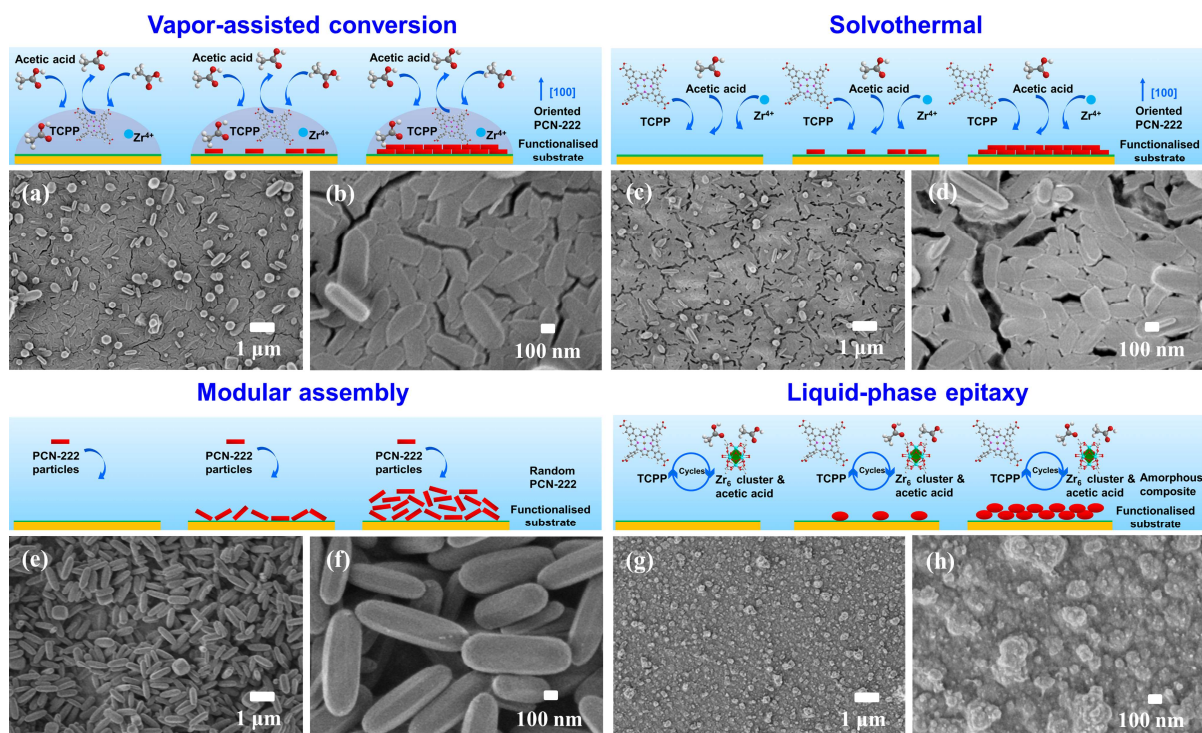
Figure 2.23 SEM images of PCN-222 films fabricated by (a-b) VAC, (c-d) solvothermal, (e-f) modular assembly and (g-h) LPE methods; the proposed nucleation and growth processes involved in each method are schematically illustrated on top of these SEM images. All films were prepared on the – COOH functionalised gold substrates (1 cm x 1 cm) (relevant details: VAC deposition was performed using 30 µL freshly prepared MOF precursor solution with acetic acid as modulator (r_M = 219 eq.), at 100 °C for 3 h; modular assembly deposition was conducted with five consecutive stamping cycles; LPE deposition was done over thirty consecutive cycles).
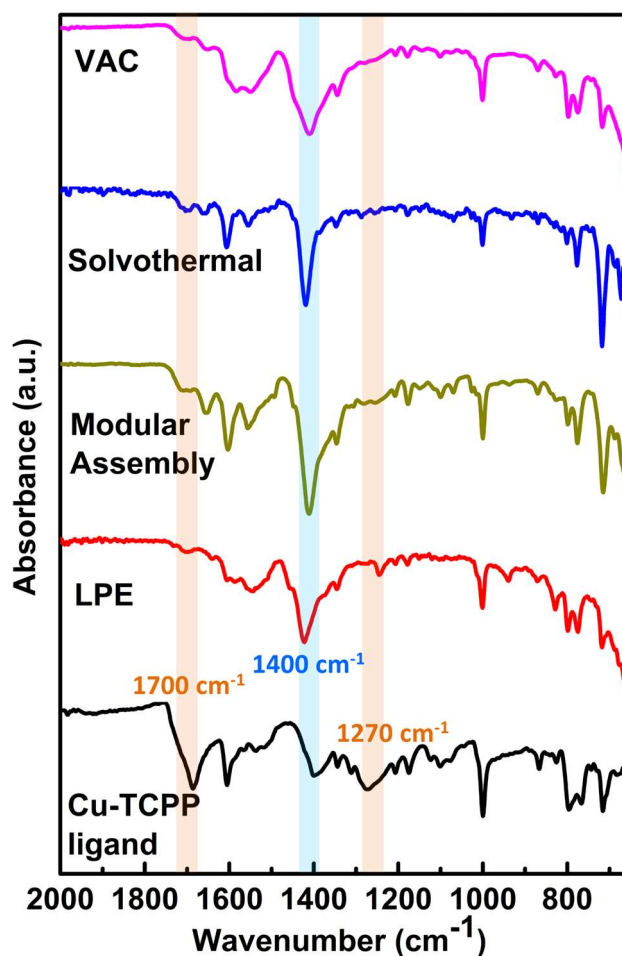
Figure 2.24 ATR-IR spectra of CuTCPP ligand and PCN-222 films fabricated on –COOH terminated gold substrates by VAC, solvothermal, modular assembly and LPE methods.

Thin films grown by all the aforementioned methods present similar ATR-IR spectra (**Figure 2.24**). Compared to the spectrum of CuTCPP ligand, PCN-222 films exhibit absence of peaks around 1700 cm^{-1} and 1270 cm^{-1} whereas the peak enhanced at 1400 cm^{-1} is reflective of the carboxyl coordination in CuTCPP to the Zr(IV) centres. This also suggests that the TCPP ligands, despite coordinating to Zr$_6$ SBUs failed to form a crystalline PP-MOF during the LPE film growth process.

As shown in **Figure 2.23**, SEM images of PCN-222 films fabricated by different methods were studied. Top-view SEM images reveal that VAC could assemble a highly smooth, dense and homogeneous PCN-222 film on the solid surface (**Figures 2.23a-b**) with a controlled thickness (**Figure 2.25**). High surface coverage of this film indicates its tendency towards anchoring with the –COOH functionalised substrates. Identification of PCN-222 crystallites with two different grain sizes on top of the film affirmed the coexistence of two individual nucleation processes

accompanying the film growth. Firstly, a heterogeneous nucleation was initiated on the solid surface and then a homogeneous nucleation occurred in the liquid volume left on the film surface.[15] The homogeneous nucleation could be plausibly attributed to a change in the ratio of reactants that occupied the remaining liquid volume. Similarly, the solvothermally grown PCN-222 film exhibits a smooth, dense and homogeneous morphology with intergrown rod-shaped crystallites. All these rod-shaped crystallites aligned in parallel to the substrate plane *i.e.* along the *a* axis. This matches well with the GIXRD pattern, serving an evidence of the [100] reflection. The 3D PCN-222 film prepared by modular assembly exhibited a rough surface with random rod crystallites densely packed on the substrate. This is much different from the smooth and flat surface of 2D PP-MOF films obtained with high-aspect-ratio flaky nanosheets. Consistent with XRD pattern (**Figure 2.16**), the film grown via LPE was amorphous on the substrate surface. This is due to a high energy barrier of crystallisation in PCN-222, under the mild LPE immersion steps. SEM images of the PCN-222 films prepared by VAC on silicon and ITO substrates exhibited a similar morphology: smooth, dense, and homogeneous surface (**Figure 2.26**), more specifically.
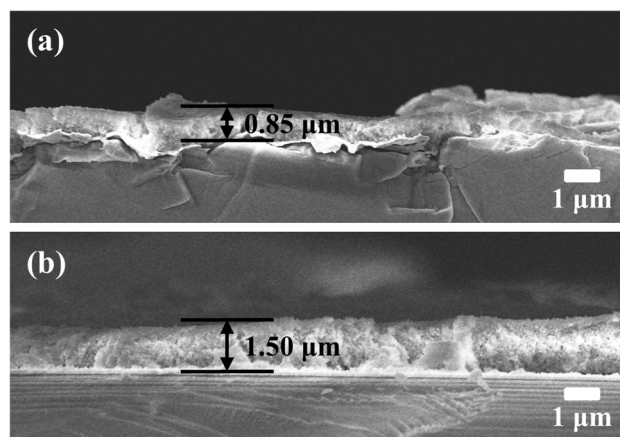
Figure 2.25 Cross-section SEM images of PCN-222 films grown by VAC method on –COOH terminated gold substrate with (a) 30 μL and (b) 60 μL of precursor solution.
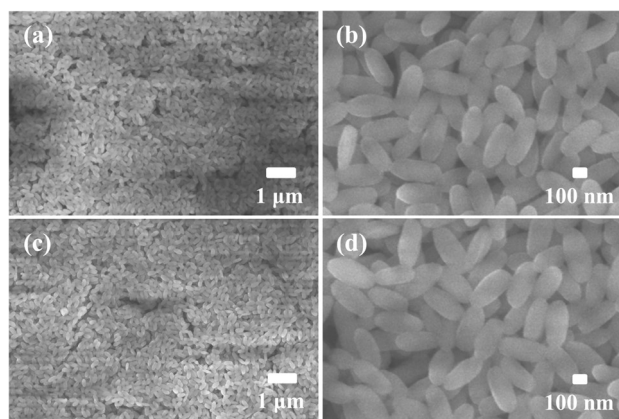
Figure 2.26 SEM images of PCN-222 film grown on silicon (a-b) and ITO (c-d) by VAC.

Surface roughness of the differently prepared PCN-222 films were also investigated (**Figure 2.27**). In agreement with SEM images, each of the films grown via VAC and solvothermal methods present a smooth surface with low roughness ($R_a \sim 2.2$ nm and 3.6 nm respectively, **Table 2.2**). In contrast, the film prepared by modular assembly presents a higher but acceptable surface roughness. Despite our failure to obtain a crystalline PCN-222 film, this amorphous film obtained via LPE reveals a smooth surface, characterised by a low $R_a \sim 4.0$ nm.
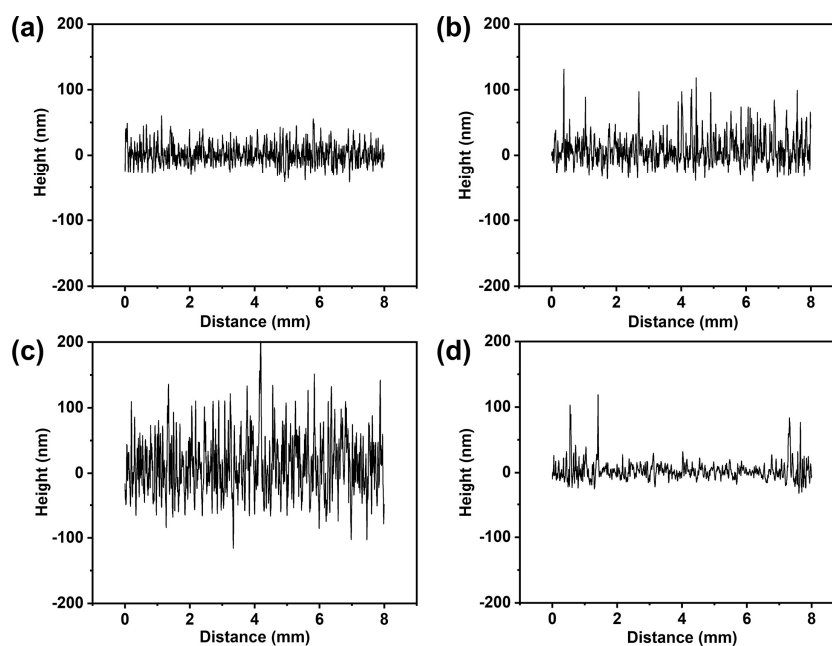
Figure 2.27 Roughness profiles of PCN-222 films fabricated on –COOH terminated gold substrates by (a) VAC, (b) solvothermal, (c) modular assembly and (d) LPE methods.

Table 2.2. Surface roughness of PCN-222 films fabricated via different methods.

Methods	R_a (nm)	R_q (nm)

VAC	2.2	2.7
Solvothermal	3.6	4.6
Modular assembly	5.5	6.9
LPE	4.0	4.7

To obtain further insights into the feasibility of utilising VAC in the fabrication of 3D PP-MOF films, *viz.* PCN-224 and MOF-525 with distinct framework topologies and structures, they were also grown on the –COOH functionalised gold substrates with the help of VAC (see **Tables S4** and **S5** in Chapter 5 for details).

For the PCN-224 film on functionalised surfaces, a preferred crystallite orientation along the [200] direction could be found (**Figures 2.28** and **2.29**). The influence of varying modulator concentrations in the formation of PCN-224 films could also be examined. According to the GIXRD pattern, when the r_M is 437, the reaction system yielded randomly oriented PCN-224 phase (with little PCN-222 phase). On the contrary, oriented and crystalline PCN-224 film was obtained with a ratio of 874 (**Figure 2.30**). This observed random orientation in PCN-224 at 437 eq. of modulator concentration could be attributed to the fast nucleation process occurring at low modulator levels, followed by an imprecise control over the growth orientation. Moreover, similar to the PCN-222 film formation, a mere 3 h reaction time was found enough for the nucleation and growth of a crystalline and oriented PCN-224 film. When the duration was prolonged to 12 h, the film obtained failed to strike any difference from the one obtained after 3h (**Figure 2.31**). The impact of reaction temperature was studied as well; the GIXRD patterns suggested that high temperature could induce a randomly oriented growth in the film (**Figure 2.32**). This might be attributed to the faster nucleation process and a concomitant loss of precise control over the oriented film growth processes at high temperatures, prompted by selective nucleation.
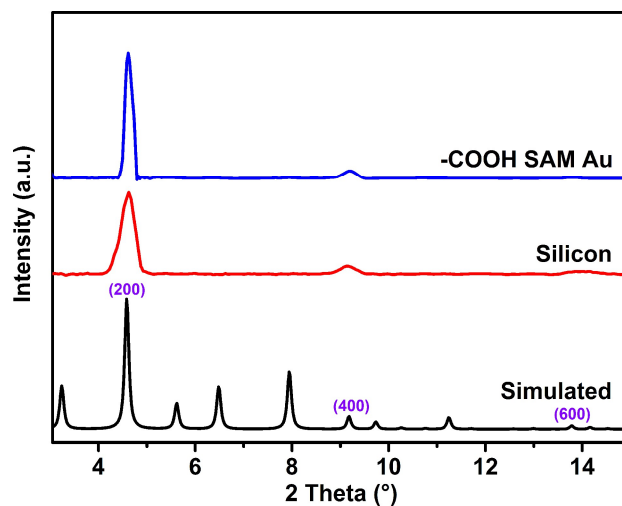
Figure 2.28 GIXRD patterns of PCN-224 films grown by VAC method on different functionalised substrates.
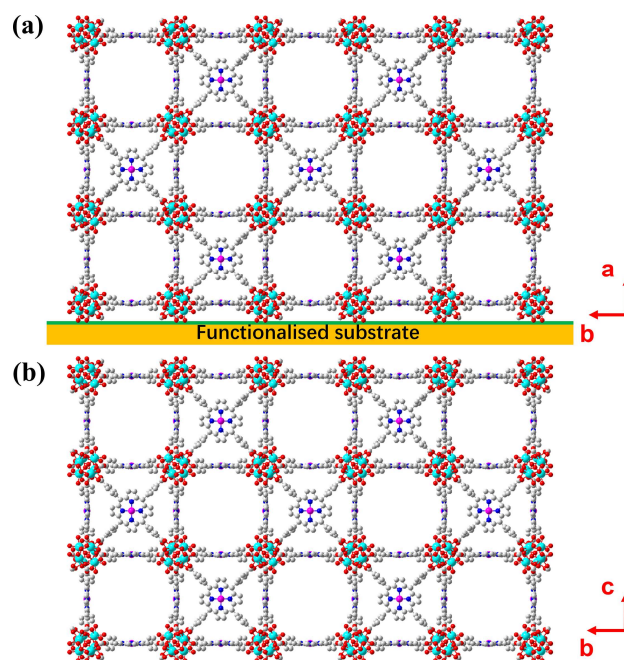
Figure 2.29 (a) Side-view scheme (*ab* plane) of PCN-224 film grown upon functionalised substrate along *a* axis ([200] direction); (b) the *bc* plane of PCN-224 film which nucleated on the substrate surface.
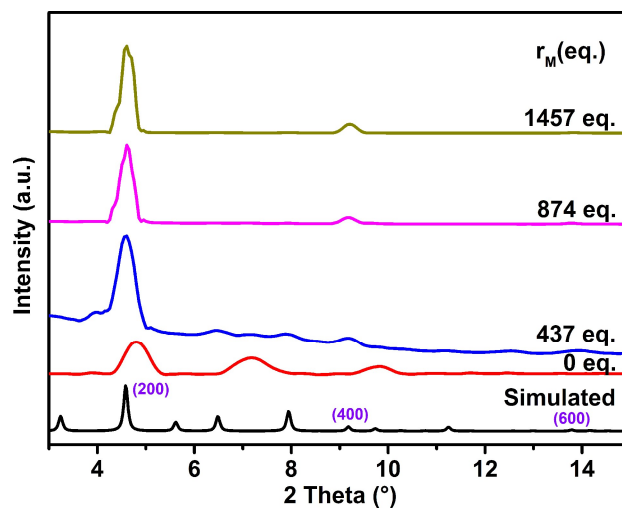
Figure 2.30 GIXRD patterns of PCN-224 films grown on –COOH terminated gold substrates via VAC method with different modulator to metal ratios (r_M).
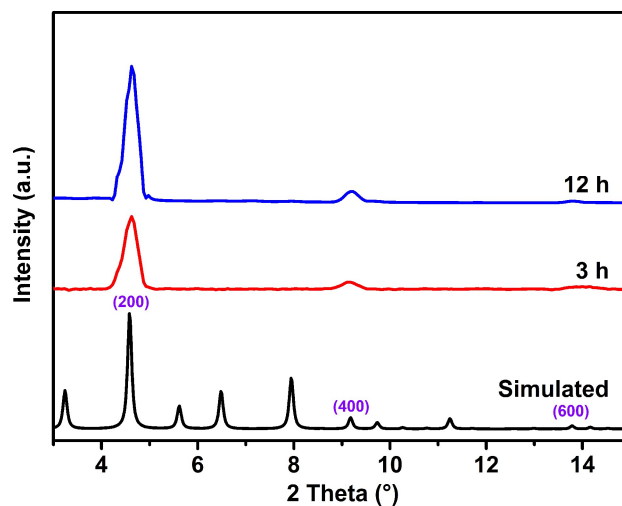
Figure 2.31 GIXRD patterns of PCN-224 films grown on –COOH terminated gold substrates via VAC method using different reaction time.
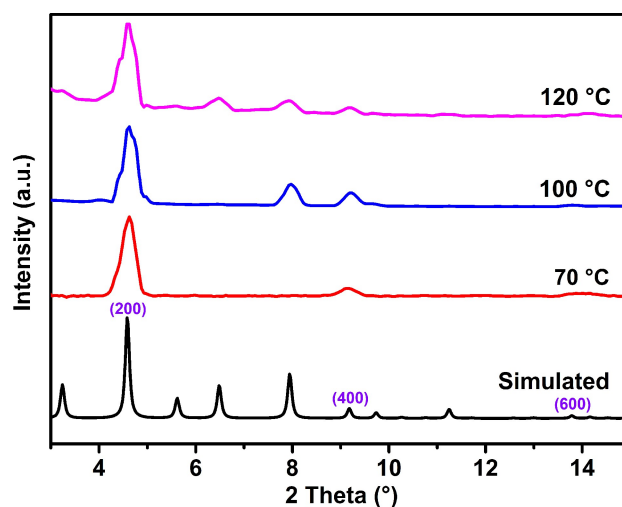
Figure 2.32 GIXRD patterns of PCN-224 films grown on –COOH terminated gold substrates via VAC

method on different reaction temperatures.

The SEM images and roughness profile indicate a smooth, dense, homogeneous and crystalline PCN-224 film fabricated via VAC on solid surface (**Figures 2.33, 2.34** and **Table 2.3**). Magnified version of SEM reveals the dense growth of cubic crystallites, all of uniform size. The sporadic MOF crystallites on top of the film are due to a secondary nucleation process.
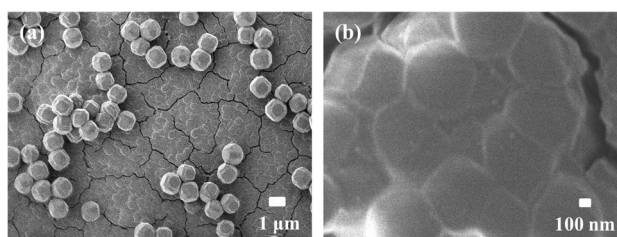
Figure 2.33 SEM images of PCN-224 film grown on –COOH terminated gold substrate via VAC method; note that in the VAC deposition method, 30 μL freshly prepared MOF precursor solution is used with acetic acid as modulator (r_M = 1457) at 70 °C for 3 h.
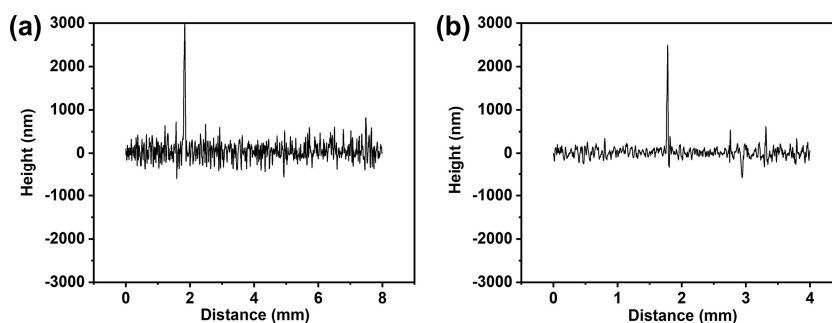
Figure 2.34 Roughness profiles of (a) PCN-224 and (b) MOF-525 films fabricated on –COOH terminated gold substrates by VAC method.

Table 2.3 Surface roughness of PCN-224 and MOF-525 films fabricated by VAC.

MOFs	R_a (nm)	R_q (nm)
PCN-224	13.1	16.5
MOF-525	8.5	10.3

Regarding the VAC assisted fabrication of MOF-525 films on functionalised gold substrate, unlike PCN-222 and PCN-224, no preferred crystallite orientation was noted in the MOF-525 films (**Figures 2.35** and **2.36**). This is plausibly ascribed to the fully bridged 12-connecting Zr_6 clusters that results in a myriad of choices while nucleating and while getting aligned as part of the film growth *i.e.* when the clusters get anchored on the terminal organic groups of SAM on solid surfaces.
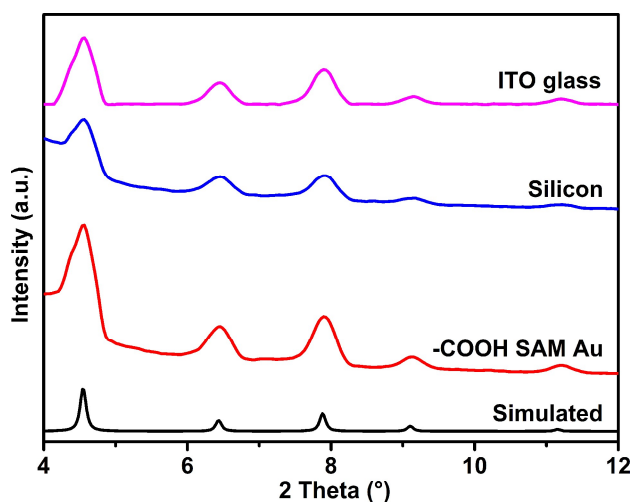
Figure 2.35 GIXRD patterns of MOF-525 films grown by VAC method on different functionalised substrates.
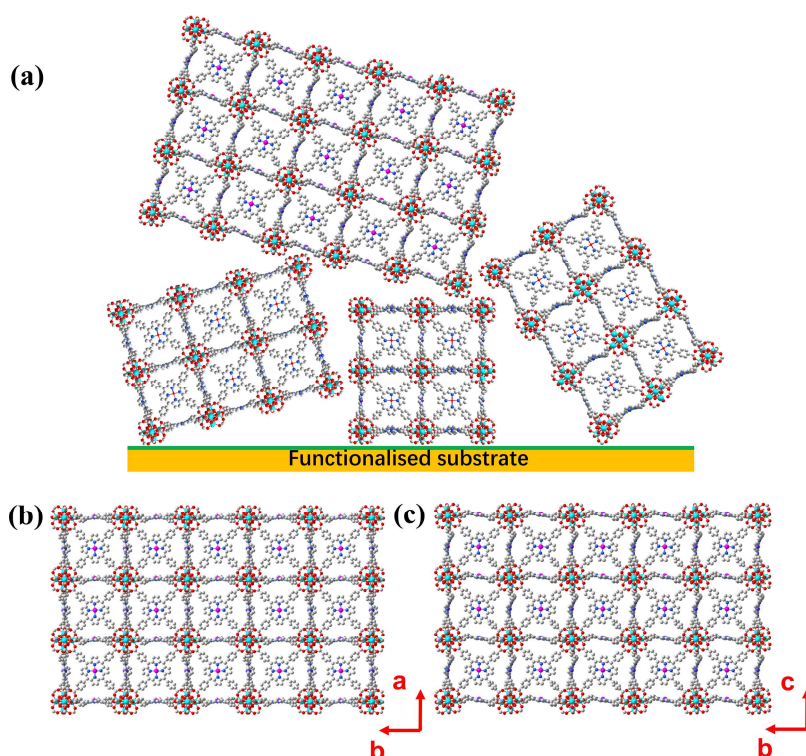
Figure 2.36 (a) Side-view scheme of the MOF-525 film randomly grown upon functionalised substrate; (b) the *ab* plane and (c) *bc* plane of MOF-525.

As shown in **Figure 2.37**, GIXRD patterns indicate that the MOF phase changes slightly from PCN-222 to MOF-525 with an increase in the modulator concentration. When the r_M is at or below 219, the crystalline PCN-222 phase films were obtained even at a low Zr/TCPP reactant ratio (Zr/TCPP was 2/1 for MOF-525, and Zr/TCPP was 3/1 for PCN-222, corresponding to their compositional ratios in respective MOF structures). When the modulator concentration was in between 365

eq. and 584 eq. of the $ZrOCl_2 \cdot 8H_2O$, the film appeared to be a mixed MOF phase of PCN-222 and MOF-525. A crystalline MOF-525 film could be obtained with $r_M \sim$ 730, but with random orientation. Despite the high symmetry of MOF-525, crystalline films resulted within 3 hours. Morphology and nature of this film remained unchanged even after subjecting to a prolonged reaction time of 12 h (**Figure 2.38**). These SEM results are indicative of the propensity of our pursued VAC method in order to afford dense, homogeneous and crystalline MOF-525 films. The MOF-525 crystallites were found packed on the –COOH functionalised gold substrate with random orientation, consistent with the GIXRD pattern (**Figure 2.39**).
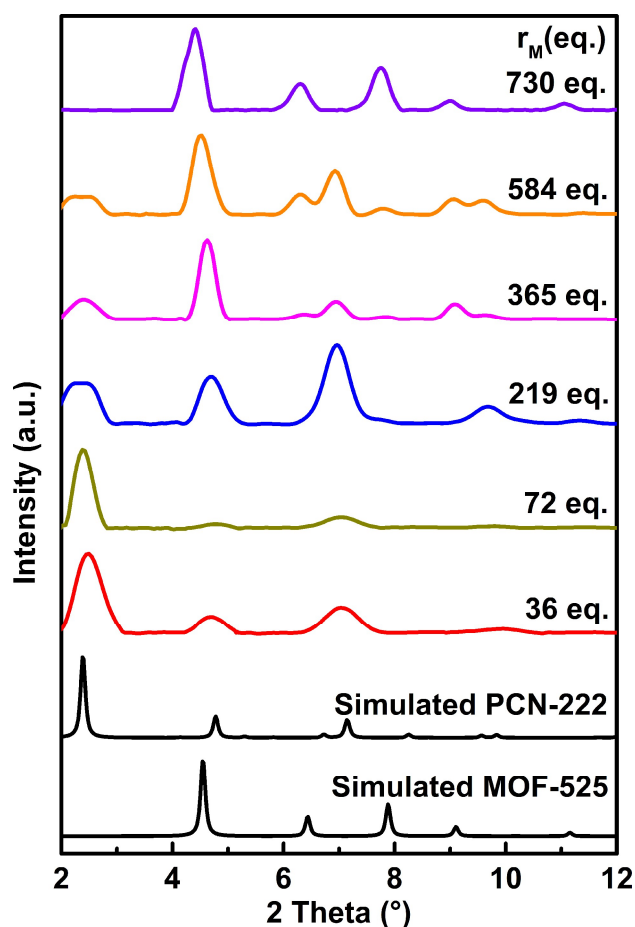
Figure 2.37 GIXRD patterns of MOF-525 films grown on –COOH terminated gold substrates via VAC method with different modulator to metal ratios (r_M)
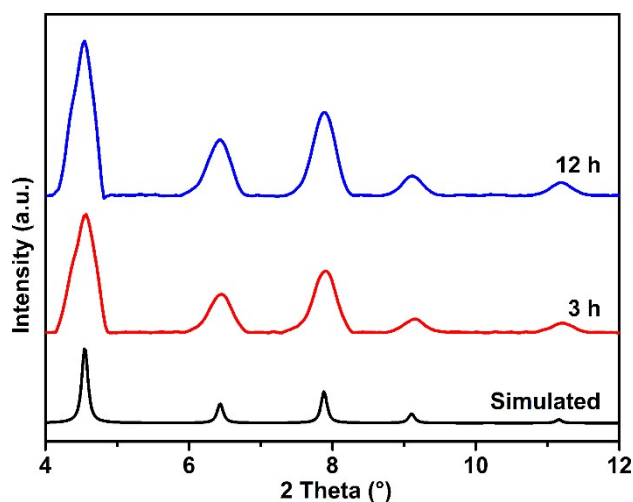
Figure 2.38 GIXRD patterns of MOF-525 films grown on –COOH terminated gold substrates via VAC method using different reaction times.
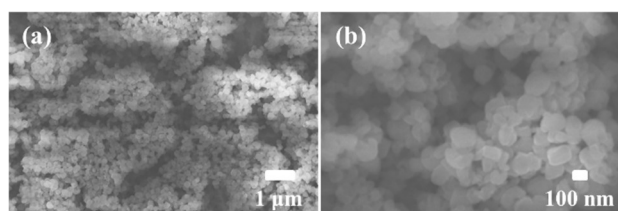
Figure 2.39 SEM images of MOF-525 film grown on –COOH terminated gold substrate via VAC method; note that during VAC deposition, 30 μL freshly prepared MOF precursor solution is used with acetic acid as modulator (r_M = 730) at 80 °C for 3 h.

That a prototypal class of 3D PP-MOF films, comprised of alike porphyrin linkers and metal ion based clusters, are amenable to solid surface fabrication by fine-tuning the modulator content becomes evident from our foregoing experimental results.

2.2.3 Adsorption properties of differently fabricated PP-MOF films

As discussed above, the crystallinity, morphology and thickness of the PP-MOF films are controlled to a large extent by the preparation method(s) involved. Meanwhile, the preparation conditions affording the PP-MOF films play a key role in controlling their properties. Treating vapour adsorption properties as our studied property amenable to film growth based fine-tuning, ample scopes to examine the distinctly prepared thin films' sorption features remain. Upon recording vapour sorption isotherms by an environmentally controlled QCM detector, the prepared series of 2D and 3D PP-MOF films revealed interesting trends as discussed following.

For the 2D PP-MOFs, each of the four distinctly prepared Zn$_2$(ZnTCPP) films were marked with a typical type I Langmuir isotherm for methanol vapour at 25 °C (**Figure 2.40a**). These isotherms are signatures of their microporosity and suggest facile diffusion of methanol occurs into each of their polar pores replete with carboxyl groups. The four films exhibit different methanol adsorption capacities at P/P$_0$ of 0.95, suggestive of their differing polar natures.[32] Compared to the solvothermally fabricated film recording an uptake of 3.5 mmol g^{-1} methanol vapour, the films obtained using modular assembly, LPE and VAC exhibited higher uptakes: 5.6 mmol g^{-1}, 6.3 mmol g^{-1} and 5.8 mmol g^{-1}, respectively. Apart from offering insights into their relative polar characteristics, this trend is in good agreement with excellent crystallinity of the films. The lower methanol adsorption amount (3.5 mmol g^{-1}) of the solvothermally grown film can be ascribed well to the disparate growth of randomly oriented bulk Zn$_2$(ZnTCPP) MOF on the substrate surface during the solvothermal process. [4]
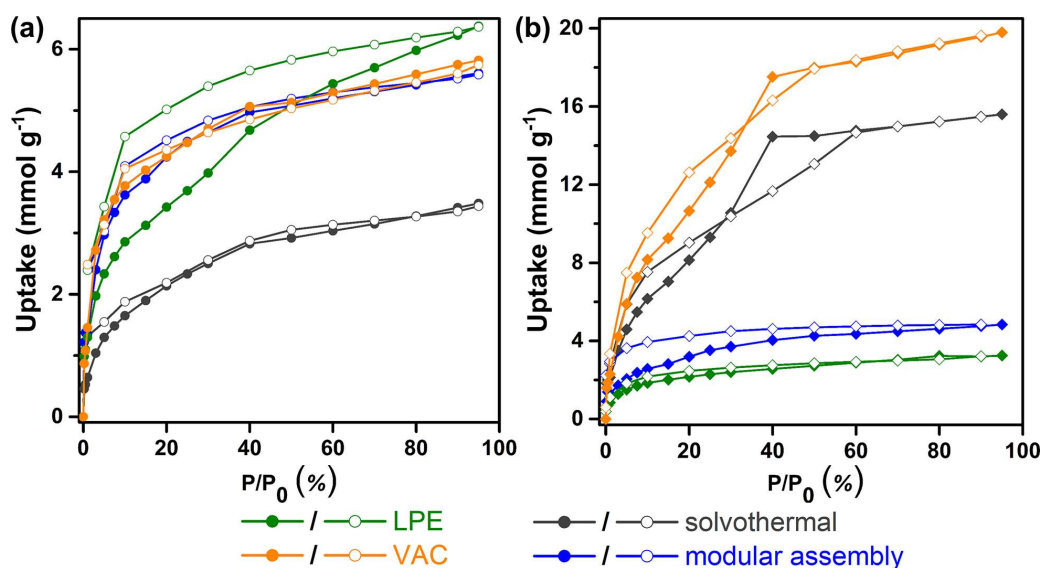
Figure 2.40 Methanol vapour sorption isotherms at ambient temperature (25 °C) using an environmentally controlled quartz crystal microbalance (BELQCM-4 equipment) of (a) Zn$_2$(ZnTCPP) and (b) PCN-222 films fabricated by VAC, solvothermal, modular assembly and LPE methods on the –COOH functionalised Au-coated QCM substrates.

In contrast to these similarly behaving 2D PP-MOFs, among the four distinctly prepared 3D PP-MOFs, two Zn$_2$(ZnTCPP) films *i.e.* the ones derived by LPE and modular assembly were noted to exhibit typical type I Langmuir isotherms for methanol vapour at 25 °C (**Figure 2.40b**). Typical type IV isotherms were observed for the two other films fabricated via VAC and solvothermal techniques, marked with

a steep increase at P/P_0 ~ 0.3, indicating their mesoporosity.[26a] Compared to the films fabricated via LPE and modular assembly, the oriented PCN-222 films obtained via VAC and solvothermal methods demonstrated much higher amounts of adsorbed methanol, 19.8 mmol g^{-1} and 15.6 mmol g^{-1} respectively, at P/P_0 ~ 0.95. This is attributed to the oriented, smooth and dense morphology of the PCN-222 films grown by VAC and solvothermal methods, which offer a more periodic, uniform and compact pores, thus leading to an enhanced adsorption property.[10a, 17a, 23] The lower methanol affinity (4.9 mmol g^{-1}) in the film fabricated via modular assembly is ascribed to the stacks of randomly oriented PCN-222 rod crystallites on the substrate surface.[10a] Despite the absence of crystallinity, the LPE grown film exhibits a micropore filling of 3.2 mmol g^{-1} methanol uptake, an indication to its guest-accessibility. The PCN-224 film prepared via VAC shows a considerable methanol adsorption uptake (16.5 mmol g^{-1}) at 25 °C, proving the high porosity of the oriented PCN-224 film (**Figure 2.41**). The randomly oriented MOF-525 film exhibits 10.2 mmol g^{-1} uptake of methanol (**Figure 2.42**).
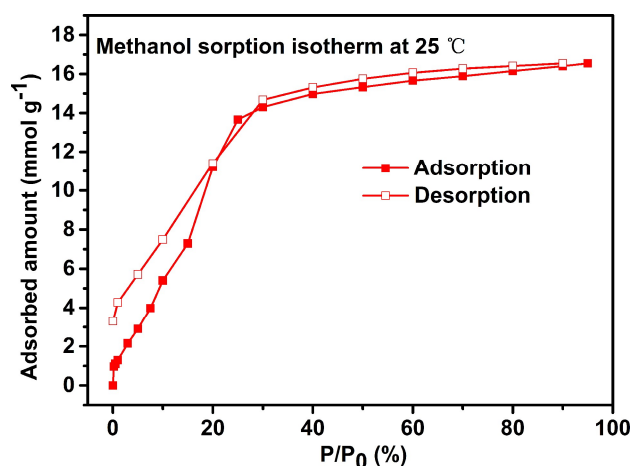
Figure 2.41 Methanol sorption isotherms at ambient temperature (25 °C) of PCN-224 film fabricated by VAC method on the –COOH terminated Au-coated QCM substrate.
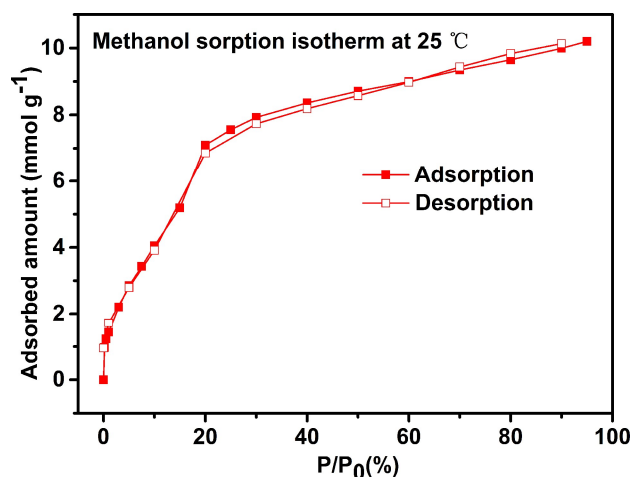
Figure 2.42 Methanol sorption isotherms at ambient temperature (25 °C) of MOF-525 film fabricated by VAC method on the –COOH terminated Au-coated QCM substrate.

2.3 Conclusions

In summary, we firstly developed VAC as a facile and versatile route to grow highly crystalline, smooth, dense, homogeneous and oriented films of both 2D and 3D PP-MOFs on various solid surfaces. Key details regarding the parameters associated in controlling the nucleation and growth of PP-MOF films, including the reactant and modulator concentration, the droplet volume, reaction temperature and reaction time, have been investigated. Our study identifies the important role played by the modulator in prompting nucleation and to also facilitate oriented film growth. The obtained PP-MOF films reveal a considerable saturation uptake of methanol at room temperature, suggesting their high guest-accessible volumes and polar Connolly surfaces. Moreover, different methods (viz., VAC, solvothermal, modular assembly and LPE) could be critically compared for easy understanding of the mechanism(s) behind PP-MOF films nucleation and growth. This study proposes to provide a point of reference for all future research revolving around the preparation of PP-MOF thin films.

2.4 References

[1]   S. R. Batten, N. R. Champness, X.-M. Chen, J. Garcia-Martinez, S. Kitagawa, L. Öhrström, M. O'Keeffe, M. P. Suh, J. Reedijk, *Pure Appl. Chem.* **2013**, 85, 1715.

[2]   P. Falcaro, R. Ricco, C. M. Doherty, K. Liang, A. J. Hill, M. J. Styles, *Chem. Soc. Rev.* **2014**, 43, 5513.

[3]   a) J. Liu, W. Zhou, J. Liu, I. Howard, G. Kilibarda, S. Schlabach, D. Coupry, M. Addicoat, S. Yoneda, Y. Tsutsui, *Angew. Chem. Int. Ed.* **2015**, 54, 7441; b) D. Micheroni, G. Lan, W. Lin, *J. Am. Chem. Soc.* **2018**, 140, 15591; c) G. Xu, K. Otsubo, T. Yamada, S. Sakaida, H. Kitagawa, *J. Am. Chem. Soc.* **2013**, 135, 7438.

[4]   M. Zhao, Y. Wang, Q. Ma, Y. Huang, X. Zhang, J. Ping, Z. Zhang, Q. Lu, Y. Yu, H. Xu, Y. Zhao, H. Zhang, *Adv. Mater.* **2015**, 27, 7372.

[5]   a) C.-H. Su, C.-W. Kung, T.-H. Chang, H.-C. Lu, K.-C. Ho, Y.-C. Liao, *J. Mater. Chem. A* **2016**, 4, 11094; b) P. M. Usov, B. Huffman, C. C. Epley, M. C. Kessinger, J. Zhu, W. A. Maza, A. J. Morris, *ACS Appl. Mater. Interfaces* **2017**, 9, 33539.

[6]   L. Dumée, L. He, M. Hill, B. Zhu, M. Duke, J. Schütz, F. She, H. Wang, S. Gray, P. Hodgson, L. Kong, *J. Mater. Chem. A* **2013**, 1, 9208.

[7]   D. Jiang, A. D. Burrows, Y. Xiong, K. J. Edler, *J. Mater. Chem. A* **2013**, 1, 5497.

[8]   W.-J. Li, M. Tu, R. Cao, R. A. Fischer, *J. Mater. Chem. A* **2016**, 4, 12356.

[9]   a) W. Li, S. Xue, S. Watzele, S. Hou, J. Fichtner, A. L. Semrau, L. Zhou, A. Welle, A. S. Bandarenka, R. A. Fischer, *Angew. Chem. Int. Ed.* **2020**, 59, 5837; b) S. Wannapaiboon, M. Tu, R. A. Fischer, *Adv. Funct. Mater.* **2014**, 24, 2696.

[10]   a) S. M. Yoon, J. H. Park, B. A. Grzybowski, *Angew. Chem. Int. Ed.* **2017**, 129, 133; b) C.-W. Kung, T.-H. Chang, L.-Y. Chou, J. T. Hupp, O. K. Farha, K.-C. Ho, *Chem. Commun.* **2015**, 51, 2414; c) P. M. Usov, S. R. Ahrenholtz, W. A. Maza, B. Stratakes, C. C. Epley, M. C. Kessinger, J. Zhu, A. J. Morris, *J. Mater. Chem. A* **2016**, 4, 16818.

[11]   a) R. Makiura, S. Motoyama, Y. Umemura, H. Yamanaka, O. Sakata, H. Kitagawa, *Nature materials* **2010**, 9, 565; b) S. Motoyama, R. Makiura, O.

Sakata, H. Kitagawa, *J. Am. Chem. Soc.* **2011**, 133, 5640.

[12] G. Xu, T. Yamada, K. Otsubo, S. Sakaida, H. Kitagawa, *J. Am. Chem. Soc.* **2012**, 134, 16524.

[13] a) J. Liu, W. Zhou, J. Liu, Y. Fujimori, T. Higashino, H. Imahori, X. Jiang, J. Zhao, T. Sakurai, Y. Hattori, W. Matsuda, S. Seki, S. K. Garlapati, S. Dasgupta, E. Redel, L. Sun, C. Wöll, *J. Mater. Chem. A* **2016**, 4, 12739; b) D. J. Li, Z. G. Gu, I. Vohra, Y. Kang, Y. S. Zhu, J. Zhang, *Small* **2017**, 13.

[14] M. C. So, S. Jin, H.-J. Son, G. P. Wiederrecht, O. K. Farha, J. T. Hupp, *J. Am. Chem. Soc.* **2013**, 135, 15698.

[15] E. Virmani, J. M. Rotter, A. Mähringer, T. Von Zons, A. Godt, T. Bein, S. Wuttke, D. D. Medina, *J. Am. Chem. Soc.* **2018**, 140, 4812.

[16] a) Y. Wang, M. Zhao, J. Ping, B. Chen, X. Cao, Y. Huang, C. Tan, Q. Ma, S. Wu, Y. Yu, *Adv. Mater.* **2016**, 28, 4149; b) Y. Zhao, L. Jiang, L. Shangguan, L. Mi, A. Liu, S. Liu, *J. Mater. Chem. A* **2018**, 6, 2828; c) Y. Y. Wang, S. M. Chen, R. Haldar, C. Wöll, Z. G. Gu, J. Zhang, *Adv. Mater. Interfaces* **2018**, 5, 1800985; d) E.-Y. Choi, C. A. Wray, C. Hu, W. Choe, *CrystEngComm* **2009**, 11, 553.

[17] a) Z. Wang, K. Rodewald, R. Medishetty, B. Rieger, R. A. Fischer, *Cryst. Growth Des.* **2018**, 18, 7451; b) D. Zacher, A. Baunemann, S. Hermes, R. A. Fischer, *J. Mater. Chem.* **2007**, 17, 2785.

[18] K. M. Ishihara, F. Tian, *Langmuir* **2018**, 34, 15689.

[19] B. Liu, O. Shekhah, H. K. Arslan, J. Liu, C. Wöll, R. A. Fischer, *Angew. Chem. Int. Ed.* **2012**, 51, 807.

[20] S. Hermes, D. Zacher, A. Baunemann, C. Wöll, R. A. Fischer, *Chem. Mater.* **2007**, 19, 2168.

[21] M. Tian, F. Pei, M. Yao, Z. Fu, L. Lin, G. Wu, G. Xu, H. Kitagawa, X. Fang, *Energy Storage Mater.* **2019**, 21, 14.

[22] J. Liu, C. Wöll, *Chem. Soc. Rev.* **2017**, 46, 5730.

[23] S. Wannapaiboon, K. Sumida, K. Dilchert, M. Tu, S. Kitagawa, S. Furukawa, R. A. Fischer, *J. Mater. Chem. A* **2017**, 5, 13665.

[24] T. Tsuruoka, S. Furukawa, Y. Takashima, K. Yoshida, S. Isoda, S. Kitagawa, *Angew. Chem. Int. Ed.* **2009**, 121, 4833.

[25] a) Y. Huang, C.-a. Tao, R. Chen, L. Sheng, J. Wang, *Nanomaterials* **2018**, 8,

676; b) W. Yin, C.-a. Tao, F. Wang, J. Huang, T. Qu, J. Wang, *Sci. China Mater.* **2017**, 61, 391; c) W. Yin, C.-a. Tao, X. Zou, F. Wang, T. Qu, J. Wang, *Nanomaterials* **2017**, 7, 242.

[26]   a) D. Feng, Z. Y. Gu, J. R. Li, H. L. Jiang, Z. Wei, H. C. Zhou, *Angew. Chem. Int. Ed.* **2012**, 51, 10307; b) D. Feng, W.-C. Chung, Z. Wei, Z.-Y. Gu, H.-L. Jiang, Y.-P. Chen, D. J. Darensbourg, H.-C. Zhou, *J. Am. Chem. Soc.* **2013**, 135, 17105; c) W. Morris, B. Volosskiy, S. Demir, F. Gándara, P. L. McGrier, H. Furukawa, D. Cascio, J. F. Stoddart, O. M. Yaghi, *Inorg. Chem.* **2012**, 51, 6443.

[27]   a) M. Oldenburg, A. Turshatov, D. Busko, S. Wollgarten, M. Adams, N. Baroni, A. Welle, E. Redel, C. Wöll, B. S. Richards, *Adv. Mater.* **2016**, 28, 8477; b) H.-Q. Xu, J. Hu, D. Wang, Z. Li, Q. Zhang, Y. Luo, S.-H. Yu, H.-L. Jiang, *J. Am. Chem. Soc.* **2015**, 137, 13440.

[28]   G. Zahn, H. A. Schulze, J. Lippke, S. König, U. Sazama, M. Fröba, P. Behrens, *Microporous Mesoporous Mater.* **2015**, 203, 186.

[29]   Z. Fu, G. Xu, *Chem. Rec.* **2017**, 17, 518.

[30]   D. Feng, Z.-Y. Gu, Y.-P. Chen, J. Park, Z. Wei, Y. Sun, M. Bosch, S. Yuan, H.-C. Zhou, *J. Am. Chem. Soc.* **2014**, 136, 17714.

[31]   a) D. Zacher, R. Schmid, C. Woell, R. A. Fischer, *Angew. Chem. Int. Ed.* **2011**, 50, 176; b) O. Shekhah, H. Wang, D. Zacher, R. A. Fischer, C. Wöll, *Angew. Chem. Int. Ed.* **2009**, 48, 5038.

[32]   S. Mukherjee, A. V. Desai, S. K. Ghosh, *Coord. Chem. Rev.* **2018**, 367, 82.

Chapter 3

Porphyrinic MOF Film for Multifaceted Electrochemical Sensing*
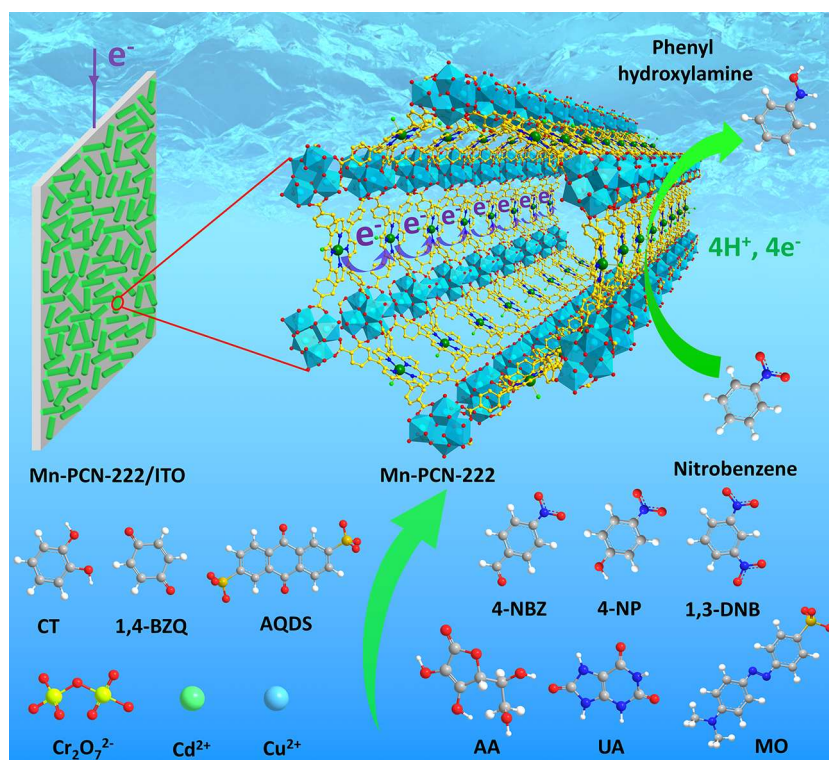
Abstract

Electrochemical sensors are indispensable in clinical diagnosis, biochemical detection and environmental monitoring, thanks to their ability to detect analytes in real-time with direct electronic readout. However, electrochemical sensors are challenged by sensitivity – the need to detect low concentrations, and selectivity – to detect specific analytes in multicomponent systems. Herein, a porphyrinic metal-organic framework (PP-MOF), Mn-PCN-222 is deposited on a conductive indium tin oxide (ITO) surface. It affords Mn-PCN-222/ITO, a versatile voltammetric sensor able to detect redox-active analytes such as inorganic ions, organic hazardous substances and pollutants, including nitroaromatics, phenolic and quinone-hydroquinone toxins, heavy metal ions, biological species, as well as azo dyes. As a working electrode, the high surface area of Mn-PCN-222/ITO enables high currents, and therefore leverages highly sensitive analysis. The metalloporphyrin centre facilitates analyte-specific redox catalysis to simultaneously detect more than one analyte in binary and ternary systems allowing for detection of a wide array of trace pollutants under real-world conditions, most with high sensitivity.

3.1 Introduction

Electrochemical sensing stems from changes in the detectable electric signal caused by the interactions between electrode and specific analytes. Thanks to its advantages, such as quick response, high efficiency, simple operation, and analyte-specific redox potentials that open specific windows for detection, electrochemical sensors have spurred considerable research interest and have been widely used in clinical diagnosis, biochemistry and environmental monitoring.[1] Besides potentiometric sensors, voltammetric (= Volt- / Amperometric) sensors are the most common kind. Here analyte-specific redox reactions are detected by measuring the corresponding electrical current in response to changes in the applied electrochemical potential.[1b, 2] This has propelled cyclic voltammetry (CV) as a front-runner for sensing redox-active analytes. Here, the applied potential at the working electrode is varied back and forth at a certain scan rate over a specific potential range. By plotting the current response *versus* the applied potential, a cyclic voltammogram trace is obtained,[3] which is symmetric in the case of reversible redox reactions at the electrode surface and non-symmetric otherwise. Despite such successful technological examples as the Clark electrode for detection of oxygen,[4] the high sensitivity and universality of electrochemical sensors (*i.e.*, the ability to detect a wide range of analytes such as organic pollutants, heavy ions, biological markers and azo dyes) remain unmet challenges until today.

Metal-organic frameworks (MOFs), composed of organic linkers and inorganic metal nodes (or clusters), have drawn enormous attention due to their well-defined porous structures with high surface areas, good stability and tailored functionalities.[5] These features lead to an increased propensity for the analytes to get concentrated and to expedite rapid mass transfer of the analytes across a large surface area. This in turn amplifies the voltammetric current as a characteristic signal response and thereby enhances sensitivity, making MOFs promising for electrochemical sensing.[1a, 6] On the other hand, thanks to their π-conjugated macrocyclic structures, porphyrins and metalloporphyrins demonstrate good electron transfer and selective redox catalytic properties, thus befitting to electrochemically sense several target analytes.[7]

Considering these advantages of MOFs and porphyrins, we develop porous

porphyrinic MOFs (PP-MOFs) treating these as molecular building blocks. In the pursuit of electrochemical sensing, PCN-222 (PCN, porous coordination network), a prototypical PP-MOF constructed from Zr_6 cluster and tetrakis(4-carboxyphenyl)-porphyrin (TCPP) ligand is used. PCN-222 features ultrahigh surface areas (> 2000 m^2/g).[8] Its 1D hexagonal mesopores ($\sim$ 3.0 nm) replete with porphyrin sites (**Figure 3.1a**) endow it as a potent lead to enable electrocatalytic sensing.[9] In pursuit of electrochemical applications, integration of PP-MOFs onto solid surfaces in the form of films is a prerequisite that we achieve herein.[10]

Recently, Mn-PCN-222 modified with poly-glutamic acid has been utilized earlier as an electrochemical H_2O_2 sensor.[9b] Nevertheless, the suitability of Mn-PCN-222 rests upon rationally combining metalloporphyrin redox sites with porosity, each enabling facile electron transfer and analyte transport. This, in unison, leads to a miscellany of sensing performances while detecting several analytes. Low detection limits are manifested herein, that cover both inorganic substrates and organic pollutants. Also, critical analysis of such a multifaceted detection process remains an uncharted territory. Herein, we forge ahead with our detailed electrochemical studies to fill this knowledge gap by selecting to study Mn-PCN-222 as a versatile sensor.

In this study, a facile and straightforward modular assembly technique for liquid-phase depositing of Mn-PCN-222 (manganese metalloporphyrin) film on conductive indium tin oxide (ITO) glass leads us to fabricate the Mn-PCN-222/ITO electrode (**Figure 3.1b**).[8b, 11] Herein, solvothermally synthesized PP-MOF nanoparticles (NPs) serve as thin film precursors. Thanks to hydrophobicity, these PP-MOF NPs spontaneously spread out as a thin film on water, from which they are easily transferred to the substrate. This simple stamping results in a very homogeneous thin film of assembled NPs. Overall, our observations introduce modular assembly as a reliable and efficient way of preparing PP-MOF film electrodes for multifunctional electrochemical sensors. To the best of our knowledge, this is the first report of an electrochemical sensor built from modular assembly.
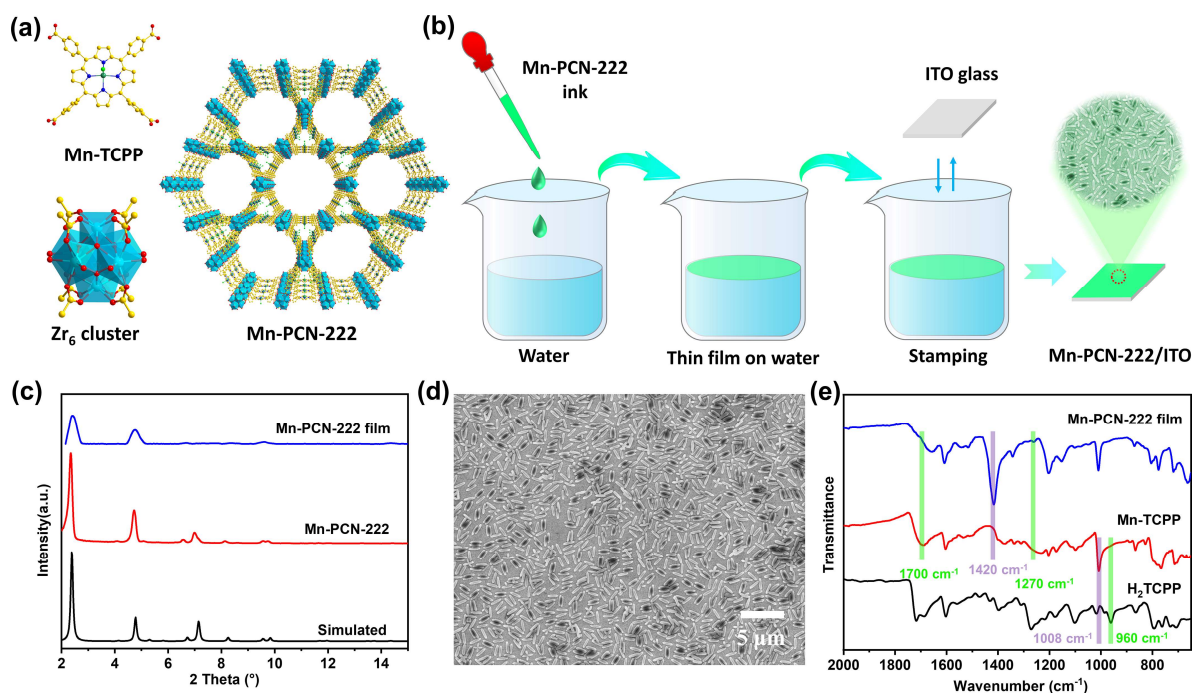
Figure 3.1 (a) Structures of the building blocks: Mn-TCPP ligand and Zr_6 cluster sustaining Mn-PCN-222; the framework structure of Mn-PCN-222 with 1D triangular microchannels and hexagonal mesochannels. H atoms are omitted for clarity. Color scheme: C, yellow; O, red; N, blue; Cl, olive green and Mn, cyan. (b) Schematic illustration of the modular assembly driven synthetic route leading to a Mn-PCN-222/ITO electrode. (c) Simulated and experimental PXRD patterns of the bulk Mn-PCN-222 and GIXRD patterns of the Mn-PCN-222 film fabricated by modular assembly. (d) SEM images of the Mn-PCN-222 film casted on ITO glass. (e) ATR-IR spectra of free H_2TCPP ligand, Mn-TCPP ligand and Mn-PCN-222 film.

3.2 Results and Discussion

Powder Powder X-ray diffraction (PXRD) patterns of the Mn-PCN-222 powder and its film obtained via modular assembly are shown in **Figure 3.1c**. These diffraction patterns are found to be in good agreement with the simulated XRD profile, suggesting bulk phase purity of the crystallized samples and confirming that the obtained thin film solely comprise the Mn-PCN-222 crystallites.[8, 12] Scanning electron microscopy (SEM) of an Mn-PCN-222 film-modified ITO electrode shows the film to be composed of rod-shaped Mn-PCN-222 crystallites (length ~ 1 μm) evenly dispersed on the ITO surface (**Figure 3.1d**). In principle, if the properties of building blocks are synergized, such a uniform coverage of Mn-PCN-222 crystallites on the conductive surface of ITO should indeed lead to an efficient electrochemical sensor.[10b] Energy-dispersive X-ray spectroscopy (EDX) confirms a uniform distribution of Mn elements across the Mn-PCN-222 thin film (**Figure 3.2**).

Attenuated total reflection infrared spectroscopy (ATR-IR) spectra and ultraviolet-visible spectroscopy (UV-Vis) spectra are recorded to further identify the compositions of the prepared Mn-PCN-222 film (**Figures 3.1e and 3.3**). In contrast to the free H_2TCPP ligand, the metallisation of Mn-TCPP ligand is evidenced by disappearance of the N–H stretching vibration at 960 cm^{-1} and appearance of a new peak at 1008 cm^{-1} assigned to Mn-N bonds.[8b, 13] The latter signature is also found in the Mn-PCN-222 film (**Figure 3.1e**). This is well aligned with the EDX and UV-Vis spectra (**Figures 3.2 and 3.3**). Moreover, compared to the spectrum of Mn-TCPP, Mn-PCN-222 films exhibit an absence of characteristic peaks around 1700 cm^{-1} (C=O bonds) and 1270 cm^{-1} (C-O bonds) whereas strong peaks at 1420 cm^{-1} (COO symmetric stretch band) appear, reflective of the carboxyl group coordinating to the Zr_6 centres in Mn-TCPP.[8b, 14] To verify the loading of Mn-PCN-222 onto the ITO electrode each time, UV-vis spectra of 10 independent samples are investigated and the absorbances at 465 nm are noted (**Table 3.1**).[13a] An average absorbance of 0.1421 a.u. (**Figure 3.4**) is observed, whereas its excellent reproducibility is evidenced by the low relative standard deviation (RSD) of just 3.0%. The porosity of bulk Mn-PCN-222 is examined by N_2 adsorption experiments and the typical type-IV isotherm is accompanied by a steep rise at *ca.* P/P_0 = 0.3, suggesting both micro and mesoporosity (**Figure 3.5**). The pore size distribution profile indicates two types of pores with sizes of ~ 1.3 nm and ~ 3.0 nm, assigned to the coexistence of 1D triangular microchannels and hexagonal mesochannels, respectively in the framework structure (**Figure 3.1a**).[8a] Applying Rouquerol criteria to the 77 K N_2 isotherm, the Brunauer-Emmett-Teller (BET) surface area is evaluated as high as 2013 m^2/g.[15] A methanol sorption isotherm recorded on the environmentally controlled quartz crystal microbalance (BEL-QCM) confirms the high porosity of film-desposited NPs (**Figure 3.6**). The large 1D mesochannels and high surface area, in principle, should prove beneficial to enable rapid analyte aggregation and mass transport.[8a, 9a, 9b]
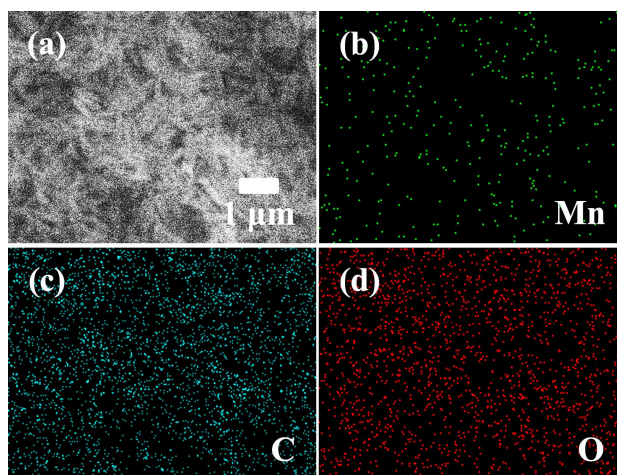
Figure 3.2 EDX elemental mapping images of Mn-PCN-222/ITO electrode.
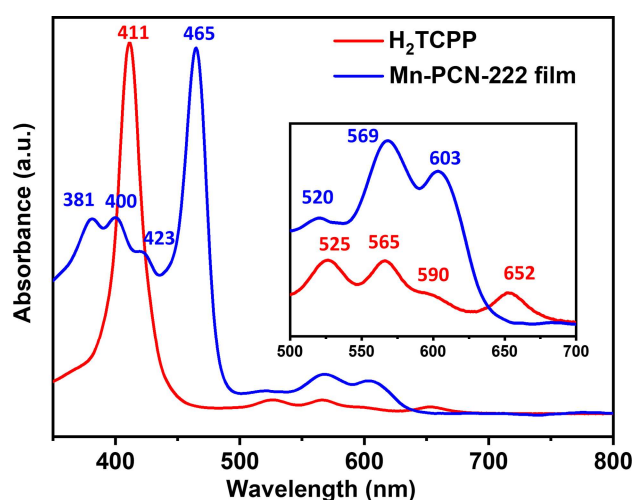
Figure 3.3 UV-Vis spectra of free H₂TCPP ligand and Mn-PCN-222 film. Inset presents a zoomed view of the enlarged Q-band region for clarity. The UV-Vis spectrum of H₂TCPP ligand presents a strong Soret band at 411 nm together with four Q-bands at 525, 565, 590, and 652 nm.[8b] The Soret band of Mn-PCN-222 films was noticed to undergo a red shift to 465 nm, with three weak Q bands at 520, 569 and 603 nm respectively, confirming the metalation of porphyrin rings by Mn(III) in the Mn-PCN-222 film;[13a] moreover, no characteristic peak of the free TCPP or other new metallized TCPP could be observed after the possible leaching or substitution of Mn(III) ions; this confirms the absence of Mn leaching and substitution by other metal ions during the synthesis of Mn-PCN-222 and film fabrication.

Table 3.1 Comparation of the UV-vis absorbances of ten Mn-PCN-222/ITO electrodes.

Samples	1	2	3	4	5	6	7	8	9	10
Absorbances at 465 nm	0.143	0.142	0.148	0.144	0.137	0.143	0.149	0.139	0.136	0.140
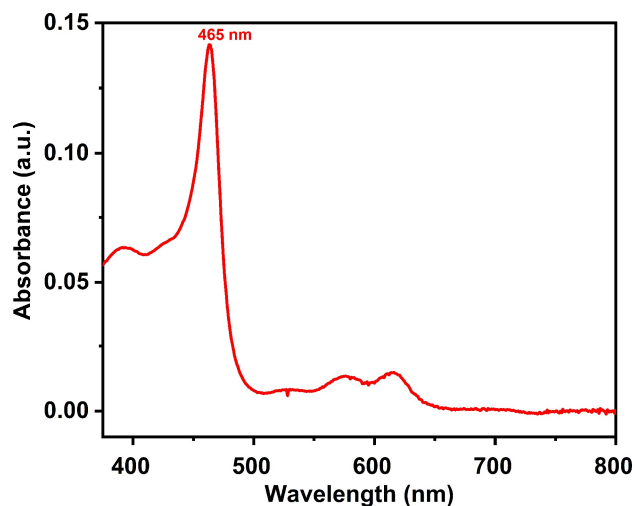
Figure 3.4 UV-Vis spectrum of Mn-PCN-222/ITO electrode (1 cycle thin film) with an absorbance of 0.1421 a.u. at 465 nm.
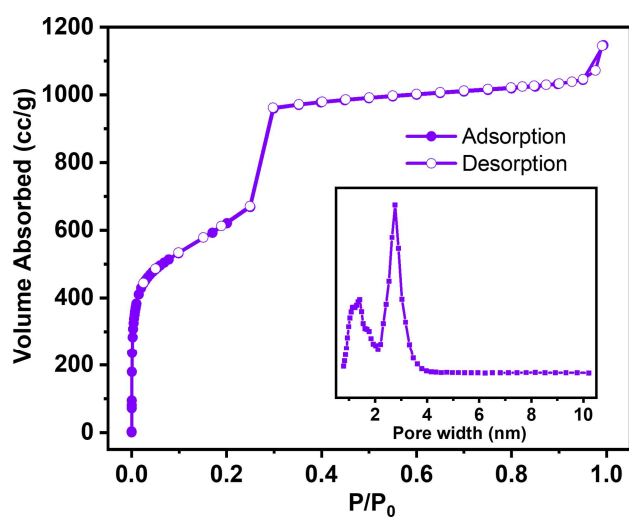
Figure 3.5 N$_2$ sorption isotherms for Mn-PCN-222 at 77 K. Inset shows DFT pore size distribution for Mn-PCN-222 based on the isotherms.
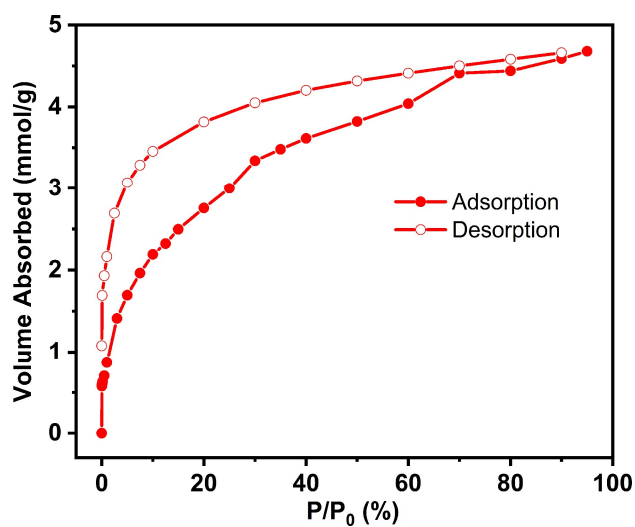
Figure 3.6 Methanol sorption isotherms at ambient temperature (25 °C) of Mn-PCN-222 film

fabricated by modular assembly.

After characterizing the prepared Mn-PCN-222 film, as a proof of concept, we begin to critically examine their functions as electrochemical sensors. Before testing any other hazardous inorganic and organic substances, one of the most common representatives of nitroaromatic compounds, nitrobenzene (NB), is chosen as a model toxin. Chasing after CV based sensing, this compound allows us to optimize the critical parameters, *e.g.*, scan rate, pH, accumulation time. It also offers to study selectivity, stability, recyclability and reproducibility, in which the currents of CV reduction peaks correspond to signal readouts.

Both toxicity and carcinogenicity aspects are well-documented for nitroaromatics, particularly nitrobenzene (NB) and their derivatives. These can pose threats to human health and the environment even at low concentrations of *ca.* 2 mg L^{-1}.[16] Rapid and efficient detection of NB in water is, therefore, a matter of high societal and environmental relevance. To begin with, as an electrochemical sensor for NB detection, the Mn-PCN-222/ITO electrode is studied and the corresponding sensitivity and selectivity of detection are determined. In the absence of NB, a pair of redox peaks are observed on the CV curve at *ca.* –0.45 V and –0.32 V (**Figure 3.7a**), corresponding to the reversible couple of Mn(III)/Mn(II) on Mn-PCN-222.[17] The Mn-PCN-222/ITO-modified electrode exhibited a sharp, irreversible reduction peak at –0.77 V in the presence of 100 μM NB. This could be attributed to the direct reduction of NB to phenylhydroxylamine in neutral medium, concomitant with the transfer of four electrons and protons (**Figure 3.7c**).[16b, 16c] Relying upon this reduction, the modified electrode shows potential as an electrochemical sensor for NB detection. The detailed process and putative mechanisms for the electrocatalytic NB reduction on the Mn-PCN-222/ITO can be described as follows: first, the large surface area of Mn-PCN-222 and the highly π-conjugated porphyrin ring (π-π interactions with NB) contribute to the aggregation of NB molecules; on top of this, the porphyrin ligands feature intrinsic redox activity, which would contribute to the electrochemical sensing of redox-active NB analytes; under an external voltage, the Mn(III) porphyrin centres of Mn-PCN-222 are reduced to Mn(II) porphyrins state and serve as electron donors. Meanwhile, thanks to the strong electron-withdrawing nature of the nitro group, NB acts as an excellent electron acceptor, thus affording an electron donor-acceptor (EDA) system formed between the porphyrin centres

and the NB molecules; this EDA system facilitates sequential electron transfer to the nitro group, followed by protonation, thereby culminating in the reduction of NB.[7a, 16c, 18]
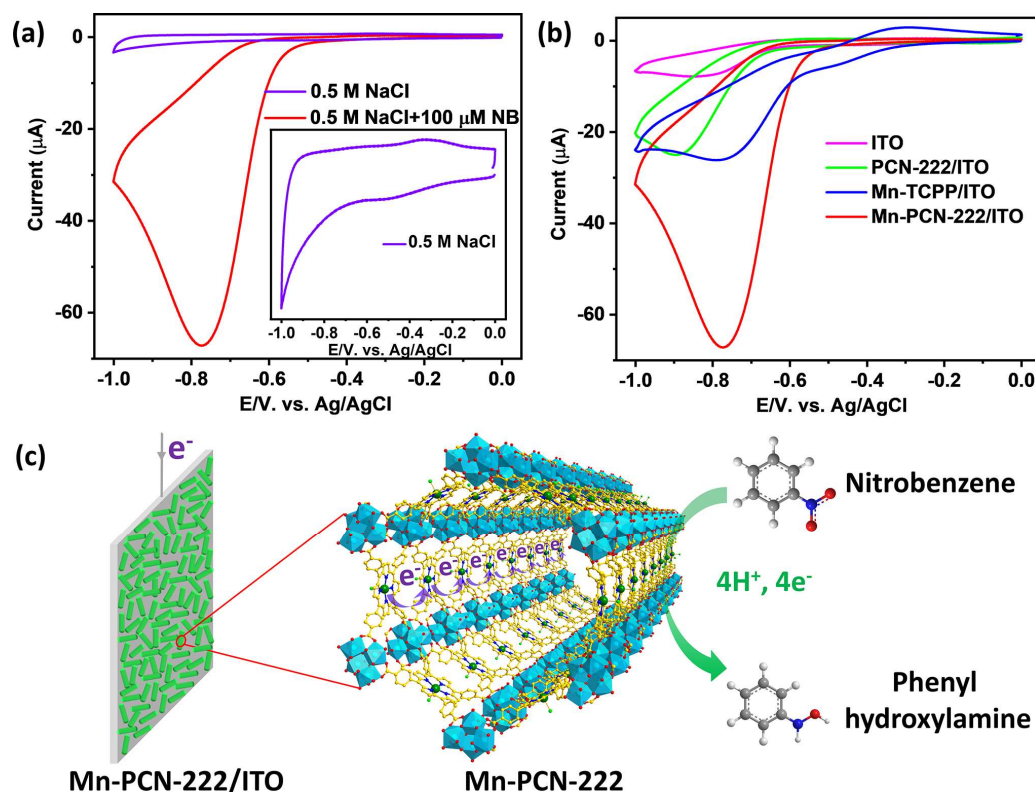
Figure 3.7 (a) CV profiles of the Mn-PCN-222/ITO electrode in 0.5 M NaCl solution in the presence or absence of 100 μM NB at a scan rate of 50 mV s^{-1}. Inset: an enlarged CV curve obtained in the absence of 100 μM NB for comparative clarity. (b) CV curves recorded on different electrodes targeting the reduction of 100 μM NB. (c) Schematic illustration of the plausible mechanism of NB reduction on the Mn-PCN-222/ITO electrode.

To further evaluate NB reduction performances of the Mn-PCN-222/ITO electrode and to rationally compare, a) bare ITO; b) non-metallated PCN-222/ITO; and c) Mn-TCPP/ITO electrodes are also prepared separately. As shown in **Figure 3.7b**, the bare ITO shows a weak current response with –0.06 V negative shifts for NB compared to that of Mn-PCN-222/ITO electrode, clearly revealing its poor response as a redox catalyst towards NB. Regarding the as-prepared modified electrodes, the Mn-PCN-222/ITO electrode also exhibits superior electrochemical behaviour. A three-fold increase in reduction current is observed against the non-metallated PCN-222/ITO electrode. The better electrocatalytic activity towards NB is attributed to the faster charge hopping and improved redox activity after coordination of Mn(III) to the porphyrin centres (**Figure 3.7c**).[9d, 10c, 19] Moreover,

among the metallated M-PCN-222 (M = Mn, Fe, Co, Cu, and Zn) variants, Mn-PCN-222/ITO ranks as the front runner for NB reduction (**Figures 3.8-3.10**). Meanwhile, a Mn-TCPP/ITO electrode is also prepared for comparison. Quantified by UV-Vis, the catalytically active Mn-TCPP are equally loaded on both Mn-TCPP/ITO and Mn-PCN-222/ITO electrodes (**Figure 3.11**). The superiority of Mn-PCN-222 with high surface area, large 1D mesochannels and ordered accessible active sites is evidenced by the comparative examination of Mn-TCPP/ITO electrodes (**Figure 3.7b**).
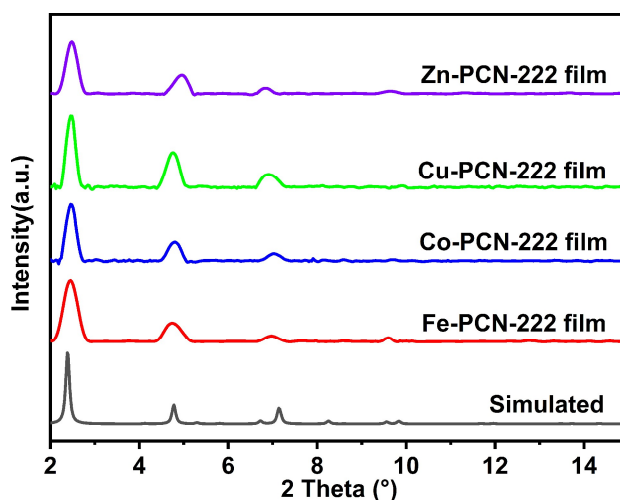
Figure 3.8 Simulated PXRD patterns of the bulk M-PCN-222 and experimental GIXRD patterns of the M-PCN-222 film on ITO glass fabricated by modular assembly.
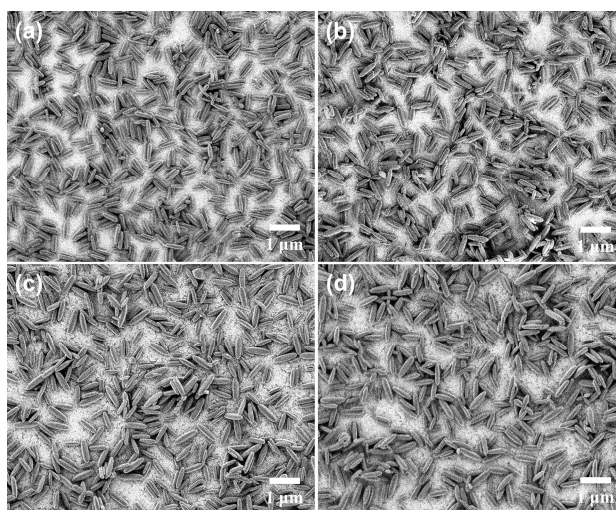
Figure 3.9 SEM images of the a) Fe-PCN-222/ITO, b) Co-PCN-222/ITO, c) Cu-PCN-222/ITO, d) Zn-PCN-222/ITO electrodes
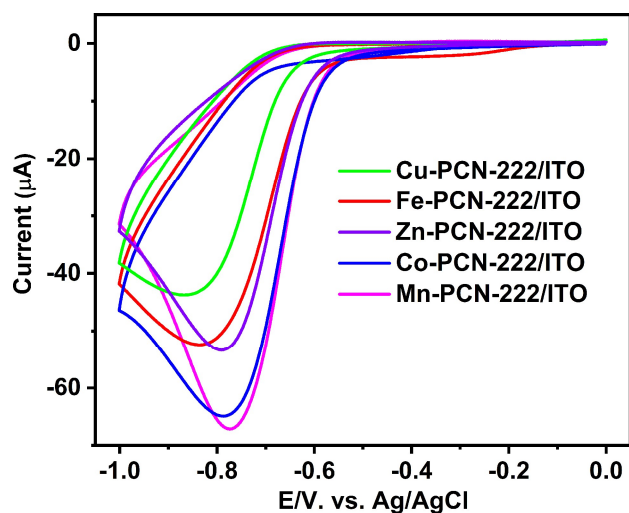
Figure 3.10 CV curves recorded on different M-PCN-222/ITO electrodes targeting the reduction of 100 µM NB.
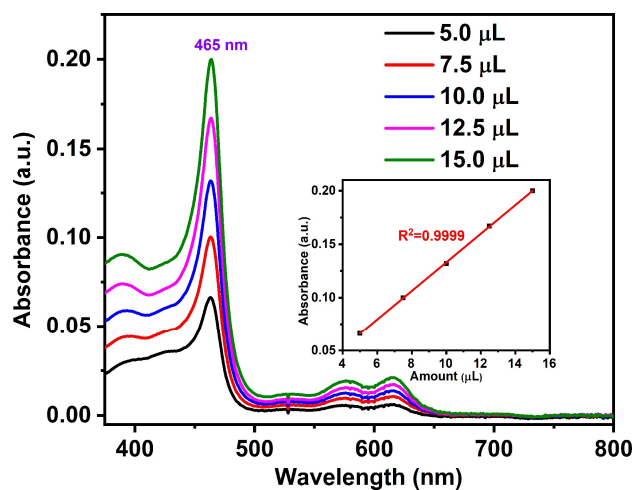
Figure 3.11 UV-Vis spectra of Mn-TCPP solution with different loading amount of 0.5 mg mL^{-1} Mn-TCPP in N, N-dimethylformamide (DMF) solution. Note that plot of absorbance at 465 nm *versus* loading amount inserted. Based on the obtained linear plot (A/ a.u. = 0.01344 v/ μL - 0.001), and the average absorbance of 0.1421 a.u. was revealed by Mn-PCN-222/ITO (Figure S3), 10.7 μL of the Mn-TCPP solution was coated on the ITO to prepare the Mn-TCPP/ITO electrode.
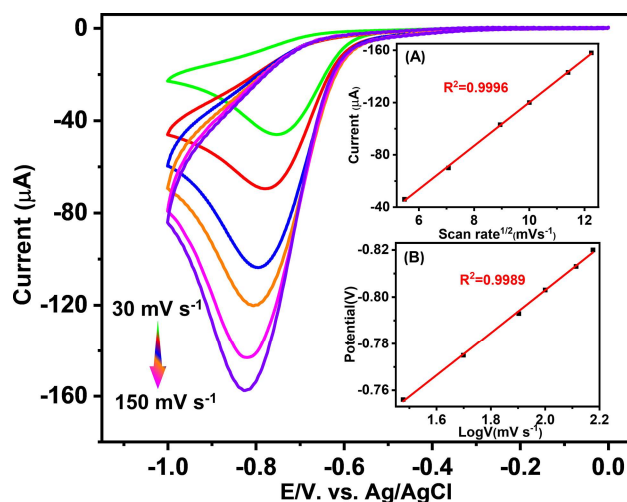
Figure 3.12 CV curves obtained at different scan rates for the Mn-PCN-222/ITO electrode aimed at the reduction of 100 µM NB in pH 7; inset A: linear plot of the peak current *versus* the square root of scan rate; inset B: the linear relationship between the reduction peak potential (E_{pc}) and logarithm of the scan rates (E_{pc} = -0.6206 − 0.09116 log v). The electron transfer number (n) of the cathodic reduction process can be estimated according to Laviron's equation [20]:

$$E_{PC} = E_0 - \frac{2.303RT}{\alpha nF} \log v$$

where E^0 is the formal potential; R is universal gas constant (8.314J/mol·K); T is temperature (298.15K); α is electron transfer coefficient and n is electron transfer number; F is the Faraday constant (96485 C/mol); v is the scan rate. Based on the slope (-0.09116), αn is calculated as 0.649; the electron transfer coefficient (α) for NB reduction is 0.171,[20d] the electron transfer number (n) is estimated to be 3.8, suggesting a 4 electrons transfer process.

The effect of scan rate (ranging from 30 to 150 mV s^{-1}) towards NB reduction is assessed by cyclic voltammetry (**Figure 3.12**). The reduction peak current increased linearly with respect to the square root of scan rate with a correlation coefficient R^2 of 0.9996. This suggests a typical diffusion-controlled process to drive the electrochemical reduction of NB at the modified electrode.[16b-d] Moreover, the electron transfer number for cathodic NB reduction is estimated as 3.8 according to Laviron's equation,[20] suggesting a 4 electrons transfer process. Conversely, the chronoamperometric response of Mn-PCN-222/ITO towards different NB concentrations reveals the diffusion coefficient for NB to be 6.178 × 10^{-6} cm^2 s^{-1} based on Cottrell's equation (**Figure 3.13**).[9a, 9c, 9d]
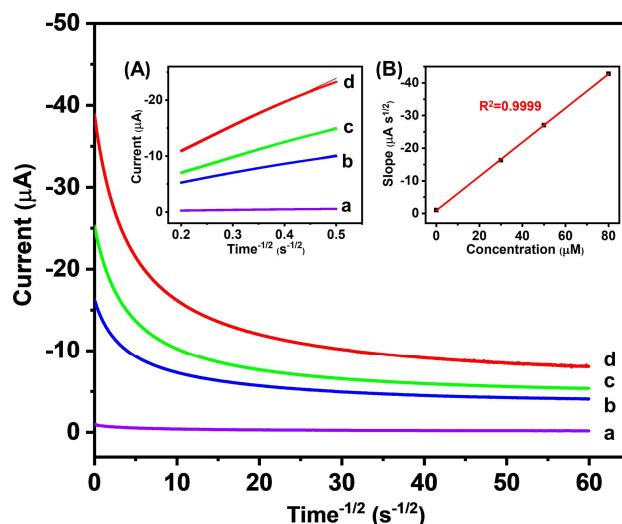
Figure 3.13 Chronoamperometric response at the Mn-PCN-222/ITO in with different concentrations of NB: (a) 0, (b) 30, (c) 50, (d) 80 μmol L^{-1}. Inset A: the linear relationship between the peak current (I) and t$^{-1/2}$ derived from the chronoamperogram data. Inset B: Linear dependence of the slopes of the lines in inset A against the NB concentrations. In order to obtain the diffusion coefficient D, we chose line c (50 μmol L^{-1}, slope = 27.06), according to the Cottrell's equation:[9d]

$$I(A) = nFAD^{1/2}c\pi^{-1/2}t^{-1/2}$$

where n is the number of electrons transferred (4); F is the Faraday constant (96485 C/mol); A is the electrode area (1 cm^2); D is the diffusion coefficient (cm^2 s^{-1}); c is the NB concentration (mol mL^{-1}) of NB (5× 10^{-8} mol mL^{-1}); I is the current (A) controlled by the diffusion of NB from the solution to the electrode/solution interface. According to the Cottrell's equation in the diffusion-controlled process, the diffusion coefficient D for NB could be obtained from the slope and estimated to be 6.178 × 10^{-6} cm^2 s^{-1}.
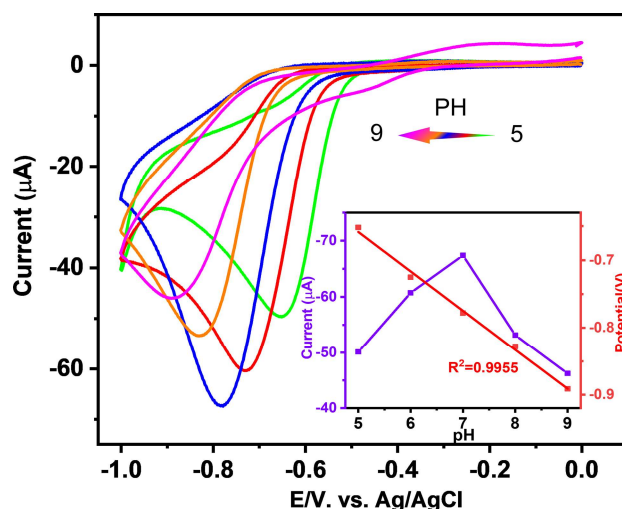
Figure 3.14 CV curves recorded on the Mn-PCN-222/ITO electrode corresponding to the reduction of 100 μM NB at a fixed scan rate of 50 mV s^{-1} in different pH (5 to 9); inset shows the dual plots of peak current and potential *versus* PH.

pH is another key parameter that may profoundly influence the performance of a voltammetric sensor, *i.e.*, the respective redox potential and the kinetics of the redox reaction. Herein, CV curves of Mn-PCN-222/ITO electrode are recorded across different pH (4 to 10) (**Figure 3.14**). CV profiles recorded at a relatively high H$^+$ concentration (pH 5) exhibit an increased reduction current at −1.0 V, corresponding to a side reaction of hydrogen evolution reaction (HER). Concurrently, during reduction, a low H$^+$ concentration (at pH 9) hinders the subsequent NB reduction due to the increased difficulty in protonation. In comparison with solutions of varying pH, the maximum peak-current response towards NB reduction is found to be achieved at pH 7.[16b-d] Hence, pH 7 is concluded to be the optimum pH for detecting NB on the Mn-PCN-222/ITO electrode. Moreover, with increasing pH, the reduction peak potential (E$_p$) exhibits a linear shift to the negative end with the corresponding equation of E$_p$(V) = −0.0581 pH−0.368. The slope of 58.1 mV pH^{-1} is found in close agreement with the theoretical value, 59 mV pH^{-1}, indicating that an equal number of protons and electrons are transferred during NB reduction.[21] Simply put, the pH dependence of electrochemical behaviour reflects the influence of H$^+$ on NB reduction while studying the electrode, which in turn corresponds to the mechanism of NB reduction.[16b-d]

The influence of another parameter, *viz.* accumulation time, is also investigated by altering the accumulation time just before measuring the cyclic voltammograms (**Figure 3.15**). Under a low NB concentration of 10 μM, the CV response currents increase as a function of the time of accumulation. This is attributed to the increased amount of NB molecules aggregated on the Mn-PCN-222/ITO electrode. Thereafter, the current peak values remain nearly constant after an accumulation time > 90 s, presumably due to NB saturation of the modified electrode under a dynamic equilibrium. Interestingly, a rapid saturation is achieved at a high NB concentration (100 μM). This could be ascribed to the high surface area and large 1D mesochannels of Mn-PCN-222, leading to rapid analyte aggregation and mass transport.[8a, 9b] According to these results in **Figure 3.15**, 90 s is selected as the optimum accumulation time for further investigation.
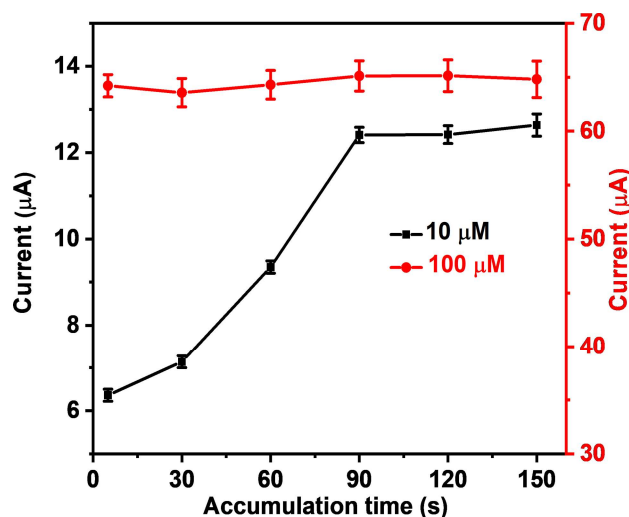
Figure 3.15 plot of peak current as function of accumulation time corresponding to NB reduction at two different concentrations.
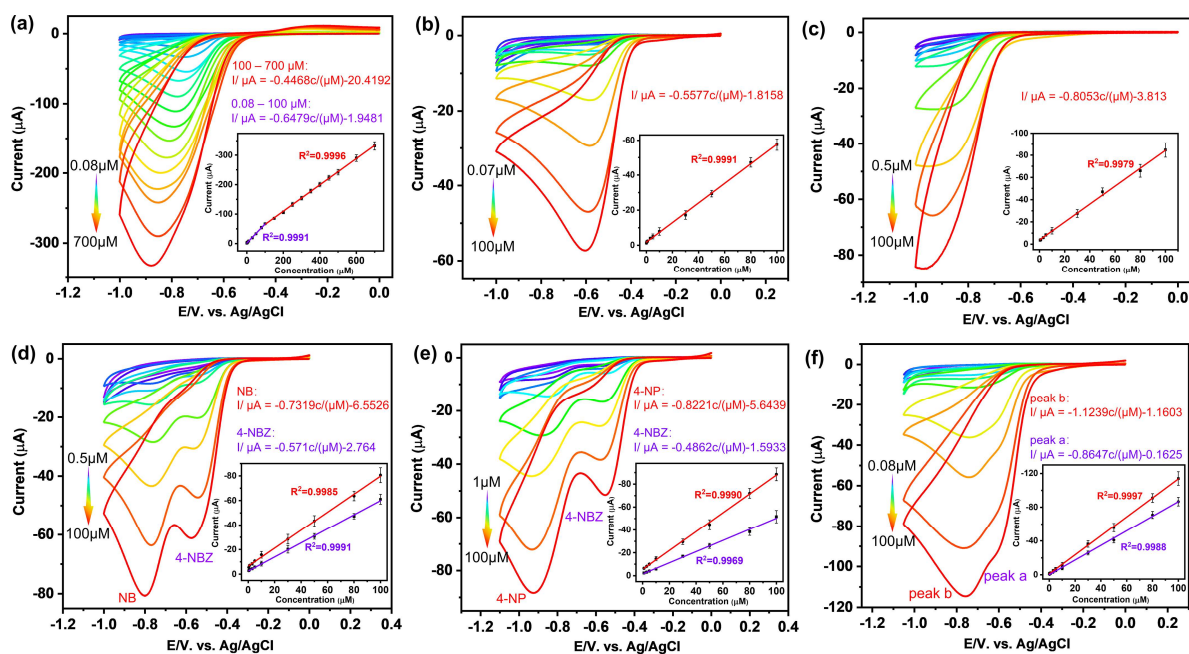
Figure 3.16 CV curves of the Mn-PCN-222/ITO electrode towards the detection of (a) NB, (b) 4-NBZ, (c) 4-NP, (d) NB and 4-NBZ, (e) 4-NP and 4-NBZ, (f) 1,3-DNB at different concentrations; inset shows linear trend of the peak current *versus* concentration of corresponding analytes.
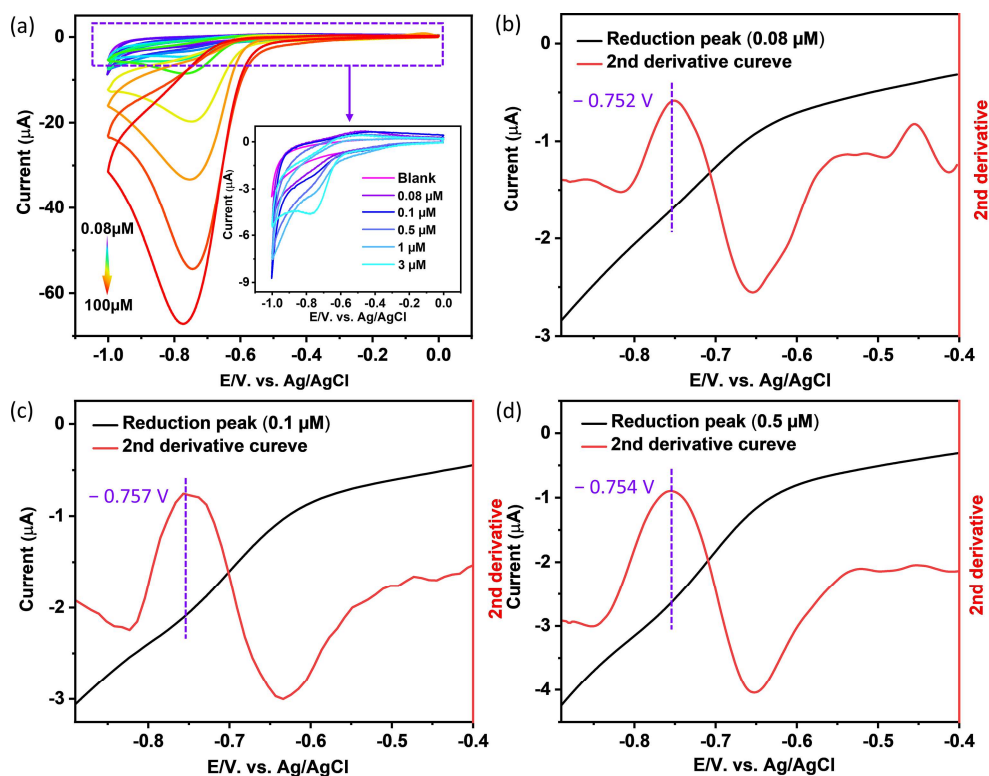
Figure 3.17 (a) Zoomed CV curves of the Mn-PCN-222/ITO electrode towards trace NB detection ranging from 0.08 up to 100 µM; inset shows the CV curves of low concentrations from 0.08 to 3 µM, and the curve of the blank solution is added for comparing. Second derivative curves of CV curves during the reduction peaks at low concentration of (b) 0.08 µM, (c) 0.1 µM and (d) 0.5 µM, identifying the reduction peak positions at − 0.752 V, − 0.757 V and − 0.754 V, respectivety. The peak positons of low concentration show average of − 0.754 V with a standard deviation of 0.003, which are employed to define the response position on blank tests for LOD calculation (**Table 3.2**).
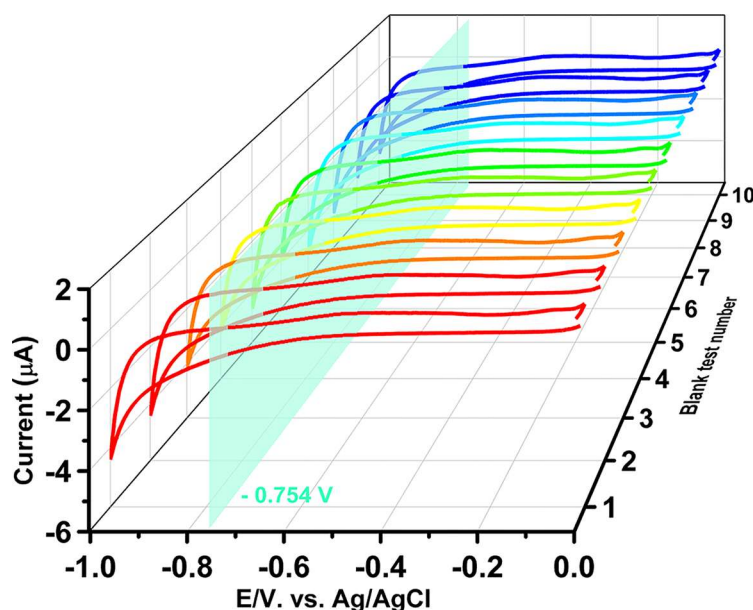
Figure 3.18 CV curves of ten blank tests (without NB) on Mn-PCN-222/ITO; the reduction current responses at potential of − 0.754 V (**Figure 3.17**) are collected and listed on **Table 3.2** to calculate

the standard deviation of blank tests.

Table 3.2 Current responses of ten blank tests (without NB) on Mn-PCN-222/ITO.

Samples	1	2	3	4	5	6	7	8	9	10	Standard deviation
Current responses (µA) at – 0.754 V[a]	0.866	0.855	0.858	0.851	0.848	0.862	0.864	0.848	0.853	0.851	0.007

[a] the response potential for blank tests is based on the average potential of reduction peaks at low NB concentrations (**Figure 3.17**).

The feasibility of Mn-PCN-222/ITO electrode for NB detection is confirmed under optimized conditions with the addition of different concentrations of NB (**Figure 3.16a**; for zoomed views of the low concentrations, see **Figure 3.17**). Notably, the corresponding reduction peak currents (I) increased linearly with the increase in NB concentration (c) ranging from 0.08 up to 700 μM with high correlation coefficients ($R^2 > 0.999$). According to the criterion of United States of Environmental Protection Agency (USEPA), the acceptable limit of NB in water is 2 mg L^{-1} (16.25 μM),[16a, 16c] falling within the detectable range of the modified electrode, thus suggesting its potential for NB detection. In addition, the sensitivity is determined to be 0.6479 μA μM^{-1} cm^{-2} (0.08 – 100 μM) and 0.4468 μA μM^{-1} cm^{-2} (100 – 700 μM), respectively. The slight difference of sensitivity is likely to be an outcome of the following concentration-guided factors: a) the abundance of catalytic sites implies their easy accessibility for the absorbed NB molecules at low concentrations; b) nevertheless at higher concentrations, these sites become sequestered owing to saturation with NB, thus compromising the sensitivity.[9a-c] The limit of detection (LOD) is calculated as low as 0.03 μM (3×S_b/slope, **Figure 3.18, Table 3.2**). Compared to the previously reported modified electrodes for NB detection, the proposed Mn-PCN-222/ITO electrode sets a benchmark analytical response towards NB in terms of a wide linear response and low LOD (**Table S6** in Chapter 5). Its electrocatalytic activity towards NB detection stands out, and can be correlated to its large surface area, expedited preconcentration, rapid mass transport and high density of the accessible, ordered active sites in Mn-PCN-222.[8a, 9a, 9b]
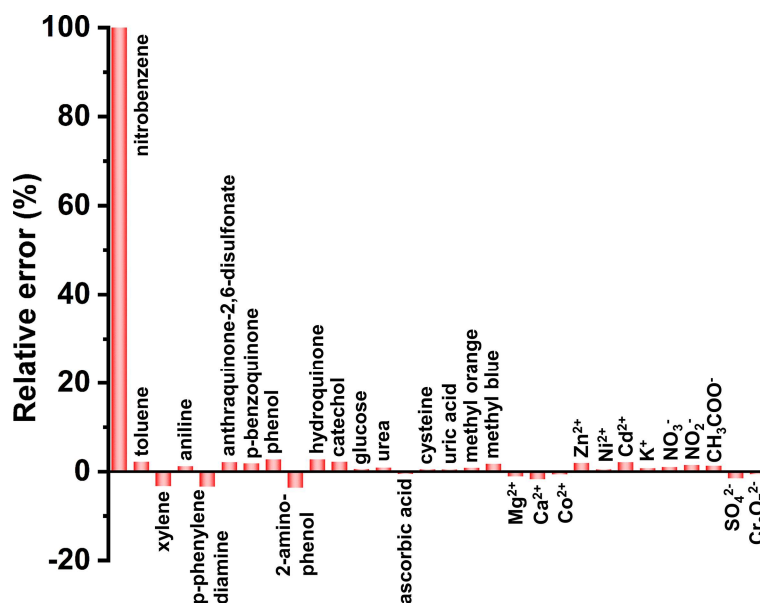
Figure 3.19 Interference study of the Mn-PCN-222/ITO electrode towards the detection of NB; the percentages of relative errors denoted the changes of peak current response of NB reduction, each corresponding to additions of 10 fold of different interferents.

We evaluated the selectivity of the Mn-PCN-222/ITO electrode towards NB (50 μM) in the presence of 10 fold molar excess of other typical interferents (**Figure 3.19**). It can be seen that common metal ions and biological species only induce negligible interference (< 2 %) whereas phenolic compounds, quinone and benzene derivatives only trigger measly effects (< 4 %) on the NB detection performance. These results indicate the potential of the modified electrodes for selectively detecting NB, even in the presence of an excess of these potentially interfering species.

To further confirm practical viability, the modified electrode is employed to detect NB in real water samples (tap water and river water) with addition of NB of different concentrations (10 μM, 20 μM and 30 μM) and analyzed by cyclic voltammograms (**Table 3.3**). The Mn-PCN-222/ITO electrode featured excellent recoveries (the percentages of measured concentrations to the corresponding added concentrations) towards NB detection (96.2 to 102.5 %) in real samples, suggestive of its suitability as NB sensor to detect water contamination. [16b, 16c]

Table 3.3 Detection of NB in real water samples using Mn-PCN-222/ITO electrodes.

Samples[a]	Added (μM)	Found[b] (μM)	Recovery (%)
Tap water	10.0	9.84	98.4
	10.0	19.6	98.9

	10.0	30.76	102.5
	10.0	9.82	98.2
River water	10.0	19.28	96.4
	10.0	28.85	96.2

[a] the tap water was collected in Technical University of Munich, Garching b. Munich, and the river water is from wiesäckerbach river in the campus; [b] standard deviation method (n=3).
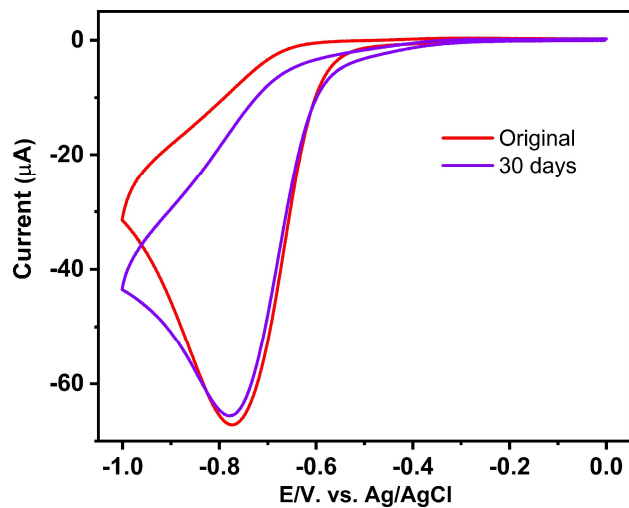
Figure 3.20 CV curves of NB (100 μM) detection on Mn-PCN-222/ITO at the initial time and after 30 days.
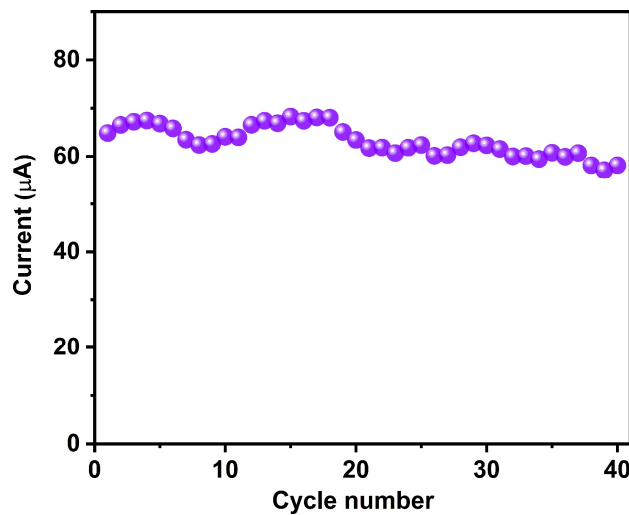
Figure 3.21 Recyclability study of a single Mn-PCN-222/ITO modified electrode for 40 times recycling detection of NB (100 μM).
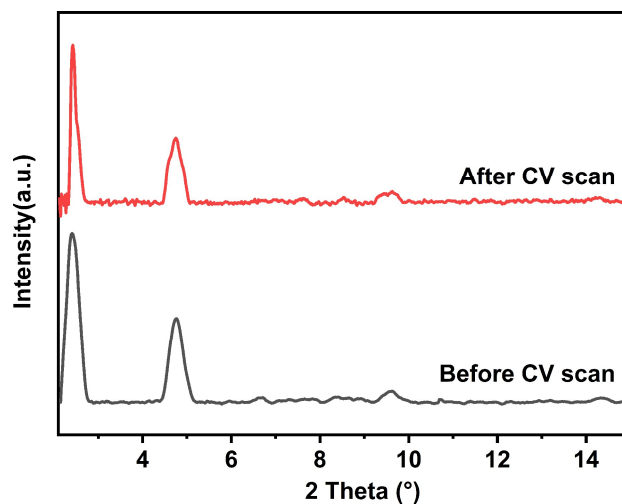
Figure 3.22 GIXRD patterns of the Mn-PCN-222/ITO electrodes before CV scan and after 10 repetitive cyclic voltammograms scans.
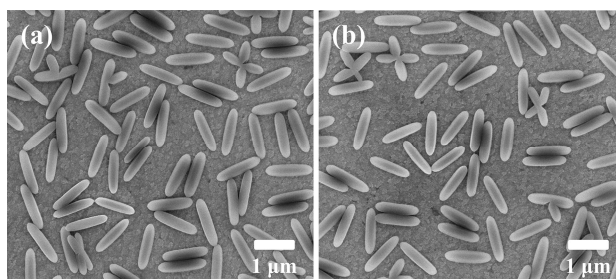
Figure 3.23 SEM images of the Mn-PCN-222/ITO electrodes a) before CV scan and b) after 10 repetitive cyclic voltammograms scans.
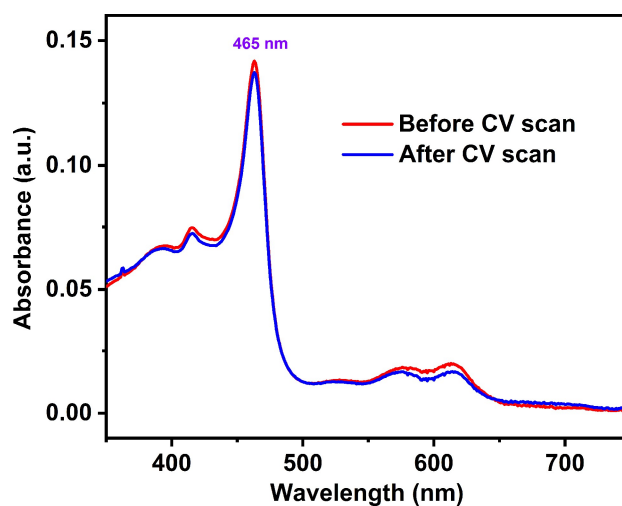
Figure 3.24 UV-Vis spectra of Mn-PCN-222/ITO before and after 10 repetitive cyclic voltammetric scans. Measly decrease of the absorbance (0.1421 a.u. to 0.1372 a.u.) at 465 nm confirms the excellent mechanical stability of Mn-PCN-222 anchored on ITO surface.
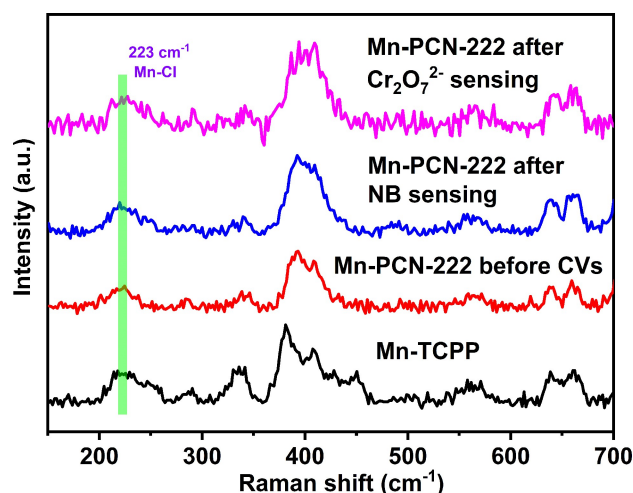
Figure 3.25 Raman spectra of Mn-TCPP, Mn-PCN-222/ITO before and after 10 repetitive cyclic voltammetric scans of NB and $Cr_2O_7^{2-}$ species. The Mn–Cl stretching vibration at 223 cm^{-1} of Mn-TCPP-Cl ligands remain in both the Mn-PCN-222 film sensor forms: as-prepared and the one after analytes post-sensing, suggesting the retention of Mn-PCN-222 molecular structure during the sensor preparation and its utilisation.
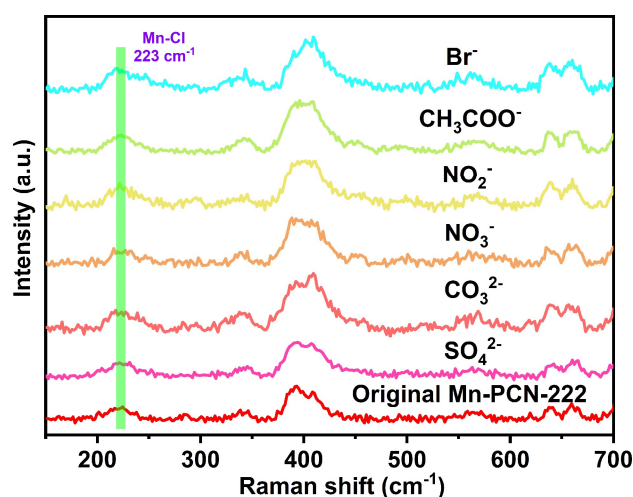
Figure 3.26 Raman spectra of Mn-PCN-222/ITO sensors before and after 10 repetitive cyclic voltammetric scans (-1 to 0 V, same range to the NB sensing experiment) in solutions of several different anionic species (SO_4^{2-}, CO_3^{2-}, NO_3^{-}, NO_2^{-}, CH_3COO^{-}, Br^{-}, concentration: 1 mmol/L each) The Mn–Cl vibrations (223 cm^{-1}) of original Mn-PCN-222/ITO show no change or shift after CV tests in different anionic species solutions, establishing the stability of the terminal chloride ligands towards common anionic species during the sensing process condition.

Table 3.4 Peak current of ten different Mn-PCN-222/ITO electrodes for NB (100 μM) detection.

Samples	1	2	3	4	5	6	7	8	9	10
Peak current (μA)	67.009	64.965	67.91	69.226	68.718	69.786	66.755	65.138	64.815	67.679

Material stability, recyclability and reproducibility are important parameters for electrochemical sensors. Mn-PCN-222/ITO exhibits excellent stability substantiated

by the retention of nearly 97.3% of its initial response after 30 days (**Figure 3.20**). The high stability originates from the stable Zr_6 cluster and strong chelating effect between Mn(III) and the porphyrins.[8a, 9b, 9c] The electrode also shows good recyclability with a RSD of 4.98 % (< 5%) for 40 measurement cycles (**Figure 3.21**). Meanwhile, a comparison of the XRD patterns, SEM images, UV-Vis spectra and Raman spectra on the modified electrodes reveals identical crystalline features and morphologies, changeless coating condition as well as same molecular structures before and after consecutive detection measurements, indicating their excellent electrochemical and mechanical stability (**Figures 3.22-3.26**). Furthermore, 10 independent Mn-PCN-222/ITO electrodes are examined. A RSD of 2.67 % (< 5%) (**Table 3.4**) suggests outstanding reproducibility of the modified electrode.

Aligned with the observations made in our foregoing experiments, the feasibility of Mn-PCN-222/ITO for NB detection becomes clear. To verify the versatility of the proposed modified electrode, electrochemical detection of other nitroaromatic compounds (NACs), *viz.* 4-nitrobenzaldehyde (4-NBZ), 4-nitrophenol (4-NP), 1,3-dinitrobenzene (1,3-DNB) are investigated in individual and/or simultaneous modes (**Figures 3.16b-f**). Although a reduction peak appears due to the presence of a nitro group, the peak potentials for 4-NBZ and 4-NP register clear shifts compared to that of NB due to the withdrawal or donation of electron density at the nitro group by different substituent groups at the NAC rings.[16d, 22] The -CHO group in 4-NBZ withdraws the electron density from the aromatic ring, then resulting in an electron-deficient nitro group that is more easily reduced. Therefore, a positive shift of reduction potential is observed for 4-NBZ (-0.60 V). On the contrary, the electron-donating group –OH in 4-NP facilitates a negative shift of the reduction potential to –0.95 V. As shown in **Figures 3.16b** and **3.16c**, the Mn-PCN-222/ITO exhibits linear responses to 4-NBZ (0.07–100 μM) and 4-NP (0.5–100 μM) with high correlation coefficients (0.9991 and 0.9979, respectively). The LOD for the detection of 4-NBZ and 4-NP detection are 0.030 μM and 0.106 μM, respectively. Notably, the Mn-PCN-222/ITO shows a good analytical response compared to 4-NBZ and 4-NP sensors reported in the literature (**Tables S7, S8** in Chapter 5). **Figure 3.16d** establishes the simultaneous detection of NB and 4-NBZ with two well-resolved and distinct reduction peaks. On top of this, Mn-PCN-222/ITO detects NB and 4-NBZ mixtures in real water samples (tap and river water) with addition of different

concentrations of NB (10 μM, 20 μM and 30 μM) and 4-NBZ (10 μM, 15 μM and 20 μM) at appreciable recoveries of 93.6 to 103.9 % (**Table 3.5**). Meanwhile, the Mn-PCN-222/ITO shows highly linear responses to NB and 4-NBZ in the range of 0.5 to 100 μM with LODs of 0.027 μM and 0.029 μM, respectively. Similarly, the Mn-PCN-222/ITO also achieves simultaneous detection (1–100 μM) of 4-NP and 4-NBZ with LODs of 0.103 μM and 0.034 μM, respectively (**Figure 3.16e**). Moreover, a clear electrocatalytic response despite the co-existence of NB, 4-NBZ, 4-NP, suggests its usefulness in simultaneously detecting a set of target NACs (**Figure 3.27**). The proposed electrode could also recognize the number of nitro groups in an individual NAC analyte, confirmed by the two reduction peaks while detecting 1,3-DNB (**Figure 3.16f**).[23]   For 1,3-DNB sensing, the excellent linearity observed across 0.08 to 100 μM with a LOD of 0.018 μM (based on peak b) establishes comparable sensing performances *versus* the hitherto reported electrodes (**Table S9** in Chapter 5). Systematic studies on NACs detection demonstrate high efficiency of the Mn-PCN-222/ITO not only towards single-component systems, but also in binary and ternary systems (**Figures 3.16 and 3.27**).

Table 3.5 Detection of the mixture of NB and 4-NBZ in real water samples using Mn-PCN-222/ITO electrodes.

| Samples[a]	Added (μM)		Found[b] (μM)		Recovery (%)	
	NB	4-NBZ	NB	4-NBZ	NB	4-NBZ
Tap water	10.0	10	9.82	9.36	98.2	93.6
	10.0	5	19.96	14.72	99.8	98.1
	10.0	5	31.16	19.92	103.9	99.6
River water	10.0	10	10.05	9.64	100.5	96.4
	10.0	5	19.34	14.40	96.7	96.0
	10.0	5	28.2	20.37	94.0	102.3

[a] the tap water was collected in Technical University of Munich, Garching b. Munich, and the river water is from wiesäckerbach river in the campus; [b] standard deviation method (n=3).
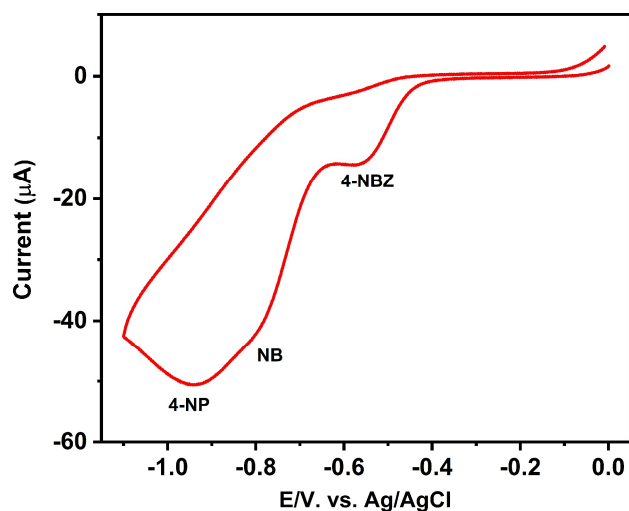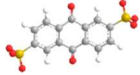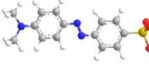
Figure 3.27 CV curve of the simultaneous detection of 4-NP (50 *μ*M), NB (50 *μ*M) and 4-NBZ (30 *μ*M).
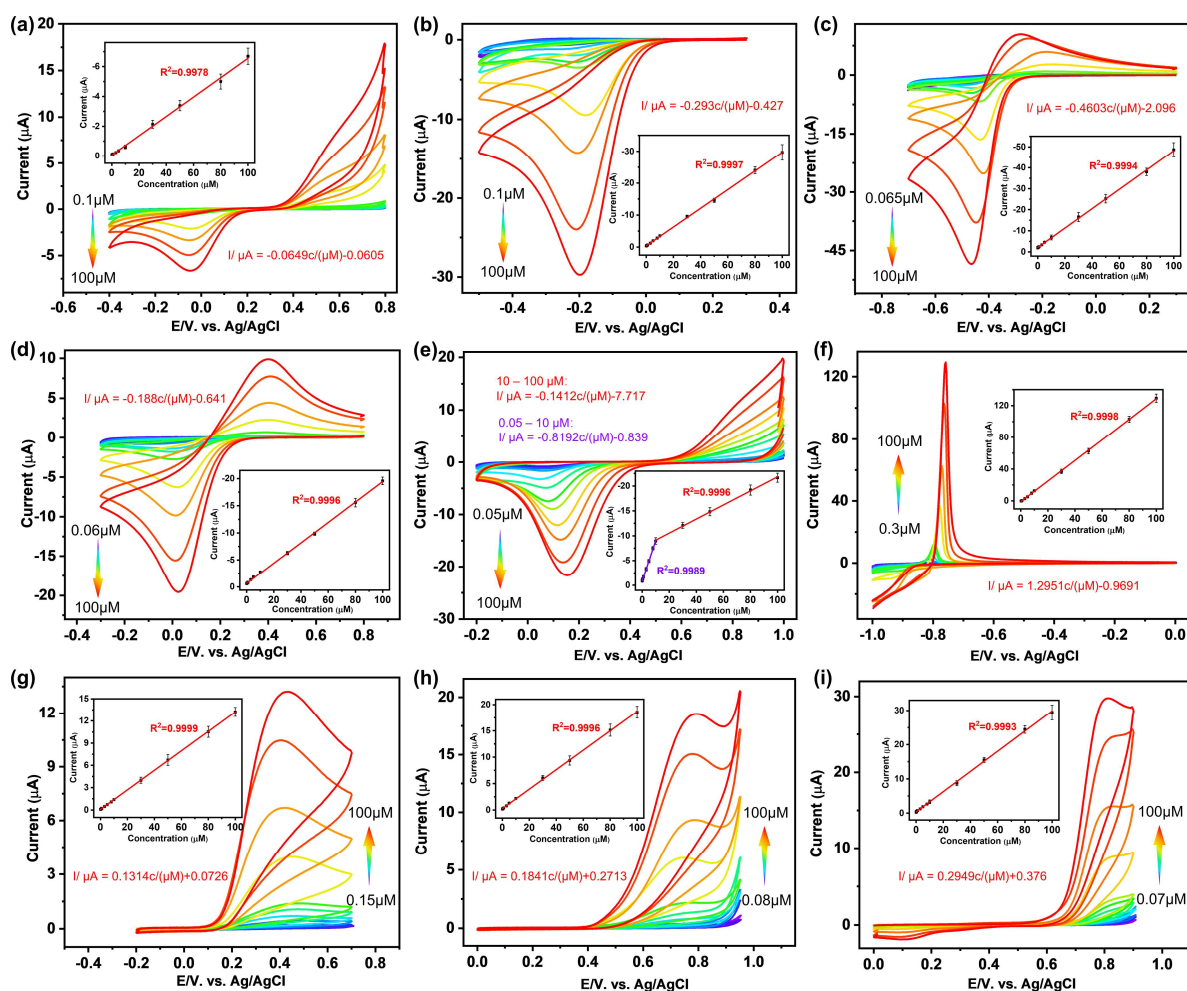
Figure 3.28 CV curves of the Mn-PCN-222/ITO corresponding to the detection of (a) catechol, (b) 1,4-benzoquinone, (c) AQDS, (d) Cu^{2+}, (e) $Cr_2O_7^{2-}$, (f) Cd^{2+}, (g) ascorbic acid, (h) uric acid, (i) methyl orange at different concentrations up to 100 *μ*M; inset shows the linear trend of the peak current *versus* analyte concentration.

To further reveal the sensory versatility of Mn-PCN-222/ITO, a series of voltammetric detections are performed on other analytes across different classes, *viz.* phenolics and quinone-hydroquinone, heavy metal ions, biological species, as well as the azo dyes. The sensing performances are detailed in **Table 3.6** and **Figure 3.28**. Upon comparing these against reported sensors, excellence of Mn-PCN-222/ITO becomes evident (**Tables S10-16** in Chapter 5). Aligned with the demonstrated analyte-specific responses, Mn-PCN-222/ITO can also simultaneously detect mixtures of three analytes from three distinct classes: CT, 1,4-BZQ and AQDS (**Figure 3.29**); Cu^{2+}, $Cr_2O_7^{2-}$ and Cd^{2+} (**Figure 3.30**); AA and UA (**Figure 3.31**), suggesting it's high upside potentials to fabricate a multifaceted sensory device in binary and ternary systems.

Table 3.6 Voltammetric detections of several analytes (belonging to different pollutant classes) on Mn-PCN-222/ITO.

Class	Analyte	Molecular structure[a]	Linear range (μM)	Limit of detection (μM)
Phenolics and quinone-hydroquinone	Catechol		0.10–100	0.047
	1,4-benzoquinone		0.10–100	0.015
	Anthraquinone-2,6-disulfonate		0.06–100	0.020
Heavy metal ions	Cu^{2+}		0.06–100	0.013
	$Cr_2O_7^{2-}$		0.05–100	0.003
	Cd^{2+}		0.30–100	0.100
Biological species	Ascorbic acid		0.15–100	0.011
	Uric acid		0.08–100	0.017
Azo dyes	Methyl orange		0.07–100	0.009

[a] Color scheme: C, grey; O, red; N, blue; H, white; S, gold; Cu, celeste; Cr, yellow and Cd, green.
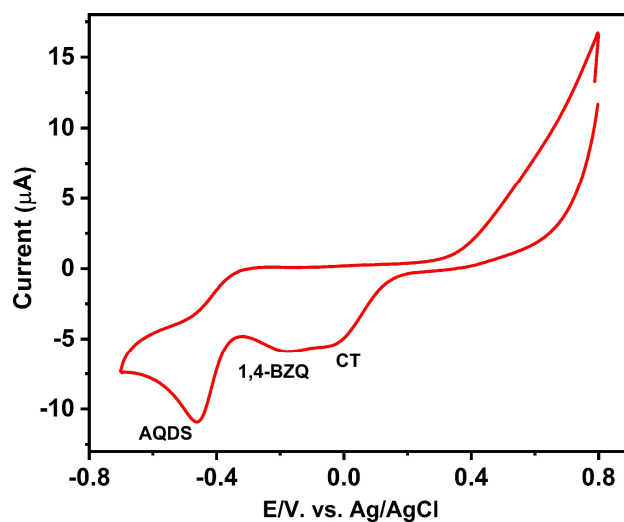
Figure 3.29 CV curve of the simultaneous detection of CT (80 μM), 1,4-BZQ (20 μM) and AQDS (20 μM).
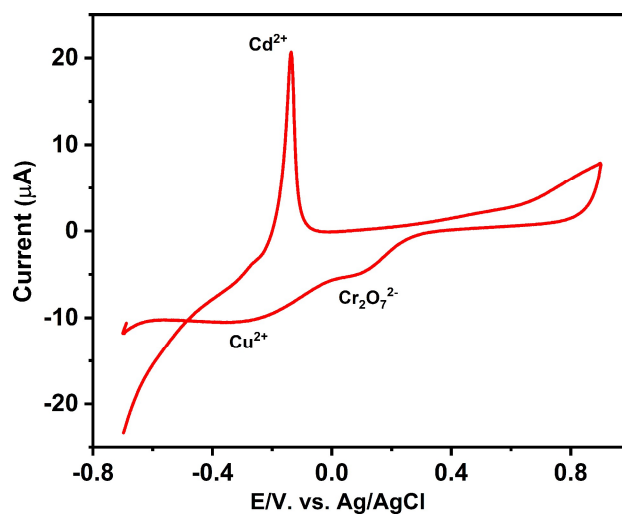
Figure 3.30 CV curve of the simultaneous detection of Cu^{2+} (50 μM), Cd^{2+} (20 μM) and $Cr_2O_7^{2-}$ (10 μM). Note the shift of potentials of the response peaks of Cu^{2+} and Cd^{2+} are possibly due to the strong oxidizing property of $Cr_2O_7^{2-}$.
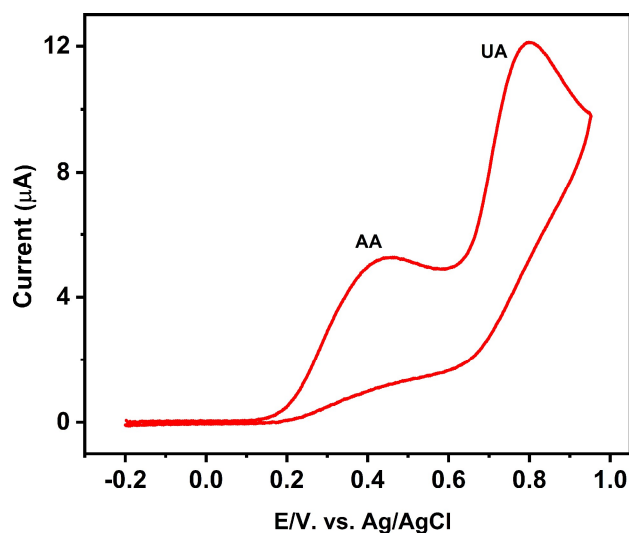
Figure 3.31 CV curve of the simultaneous detection of AA (50 μM) and UA (50 μM).

3.3 Conclusions

In summary, a fast and facile modular assembly method is harnessed to cast porphyrinic Mn-PCN-222 film on the ITO glass. The resulting Mn-PCN-222/ITO demonstrates versatile voltammetric sensing of several analytes. The ordered incorporation of metalloporphyrin units as catalytic centers across a periodic and porous Mn-PCN-222 architecture facilitates the desired features of improved sensor design: a high-density of active sites, a large surface area, rapid analyte aggregation, mass transport and a sensitive response with a large linear range. All these features contribute to its benchmark performance in sensing various analytes, *viz.*, nitroaromatics, phenolics, quinone-hydroquinone, heavy metal ions, biological species, as well as azo dyes. Sensitive detections with wide linear ranges and low LODs are obtained with Mn-PCN-222/ITO. The electrode shows high efficiency not only towards single substrates, but also retains its high performance in binary and ternary systems of increased complexity. An extension to more complex systems can be foreseen, upon conducting process/device engineering with this system. An optimal combination of selectivity, long-term stability, reproducibility and practicality of Mn-PCN-222/ITO is discovered. In essence, Mn-PCN-222/ITO not only turns out amenable to simple and efficient preparation methods, but also delivers excellent voltammetric detection performance and, therefore, holds great promise to design versatile electrochemical sensors in the future. Building upon the compositional modularity of M-PP-MOFs, varying intrinsic properties such as, pore environments,

redox-potentials/windows for each (*e.g.,* by choosing M properly or combining different M-PP-MOFs in one sensor device) paves the way for a number of related approaches, *e.g.*, redox-potentials/windows are tuneable by an *à la carte* catalogue of metal nodes and this is likely to offer another dimension to the control of electrochemical properties of M-PP-MOF based voltammetric sensors.

3.4 References

[1]   a) S. Liu, C. Lai, X. Liu, B. Li, C. Zhang, L. Qin, D. Huang, H. Yi, M. Zhang, L. Li, W. Wang, X. Zhou, L. Chen, *Coord. Chem. Rev.* **2020**, *424*, 213520; b) D. W. Kimmel, G. LeBlanc, M. E. Meschievitz, D. E. Cliffel, *Anal. Chem.* **2012**, *84*, 685-707; c) B. J. Privett, J. H. Shin, M. H. Schoenfisch, *Anal. Chem.* **2010**, *82*, 4723-4741.

[2]   a) A. J. Veloso, X. R. Cheng, K. Kerman, *Electrochemical Biosensors for Medical Applications* (Ed.: S. Higson), Woodhead Publishing, **2012**, pp. 3-40; b) M. M. Rodríguez-Delgado, G. S. Alemán Nava, J. M. Rodríguez Delgado, G. Dieck Assad, S. O. Martínez Chapa, D. Barceló, R. Parra, *Trends Analyt. Chem.* **2015**, *74*, 21-45.

[3]   a) J. F. Rusling, S. L. Suib, *Adv. Mater.* **1994**, *6*, 922-930; b) N. Elgrishi, K. J. Rountree, B. D. McCarthy, E. S. Rountree, T. T. Eisenhart, J. L. Dempsey, *J. Chem. Educ.* **2017**, *95*, 197-206.

[4]   C. C. Wu, T. Yasukawa, H. Shiku, T. Matsue, *Sens. Actuators B Chem.* **2005**, *110*, 342-349.

[5]   a) H. Furukawa, K. E. Cordova, M. O'Keeffe, O. M. Yaghi, *Science* **2013**, *341*, 1230444; b) H. C. Zhou, J. R. Long, O. M. Yaghi, *Chem. Rev.* **2012**, *112*, 673-674; c) R. J. Kuppler, D. J. Timmons, Q. R. Fang, J. R. Li, T. A. Makal, M. D. Young, D. Yuan, D. Zhao, W. Zhuang, H. C. Zhou, *Coord. Chem. Rev.* **2009**, *253*, 3042-3066; d) S. T. Meek, J. A. Greathouse, M. D. Allendorf, *Adv. Mater.* **2011**, *23*, 249-267.

[6]   a) C. S. Liu, J. Li, H. Pang, *Coord. Chem. Rev.* **2020**, *410*, 213222; b) Y. Xu, Q. Li, H. Xue, H. Pang, *Coord. Chem. Rev.* **2018**, *376*, 292-318; c) S. Kempahanumakkagari, K. Vellingiri, A. Deep, E. E. Kwon, N. Bolan, K. H. Kim, *Coord. Chem. Rev.* **2018**, *357*, 105-129; d) S. Tajik, H. Beitollahi, F. Garkani Nejad, I. Sheikhshoaie, A. S. Nugraha, H. W. Jang, Y. Yamauchi, M. Shokouhimehr, *J. Mater. Chem. A* **2021**, *9*, 8195-8220.

[7]   a) R. Paolesse, S. Nardis, D. Monti, M. Stefanelli, C. Di Natale, *Chem. Rev.* **2017**, *117*, 2517-2583; b) J. Chen, Y. Zhu, S. Kaskel, *Angew. Chem. Int. Ed.* **2021**, *60*, 5010-5035; c) H. Lee, K.-I. Hong, W.-D. Jang, *Coord. Chem. Rev.* **2018**, *354*, 46-73.

[8]   a) D. Feng, Z. Y. Gu, J. R. Li, H. L. Jiang, Z. Wei, H. C. Zhou, *Angew. Chem.*

Int. Ed. **2012**, *51*, 10307-10310; b) Z. Zhou, S. Mukherjee, J. Warnan, W. Li, S. Wannapaiboon, S. Hou, K. Rodewald, B. Rieger, P. G. Weidler, C. Wöll, R. A. Fischer, *J. Mater. Chem. A* **2020**, *8*, 25941-25950.

[9]   a) Y. Chen, X. Sun, S. Biswas, Y. Xie, Y. Wang, X. Hu, *Biosens. Bioelectron.* **2019**, *141*, 111470; b) Y. Chen, W. Huang, C. Wang, X. Zhai, T. Zhang, Y. Wang, X. Hu, *ACS Sustain. Chem. Eng.* **2020**, *8*, 13226-13235; c) Y. Wang, L. Wang, H. Chen, X. Hu, S. Ma, *ACS Appl. Mater. Interfaces* **2016**, *8*, 18173-18181; d) S. Biswas, Y. Chen, Y. Xie, X. Sun, Y. Wang, *Anal. Chem.* **2020**, *92*, 4566-4572.

[10]   a) I. Stassen, N. Burtch, A. Talin, P. Falcaro, M. Allendorf, R. Ameloot, *Chem. Soc. Rev.* **2017**, *46*, 3185-3241; b) C. H. Su, C. W. Kung, T. H. Chang, H. C. Lu, K. C. Ho, Y. C. Liao, *J. Mater. Chem. A* **2016**, *4*, 11094-11102; c) P. M. Usov, B. Huffman, C. C. Epley, M. C. Kessinger, J. Zhu, W. A. Maza, A. J. Morris, *ACS Appl. Mater. Interfaces* **2017**, *9*, 33539-33543; d) A. L. Semrau, Z. Zhou, S. Mukherjee, M. Tu, W. Li, R. A. Fischer, *Langmuir* **2021,** *37*, 6847-6863.

[11]   a) G. Xu, T. Yamada, K. Otsubo, S. Sakaida, H. Kitagawa, *J. Am. Chem. Soc.* **2012**, *134*, 16524-16527; b) G. Xu, K. Otsubo, T. Yamada, S. Sakaida, H. Kitagawa, *J. Am. Chem. Soc.* **2013**, *135*, 7438-7441.

[12]   S. M. Yoon, J. H. Park, B. A. Grzybowski, *Angew. Chem. Int. Ed.* **2017**, *56*, 127-132.

[13]   a) Q. Xu, G. Zhan, Z. Zhang, T. Yong, X. Yang, L. Gan, *Theranostics* **2021**, *11*, 1937-1952; b) K. Yu, P. Puthiaraj, W.-S. Ahn, *Appl. Catal. B* **2020**, *273*, 119059.

[14]   G. G. Oliveros, E. A. Páez Mozo, F. M. Ortega, C. Ferronato, J. M. Chovelon, *Appl. Catal. B* **2009**, *89*, 448-454.

[15]   K. S. Walton, R. Q. Snurr, *J. Am. Chem. Soc.* **2007**, *129*, 8552-8556.

[16]   a) P. S. Majumder, S. K. Gupta, *Water Res.* **2003**, *37*, 4331-4336; b) R. Emmanuel, C. Karuppiah, S. M. Chen, S. Palanisamy, S. Padmavathy, P. Prakash, *J. Hazard. Mater.* **2014**, *279*, 117-124; c) S. Kubendhiran, S. Sakthinathan, S. M. Chen, P. Tamizhdurai, K. Shanthi, C. Karuppiah, *J. Colloid. Interface. Sci.* **2017**, *497*, 207-216; d) C. Liu, X. Bo, L. Guo, *Sens. Actuators B Chem.* **2019**, *297*, 126741.

[17] Y. G. Mourzina, A. Offenhäusser, *J. Electroanal. Chem.* **2020**, *866*, 114159.

[18] a) A. Palma Cando, U. Scherf, *ACS Appl. Mater. Interfaces* **2015**, *7*, 11127-11133; b) Z. Xue, H. Lian, C. Hu, Y. Feng, F. Zhang, X. Liu, X. Lu, *Aust. J. Chem.* **2014**, *67*, 796; c) X. Lu, Y. Quan, Z. Xue, B. Wu, H. Qi, D. Liu, *Colloids Surf. B* **2011**, *88*, 396-401.

[19] a) C. W. Kung, T. H. Chang, L. Y. Chou, J. T. Hupp, O. K. Farha, K. C. Ho, *Chem. Commun.* **2015**, *51*, 2414-2417; b) S. R. Ahrenholtz, C. C. Epley, A. J. Morris, *J. Am. Chem. Soc.* **2014**, *136*, 2464-2472.

[20] a) E. Laviron, *J. Electroanal. Chem.* **1974**, *52*, 355-393; b) M. B. Gholivand, M. Khodadadian, *Biosens. Bioelectron.***2014**, *53*, 472-478; c) X. Ma, M. Chen, *Sens. Actuators B Chem.* **2015**, *215*, 445-450; d) S. Vinoth, P. M. Rajaitha, A. Pandikumar, *Compos. Sci. Technol.* **2020**, *195*, 108192.

[21] a) S. Dong, G. Suo, N. Li, Z. Chen, L. Peng, Y. Fu, Q. Yang, T. Huang, *Sens. Actuators B Chem.* **2016**, *222*, 972-979; b) K. Kunpatee, S. Traipop, O. Chailapakul, S. Chuanuwatanakul, *Sens. Actuators B Chem.* **2020**, *314*, 128059.

[22] N. Karikalan, S. Kubendhiran, S.-M. Chen, P. Sundaresan, R. Karthik, *J.Catal.* **2017**, *356*, 43-52.

[23] a) Y. Sang, Y. Cui, Z. Li, W. Ye, H. Li, X. S. Zhao, P. Guo, *Sens. Actuators B Chem.* **2016**, *234*, 46-52; b) S. Pan, L. Wang, X. Chen, Y. Tang, Y. Chen, Y. Sun, X. Yang, P. Wan, *Electrochim. Acta* **2016**, *203*, 301-308.

Chapter 4
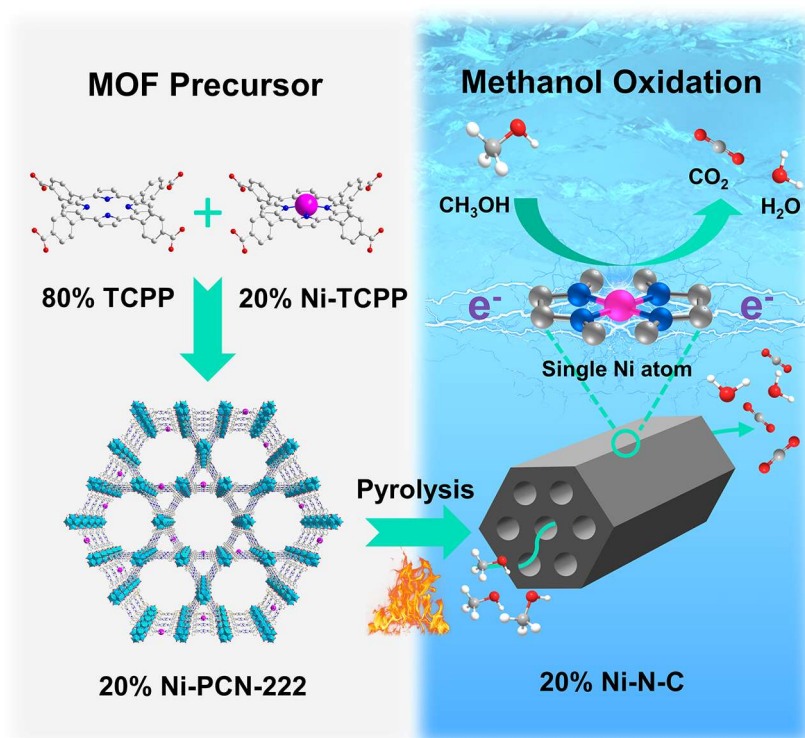
Porphyrinic MOF Derived Single-atom Electrocatalyst Enables Methanol Oxidation*

Abstract

Electrochemical methanol oxidation reaction (MOR) serves as a key route for renewable energy technologies. However, unmet challenges remain in the preparation of low-cost, efficient and robust electrocatalysts for MOR. Herein, a porphyrinic metal-organic framework (MOF) with spatially isolated Ni centres is prepared. Upon pyrolysis, this affords a single-atom Ni implanted nitrogen-doped porous carbon (20% Ni-N-C). Integrating abundant and accessible single-atom Ni sites, hierarchical porosity, excellent conductivity with stable Ni-N$_4$ moieties all in one, the derived ultra-stable 20% Ni-N-C exhibits high MOR activity and CO tolerance, thereby outperforming state-of-the-art nonprecious metal based electrocatalysts. Computational insights reveal a low energy barrier of 1.19 eV for the rate-determining step, in agreement with the experimental observations of superior MOR activity. As the first foray into improving MOR efficiency with nonprecious metal based single-atom electrocatalysts, the yet-unrealized potential for MOFs and related modular hybrids is demonstrated.

4.1 Introduction

The severe global environmental pollution and energy crises caused by the consumption of fossil energy provoke the urgent demand for clean and renewable energy.[1] In the pursuit of promising energy conversion systems, electrochemical methanol oxidation reaction (MOR) plays crucial roles. For examples, anodic MOR is the core process of methanol fuel cells, determining the energy conversion efficiency.[2] Moreover, thermodynamically favourable MOR also serve as promising candidate to replace the sluggish-kinetics anodic oxygen evolution reaction (OER) in a methanol-water electrolysis system for the efficient production of hydrogen, another promising green energy.[3] Thus, the adoption of MOR is primed to directly align with the United Nations Sustainable Development Goal (SDG) 7: *affordable and clean energy.* [4] To achieve efficient MOR, electrocatalysts play the key roles. Thus far, MOR catalysts continue to rely upon expensive Pt-derived substrates. Exacerbating this state-of-the-art, scarcity and limited durability (due to CO poisoning) of the Pt derived materials often restrict the much sought-after transition to commercial viability.[5] In this context, development of alternative noble metal-free catalysts rests on offering two things in one: high efficiency and good stability during the MOR. Nonetheless, paucity of performances often resulting in *catch-22* situations render this a non-trivial task.

In this context, Ni-based nanomaterials, such as Ni,[6] NiO,[7] Ni(OH)$_2$,[8] PtNi,[9] NiCo,[10] and NiCu[11] alloys have spurred considerable research interest for catalyzing MOR. Transformation between Ni(II) and Ni(III) facilitates electron transfer during the MOR, typically resulting in significant electrocatalytic activities. Nevertheless, handicapped by the tendency to aggregate active sites, inactive inner metal sites (in nanoparticles), deactivation by harmful intermediates, their electrocatalytic efficiencies and durability remain underexplored to a great extent.[2b, 12] Of late, single-atom catalysts (SACs) offer an alternative approach to advance the new-generation high-efficiency electrocatalysts. This research hypothesis is predicated upon extracting two-fold contributions from the stable and electrocatalytically contributing metal sites (largely present in abundance).[12c, 13] The nitrogen-stabilized single metal atom matrix all-pervasive within the derived carbons (M-N-C) is typically well-understood for presenting favourable electrochemical properties *versus* their bulk metallic counterparts.[14] The surrounding N heteroatoms tune the *d*-band electronic structure of single metal atoms, suited to improve the catalytic performance.[12b, 15]

To this end, the carbonaceous materials often reveal high electrical conductivity. Meanwhile, thanks to the strong covalent bonding between metal (M) centres and the N atoms, beyond high stability, the M-N-C SACs offer a dual resistance against active sites leaching and/or aggregation of active sites.[12c, 14b] Thanks to its reliance upon atomically dispersed Ni sites, this leads us to envision the proposed Ni-N-C SAC to exhibit superb MOR performance, perhaps to an extent that sets a new benchmark. However, despite a number of niche examples of M-N-C SACs, such SAC to catalyze MOR remains an uncharted territory.

Self-assembled from organic linkers and inorganic metal nodes (or clusters), metal-organic frameworks (MOFs) feature multiple merits of periodically porous coordination networks with high surface areas, well-defined pore structures and tailored functionalities.[16] Targeting the strategic formation of SACs through pyrolysis, these features allow the MOFs to function as ideal precursors.[17] However, due to high surface energy, single atoms across MOF structures typically show high propensity for aggregation during pyrolysis.[14a] Meanwhile, controlling the chemical configuration and electronic structure of single atoms poses challenge. Conversely, thanks to their π-conjugated macrocyclic structures flanked by four porphyrin N stabilized Ni (II) centres, nickel metalloporphyrins can be readily adopted as organic ligands while putting together the Ni-N-C SACs. Besides, in MOF precursors, introduction of metal-free porphyrin analogues facilitates controlled regulation of the distances between the adjacent metalloporphyrin ligands, effectively restraining the aggregation of metal atoms during pyrolysis. This unsurprisingly enables the desired formation of a carbonaceous matrix replete with single metal sites.[13] Moreover, the obtained MOF-derived SACs can largely inherit considerable surface area and hierarchical pore structures from the pristine MOFs. This transition expedites active site exposure and mass transfer of methanol molecules, hence contributing to the MOR performance.

Herein, we develop a Ni-N-C SAC for MOR, originating from a prototypical porphyrinic MOF, PCN-222 (PCN, porous coordination network) as the precursor.[18] PCN-222, constructed from Zr_6 cluster and tetrakis(4-carboxyphenyl)-porphyrin (TCPP) ligand, features ultrahigh surface areas (> 2000 m^2/g) and 1D hexagonal mesopores (~ 3.0 nm) (**Figure 4.1a**).[18-19] In this study, adopting a mixed ligand strategy, a series of isostructural PCN-222 are prepared with specific molar ratios of Ni-TCPP and H_2-TCPP. The prepared series is defined as n% Ni-PCN-222 (n% represents the molar ratio of Ni-TCPP in mixed ligand, *viz.*, 0%, 20%, 40%, and 100%). With low loading at 20%, the adjacent Ni-TCPP

ligands in 20% Ni-PCN-222 network feature a relatively long spatial distance, effectively inhibiting the Ni atoms from aggregation. This in turn leads to the formation of single Ni atoms after pyrolysis (**Figure 4.1a**). The proposed Ni-based SACs, defined as 20% Ni-N-C, exhibits superior MOR performance with low onset potential, high activity and stability. To the best of our knowledge, this is the first report of Ni-based SACs to catalyze MOR.

4.2 Results and Discussion
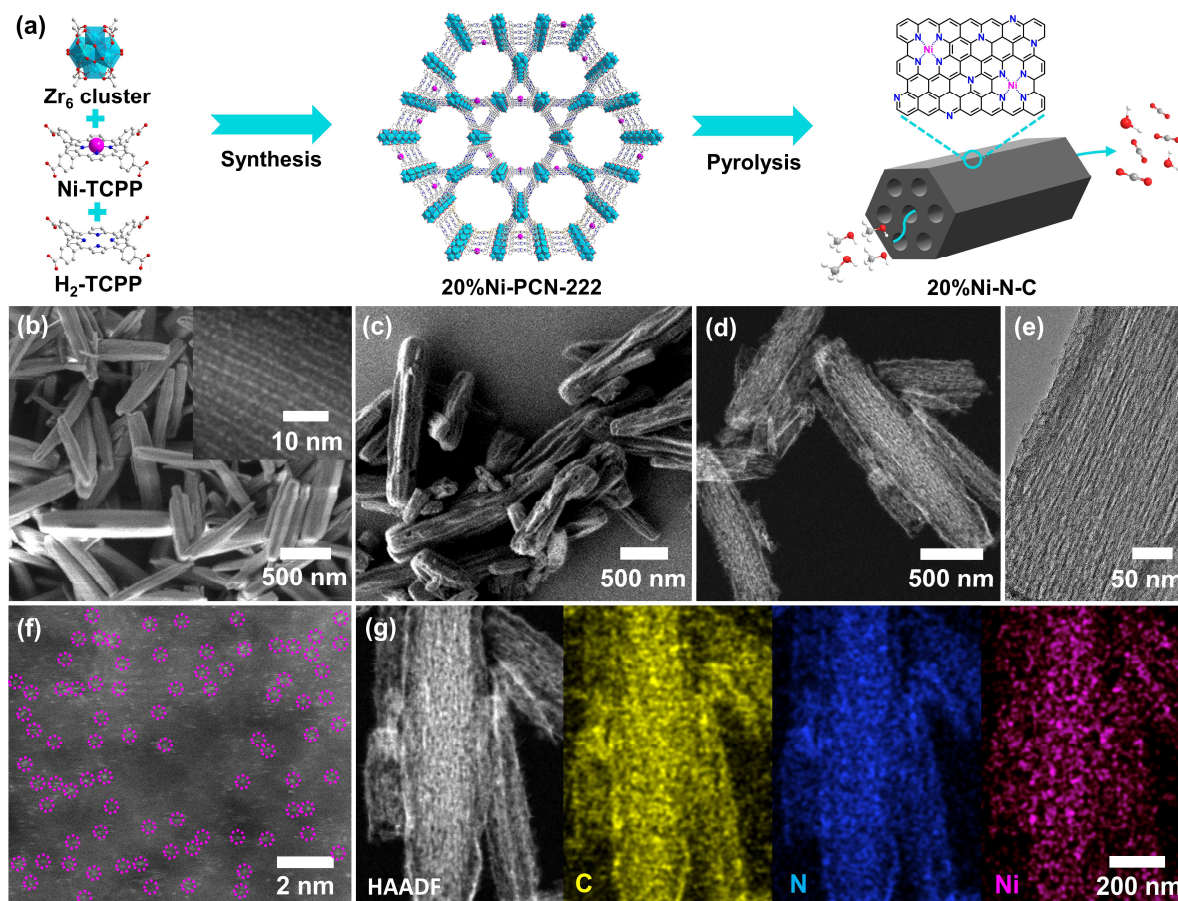
Figure 4.1 (a) Schematic illustration of the mixed-ligand strategy guided MOF formation that affords single Ni atoms in the derived 20% Ni-N-C. H atoms are omitted for clarity. Color codes: C, grey; O, red; N, blue; H, white, and Ni, pink. (b) SEM image of 20% Ni-PCN-222. Inset: HAADF-STEM image showing the 1D mesochannel structure in 20% Ni-PCN-222. (c) SEM and (d) TEM images of 20% Ni-N-C. (e) Enlarged TEM image of 20% Ni-N-C showing highly oriented mesochannels. (f) HAADF-STEM image of 20% Ni-N-C. Bright contrasts interpreted as isolated Ni atoms are encircled in pink. (g) HAADF-STEM image and EDX mapping images of the C, N, and Ni elements in 20% Ni-N-C.

Ni-PCN-222 with different Ni-TCPP loading ratios (0%, 20%, 40%, 100%) are successfully synthesized and all show similar 77 K N_2 isotherms and uniform pore size distributions (**Figures 4.2** and **4.3**). A typical type-IV N_2 isotherm observed across all the frameworks accompanied by a steep rise at *ca.* $P/P_0 = 0.3$, indicate

both micro and mesoporosity with pore sizes of ~ 1.3 nm and ~ 3.0 nm, assigned to their 1D triangular microchannels and hexagonal mesochannels, respectively (**Figures 4.3** and **4.1a**).[18-19] Taking 20% Ni-PCN-222 as a representative, the Brunauer-Emmett-Teller (BET) surface area is evaluated as high as 2149 m^2/g based on Rouquerol criteria to the 77 K N$_2$ isotherm.[20] Scanning electron microscopy (SEM) analysis of 20% Ni-PCN-222 show a rod-shaped morphology with a crystallite length of around 1.3 μm (**Figure 4.1b**). High-angle annular darkfield scanning transmission electron microscopy (HAADF-STEM) reveals the highly oriented mesochannels (**Figure 4.1b, inset**), in agreement with the Ni-PCN-222 crystal structure with the corresponding pore size distribution profiles (**Figure 4.1a** and **4.3**). Energy-dispersive X-ray (EDX) spectroscopy elemental mapping confirms a uniform distribution of Ni across the 20% Ni-PCN-222 (**Figure 4.4**). With the stepwise increase of Ni-TCPP loading, attenuated total reflection infrared spectroscopy (ATR-IR) spectra of n% Ni-PCN-222 show appearance and intensification of a new peak at 1002 cm^{-1} assigned to Ni-N bonds; while the N–H stretching vibration at 962 cm^{-1} decrease and eventually disappear, indicating an increase of the Ni-TCPP integrated into the studied frameworks (**Figure 4.5**).
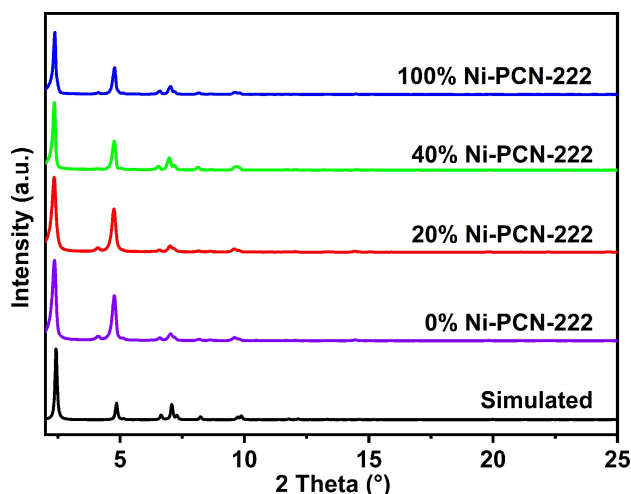
Figure 4.2 PXRD patterns of the n% Ni-PCN-222 phases with different Ni-TCPP loading (n = 0, 10, 20, 40 and 100). These X-ray diffraction patterns are found to be in good agreement with the simulated XRD profile, suggesting bulk phase purity.
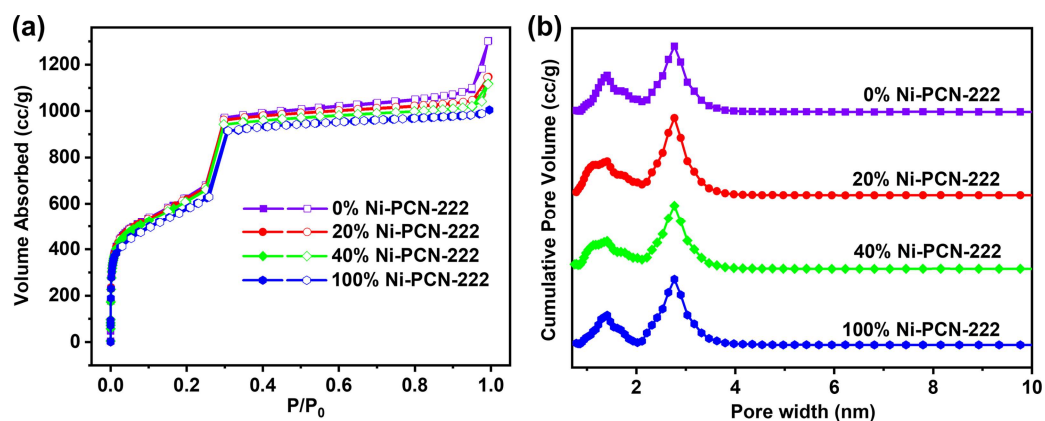
Figure 4.3 (a) N_2 sorption isotherms for n% Ni-PCN-222 with different Ni-TCPP loading at 77 K; b) DFT pore size distributions for n% Ni-PCN-222 based on the isotherms (n = 0, 10, 20, 40 and 100).
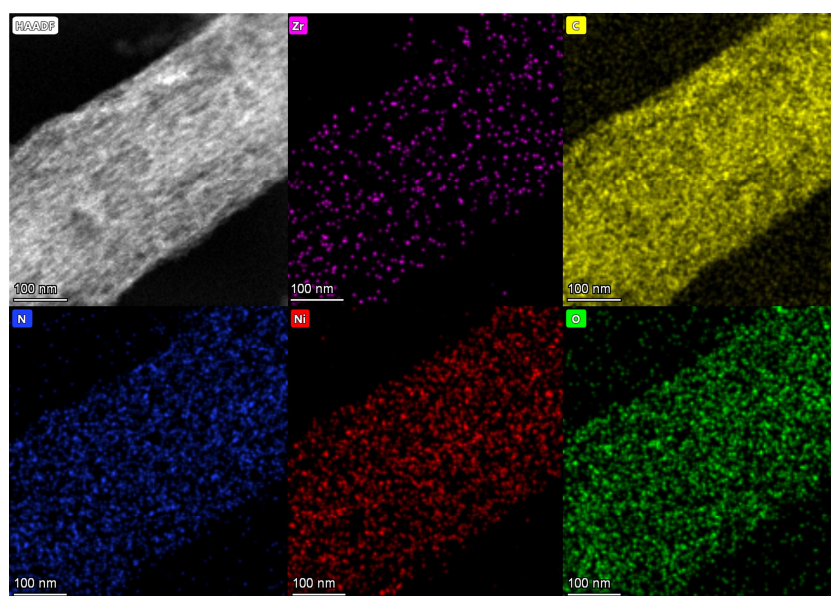
Figure 4.4 HAADF-STEM image and EDX elemental mapping images of 20% Ni-PCN-222 for zirconium (pink), carbon (yellow), nitrogen (blue), nickel (red), and oxygen (green).
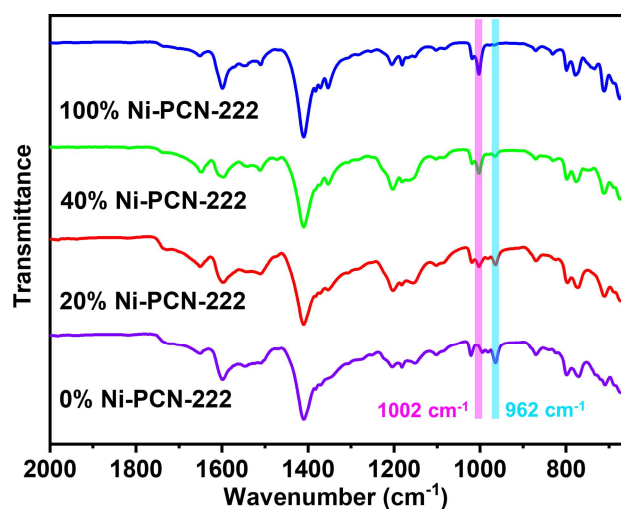
Figure 4.5 ATR-IR spectra of n% Ni-PCN-222 with different Ni-TCPP loading ratios (n = 0, 10, 20, 40

and 100).

Upon pyrolysis of n% Ni-PCN-222, composites with obvious ZrO_2 phase are obtained, named as n% Ni-N-C/ZrO_2 (**Figure 4.6**). For the 20% Ni-N-C/ZrO_2, only the ZrO_2 phase is found with the absence of any metallic Ni, thereby suggesting a highly disperse nature of Ni, steering clear of aggregation.[13a] Conversely, with higher Ni-TCPP ratios in the MOF structure, the obtained 40% Ni-N-C/ZrO_2 exhibit new peaks around 44.5° and 51.8° assigned to the diffraction of metallic Ni species.[14b] An enhanced signature of Ni-containing species is also found in 100% Ni-N-C/ZrO_2. Upon removing the ZrO_2 by hydrofluoric acid (HF), the derived N-doped carbons (n% Ni-N-C) with uniform rod-like shape are finally obtained (**Figure 4.1c**). The powder X-ray diffraction (PXRD) patterns show two broad diffraction peaks at *ca.* 25° and 45°, corresponding to the (002) and (101) planes of graphitized carbons (**Figure 4.7**).[13a] Distinct peaks for metallic Ni are observed in 100%Ni-N-C (**Figure 4.7**), further confirming the existence of Ni nanoparticles. This is also in good agreement with the TEM and EDX mapping analyses (**Figure 4.8**). That there is no detectable Ni in the final 40% Ni-N-C in comparison to 40% Ni-N-C/ZrO_2 is perhaps caused by the removal of exposed Ni nanoparticles after HF etching.[21] However, small aggregated Ni nanoparticles are indeed detected via the TEM images (**Figure 4.9**). Consistent with 20% Ni-N-C/ZrO_2, neither were reflections of metallic detected in the PXRD pattern of 20% Ni-N-C (**Figure 4.7**) nor identifiable metal nanoparticles found in the corresponding TEM images (**Figures 4.1d and 4.1e**). EDX spectrum and elemental mapping exhibit the existence and uniform distribution of Ni, N and C in 20% Ni-N-C (**Figures 4.10 and 4.1g**). As a proof of concept, the atomically dispersed Ni can be seen directly by HAADF-STEM imaging, with single Ni atoms appearing as randomly dispersed bright dots across the matrix (**Figure 4.1f**).[14b] The Ni loading is examined by inductively coupled plasma optical emission spectrometry (ICP-OES) and recorded as high as 1.69 wt.% (**Table 4.1**), comparable to M- N-C SACs derived from metalloporphyrinic MOFs.[13b] These results prove the success of our adopted mixed ligand strategy in bringing about the successful fabrication of Ni-based SACs in 20% Ni-N-C, despite low Ni-TCPP loading ratios.
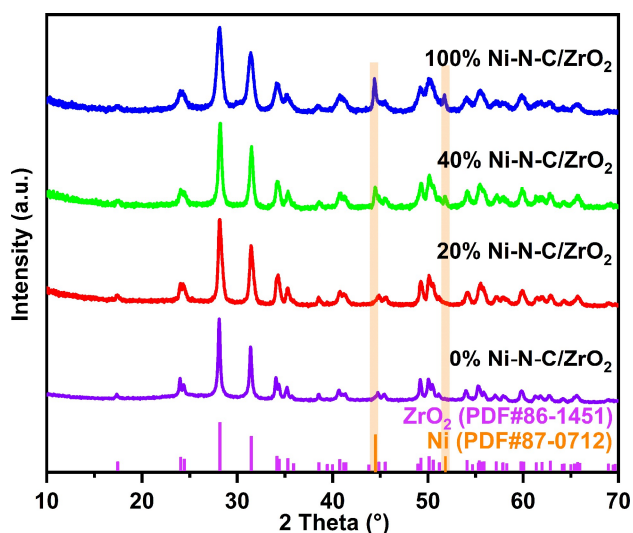
Figure 4.6 PXRD patterns of n% Ni-N-C/ZrO$_2$ obtained upon pyrolysis of n% Ni-PCN-222 with different Ni-TCPP loading (n = 0, 10, 20, 40 and 100) and the corresponding standard joint committee on powder diffraction standards (JCPDS) cards of ZrO$_2$ and Ni.
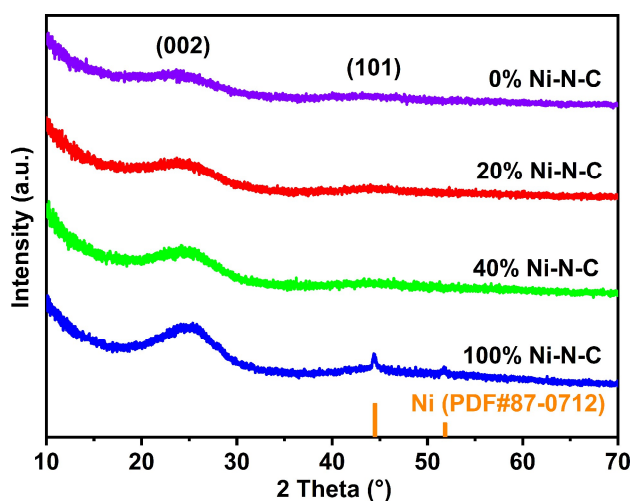
Figure 4.7 PXRD patterns of n% Ni-N-C obtained from n% Ni-N-C/ZrO$_2$ after HF etching (n = 0, 10, 20, 40 and 100) and the corresponding standard JCPDS card of metallic Ni.
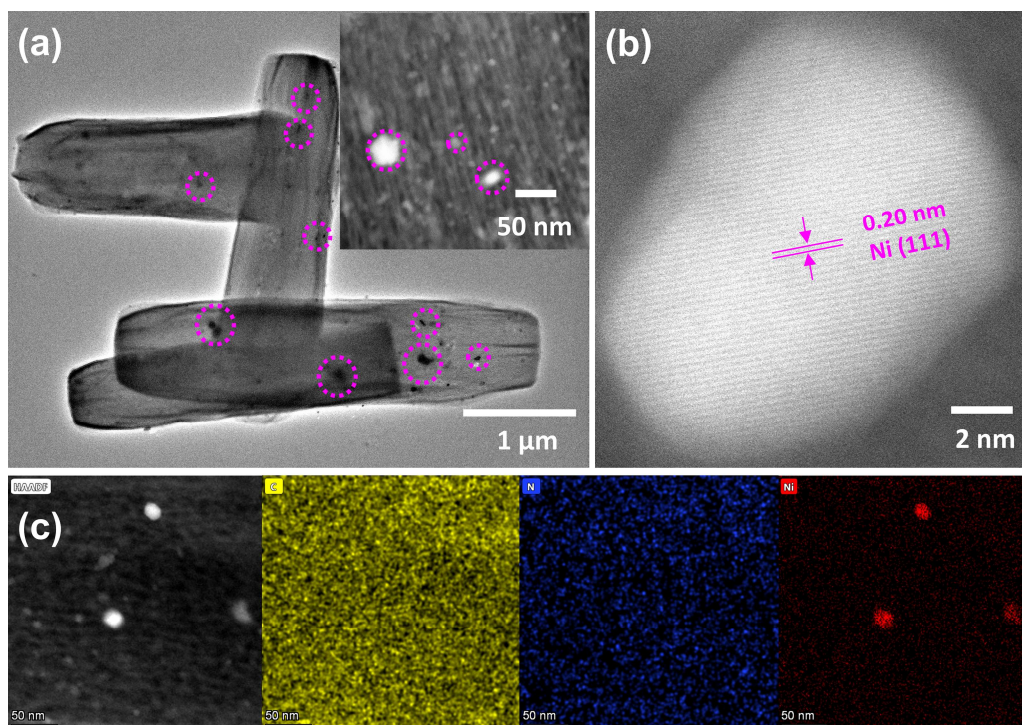
Figure 4.8 (a) TEM image of 100% Ni-N-C, showing metallic Ni nanoparticles dispersed in rod-like samples; inset: HAADF-STEM image presenting the mesochannels. (b) HAADF-STEM image showing the lattice fringe of the aggregated Ni nanoparticles. (c) HAADF-STEM and EDX elemental mapping images of carbon (yellow), nitrogen (blue) and nickel (red) images of 100% Ni-N-C, further confirming the formation of aggregated Ni nanoparticles.
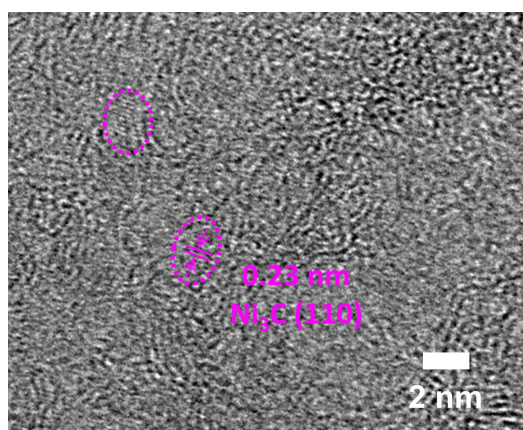
Figure 4.9 HAADF-STEM image of 40% Ni-N-C. The nanocrystallites are marked by pink circles.
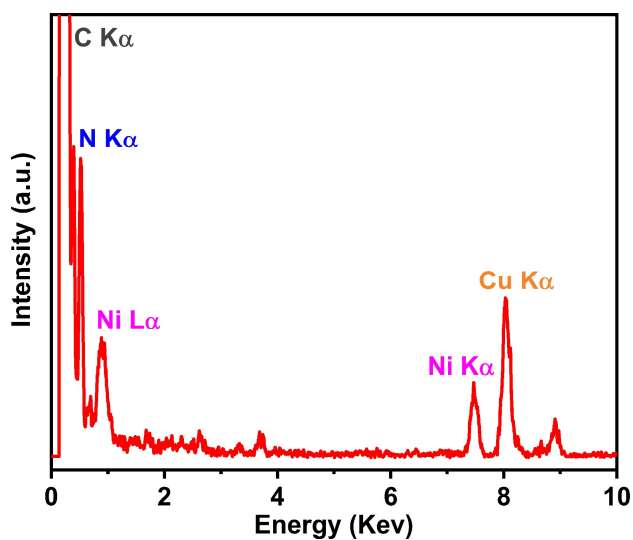
Figure 4.10 EDX spectrum of 20% Ni-N-C.
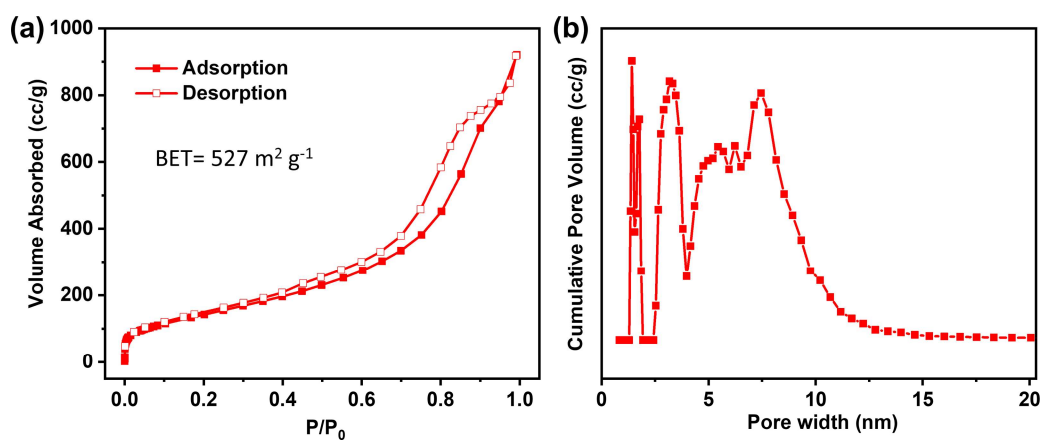
Figure 4.11 (a) N_2 sorption isotherm of 20% Ni-N-C at 77 K and (b) the corresponding pore size distribution based on non-local density functional theory (NLDFT) model.
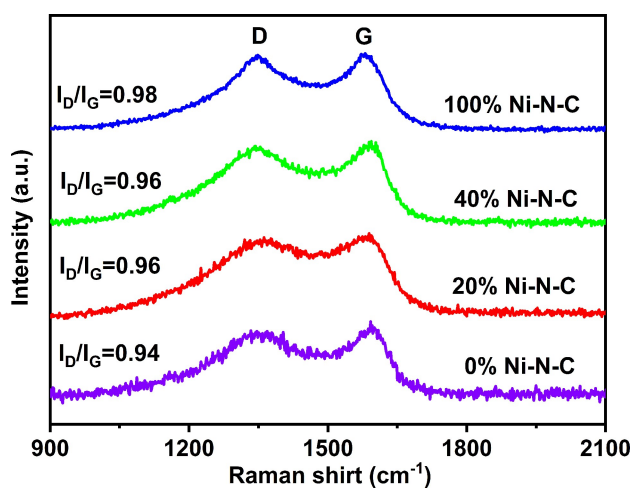
Figure 4.12 Raman spectra of n% Ni-N-C (n = 0, 10, 20, 40 and 100).
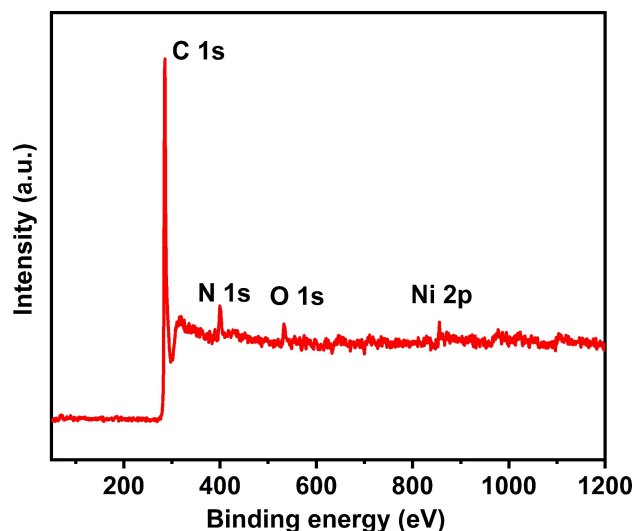
Figure 4.13 Survey XPS spectrum of 20% Ni-N-C.

Table 4.1. Metal contents of 20% M-N-C and n% Ni-N-C samples obtained from ICP-OES.

Catalysts	20% Ni-N-C	20% Fe-N-C	20% Cu-N-C	20% Zn-N-C	20% Mn-N-C	20% Co-N-C	40% Ni-N-C	100% Ni-N-C
Metal contents (wt. %)	1.69	1.83	1.43	1.67	1.45	1.91	4.54	6.85

By TEM imaging, the porous structure with highly oriented mesochannels of 20% Ni-N-C can be unambiguously identified (**Figure 4.1e**). In addition, the N_2 isotherm at 77 K reveals a high BET surface area of 527 m^2 g^{-1} whereas the observed hysteresis loop at *ca.* P/P_0 of 0.7–0.9 manifests its mesoporosity (**Figure 4.11a**). The pore size distribution profile further indicates the hierarchical porosity with pore sizes of ~ 1.4 nm, 3.3 nm and 7.5 nm. The high surface area and hierarchical porosity are beneficial to the active site accessibility and mass transfer, key to effectuate an enhanced catalytic performance (**Figure 4.11b**). Furthermore, the Raman spectrum of 20% Ni-N-C reveals a low intensity ratio I_D/I_G ~ 0.96 of the D band (*ca.* 1348 cm^{-1}) and G band (*ca.* 1592 cm^{-1}) suggesting its high graphitization degree; therefore beneficial to electron transfer during the electrocatalysis (**Figure 4.12**). The chemical composition and electronic state of 20% Ni-N-C are also examined by X-ray photoelectron spectroscopy (XPS). The survey XPS spectrum unveils the existence of C, N, O, and Ni elements (**Figure 4.13**). Upon fitting the high-resolution N 1s XPS spectrum, five configurations are observed: pyridine N (398.5 eV), Ni-N (399.2 eV), pyrrole N (400.1 eV), graphitic N (401.3 eV) and oxidized N (403.2 eV), respectively (**Figure 4.14a**), revealing the existence of Ni-N_X species originated from Ni-TCPP upon pyrolysis.[13b] The Ni $2p_{3/2}$ spectrum shows

two peaks at binding energies of 855.4 eV (Ni $2p_{3/2}$) and 872.7 eV (Ni $2p_{1/2}$), suggesting the oxidation state of Ni (close to Ni^{2+}) in the $Ni-N_X$ species (**Figure 4.14b**).[13b] Moreover, X-ray absorption near edge structure (XANES) and Fourier transform-extend X-ray absorption fine structure (FT-EXAFS) measurements are employed to further identify the electronic structure and chemical configuration of the Ni species in 20% Ni-N-C SACs. As shown in the Ni K-edge XANES spectra, the energy adsorption edge of 20% Ni-N-C falls between the Ni foil and NiO. This implies Ni to be positively charged, also manifests the attraction of electrons towards the neighboring N atoms (**Figure 4.14c**).[14b] This is well aligned with the XPS result (**Figure 4.14b**). FT-EXAFS spectrum in **Figure 4.14d** reveals a dominating feature at *ca.* 1.41 Å (phase-uncorrected) assigned to the Ni-N coordination in the 20% Ni-N-C. In parallel, the absence of Ni-Ni (*ca.* 2.17 Å) and Ni-O (*ca.* 1.65 Å) features (corresponding to metallic Ni and bulk NiO, respectively) indicates an atomic dispersion of Ni in 20% Ni-N-C.[14b] To further shed light on the coordination environment of Ni atom, EXAFS fitting has been performed (**Figures 4.14e** and **4.14f, Table 4.2**). The fitting result reveals a single Ni atom to be coordinated by ∼ 4 N atoms, *i.e.*, in the form of $Ni-N_4$ moieties in 20% Ni-N-C.[11b]
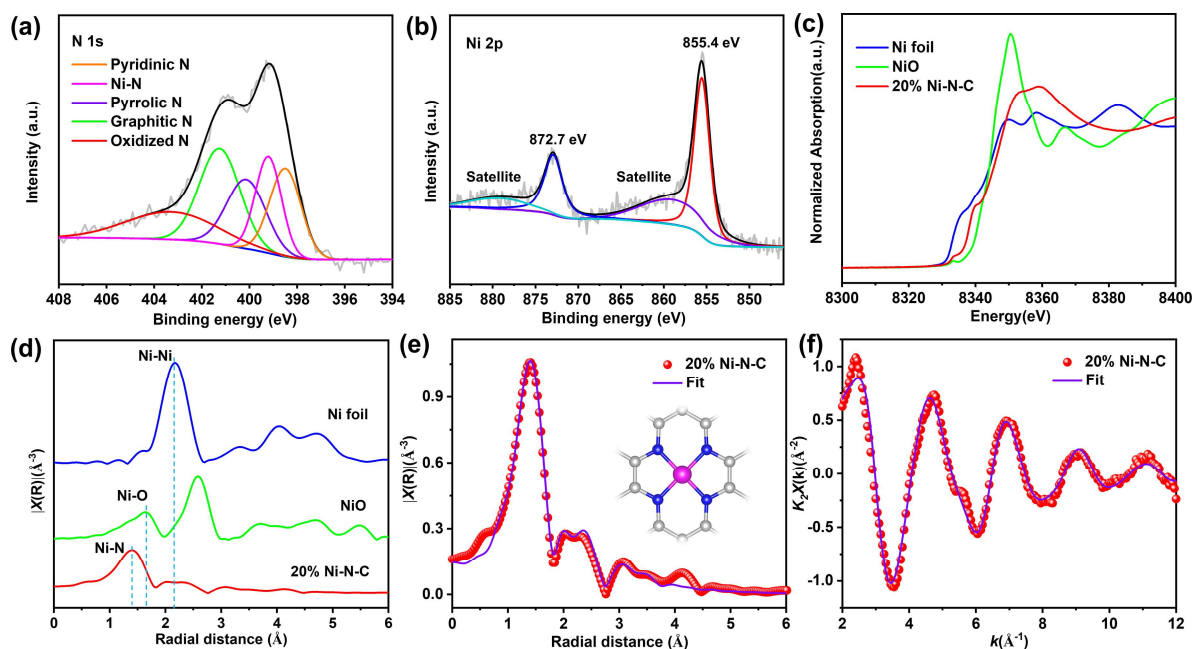
Figure 4.14 High-resolution XPS spectra of (a) N 1s and (b) Ni 2p of 20% Ni-N-C. (c) Ni K-edge XANES and (d) FT-EXAFS spectra of 20% Ni-N-C in comparison with the corresponding spectra for NiO and Ni foil. (e) EXAFS fitting for 20% Ni-N-C (inset: model of 20% Ni-N-C. Color codes: Ni pink, N blue, C grey spheres). (f) k^2-weighted EXAFS fitting of 20% Ni-N-C.

Table 4.2. Parameters of the Ni K-edge EXAFS fitting results for 20% Ni-N-C.

Shell	CN	R (Å)	σ^2 ($\times 10^{-3}$ Å^2)
Ni-N	4.7 ± 0.8	1.869 ± 0.012	7.2 ± 1.6
Ni-C	5.0 ± 3.8	2.825 ± 0.060	19.1[a]
Ni-C	3.8 ± 2.3	3.218 ± 0.042	8.3 [a]
Ni-C	6.6 ± 7.7	4.213 ± 0.117	17.2 [a]

CN: coordination number; R: interatomic distance between the absorber and the backscatter atoms; σ^2: Debye-Waller factor to describe the variance due to disorder (both lattice and thermal). The dominating coordination of Ni single atom sites as the Ni-N is revealed in EXAFS fitting of 20% Ni-N-C.

[a] this parameter was kept fixed during the fitting.

As a proof-of-concept study, after characterizing the proposed 20% Ni-N-C SACs, MOR electrocatalytic performances are critically evaluated. **Figure 4.15** shows the cyclic voltammetry (CV) curves of 20% Ni-N-C and its counterparts 0% Ni-N-C, 40% Ni-N-C and 100% Ni-N-C in N_2-saturated 1M aqueous KOH solution at a scan rate of 50 mV s^{-1}. Upon loading the Ni species, 20%, 40% and 100% Ni-N-C present a pair of well-defined redox peaks at *ca.* 1.30 V and 1.38 V on the CV curves. These correspond to the interconversion of Ni(II)/Ni(III) redox couples after activation treatment during CV.[2b, 22] 0% Ni-N-C, without any Ni doping, shows no redox peak. Among all the catalysts, 20% Ni-N-C exhibits a higher enclosed area under the CV curve and higher anodic and cathodic peak current densities, suggesting an adequate exposure of active sites with higher content present in 1M KOH solution. **Figure 4.16a** shows a comparative CV performance assessment for the 20% Ni-N-C when recorded in the absence and in the presence of 1M methanol. The MOR current density increase at *ca.* 1.35 V *versus* RHE, the same voltage at which Ni(II) undergoes oxidation to Ni(III). This alludes to the methanol oxidation process on the resulting Ni(III) active sites, consistent with the proposed mechanisms of electrocatalytic MOR on Ni-based catalysts.[2b] There is a slight rise of current density above 1.65 V, likely caused by a side reaction in the form of oxygen evolution reaction (OER).[23] Similar observations are also made in the CV, when only KOH electrolyte is used (**Figure 4.16a**).
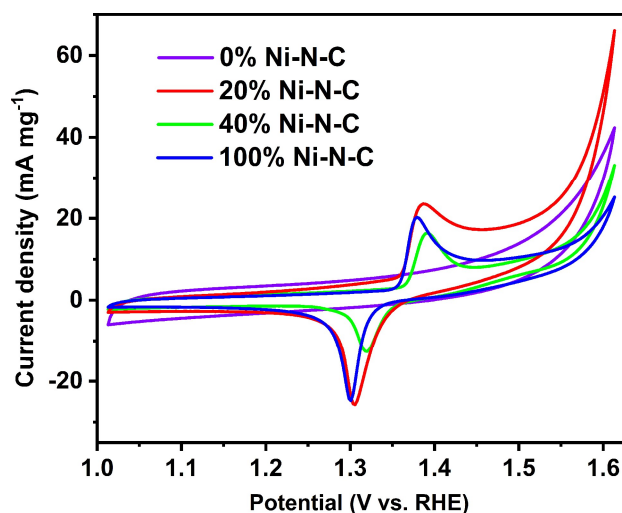
Figure 4.15 CV curves of n% Ni-N-C electrocatalysts in 1 M KOH at a scan rate of 50 mV s^{-1} (n = 0, 10, 20, 40 and 100).
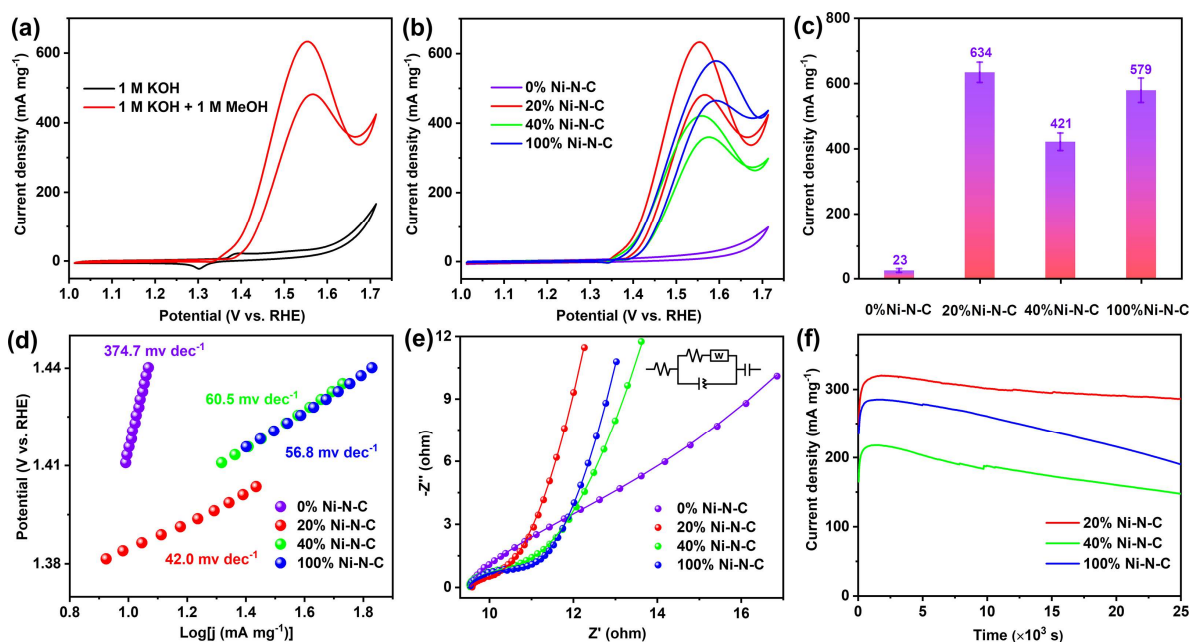
Figure 4.16 (a) CV profiles of the 20% Ni-N-C in 1 M KOH solution in the presence or absence of 1 M methanol at a scan rate of 50 mV s^{-1}. (b) CV curves recorded on different catalysts targeting methanol oxidation. (c) MOR activities and (d) Tafel plots of various catalysts as regards MOR. The mass activity of 0% Ni-N-C is assumed as the current density at 1.55 V, same as the MOR peak potential of 20% Ni-N-C. (e) Nyquist plots of n% Ni-N-C (n = 0%, 20%, 40%, 100%) catalysts in 1 M KOH + 1 M methanol electrolyte. (f) Chronoamperometric plots of 20% Ni-N-C, 40% Ni-N-C and 100% Ni-N-C at 1.46 V *versus* RHE.

To further study the electrocatalytic properties of the obtained Ni-based catalysts, the surface coverage of catalytic Ni(II)/Ni(III) redox species (Γ*) are examined on the basis of CV curves recorded at different scan rates (**Figure 4.17**).[10, 24] The surface coverage Γ* value of the 20% Ni-N-C is calculated ~ 5.30

×10^{-6} mol cm^{-2}, higher than those of its counterparts, 40% Ni-N-C (3.81×10^{-6} mol cm^{-2}) and 100% Ni-N-C (4.51×10^{-6} mol cm^{-2}) (**Figures 4.17d, e and f**). The larger surface coverage of Ni-based intermediates further highlights the full exposure of more Ni active sites in 20% Ni-N-C SACs compared to the 40% Ni-N-C and 100% Ni-N-C with bulk Ni species (**Figures 4.17a, b and c**). This is again consistent with its higher redox peak currents. Furthermore, the electrochemically active surface area (ECSA) of our prepared Ni-N-C catalysts are also estimated using the double-layer capacitance as reference obtained from the CV curves in non-Faradaic region (**Figure 4.18**).[24, 25] 20% Ni-N-C catalyst features a higher ECSA among Ni-N-C catalysts, hinting at the existence of more accessible active sites for its high-performing MOR electrocatalysis.
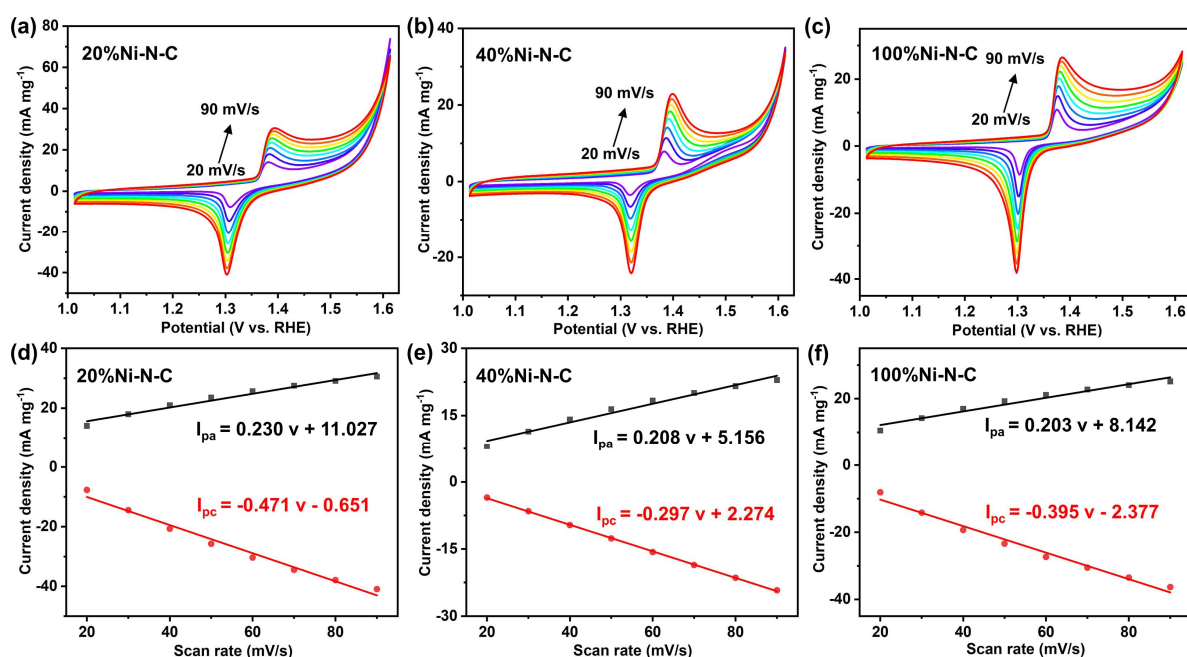
Figure 4.17 CV curves of (a) 20% Ni-N-C, (b) 40% Ni-N-C and (c)100% Ni-N-C respectively in 1 M KOH solution at different scan rates (20, 30, 40, 50, 60, 70, 80 and 90 mV s^{-1}); linear plots of anodic and cathodic current densities on different catalysts (d, e, and f) *versus* the scan rates. As shown in the figures (d, e, and f), the anodic and cathodic peak current densities increase linearly with respect to the scan rate. Therefore, the surface coverage of catalytic Ni(II)/Ni(III) redox species (Γ*) can be estimated according to the following equation. [22]

$$I_p = \frac{n^2 F^2}{4RT} \nu A \Gamma^*$$

where I$_p$ is the peak current density; n is electron transfer number of the interconversion of Ni(II)/Ni(III), i.e. 1; F is the Faraday constant (96485 C/mol); R is universal gas constant (8.314J/mol·K); T is temperature (298.15K); v is the scan rate; A is the geometric surface area of the glassy carbon electrode (0.0706 cm^2) and Γ* is the surface coverage of Ni(II)/Ni(III) redox species.

Based on the slopes of linear plot between anodic and cathodic peak current densities (Ip) and the scan rates (v), the surface coverage (Γ*) of different Ni-based catalysts can be calculated. For the calculation, the average of slopes on anodic and cathodic values are adopted. For example, 20% Ni-N-C exhibit an average of slopes: (0.230+0.471)/2, as 0.351, thus the slope $0.351 = (n^2F^2/4RT)A\Gamma^* = 66285.644 \Gamma^*$, $\Gamma^* = 5.30 \times 10^{-6}$ mol cm^{-2}. The Γ* values of 40% Ni-N-C and 100% Ni-N-C are similarly calculated as 3.81×10^{-6} mol cm^{-2} and 4.51×10^{-6} mol cm^{-2} respectively.
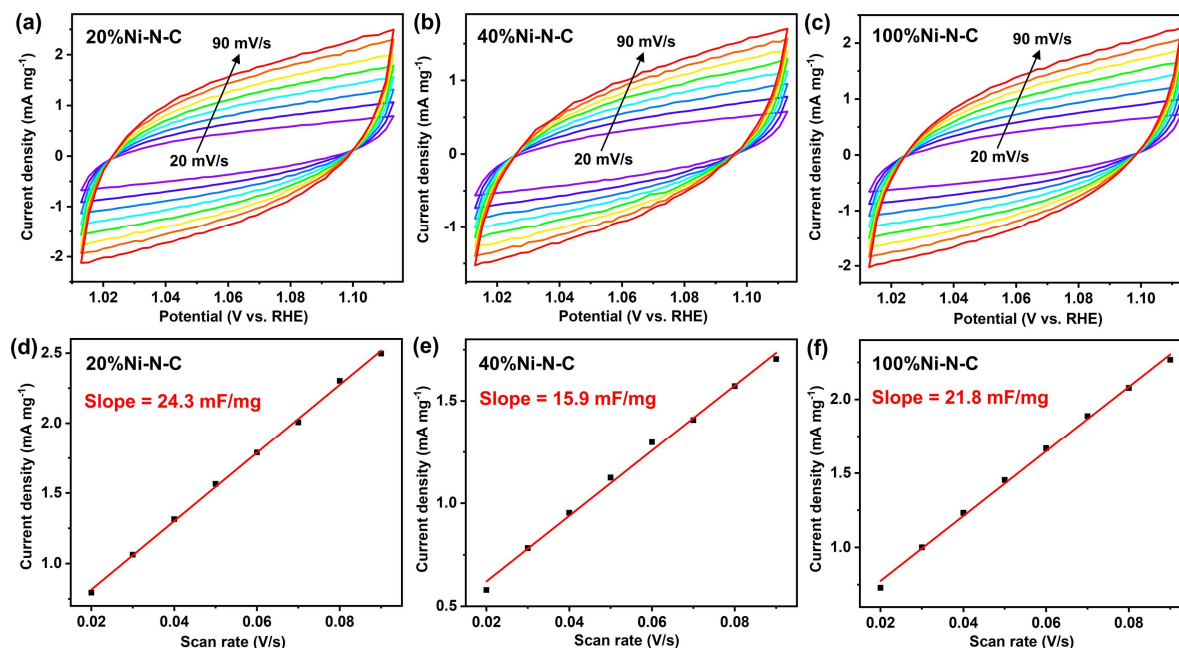
Figure 4.18 CV responses of (a) 20% Ni-N-C, (c) 40% Ni-N-C and (e)100% Ni-N-C respectively recorded in a non-Faradaic region (1.013 - 1.113V) in 1 M KOH solution with the presence of 1M methanol at different scan rates (20, 30, 40, 50, 60, 70, 80 and 90 mV s^{-1}); corresponding linear plots of anodic charge current densities measured at 1.113 V *versus* scan rates, in which slope is equal to the double-layer capacitance (C_d) of the electrocatalytic system. Thus, the electrochemically active surface area (ECSA) can be estimated with the double-layer capacitance as reference (ECSA = C_{dl}/C_s, C_s is a general specific capacitance, constant for Ni-based catalysts). The higher double-layer capacitance of 20% Ni-N-C indicates its higher ECSA, manifesting the existence of more accessible active sites for the MOR electrocatalysis.

Encouraged by the hierarchical porosity and high-content of single-atom Ni active sites of 20% Ni-N-C, we investigated its MOR performance. Targeting subsequent MOR investigations, after an assessment of oxidation performance under different methanol concentrations, 1 M methanol is chosen to accompany the electrolyte (**Figure 4.19**). As shown in **Figures 4.16b** and **4.16c**, 20% Ni-N-C features the highest MOR current density of 634 mA mg^{-1} at a lower potential of 1.55 V when compared to its analogues. In addition, the current densities normalized by mass of Ni are also evaluated and 20% Ni-N-C exhibits a four times

higher current density than that of 20% Ni-N-C and 100% Ni-N-C (**Figure 4.20**). These signify significantly superior activity of the single-atom Ni sites towards MOR than the bulk Ni metallic catalysts. Moreover, MOR current density of 20% Ni-N-C starts to increase at a lower potential, exhibiting lower onset potential than those of the other bulk Ni metallic analogues (**Figure 4.21**). This further indicates its higher activity for methanol oxidation. Meanwhile, with an increase in the Ni to ligand ratio, a performance boost (for 100% Ni-N-C) is also found, relative to 40% Ni-N-C (**Figures 4.16b**). Substantiated by the redox species surface coverage (Γ^*) and ECSA (**Figures 4.17** and **4.18**), this is a likely outcome of the increased active site density in 100% Ni-N-C. That the CV curve of 0% Ni-N-C without Ni doping shows an inert response to MOR suggesting the intrinsic catalytic role played by the Ni-based active sites. The intrinsic MOR activity of Ni is further supported by comparing the electrocatalytic responses across a range of 20% M-N-C analogues, where M was varied along Ni, Fe, Cu, Zn, Mn and Co. These SAC variants are similarly prepared upon pyrolysis of corresponding 20% M-PCN-222 (**Figure 4.22, Table 4.1**). Notably, only 20% Ni-N-C manifests an obvious catalytic response, suggesting the MOR to occur exclusively on specific Ni sites (**Figure 4.23**). To further elucidate the superb performance of 20% Ni-N-C, Tafel slope on MOR is investigated. As shown in **Figure 4.16d,** 20% Ni-N-C exhibits a Tafel slope of 42.0 mV dec^{-1}, lower than each of its analogues, 0% Ni-N-C (374.7 mV dec^{-1}), 40% Ni-N-C (60.5 mV dec^{-1}) and 100% Ni-N-C (56.8 mV dec^{-1}). In the pursuit of advancing MOR electrocatalysts, a more favourable kinetics stands out, thanks to the highly distributed nature of single-atom Ni sites in the N doped carbon matrix. Electrochemical impedance spectroscopy (EIS) is also recorded to thoroughly investigate the overall electrocatalytic kinetics for MOR. To be more specific, this approach rests on assessing the interfacial charge-transfer resistance (R_{ct}) [2b, 24, 26]. The Nyquist plots in **Figure 4.16e** present a smaller semicircle of 20% Ni-N-C compared to its other counterparts, revealing a lower R_{ct} and favourable MOR kinetics on the 20% Ni-N-C interface (**Table 4.3**). Also, the high Warburg slope of the straight line in low frequency region of 20% Ni-N-C indicates the fast diffusion process during MOR [26].
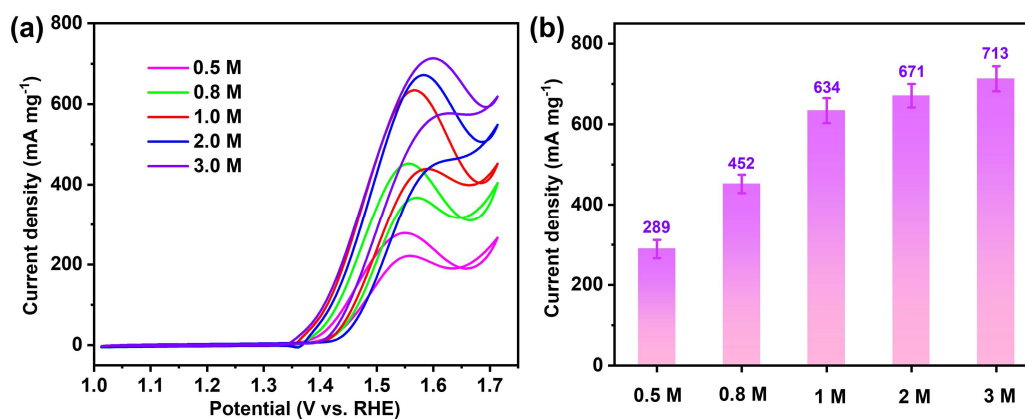
Figure 4.19 (a) CV curves of MOR on 20% Ni-N-C and (b) corresponding mass activity recorded at a scan rate of 50 mV s^{-1} in 1 M KOH with different methanol concentrations. As shown in the figure, the MOR current responses is approximately proportional to the methanol concentration in the range of 0.5 - 1 M, revealing a controlled diffusion in the low concentration range. Upon further increasing the concentration to 2 and 3 M, the peak current density improves slightly, suggesting that a mixed-control depends on both diffusion and reaction-kinetics.[2b] As a result, compared to 2 M and 3 M, 1 M turns out more favourable, therefore selected as the optimum concentration for further investigation.
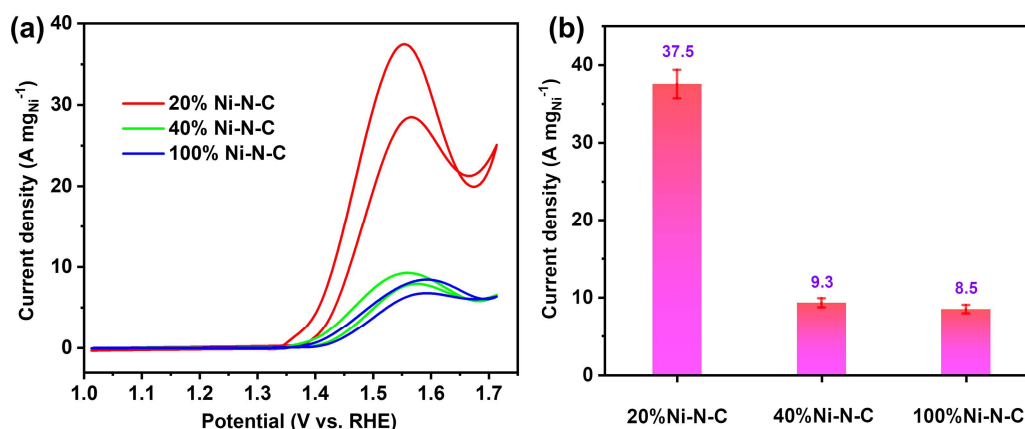
Figure 4.20. (a) CV curves and (b) current densities of MOR on 20% Ni-N-C, 40% Ni-N-C and 100% Ni-N-C based on the mass of Ni species in 1 M KOH + 1 M methanol at a scan rate of 50 mV s^{-1}.

118
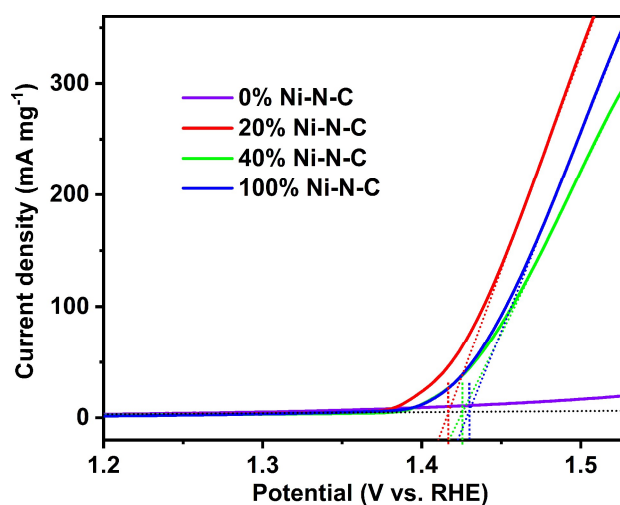
Figure 4.21. Enlarged CV curves of different catalysts in 1 M KOH + 1 M methanol at a scan rate of 50 mV s^{-1}. The onset potentials of 20% Ni-N-C, 40% Ni-N-C and 100% Ni-N-C are evaluated by the tangent lines of CV curves, as 1.415 V, 1.426 V and 1.430 V, respectively.
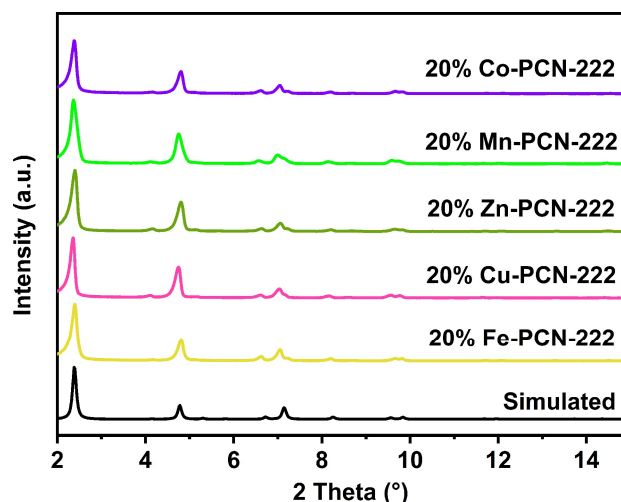
Figure 4.22 PXRD patterns of 20% M-PCN-222 prepared with different M-TCPP ligands. These diffraction patterns are found to be in good agreement with the simulated XRD profile, suggesting bulk phase purity.
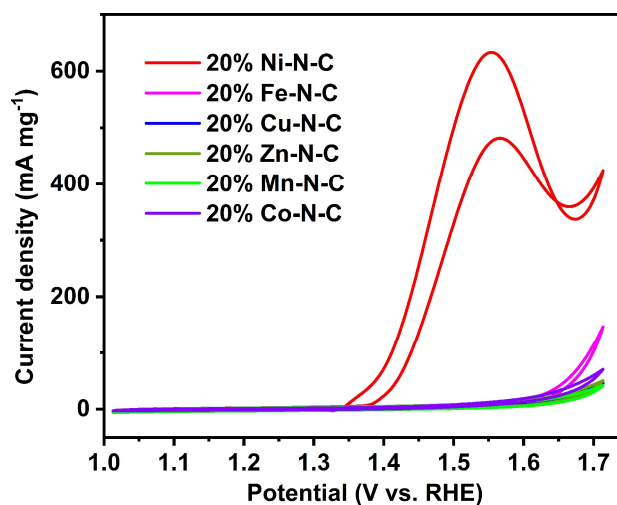
Figure 4.23 CV curves of MOR on various 20% M-N-C obtained upon pyrolysis of the corresponding 20% M-PCN-222 in 1 M KOH + 1 M methanol at a scan rate of 50 mV s^{-1}.

Table S3. Interfacial charge-transfer resistance (R_{ct}) of n% Ni-N-C samples in 1 M KOH + 1 M methanol electrolyte.

Catalysts	0% Ni-N-C	20% Ni-N-C	40% Ni-N-C	100% Ni-N-C
R_{ct} (Ω)	8.26	0.91	1.56	1.53

Apart from comparing performances between the Ni-N-C samples of different Ni dopings, the CV curve of 20% Ni-N-C/ZrO$_2$ also registers an inferior MOR response *versus* that for 20% Ni-N-C (**Figure 4.24**). This result is a likely

consequence of the low surface area, narrow pore aperture (resulting in poor mass transfer and low density of accessible, active sites) and slow charge transfer in 20% Ni-N-C/ZrO$_2$ without the removal of inactive ZrO$_2$ by HF etching (**Figures 4.11, 4.24-4.26**). Meanwhile, 20% Ni-N-C also exhibits much better MOR activity than mixed Ni-N-C, which is derived from the physical mixture of 20% Ni-TCPP and 80% H$_2$-TCPP in molar ratio. The mixed Ni-N-C features a highly aggregated Ni species and extremely poor porosity, accounting for its unsatisfactory MOR performance (**Figures 4.24, 4.26-4.29**). This in turn elaborates the superiority of MOFs as precursors. The influence of the pyrolysis temperature is also investigated. Compared to the 20% Ni-N-C pyrolyzed at 700 ℃, significantly higher MOR current densities are achieved on samples obtained at 800 ℃ and 900 ℃, which is probably ascribed to the higher graphitization degree and thus superior electron transfer of the catalyst pyrolyzed at higher temperature (**Figures 4.30-4.32**). A minor influence on MOR activity is observed when temperature increases from 800 ℃ and 900 ℃, implying the limitation from other factors. On top of this, excellent electrocatalytic oxidation performances for other alcohols, *viz.* ethanol and isopropanol, are also observed on 20% Ni-N-C, revealing its versatility and potential relevance in alcohol-based fuel cells (**Figure 4.33**).
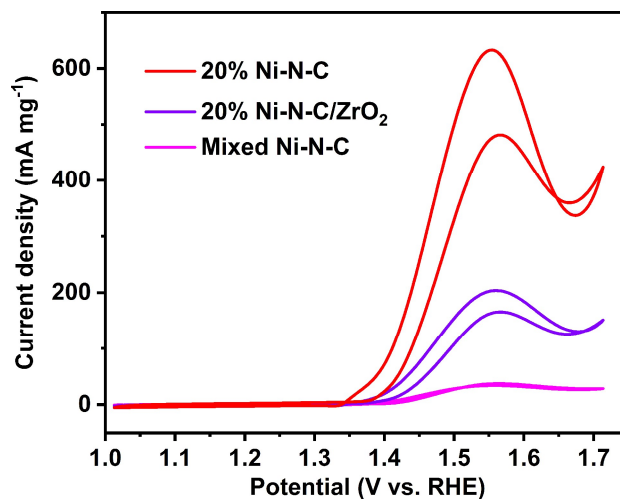
Figure 4.24 CV curves of MOR on 20% Ni-N-C, 20% Ni-N-C/ZrO$_2$ and mixed Ni-N-C in 1 M KOH + 1 M methanol at a scan rate of 50 mV s^{-1}.
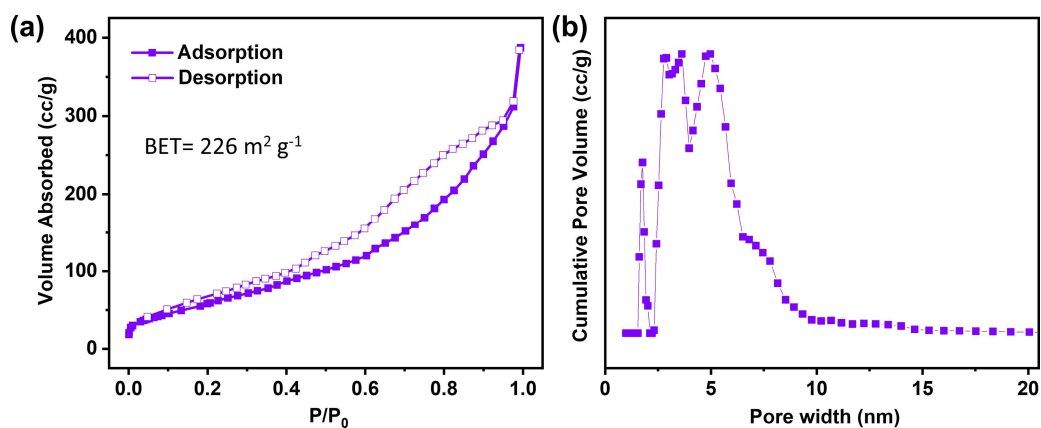
Figure 4.25 (a) N_2 sorption isotherm of 20% Ni-N-C/ZrO_2 at 77 K and (b) the corresponding pore size distribution profile based on NLDFT model.
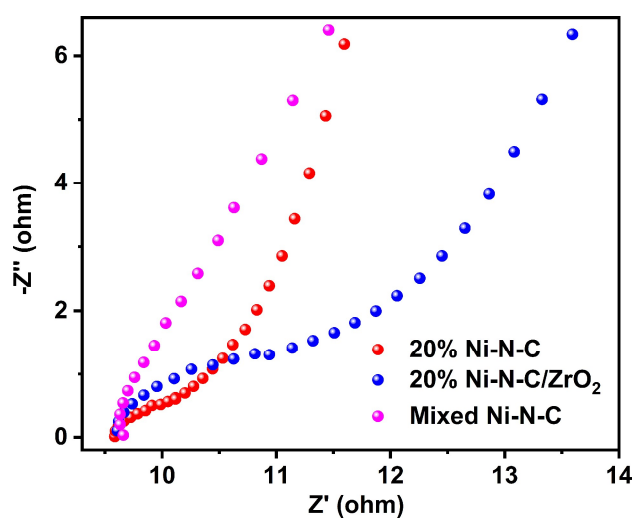
Figure 4.26 Nyquist plots of 20% Ni-N-C, 20% Ni-N-C/ZrO_2 and mixed Ni-N-C in 1 M KOH + 1 M methanol electrolyte.
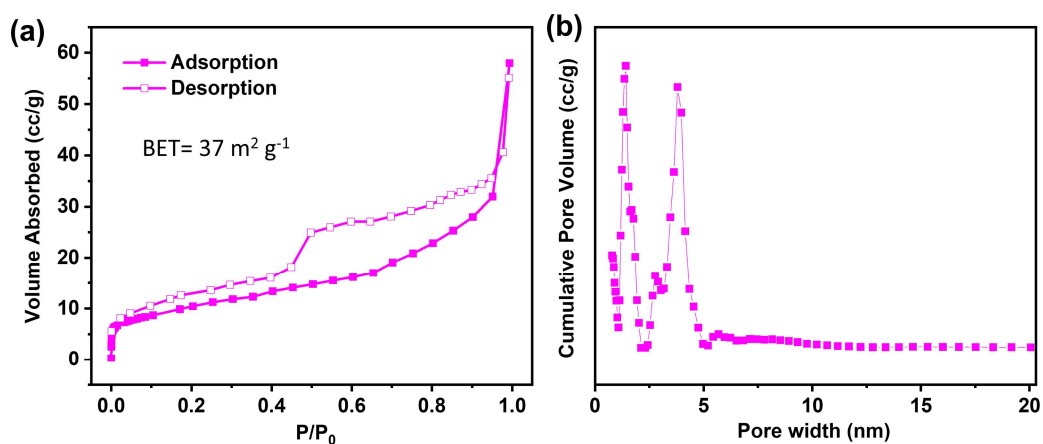
Figure 4.27 (a) N_2 sorption isotherm of mixed Ni-N-C at 77 K and (b) the corresponding pore size distribution profile based on NLDFT model.
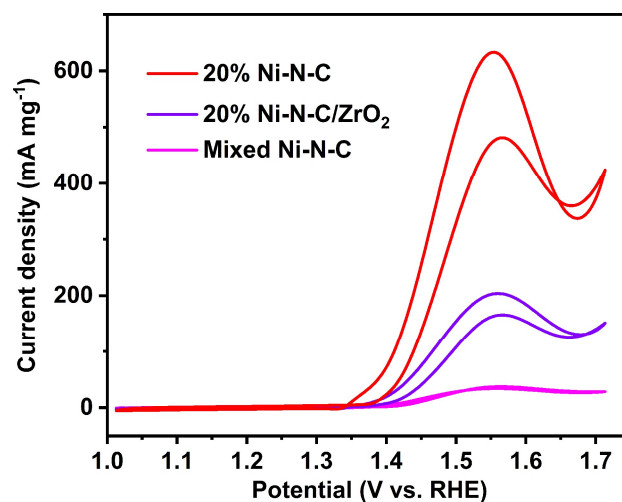
Figure 4.28 PXRD pattern of mixed Ni-N-C and the corresponding standard JCPDS card of Ni.
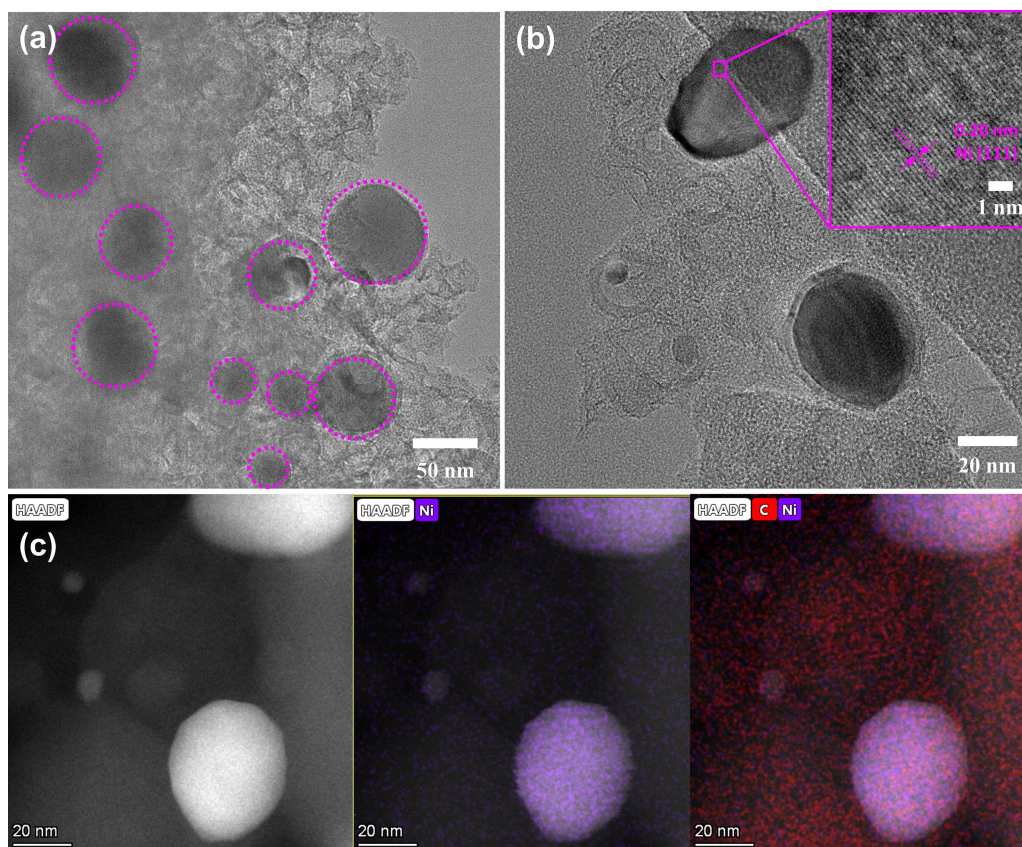
Figure 4.29 (a) TEM image of mixed Ni-N-C, showing the metallic Ni nanoparticles dispersed in the samples. (b) HAADF-STEM image showing the lattice fringe of the aggregated Ni nanoparticles. (c) HAADF-STEM and EDX elemental mapping images of Mix-Ni-N-C, further confirming the formation of aggregated Ni nanoparticles.
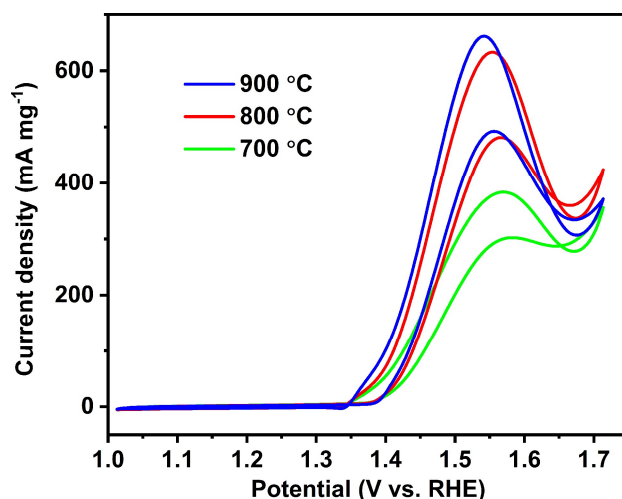
Figure 4.30 CV curves for the MOR on 20% Ni-N-C pyrolyzed at 700 ℃, 800 ℃ and 900 ℃ in 1 M

KOH + 1 M methanol at a scan rate of 50 mV s⁻¹.
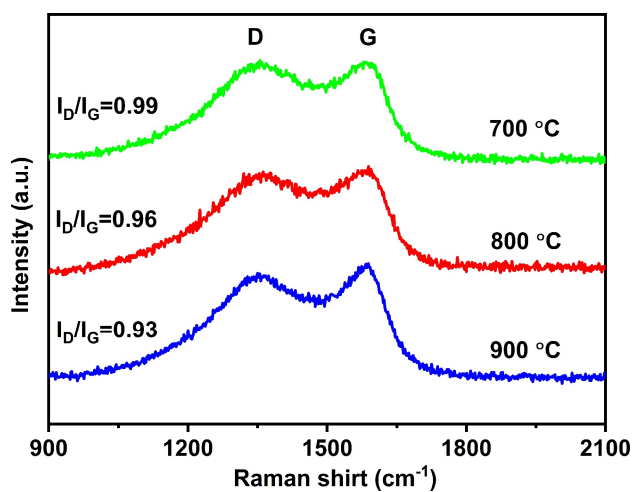
Figure 4.31 Raman spectra of 20% Ni-N-C pyrolyzed at 700 ℃, 800 ℃ and 900 ℃.
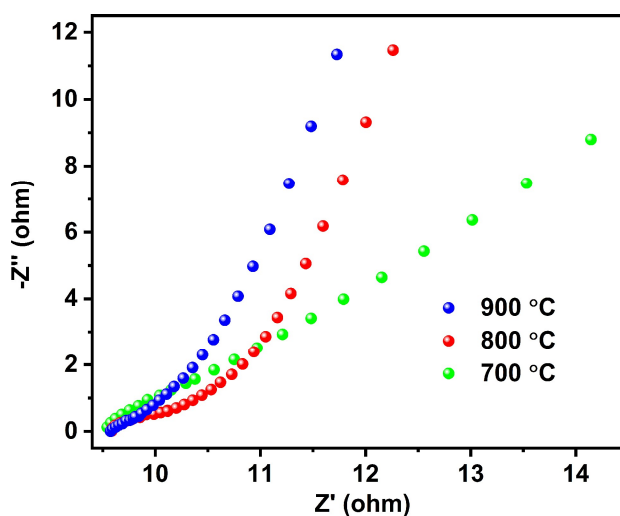
Figure 4.32 plots of 20% Ni-N-C pyrolyzed at 700 ℃, 800 ℃ and 900 ℃ in 1 M KOH + 1 M methanol

electrolyte.
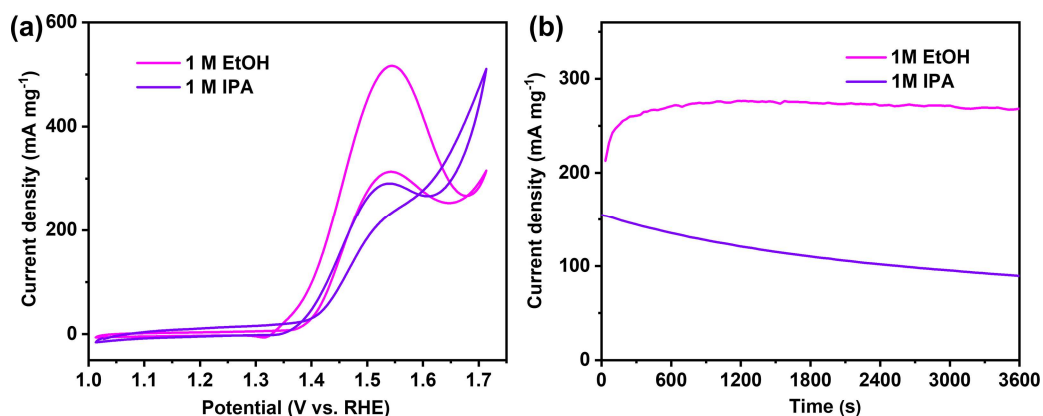
Figure 4.33 (a) CV curves of oxidation of other different alcohols on 20% Ni-N-C in 1 M KOH + 1 M alcohol (ethanol and isopropanol, respectively) at a scan rate of 50 mV s^{-1}. (b) Chronoamperometric plots of oxidation of ethanol and isopropanol on 20% Ni-N-C at 1.46 V *vs.* RHE in 1 M KOH + 1 M alcohol electrolyte.

The electrocatalytic stability of 20% Ni-N-C is evaluated by chronoamperometry performing at 1.46 V *versus* RHE in 1M KOH solution containing 1M methanol for 25000 seconds (**Figure 4.16f**). A short-time increase of current densities is observed on all catalysts in the early stage, possibly due to the activation of Ni active sites.[27] After long-term stability, 20% Ni-N-C achieves nearly 90.0% retention of its initial current response, as 286 mA mg^{-1}, higher than that of 71.1% on 40% Ni-N-C (148 mA mg^{-1}) and 67.0% on 100% Ni-N-C (190 mA mg^{-1}), indicating a more superior durability and activity.

The enhanced stability of 20% Ni-N-C is likely attributed to Ni-N$_4$ moieties with strong covalent effect between Ni and surrounding N atoms, thus a stabilization of Ni centres.[12c, 14b] EDX elemental mapping images of 20% Ni-N-C exhibit the existence and homogeneous distribution of Ni after MOR electrocatalysis (**Figure 4.34**). Moreover, the HAADF-STEM images and PXRD further confirm the single Ni atom state in the catalyst without leaching and aggregation after MOR, almost same to the pristine one (**Figures 4.35-4.37** and **4.1f**). XANES and EXAFS are also performed to probe possible changes in the chemical states of Ni and its coordination structure. As shown in **Figure 4.38**, XANES and EXAFS spectra of 20% Ni-N-C present almost same features after MOR, indicating negligible changes in the properties of the single-atom Ni sites. With these evaluations, the remarkable MOR stability of 20% Ni-N-C stands out.
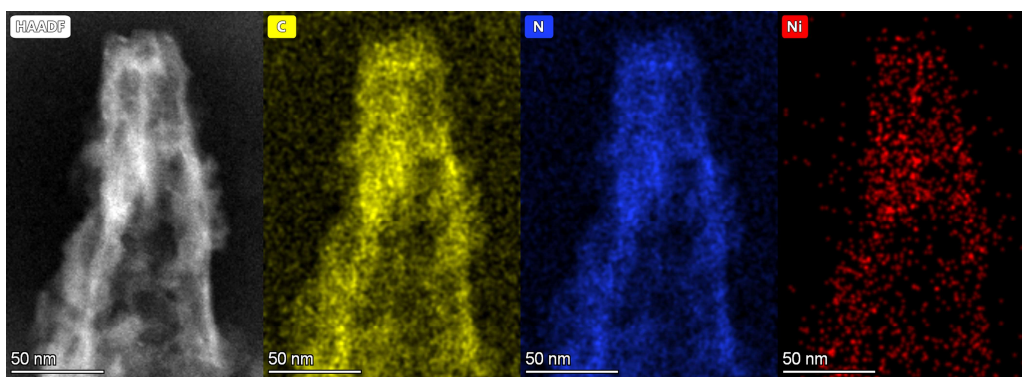
Figure 4.34 HAADF-STEM and EDX elemental mapping images of carbon (yellow), nitrogen (blue) and nickel (red) of 20% Ni-N-C after MOR electrocatalysis.
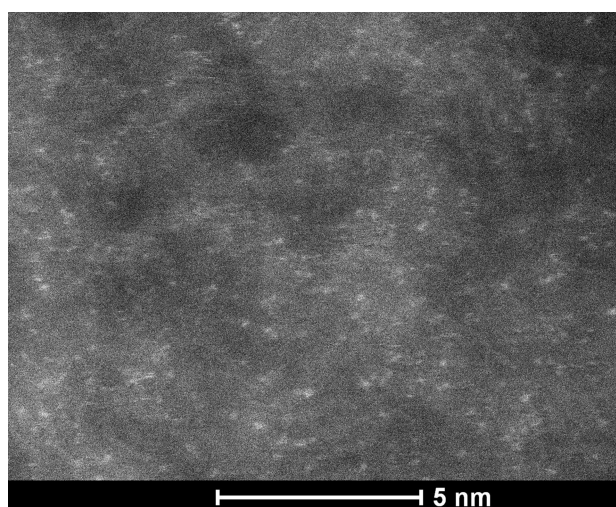
Figure 4.35 HAADF-STEM image of 20% Ni-N-C after MOR electrocatalysis.
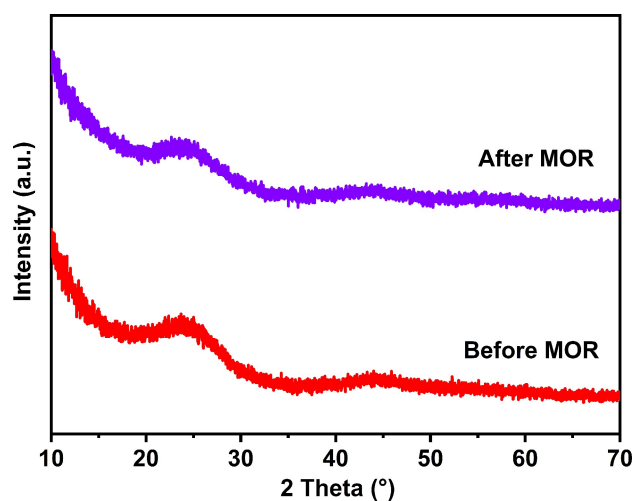
Figure 4.36 PXRD patterns of the 20% Ni-N-C before and after MOR electrocatalysis.
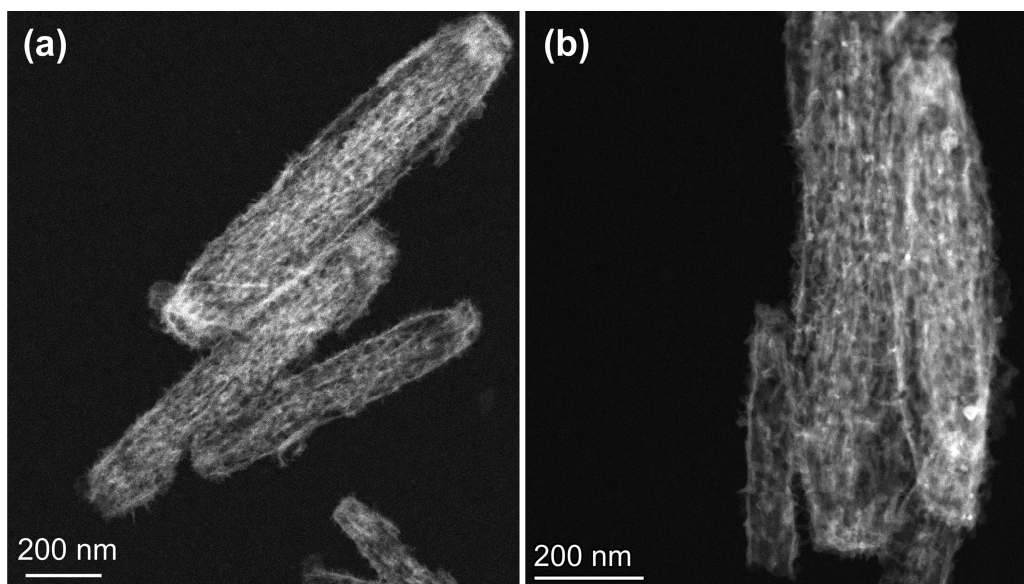
Figure 4.37 HAADF-STEM images of 20% Ni-N-C before and after MOR electrocatalysis.
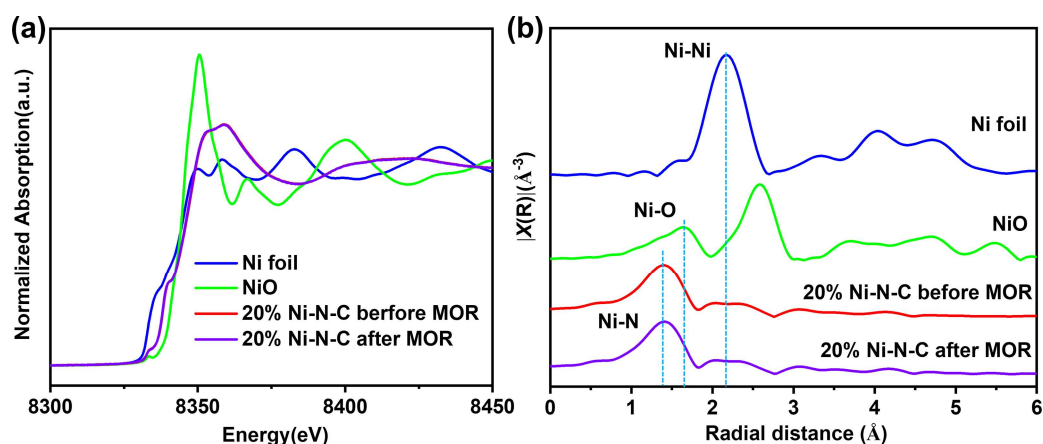
Figure 4.38 (a) Ni K-edge XANES and (b) FT-EXAFS of 20% Ni-N-C before and after MOR electrocatalysis, and of Ni metal and NiO as references.

The overall MOR performance of the proposed 20% Ni-N-C is rationally compared with other hitherto reported state-of-the-art electrocatalysts, including Ni-based and other non-noble metal catalysts under similar testing conditions (**Table S17** in Chapter 5). Notably**,** 20% Ni-N-C features a superior performance to these electrocatalysts in terms of some critical criteria, *i.e.* high current density, long-time durability, low onset and oxidation peak potentials. The remarkable performance of 20% Ni-N-C can be correlated to the synergy of its large surface area, hierarchical porosity, rapid charge transfer and mass transfer, high density of the accessible single Ni active sites and stable Ni-N$_4$ moieties.
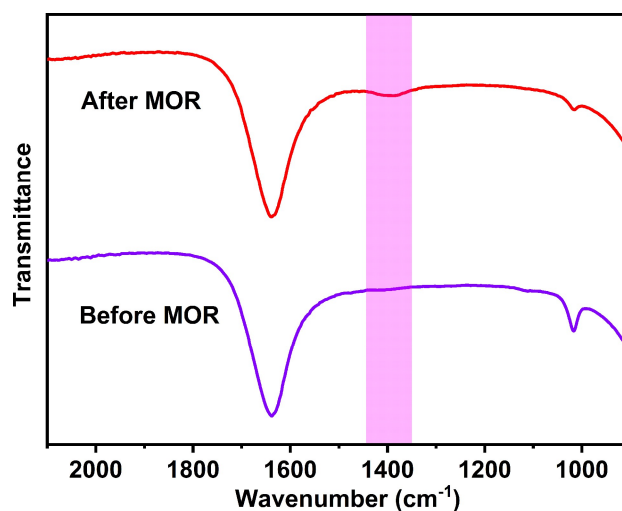
Figure 4.39 (a). ATR-IR spectra of the electrolyte before and after MOR electrocatalysis. As shown in the figure, the electrolyte spectrum before MOR electrocatalysis only presents two characteristic peaks of methanol at around 1014 cm^{-1} and 1638 cm^{-1} while a new peak appears at *ca.* 1400 cm^{-1} assigned to CO_3^{2-} after the MOR electrocatalysis. [28] This confirms the eventual formation of CO_2 in KOH solution, after MOR.
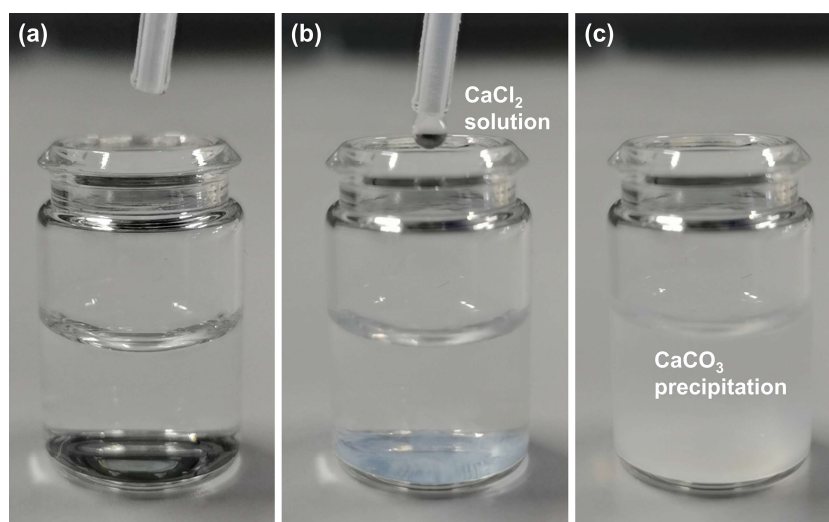
Figure 4.40 (a) The electrolyte after MOR electrocatalysis. Pictures (b) and (c) show the formation of $CaCO_3$ after the addition of $CaCl_2$ solution, which indicates the existence of CO_3^{2-} after MOR electrocatalysis. This observation, in turn, proves the eventual formation of CO_2 in KOH solution after MOR.

After MOR process on 20% Ni-N-C, the methanol is eventually converted into CO_2 products, evidenced by the formation of CO_3^{2-} in KOH solution (**Figures 4.39** and **4.40**). To gain an in-depth understanding of the catalytic behaviour and remarkable activity of 20% Ni-N-C on methanol oxidation to CO_2 process, density functional theory (DFT) calculation is performed. Based on our calculated energy landscape, an optimized MOR pathway of $CH_3OH^* \rightarrow CH_2OH^* \rightarrow CH_2O^* \rightarrow CHO^*$

→ CO* → COOH* → CO₂* on 20% Ni-N-C is proposed (* represents adsorbed intermediates; **Figures 4.41 and 4.42, Table S18** and **S19** in Chapter 5). Among all the elementary reaction steps, the first dehydrogenation step of $CH_3OH^* \rightarrow CH_2OH^*$ shows a relatively higher energy barrier (1.19 eV) than the other subsequent steps. This verifies the dehydrogenation to be the rate-determining step (RDS). However, after comparing against all the previously reported MOR electrocatalysts, the Gibbs free energy change on 20% Ni-N-C is only found to be low when compared to other previously reported MOR electrocatalysts (**Table S20** in Chapter 5). This verifies its superior reaction kinetics and benchmark activity. Besides, the CO* intermediate features an adsorption energy of 0.77 eV, significantly lower than the reported Pt catalyst (1.06 eV), thereby suggestive of the mitigation of CO poisoning.[29] This observation also demonstrates the excellent CO tolerance of 20% Ni-N-C, in agreement with the computed results (**Figure 4.43**). The adsorption energy of CO* on 20% Ni-N-C is neither too strong nor too weak; abiding by the Sabatier principle on electrocatalyts design, this aspect contributes to its two-fold excellence: benchmark MOR activity and high durability.[30]
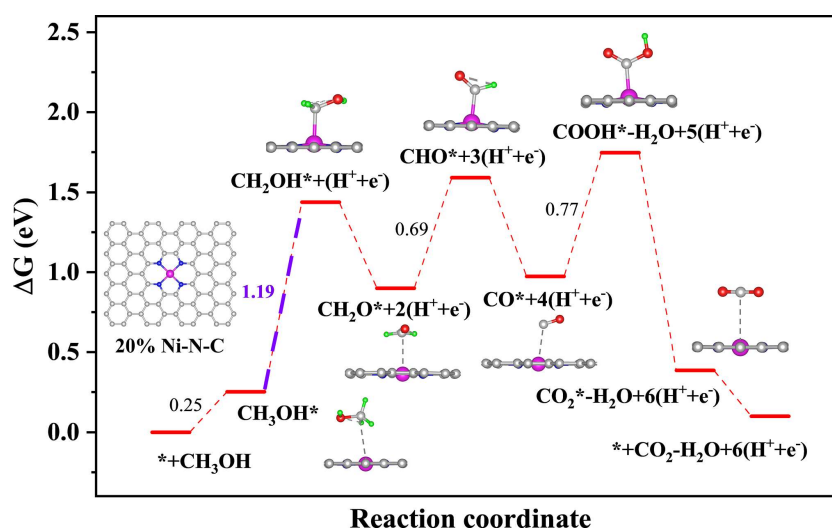
Figure 4.41 Schematic diagram of the MOR pathway and calculated free energy landscape on 20% Ni-N-C. (Insert: model of 20% Ni-N-C and MOR intermediates adsorbed on 20% Ni-N-C. Color codes: Ni pink, N blue, C grey, O red, H green spheres).
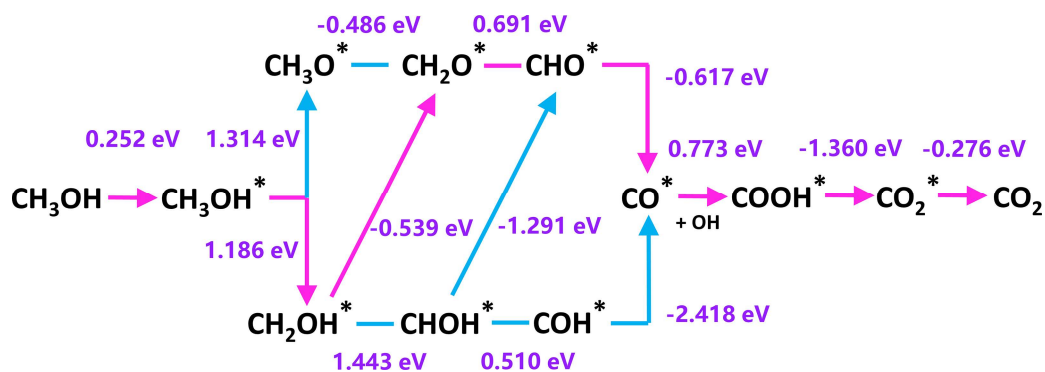
Figure 4.42 The possible MOR pathways on the electrocatalyst surface.[31] In the proposed 20% Ni-N-C with Ni-N$_4$-C$_x$ matrix, the single Ni atoms serve as MOR active sites. After evaluation of all the possibilities, optimized MOR process on 20% Ni-N-C is along the pathway of CH$_3$OH* → CH$_2$OH* → CH$_2$O* → CHO* → CO* → COOH* → CO$_2$* (pink pathway; also in Figure 4.41). Specifically, after the C of methanol molecule absorbed on the Ni site, the C-H bond first breaks instead of the O-H bond under the action of catalyst, and CH$_2$OH* is obtained. The second electron transfer occurs when the O-H bond breaks and another hydrogen atom is desorbed, while the carbon atom remains the adsorption site. In the next two steps, the two C-H bonds break separately, resulting in the CO* intermediate. In alkaline environment, O atom easily adsorbs a hydroxide radical to obtain COOH*. In the sixth step, the O-H bond of COOH breaks and CO$_2$* is obtained. Finally, carbon dioxide is desorbed from Ni atoms in the matrix and the catalytic reaction is completed. The adsorption sites in all processes are C atom adsorbed on Ni atom. In the alkaline media, the overall MOR process on 20% Ni-N-C can be depicted by the equation: CH$_3$OH + 6OH$^-$ - 6e$^-$ → CO$_2$ + 5H$_2$O.
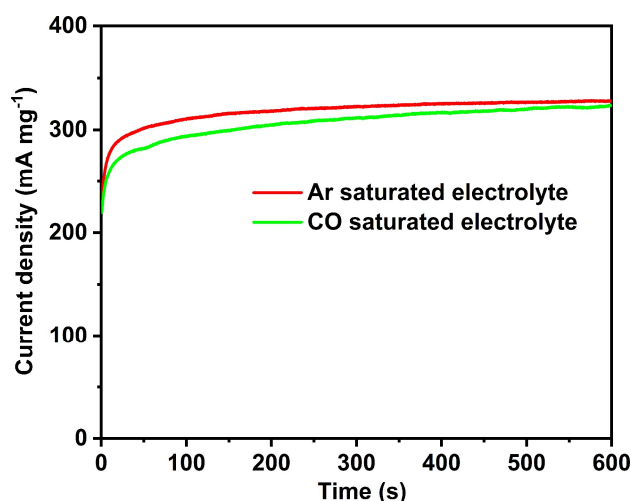
Figure 4.43 Chronoamperometric plots of MOR on 20% Ni-N-C at 1.46 V *vs.* RHE in Ar or CO saturated 1 M KOH + 1 M methanol electrolyte. As shown in the figure, 20% Ni-N-C show a tiny difference of MOR in Ar or CO saturated solution, revealing excellent resistance towards CO poisoning.

4.3 Conclusion

In summary, a simple mixed ligand strategy is leveraged to control spatial intermetallic distances (between the Ni centres) in porphyrinic MOF precursors, culminating in a single-atom catalyst, 20% Ni-N-C. A high loading of 1.69 wt.% of atomically dispersed Ni(II) atoms in the N doped porous carbon matrix brings forth the amalgamation of many features: a) an abundance of single-atom Ni active sites promoting MOR; b) hierarchical porosity (accessible active sites) with highly oriented mesochannels fostering rapid mass transport; c) excellent conductivity boosting fast charge transfer; and d) stable Ni-N$_4$ moieties to glean satisfactory durability. All these features together, enable 20% Ni-N-C to deliver a benchmark performance towards electrochemical methanol oxidation. The demonstration of high MOR activity is two-fold: a low onset potential with superb mass activity, *i.e.*, 634 mA mg^{-1} at 1.55 V *versus* RHE and an impressive durability with superior CO tolerance, substantiated by 90% retention of the initial activity after 25000 s of conducting the MOR test. DFT calculations validate the proposed MOR pathway and explore the corresponding RDS of MOR on 20% Ni-N-C with a lower energy barrier, elucidating its superior MOR activity. In essence, 20% Ni-N-C SACs not only fast-track simple and efficient electrocatalyst preparations, it also delivers excellent MOR performance and versatility in oxidizing other alcohol analogues. Although the high oxidation potential of non-precious-based catalysts still keeps their commercial use elusive in fuel cells, studies to overcome this *Achilles heel* are in progress, and it is only a matter of time that will take these studies to fruition. As a first-of-its-kind in non-precious metal based SACs, this proof-of-concept study paves smarter routes for advancing efficient MOR alternatives. Harnessing modular porphyrinic MOF platforms while adopting the concept of fabricating SACs will essentially allow electrochemists to fine-tune the pore environments, active site configurations, electronic interactions (along the metal-support), opening a new dimension to control the electrocatalytic properties of SACs.

4.4 References

[1]   S. Chu, Y. Cui, N. Liu, *Nat. Mater.* **2016**, *16*, 16-22.

[2]   a) Z. Xia, X. Zhang, H. Sun, S. Wang, G. Sun, *Nano Energy* **2019**, *65*, 104048; b) Y. P. Wu, J. W. Tian, S. Liu, B. Li, J. Zhao, L. F. Ma, D. S. Li, Y. Q. Lan, X. Bu, *Angew. Chem. Int. Ed.* **2019**, *58*, 12185-12189.

[3]   a) Y. Xu, M. Liu, M. Wang, T. Ren, K. Ren, Z. Wang, X. Li, L. Wang, H. Wang, *Appl. Catal. B* **2022**, *300*, 120753; b) J. Hao, J. Liu, D. Wu, M. Chen, Y. Liang, Q. Wang, L. Wang, X.-Z. Fu, J.-L. Luo, *Appl. Catal. B* **2021**, *281*, 119510; cS. Uhm, H. Jeon, T. J. Kim, J. Lee, *J. Power Sources* **2012**, *198*, 218-222.

[4]   R. Bleischwitz, C. Spataru, S. D. VanDeveer, M. Obersteiner, E. van der Voet, C. Johnson, P. Andrews-Speed, T. Boersma, H. Hoff, D. P. van Vuuren, *Nat. Sustain.* **2018**, *1*, 737-743.

[5]   aN. Kakati, J. Maiti, S. H. Lee, S. H. Jee, B. Viswanathan, Y. S. Yoon, *Chem. Rev.* **2014**, *114*, 12397-12429; bY. Liu, B. Hu, S. Wu, M. Wang, Z. Zhang, B. Cui, L. He, M. Du, *Appl. Catal. B* **2019**, *258*, 117970; cX. Long, P. Yin, T. Lei, K. Wang, Z. Zhan, *Appl. Catal. B* **2020**, *260*, 118187.

[6]   R. M. Abdel Hameed, R. M. El-Sherif, *Appl. Catal. B* **2015**, *162*, 217-226.

[7]   W. Yang, X. Yang, J. Jia, C. Hou, H. Gao, Y. Mao, C. Wang, J. Lin, X. Luo, *Appl. Catal. B* **2019**, *244*, 1096-1102.

[8]   B. Dong, W. Li, X. Huang, Z. Ali, T. Zhang, Z. Yang, Y. Hou, *Nano Energy* **2019**, *55*, 37-41.

[9]   P. Yang, X. Yuan, H. Hu, Y. Liu, H. Zheng, D. Yang, L. Chen, M. Cao, Y. Xu, Y. Min, Y. Li, Q. Zhang, *Adv. Funct. Mater.* **2018**, *28*, 1704774.

[10]   X. Cui, W. Guo, M. Zhou, Y. Yang, Y. Li, P. Xiao, Y. Zhang, X. Zhang, *ACS Appl. Mater. Interfaces* **2015**, *7*, 493-503.

[11]   I. S. Pieta, A. Rathi, P. Pieta, R. Nowakowski, M. Hołdynski, M. Pisarek, A. Kaminska, M. B. Gawande, R. Zboril, *Appl. Catal. B* **2019**, *244*, 272-283.

[12]   aD. M. Koshy, A. T. Landers, D. A. Cullen, A. V. Ievlev, H. M. Meyer, C. Hahn, Z. Bao, T. F. Jaramillo, *Adv. Energy Mater.* **2020**, *10*, 2001836; bD. M. Koshy, S. Chen, D. U. Lee, M. B. Stevens, A. M. Abdellah, S. M. Dull, G. Chen, D. Nordlund, A. Gallo, C. Hahn, *Angew. Chem. Int. Ed.* **2020**, *132*, 4072-4079; cW. Liu, Y. Chen, H. Qi, L. Zhang, W. Yan, X. Liu, X. Yang, S. Miao, W. Wang, C. Liu, A. Wang, J. Li, T. Zhang, *Angew. Chem. Int. Ed.* **2018**, *57*, 7071-7075.

[13] aL. Jiao, G. Wan, R. Zhang, H. Zhou, S. H. Yu, H. L. Jiang, *Angew. Chem. Int. Ed.* **2018**, *57*, 8525-8529; bL. Jiao, W. Yang, G. Wan, R. Zhang, X. Zheng, H. Zhou, S. H. Yu, H. L. Jiang, *Angew. Chem. Int. Ed.* **2020**, *59*, 20589-20595.

[14] aL. Jiao, R. Zhang, G. Wan, W. Yang, X. Wan, H. Zhou, J. Shui, S. H. Yu, H. L. Jiang, *Nat. Commun.* **2020**, *11*, 2831; bQ. Fan, P. Hou, C. Choi, T. S. Wu, S. Hong, F. Li, Y. L. Soo, P. Kang, Y. Jung, Z. Sun, *Adv. Energy Mater.* **2019**, *10*, 1903068.

[15] aP. Kuang, Y. Wang, B. Zhu, F. Xia, C. W. Tung, J. Wu, H. M. Chen, J. Yu, *Adv. Mater.* **2021**, *33*, e2008599; bC. Wang, F. Hu, H. Yang, Y. Zhang, H. Lu, Q. Wang, *Nano Res.* **2016**, *10*, 238-246.

[16] aH. Furukawa, K. E. Cordova, M. O'Keeffe, O. M. Yaghi, *Science* **2013**, *341*, 1230444; bH. C. Zhou, J. R. Long, O. M. Yaghi, *Chem. Rev.* **2012**, *112*, 673-674.

[17] aL. Jiao, H.-L. Jiang, *Chem* **2019**, *5*, 786-804; bH. Huang, K. Shen, F. Chen, Y. Li, *ACS Catal.* **2020**, *10*, 6579-6586.

[18] D. Feng, Z. Y. Gu, J. R. Li, H. L. Jiang, Z. Wei, H. C. Zhou, *Angew. Chem. Int. Ed.* **2012**, *51*, 10307-10310.

[19] aZ. Zhou, S. Mukherjee, S. Hou, W. Li, M. Elsner, R. A. Fischer, *Angew. Chem. Int. Ed.* **2021**, *60*, 20551-20557; bZ. Zhou, S. Mukherjee, J. Warnan, W. Li, S. Wannapaiboon, S. Hou, K. Rodewald, B. Rieger, P. G. Weidler, C. Wöll, R. A. Fischer, *J. Mater. Chem. A* **2020**, *8*, 25941-25950.

[20] K. S. Walton, R. Q. Snurr, *J. Am. Chem. Soc.* **2007**, *129*, 8552-8556.

[21] J.-T. Han, Z.-H. Xue, K. Zhang, H.-H. Wang, X.-H. Li, J.-S. Chen, *ACS Catal.* **2020**, *10*, 12569-12574.

[22] J. Li, Z. Luo, Y. Zuo, J. Liu, T. Zhang, P. Tang, J. Arbiol, J. Llorca, A. Cabot, *Appl. Catal. B* **2018**, *234*, 10-18.

[23] D. Wu, W. Zhang, D. Cheng, *ACS Appl. Mater. Interfaces* **2017**, *9*, 19843-19851.

[24] A. A. Dubale, Y. Zheng, H. Wang, R. Hubner, Y. Li, J. Yang, J. Zhang, N. K. Sethi, L. He, Z. Zheng, W. Liu, *Angew. Chem. Int. Ed.* **2020**, *59*, 13891-13899.

[25] X. Cui, P. Xiao, J. Wang, M. Zhou, W. Guo, Y. Yang, Y. He, Z. Wang, Y. Yang, Y. Zhang, Z. Lin, *Angew. Chem. Int. Ed.* **2017**, *56*, 4488-4493.

[26] S. Rezaee, S. Shahrokhian, *Appl. Catal. B* **2019**, *244*, 802-813.

[27] Y. An, H. Ijaz, M. Huang, J. Qu, S. Hu, *Dalton Trans.* **2020**, *49*, 1646-1651.

[28] X. Wang, S. Xi, W. S. V. Lee, P. Huang, P. Cui, L. Zhao, W. Hao, X. Zhao, Z. Wang, H. Wu, H. Wang, C. Diao, A. Borgna, Y. Du, Z. G. Yu, S. Pennycook, J. Xue, *Nat. Commun.* **2020**, *11*, 4647.

[29] L. Xiong, Z. Sun, X. Zhang, L. Zhao, P. Huang, X. Chen, H. Jin, H. Sun, Y. Lian, Z. Deng, M. H. Rummerli, W. Yin, D. Zhang, S. Wang, Y. Peng, *Nat. Commun.* **2019**, *10*, 3782.

[30] P. Sabatier, *La catalyse en chimie organique*, **1920**.

[31] a) T. Sheng, X. Lin, Z. Y. Chen, P. Hu, S. G. Sun, Y. Q. Chu, C. A. Ma, W. F. Lin, *Phys. Chem. Chem. Phys.* **2015**, *17*, 25235-25243; b) G. You, J. Jiang, M. Li, L. Li, D. Tang, J. Zhang, X. C. Zeng, R. He, *ACS Catal.* **2017**, *8*, 132-143.

Chapter 5

Experimental and analytical Details

5.1 General characterization methods

5.1.1 X-ray diffraction measurement

Powder X-ray diffraction (PXRD) of the obtained bulk MOF were collected on the X' Pert PANalytical instrument in Bragg-Brentano geometry (Cu Ka radiation, 2thera 2-25°, scan step size of 0.01°, voltage and intensity were 45 kV and 40 mA, respectively);

Grazing incidence XRD (GIXRD) measurements on MOF thin films were conducted on PANalytical Empyrean instrument with grazing incidence mode at room temperature, Cu-Ka radiation, λ = 1.54178 Å, a range of 2thera 5-25° for Zn_2(ZnTCPP) and 2-15° for 3D PP-MOF, a step of 0.01313°, an accumulation time of 1.5 s per step);

In-plane XRD patterns of Zn_2(ZnTCPP) thin films were measured with a Bruker D8 Discover with Cu $K_{\alpha1,2}$ radiation with an in-plane geometry, over a 2θ range ~ 5 to 23° using a scan-time of 2 seconds per 0.025°.

5.1.2 Scanning electron microscopy analysis

Scanning electron microscopy (SEM) images were taken by using an environmental scanning electron microscope (JEOL JSM-7500F field emission) in order to investigate the surface morphology and surface coverage of the MOF powders and MOF films (top and cross-sectional view).

5.1.3 Transmission electron microscopy analysis

Transmission electron microscopy (TEM), high-angle annular dark-field scanning TEM (HAADF-STEM) and energy-dispersive X-ray spectrometry (EDX) analysis were recorded at 300 kV with a probe-corrected FEI Titan Themis equipped with a Super-X spectrometer for energy dispersive X-ray analysis.

5.1.4 Attenuated total reflectance infrared spectroscopy

Attenuated total reflectance infrared (ATR-IR) spectra of samples were performed using a PerkinElmer instrument with an ATR sampling accessory.

5.1.5 Ultraviolet-visible spectroscopy

Ultraviolet–visible spectroscopy (UV-Vis) measurements were carried out on a UV-visible spectrophotometer (PerkinElmer Lambda 650 S UV/VIS spectrometer) with a slit of 2.0 nm, data interval 1.0 nm, the scan speed of 600.00 nm/min, and a scan range of 800.00 nm to 350.00 nm. For the measurements of digested MOF films, a small piece of the MOF thin film was dissolved in 1.0 M NaOH aqueous solution. The obtained solution was then added into a quartz cell (1.0 cm) for UV-visible measurement.

5.1.6 Methanol sorption isotherm

Methanol sorption was carried out at a controlled temperature of 25 °C on an environmental-controlled quartz crystal microbalance (BELQCM-4 instrument, BEL Japan). Prior to sorption test, the PP-MOFs films were activated by soaking them in pure CH_2Cl_2 for 24 hours at room temperature and subsequently dried in a pure N_2 stream. Additionally, the samples were placed into the BEL-QCM instrument cells and in situ heated at 50 °C under a He stream (99.999%, 100 sccm) for two hours. After the activation process, the QCM frequency was recorded when the frequency change was stable within ±5 Hz over 30 min. Afterwards, methanol sorption isotherms were collected by varying the relative vapor pressure (P/P$_0$) of the saturated vapor of probe molecules in a He gas stream at 25 °C ranging from 0.0 to 95.0 %. The mass of the PP-MOFs films and adsorption amounts were calculated from the difference of the read QCM frequency and the fundamental frequency of the bare QCM substrate according to Sauerbrey's equation.

5.1.7 X-ray photoelectron spectroscopy

X-ray photoelectron spectroscopy (XPS) data were recorded at room temperature by a JPS-9200 photoelectron spectrometer (JEOL, Japan) under a vacuum of 3×10^{-7} Torr. The X-ray beam was generated with a monochromatic Al Kα X-ray source (*hv* = 1486.7 eV; 12 kV and 20 mA) and the high-resolution spectra were obtained by an analyzer pass energy of 10 eV. The resulting data were analysed via a commercially available XPSPEAK software after correcting binding energies based on the carbon peak at 284.8 eV.

5.1.8 X-ray adsorption spectroscopy

X-ray adsorption spectroscopy (XAS) measurements were performed on at the

P65 beamline of the German electron synchrotron (DESY) in Hamburg, Germany. The PETRA III storage ring was operated at 6 GeV energy and 100 mA beam-current in top-up mode. A water-cooled Si (111) double crystal monochromator (DCM) was used for obtaining monochromatic X-rays. Two Si mirrors were installed in front of the DCM to reject higher harmonics. The XAS spectra were measured in both transmission mode using ionization chambers and in fluorescence mode using a passivated implanted planar silicon (PIPS) detector. The spot-size of X-ray beam at the sample was 1.6 mm (horizontal) × 200 μm (vertical). Spectra for both X-ray absorption near edge structure (XANES) analyses and extended X-ray absorption fine structure (EXAFS) analyses were measured in continuous scanning mode. XANES and EXAFS data analyses were performed using Athena and Artemis software packages.

5.1.9 Nuclear magnetic resonance (NMR)

Nuclear magnetic resonance (NMR) spectra of TPPCOOMe and M-TCPP in Chapters 2-3 were measured on the Bruker AV400 spectrometer in 300 MHz at room temperature. ^{1}H NMR spectra of TPPCOOMe and M-TCPP were referenced to the signals of $CDCl_3$ and DMSO-d_6, respectively.

5.1.10 N$_2$ adsorption-desorption isotherms

N$_2$ adsorption-desorption isotherms were measured on Autosorb IQ (Quantachrome) at 77 K. The Brunauer– Emmett–Teller (BET) method was utilised to calculate the specific surface area and the pore size distributions were estimated by using the density functional theory (DFT) simulation from the N$_2$ sorption curves. The samples were dried at 120 ℃ under vacuum before the measurement.

5.1.11 Raman spectroscopy

Raman spectra were collected using a Renishaw Raman Microscope spectrometer with an Ar$^+$ laser of 532 nm under room temperature.

5.1.12 Inductively coupled plasma optical emission spectrometry

Inductively coupled plasma optical emission spectrometry (ICP-OES) was using to determine the content of Ni in prepared Ni-N-C samples (Chapter 4) on ICP-OES

(700 Series ICP-OES by Agilent Technologies).

5.1.13 Surface profiles

Surface profiles of the PP-MOF films were characterised using a profilometer (DektakXT, BRUKER, Germany) with a diamond stylus in order to investigate their surface roughness.

Characterization contributions: Data of PXRD, GIXRD, ATR-IR, UV-Vis, methanol sorption, NMR, N_2 adsorption-desorption isotherms were collected and analyzed by Zhenyu Zhou. Data of in-plane XRD were collected by Dr. Peter G. Weidler and Prof. Dr. Christof Wöll, analyzed together by Dr. Peter G. Weidler, Prof. Dr. Christof Wöll and Zhenyu Zhou; Data of SEM were collected by Katia Rodewald, Prof. Dr. Bernhard Rieger and Zhenyu Zhou, and analyzed by Zhenyu Zhou. Data of TEM were collected by Dr. Markus Döblinger, Dr. Ondřej Tomanec and Prof. Dr. Michal Otyepka, and analyzed by Zhenyu Zhou. Data of XPS were collected by Dr. Christian Jandl and analyzed by Zhenyu Zhou. Data of XAS were collected and analyzed by Dr. Rachit Khare. Data of Raman were collected by Mr. Shujin Hou and analyzed by Zhenyu Zhou. Data of ICP were collected by Mr. Max Koch and analyzed by Zhenyu Zhou. Data of surface profiles were collected and analyzed by Zhenyu Zhou with the help of Ms. Shanshan Yin and Prof. Dr. Peter Müller Buschbaum.

5.2 Chemicals and materials

All reagents and solvents were purchased from commercial sources and used without further purification unless otherwise stated: Mangnese(II) chloride tetrahydrate (MnCl₂·4H₂O ， 99%), anthraquinone-2,6-disulfonate (≥ 98.0%), catechol (≥99.0%) were purchased from abcr; zinc nitrate hexahydrate (≥99%)，zinc acetate dihydrate (98%), copper(II) chloride dihydrate (99%) were purchased from Acros; zirconium(IV) oxychloride octahydrate (ZrOCl₂·8H₂O, ≥ 99.5%), methacrylic acid (99%), acetic acid (reagent grade, ≥99.5%), benzoic acid (reagent grade, ≥ 99.5%), methanol (anhydrous, 99.8%), Methyl 4-formylbenzoate (≥ 96.0%), 4-nitrophenol (≥ 99.0%), ascorbic acid (≥ 99.0%), 1,3-dinitrobenzene (anhydrous, 97%), potassium dichromate (ACS grade, ≥ 99.0%), 1,4-

benzoquinone ($\geqslant$ 99.0%), 4-nitrobenzaldehyde($\geqslant$ 99.0%) were purchased from Sigma Aldrich; meso-tetra(4-carboxyphenyl)porphine (H$_2$TCPP, TCI); N,N-dimethylformamide (DMF; spectrophotometric grade, VWR); ethanol(absolute, Th. Geyer); zirconium(IV) n-propoxide (70% w/v in n-propanol, Alfa Aesar); uric acid (99%, Alfa Aesar); gold substrate (Angstrom Engineering); silicon substrate (Siegert Wafer); ITO glass(Adrafruit). Some other commercial chemicals are also available from Acros Organics, Sigma-Aldrich, Alfa Aesar, abcr and TCI, and used without any purification.

5.3 Experimental details of Chapter 2

Experiment contributions: Zhenyu Zhou designed and prepared all the porphyrinic MOF films, performed the experiments. Dr. Soumya Mukherjee helped in simulated structure of Zn$_2$(ZnTCPP) films. Prof. Dr. Roland A. Fischer and Dr. Weijin Li supervised the project.

5.3.1 Ligand synthesis

The tetrakis(4-carboxyphenyl)porphyrin (H$_2$TCPP) ligand was purchased from TCI. Copper-involved TCPP (Cu-TCPP) ligand was synthesized based on previous reports.[1] Typically, we obtained it by three steps as follows:

1) 5,10,15,20-Tetrakis(4-methoxycarbonylphenyl)porphyrin (TPPCOOMe).

To refluxed propionic acid (100 mL) in a 500-mL three necked flask were added pyrrole (3.0, 0.043 mol) and methyl p-formylbenzoate (6.9 g, 0.042 mol), and the solution was refluxed for 12h in darkness. After the reaction mixture was cooled to room temperature, crystals were collected by suction-filtration to afford purple crystals (1.4g). 1 H NMR (300 MHz, CDCl$_3$): δ 8.81 (s, 8H), 8.43 (d, 8H), 8.28 (d, 8H), 4.11 (s, 12H), -2.83 (s, 2H).

2)   [5,10,15,20-Tetrakis(4-methoxycarbonylphenyl)porphyrinato]-Cu(II) (CuTPPCOOMe).

A solution of TPPCOOMe 0.854 g (1.0 mmol) and CuCl$_2$·2H$_2$O (2.2g, 12.8 mmol) in 100 mL of DMF was refluxed for 6 h. After the mixture was cooled to room temperature, 150 mL of H$_2$O was added. The resultant precipitate was filtered and washed with 50 mL of H$_2$O for two times. The obtained solid was dissolved in

$CHCl_3$, followed by washing three times with water. The organic layer was dried over anhydrous magnesium sulfate and evaporated to afford quantitative dark red crystals.

3) [5,10,15,20-Tetrakis(4-carboxyphenyl)porphyrinato]-Cu(II) (Cu-TCPP).

The obtained ester (0.75 g) was stirred in THF (25 mL) and MeOH (25 mL) mixed solvent, to which a solution of KOH (2.63 g, 46.95 mmol) in H_2O (25 mL) was introduced. This mixture was refluxed for 12 h. After cooling down to room temperature, THF and MeOH were evaporated. Additional water was added to the resulting water phase and the mixture was heated until the solid was fully dissolved, then the solution was acidified with 1M HCl until no further precipitate was detected. The product was collected by filtration, washed with water and dried in vacuum. 1 H NMR (300 MHz, DMSO-d_6): δ 8.80 (s, 8H), 8.37 (d, 8H), 8.28 (d, 8H).

5.3.2 Synthesis of $Zr_6O_4(OH)_4(OMc)_{12}$

$Zr_6O_4(OH)_4(OMc)_{12}$ (Hexazirconium-tetraoxy-tetrahydroxy-dodecamethacrylate) is known as a precursor to the metal secondary building unit (SBU) of zirconium-based PP-MOFs. The compound was synthesized according to the adapted procedure from Kickelbick and Schubert. In a large Schlenk flask, 1 mL of 70% w/v $Zr(OPr)_4$ (3.1 mmol) in n-propanol was mixed at room temperature with 1 mL of methacrylic acid (McOH; 11.8 mmol, 5.3 equiv) under inert gas atmosphere (Ar). After 2 weeks, the colorless crystals were collected by filtration and washing with small quantities of n-propanol. The product was dried in vacuum for 12 h and yielded the desired sample.

5.3.3 Substrates pretreatment

Au substrates (1 cm x 1 cm), Au-coated QCM substrates (AT cut type, Au electrode, diameter 14 mm, thickness 0.3 mm, and fundamental frequency ca. 4.95 MHz) were cleaned by soaking them in the mixed solution of water/H_2O_2/ammonia with a ratio of 5/1/1 at 75 °C for 15 min. Afterwards, the substrates were functionalised by immersing them into a solution of 16-mercaptohexadecanoic acid (MHDA, 20 μM) in ethanol with acetic acid (5% v/v) or in a solution of 1-mercaptoundecanol (MUD, 20 μM) in ethanol for at least 24 h at room temperature in order to obtain the –COOH or –OH terminated surface via self-assembled

monolayers formation (SAM) and subsequently rinsed with pure ethanol and dried with N_2 before the use.

The silicon-wafers (1 cm x 1 cm), ITO glass substrates (1 cm x 1 cm) were cleaned in ethanol for about 10 min in an ultrasonic bath, and then activated under UV light for 60 min in order to in order to clean and generate a surface with hydroxyl groups. The substrates were used immediately for the growth of PP-MOFs films after UV light treatment.

5.3.4 Synthesis of 2D PP-MOF films

Zn_2(ZnTCPP) film growth via VAC. For the film growth using VAC, a 20 mL glass vial with a cap equipped was used. A Raschig-ring was placed on the bottom of the vial to offer an elevated flat platform for the substrate. $Zn(NO_3)_2 \cdot 6H_2O$ (4.5 mg, 0.015 mmol), TCPP (4 mg, 0.005 mmol), acetic acid (10 µL, 1M in DMF solution) and pyrazine (0.8 mg, 0.01 mmol) were dissolved in a mixed solution DMF (1.5 mL) and ethanol (0.5 mL) as the precursor solution. A mixture of 1mL DMF/ethanol (v/v, 3/1) and 5 µL acetic acid was filled into the vial as vapour source. Afterwards, the pre-treated Au/Silicon/ITO substrates (1 cm x 1 cm) was placed on top of the Raschig-ring and fully coated with 40 µL freshly prepared MOF precursor solution. The vial was closed and was transferred into a preheated 80 °C oven where it was kept for the specified time (details in table S1). Afterwards the vial was removed from the oven and allowed to cool down for 10 min before the Zn_2(ZnTCPP) film was removed. The film was immersed in fresh DMF and ethanol several times and then dried under vacuum.

The Zn_2(ZnTCPP) film grew without acetic acid in precursor solution and vapour source also conducted in same procedure only without acetic acid in precursor solution and vapour source.

Table S1. List of atomic coordinates for the simulated structure of $Zn_2(ZnTCPP)$ films.

Atoms	x	y	z	Atoms	x	y	z
Zn1	0	0	0	C7	-0.0653	0.1694	0
Zn2	0.5	0.5	0.2929	C8	-0.0404	0.2517	0
O1	0.41519	0.41519	0.22326	H8	-0.0736	0.2965	0
N1	0.1205	0	0	N1	0	-0.1205	0
C1	0.39255	0.39255	0	C7	0.0653	-0.1694	0
C2	0.3271	0.3271	0	C8	0.0404	-0.2517	0
C3	0.29735	0.29735	0.2334	H8	0.0736	-0.2965	0
H1	0.3169	0.3169	0.39482	O1	-0.41519	-0.41519	-0.22326
C4	0.2387	0.2387	0.23537	C1	-0.39255	-0.39255	0
H2	0.21935	0.21935	0.39718	C2	-0.3271	-0.3271	0
C5	0.2089	0.2089	0	C3	-0.29735	-0.29735	-0.2334
C6	0.14505	0.14505	0	H1	-0.3169	-0.3169	-0.39482
C7	0.1694	0.0653	0	C4	-0.2387	-0.2387	-0.23537
C8	0.2517	0.0404	0	H2	-0.21935	-0.21935	-0.39718
H8	0.2965	0.0736	0	C5	-0.2089	-0.2089	0
O1	0.41519	-0.41519	-0.22326	C6	-0.14505	-0.14505	0
C1	0.39255	-0.39255	0	C7	-0.0653	-0.1694	0
C2	0.3271	-0.3271	0	C8	-0.0404	-0.2517	0
C3	0.29735	-0.29735	-0.2334	H8	-0.0736	-0.2965	0
H1	0.3169	-0.3169	-0.39482	O1	-0.41519	0.41519	-0.22326
C4	0.2387	-0.2387	-0.23537	C3	-0.29735	0.29735	-0.2334
H2	0.21935	-0.21935	-0.39718	H1	-0.3169	0.3169	-0.39482
C5	0.2089	-0.2089	0	C4	-0.2387	0.2387	-0.23537
C6	0.14505	-0.14505	0	H2	-0.21935	0.21935	-0.39718
C7	0.1694	-0.0653	0	O1	-0.41519	-0.41519	0.22326
C8	0.2517	-0.0404	0	C3	-0.29735	-0.29735	0.2334
H8	0.2965	-0.0736	0	H1	-0.3169	-0.3169	0.39482

O1	0.41519	0.41519	-0.22326	C4	-0.2387	-0.2387	0.23537
N1	0	0.1205	0	H2	-0.21935	-0.21935	0.39718
C3	0.29735	0.29735	-0.2334	N1	-0.1205	0	0
H1	0.3169	0.3169	-0.39482	C7	-0.1694	-0.0653	0
C4	0.2387	0.2387	-0.23537	C8	-0.2517	-0.0404	0
H2	0.21935	0.21935	-0.39718	H8	-0.2965	-0.0736	0
C7	0.0653	0.1694	0	C7	-0.1694	0.0653	0
C8	0.0404	0.2517	0	C8	-0.2517	0.0404	0
H8	0.0736	0.2965	0	H8	-0.2965	0.0736	0
O1	0.41519	-0.41519	0.22326	Zn2	0.5	0.5	-0.2929
C3	0.29735	-0.29735	0.2334	Zn2	-0.5	-0.5	0.2929
H1	0.3169	-0.3169	0.39482	Zn2	-0.5	0.5	0.2929
C4	0.2387	-0.2387	0.23537	Zn2	0.5	-0.5	0.2929
H2	0.21935	-0.21935	0.39718	Zn2	-0.5	-0.5	-0.2929
O1	-0.41519	0.41519	0.22326	Zn2	-0.5	0.5	-0.2929
C1	-0.39255	0.39255	0	Zn2	0.5	-0.5	-0.2929
C2	-0.3271	0.3271	0	O1	0.58481	0.41519	0.22326
C3	-0.29735	0.29735	0.2334	O1	0.58481	0.58481	0.22326
H1	-0.3169	0.3169	0.39482	O1	0.41519	0.58481	0.22326
C4	-0.2387	0.2387	0.23537	O1	0.41519	0.58481	-0.22326
H2	-0.21935	0.21935	0.39718	O1	0.58481	0.41519	-0.22326
C5	-0.2089	0.2089	0	O1	0.58481	0.58481	-0.22326
C6	-0.14505	0.14505	0				

Table S2. Recipes for the fabrication of $Zn_2(ZnTCPP)$ films by VAC.

	EXP.	Precursor solution						Droplet volume	Substrate	Temper-ature	Reaction time	Vapour source		
		$Zn(NO_3)_2 \cdot 6H_2O$	TCPP	pyrazine	acetic acid (1M in DMF)	DMF	EtOH					DMF	EtOH	Acetic acid

Variation of modulator conentration	1	4.5 mg 7.5 mmol/L	4.0 mg 2.5 mmol/L	0.8 mg 5 mmol/L	0 μl 0 mmol/L	1.5 mL	0.5 mL	30 μL	-COOH SAM gold	80 °C	3 h	1 mL	0 mL	0 μL
	2	4.5 mg 7.5 mmol/L	4.0 mg 2.5 mmol/L	0.8 mg 5 mmol/L	10 μl 5 mmol/L	1.5 mL	0.5 mL	30 μL	-COOH SAM gold	80 °C	3 h	1 mL	0 mL	5 μL
Variation of substrate type	3	4.5 mg 7.5 mmol/L	4.0 mg 2.5 mmol/L	0.8 mg 5 mmol/L	10 μl 5 mmol/L	1.5 mL	0.5 mL	30 μL	Blank gold	80 °C	3 h	1 mL	0 mL	5 μL
	4	4.5 mg 7.5 mmol/L	4.0 mg 2.5 mmol/L	0.8 mg 5 mmol/L	10 μl 5 mmol/L	1.5 mL	0.5 mL	30 μL	-OH SAM gold	80 °C	3 h	1 mL	0 mL	5 μL
	5	4.5 mg 7.5 mmol/L	4.0 mg 2.5 mmol/L	0.8 mg 5 mmol/L	10 μl 5 mmol/L	1.5 mL	0.5 mL	30 μL	Silicon wafer	80 °C	3 h	1 mL	0 mL	5 μL
	6	4.5 mg 7.5 mmol/L	4.0 mg 2.5 mmol/L	0.8 mg 5 mmol/L	10 μl 5 mmol/L	1.5 mL	0.5 mL	30 μL	ITO glass	80 °C	3 h	1 mL	0 mL	5 μL
	7	4.5 mg 7.5 mmol/L	4.0 mg 2.5 mmol/L	0.8 mg 5 mmol/L	10 μl 5 mmol/L	1.5 mL	0.5 mL	30 μL	-COOH SAM Au QCM	80 °C	3 h	1 mL	0 mL	5 μL
variation of droplet volume	8	4.5 mg 7.5 mmol/L	4.0 mg 2.5 mmol/L	0.8 mg 5 mmol/L	10 μl 5 mmol/L	1.5 mL	0.5 mL	60 μL	-COOH SAM gold	80 °C	3 h	1 mL	0 mL	5 μL
variation of solvent	9	4.5 mg 7.5 mmol/L	4.0 mg 2.5 mmol/L	0.8 mg 5 mmol/L	10 μl 5 mmol/L	0 mL	2.0 mL	30 μL	-COOH SAM gold	80 °C	3 h	0 mL	1 mL	0 μL

Zn₂(ZnTCPP) film growth via solvothermal method. $Zn(NO_3)_2 \cdot 6H_2O$ (4.5 mg, 0.015 mmol), TCPP (4 mg, 0.005 mmol), acetic acid (10 μL, 1M in DMF solution) and pyrazine (0.8 mg, 0.01 mmol) were dissolved in a mixed solution DMF (1.5 mL) and ethanol (0.5 mL) at room temperature and then the mixture were sonicated for 10 min. The –COOH functionalised Au substrate was then placed into the vial (with the activated side facing down to the bottom). Then, the reaction precursors were heated to 80 °C and kept for one day. After cooling down to room temperature, the obtained Zn_2(ZnTCPP) thin film was removed from the reaction mixture, rinsed with fresh DMF and ethanol, and dried at 50 °C under vacuum.

Zn₂(ZnTCPP) film preparation via Modular Assembly. Firstly, $Zn(NO_3)_2 \cdot 6H_2O$ (4.5 mg, 0.015 mmol), TCPP (4 mg, 0.005 mmol), acetic acid (10 μL, 1M in DMF solution) and pyrazine (0.8 mg, 0.01 mmol) were dissolved in a mixed solution DMF (1.5 mL) and ethanol (0.5 mL) at room temperature. The reaction mixtures were sonicated for 10 min and then heated to 80 °C and kept for one day. After slowly cooled to room temperature, the synthesized red powder was washed with ethanol and collected by centrifuging.

Secondly, the as-synthesized Zn_2(ZnTCPP) nanosheets were dispersed in ethanol by ultra-sonication to get a colloidal suspension (1.0 mg/cm³); The suspension was placed dropwise onto the surface of water in a beaker, and due to the hydrophobic property of the Zn_2(ZnTCPP), they spread out to form a thin film; The thin film was easily transferred to a –COOH functionalised Au substrate by stamping. The film was immersed in pure water to remove un-deposited Zn_2(ZnTCPP) nanosheets and the water on the substrate was blown away. Additional nanosheets could be repeatedly stacked in a layer-bylayer (LBL) growth fashion to create a Zn_2(ZnTCPP) thin film with the desired thickness.

Zn₂(ZnTCPP) film growth via LPE on pump system. Synthesis of Zn_2(ZnTCPP) thin films was conducted on a double-walled reaction vessel, which was heated with a silicon-oil thermostat. The solutions were pumped in and out by peristaltic pumps which were controlled by LAB view (National Instruments) on computer. For the growth of Zn_2(ZnTCPP), the –COOH functionalised Au substrate was placed in the reaction vessel (with the activated side facing down to the bottom) and alternatively treated with a 0.3 mM $Zn(OAC)_2$ in DMF/ethanol (v/v, 3/1) and 0.1

mM H_2TCPP in DMF/ethanol (v/v, 3/1) solution. The substrate was immersed into each solution for 10 min. In between these reactive steps, the substrate was rinsed with pure ethanol for 2 min. These deposition cycles were repeated 30 times (30 cycles) at 70 °C to fabricated the oriented crystalline Zn_2(ZnTCPP) thin films.

5.3.5 3D PP-MOF films preparation

a) PCN-222 films growth.

PCN-222 film growth via VAC. For the film growth using VAC, a 20 mL glass vial with a cap equipped was used. A Raschig-ring was placed on the bottom of the vial to offer an elevated flat platform for the substrate. A mixture of 1 mL DMF and 0.2 mL acetic acid was filled into the vial as vapour source. Afterwards, the pre-treated Au/Silicon/ITO substrates (1 cm x 1 cm) was placed on top of the Raschig-rings and fully coated with a drop of a freshly prepared MOF precursor solution. The vial was closed and was transferred into a preheated 100 °C oven where it was kept for the specified time (details in table S2). Afterwards the vial was removed from the oven and allowed to cool down for 10 min before the PCN-222 film was removed. The film was immersed in fresh DMF and ethanol several times and then dried under vacuum.

PCN-222 film growth via solvothermal method. $ZrOCl_2·8H_2O$ (1.9 mg, 0.006 mmol), CuTCPP (1.7 mg, 0.002 mmol), acetic acid (75 μL) were dissolved in 1 mL DMF at room temperature and then the mixture was sonicated for 10 min. The –COOH functionalised Au substrate was then placed into the vial (with the activated side facing down to the bottom). Then, the reaction precursors were heated to 100 °C and kept for one day. After cooling down to room temperature, the obtained PCN-222 film was removed from the reaction mixture, rinsed with fresh DMF and ethanol, and dried under vacuum.

PCN-222 film preparation via Modular Assembly. Firstly, the PCN-222 nanoparticles were synthesized using a solvothermal reaction. $ZrOCl_2·8H_2O$ (5.7 mg, 0.006 mmol), CuTCPP (5.1 mg, 0.006 mmol), acetic acid (225 μL) were dissolved in 3 mL DMF at room temperature and then the mixture were sonicated for 10 min. Then, the reaction precursors were heated to 100 °C and kept for one day. After slowly cooled to room temperature, the synthesized red powder was washed with fresh DMF and ethanol and collected by centrifuging.

Secondly, the as-synthesized PCN-222 nanoparticles were dispersed in ethanol by ultra-sonication to get a colloidal suspension (1.0 mg/cm^3); The suspension was placed dropwise onto the surface of water in a beaker, and due to the hydrophobic property of PCN-222, they spread out to form a thin film; The thin film was easily transferred to a –COOH functionalised Au substrate by stamping. The film was immersed in pure water to remove un-deposited PCN-222 and the water on the substrate was blown away. Additional cycles could be repeatedly stacked in a layer-by-layer (LBL) growth fashion to create a PCN-222 film with the desired thickness.

PCN-222 film growth via LPE on pump system. The synthesis of PCN-222 film was conducted on a double-walled reaction vessel, which was heated with a silicon-oil thermostat. The solutions were pumped in and out by peristaltic pumps which were controlled by LAB view (National Instruments) on computer. For the growth of PCN-222, 30 μM $Zr_6O_4(OH)_4(OMc)_{12}$ solution (mixed with acetic acid, 50 and 100 eq.) and 60 μM CuTCPP linker solution were prepared in DMF. The –COOH functionalised Au substrate was placed in the reaction vessel (with the activated side facing down to the bottom) and alternatively treated with a $Zr_6O_4(OH)_4(OMc)_{12}$ solution for 10 min and then CuTCPP linker solution for 10 min. The substrate was immersed into each solution for 10 min. Each subsequent step of dosing components was separated by a washing step of 2 min with absolute ethanol. These deposition cycles were repeated 30 times (30 cycles) at 100 °C to fabricate the PCN-222 films.

b) PCN-224 films growth.

PCN-224 film growth via VAC. For the film growth using VAC, a 20 mL glass vial with a cap equipped was used. A Raschig-ring was placed on the bottom of the bottle to offer an elevated flat platform for the substrate. A mixture of 1 mL DMF and 0.2 mL acetic acid was filled into the bottle as vapour source. Afterwards, the pre-treated Au/Silicon substrates (1 cm x 1 cm) was placed on top of the Raschig-ring and fully coated with a drop of a freshly prepared MOF precursor solution. The bottle was closed and was transferred into a preheated 70 °C oven where it was kept for the specified time (details in table S3). Afterwards the bottle was removed from the oven and allowed to cool down for 10 min before the PCN-224 film was removed. The film was immersed in fresh DMF and ethanol several times and then

dried under vacuum.

c) MOF-525 films growth

MOF-525 film growth via VAC. For the film growth using VAC, a 20 mL glass vial with a cap equipped was used. A Raschig-ring was placed on the bottom of the bottle to offer an elevated flat platform for the substrate. A mixture of 1mL DMF and 0.2 mL acetic acid was filled into the bottle as vapour source. Afterwards, the pre-treated Au/Silicon/ITO substrates (1 cm x 1 cm) was placed on top of the Raschig-ring and fully coated with a drop of a freshly prepared MOF precursor solution. The bottle was closed and was transferred into a preheated 80 °C oven where it was kept for the specified time (details in table S4). Afterwards the bottle was removed from the oven and allowed to cool down for 10 min before the MOF-525 film was removed. The film was immersed in fresh DMF and ethanol several times and then dried under vacuum.

Table S3. Recipes for the fabrication of PCN-222 films by VAC.

	EXP.	Precursor solution				Droplet volume	Substrate	Temperature	Reaction time	Vapour source	
		ZrOCl₂·8H₂O	CuTCPP	acetic acid	DMF					DMF	Acetic acid
Variation of modulator conentration	9	1.9 mg 6 mmol/L	1.7 mg 2 mmol/L	0 μL 0 mmol/L	1 mL	30 μL	-COOH SAM gold	100 °C	3 h	1 mL	0.2 mL
	10	1.9 mg 6 mmol/L	1.7 mg 2 mmol/L	25 μL 438 mmol/L	1mL	30 μL	-COOH SAM gold	100 °C	3 h	1 mL	0.2 mL
	11	1.9 mg 6 mmol/L	1.7 mg 2 mmol/L	50 μL 875 mmol/L	1 mL	30 μL	-COOH SAM gold	100 °C	3 h	1 mL	0.2 mL
	12	1.9 mg 6 mmol/L	1.7 mg 2 mmol/L	75 μL 1314 mmol/L	1 mL	30 μL	-COOH SAM gold	100 °C	3 h	1 mL	0.2 mL
	13	1.9 mg 6 mmol/L	1.7 mg 2 mmol/L	150 μL 2625 mmol/L	1 mL	30 μL	-COOH SAM gold	100 °C	3 h	1 mL	0.2 mL
	14	1.9 mg 6 mmol/L	1.7 mg 2 mmol/L	300 μL 5250 mmol/L	1 mL	30 μL	-COOH SAM gold	100 °C	3 h	1 mL	0.2 mL
Variation of precursor conentration	15	5.7 mg 18 mmol/L	5.1 mg 6 mmol/L	225 μL 3942 mmol/L	1 mL	30 μL	-COOH SAM gold	100 °C	3 h	1 mL	0.2 mL
Variation of substrate type	16	1.9 mg 6 mmol/L	1.7 mg 2 mmol/L	75 μL 1314 mmol/L	1 mL	30 μL	Silicon wafer	100 °C	3 h	1 mL	0.2 mL
	17	1.9 mg 6 mmol/L	1.7 mg 2 mmol/L	75 μL 1314 mmol/L	1mL	30 μL	ITO glass	100 °C	3 h	1 mL	0.2 mL
	18	1.9 mg 6 mmol/L	1.7 mg 2 mmol/L	75 μL 1314 mmol/L	1mL	30 μL	-COOH SAM Au QCM	100 °C	3 h	1 mL	0.2 mL
variation of droplet volume	19	1.9 mg 6 mmol/L	1.7 mg 2 mmol/L	75 μL 1314 mmol/L	1 mL	60 μL	-COOH SAM gold	100 °C	3 h	1 mL	0.2 mL
Variation of reaction time	20	1.9 mg 6 mmol/L	1.7 mg 2 mmol/L	75 μL 1314 mmol/L	1mL	30 μL	-COOH SAM gold	100 °C	12 h	1 mL	0.2 mL
Variation of reaction temperature	21	1.9 mg 6 mmol/L	1.7 mg 2 mmol/L	75 μL 1314 mmol/L	1 mL	30 μL	-COOH SAM gold	80 °C	3 h	1 mL	0.2 mL
	22	1.9 mg 6 mmol/L	1.7 mg 2 mmol/L	75 μL 1314 mmol/L	1 mL	30 μL	-COOH SAM gold	120 °C	3 h	1 mL	0.2 mL

Table S4. Recipes for the fabrication of PCN-224 films by VAC.

	EXP.	Precursor solution				Droplet volume	Substrate	Temperature	Reaction time	Vapour source	
		ZrOCl$_2$·8H$_2$O	CuTCPP	acetic acid	DMF					DMF	Acetic acid
Variation of modulator conentration	23	1.9 mg 6 mmol/L	1.3 mg 1.5 mmol/L	0 µL 0 mmol/L	1 mL	30 µL	-COOH SAM gold	70 °C	3 h	1 mL	0.2 mL
	24	1.9 mg 6 mmol/L	1.3 mg 1.5 mmol/L	150 µL 2625 mmol/L	1 mL	30 µL	-COOH SAM gold	70 °C	3 h	1 mL	0.2 mL
	25	1.9 mg 6 mmol/L	1.3 mg 1.5 mmol/L	300 µL 5250 mmol/L	1 mL	30 µL	-COOH SAM gold	70 °C	3 h	1 mL	0.2 mL
	26	1.9 mg 6 mmol/L	1.3 mg 1.5 mmol/L	500 µL 8720 mmol/L	1 mL	30 µL	-COOH SAM gold	70 °C	3 h	1 mL	0.2 mL
Variation of substrate type	27	1.9 mg 6 mmol/L	1.3 mg 1.5 mmol/L	500 µL 8720 mmol/L	1 mL	30 µL	Silicon wafer	70 °C	3 h	1 mL	0.2 mL
	28	1.9 mg 6 mmol/L	1.3 mg 1.5 mmol/L	500 µL 8720 mmol/L	1 mL	30 µL	-COOH SAM Au QCM	70 °C	3 h	1 mL	0.2 mL
Variation of reaction time	29	1.9 mg 6 mmol/L	1.3 mg 1.5 mmol/L	500 µL 8720 mmol/L	1 mL	30 µL	-COOH SAM gold	70 °C	12 h	1 mL	0.2 mL
Variation of reaction temperature	30	1.9 mg 6 mmol/L	1.3 mg 1.5 mmol/L	500 µL 8720 mmol/L	1 mL	30 µL	-COOH SAM gold	100 °C	3 h	1 mL	0.2 mL
	31	1.9 mg 6 mmol/L	1.3 mg 1.5 mmol/L	500 µL 8720 mmol/L	1 mL	30 µL	-COOH SAM gold	120 °C	3 h	1 mL	0.2 mL

Table S5. Recipes for the fabrication of MOF-525 films by VAC.

	EXP.	Precursor solution				Droplet volume	Substrate	Temperature	Reaction time	Vapour source	
		ZrOCl$_2$·8H$_2$O	CuTCPP	acetic acid	DMF					DMF	Acetic acid
Variation of modulator concentration	32	1.9 mg 6 mmol/L	2.6 mg 3 mmol/L	12.5 µL 219 mmol/L	1 mL	30 µL	-COOH SAM gold	80 °C	3 h	1 mL	0.2 mL
	33	1.9 mg 6 mmol/L	2.6 mg 3 mmol/L	25 µL 438 mmol/L	1 mL	30 µL	-COOH SAM gold	80 °C	3 h	1 mL	0.2 mL
	34	1.9 mg 6 mmol/L	2.6 mg 3 mmol/L	75 µL 1313 mmol/L	1 mL	30 µL	-COOH SAM gold	80 °C	3 h	1 mL	0.2 mL

	35	1.9 mg 6 mmol/L	2.6 mg 3 mmol/L	125 μL 2188 mmol/L	1 mL	30 μL	-COOH SAM gold	80 °C	3 h	1 mL	0.2 mL
	36	1.9 mg 6 mmol/L	2.6 mg 3 mmol/L	200 μL 3500 mmol/L	1 mL	30 μL	-COOH SAM gold	80 °C	3 h	1 mL	0.2 mL
	37	1.9 mg 6 mmol/L	2.6 mg 3 mmol/L	250 μL 4375 mmol/L	1 mL	30 μL	-COOH SAM gold	80 °C	3 h	1 mL	0.2 mL
Variation of substrate type	38	1.9 mg 6 mmol/L	2.6 mg 3 mmol/L	250 μL 4375 mmol/L	1 mL	30 μL	Silicon wafer	80 °C	3 h	1 mL	0.2 mL
	39	1.9 mg 6 mmol/L	2.6 mg 3 mmol/L	250 μL 4375 mmol/L	1 mL	30 μL	ITO glass	80 °C	3 h	1 mL	0.2 mL
	40	1.9 mg 6 mmol/L	2.6 mg 3 mmol/L	250 μL 4375 mmol/L	1 mL	30 μL	-COOH SAM Au QCM	80 °C	3 h	1 mL	0.2 mL
Variation of reaction time	41	1.9 mg 6 mmol/L	2.6 mg 3 mmol/L	250 μL 4375 mmol/L	1 mL	30 μL	-COOH SAM gold	80 °C	12 h	1 mL	0.2 mL

5.4 Experimental details of Chapter 3

Experiment contributions: Zhenyu Zhou designed and prepared the porphyrinic MOF films as sensors, performed all the electrochemical sensing experiments. Mr. Shujin Hou and Dr. Weijin Li helped Zhenyu Zhou to develop the electrocatalytic system. Prof. Dr. Roland A. Fischer and Dr. Weijin Li supervised the project.

5.4.1 Synthesis of Mn-TCPP ligands

The Mn-TCPP ligands used in Chapter 3 were synthesized according to process described in the 6.3.1 section, just change the metal salt to $MnCl_2 \cdot 4H_2O$ (2.5 g, 12.8 mmol) for porphyrin metalation. ^{1}H NMR (300 MHz, DMSO-d_6): δ 8.80 (s, 8H), 8.37 (d, 8H), 8.30 (d, 8H).

Other metal-coordinated TCPP ligands (FeTCPPCl, CoTCPP, CuTCPP and ZnTCPP) were also prepared by the same procedure except for the utilization of $FeCl_2 \cdot 4H_2O$ (2.5 g, 12.8 mmol), $CoCl_2 \cdot 6H_2O$ (3.1 g, 12.8 mmol), $CuCl_2 \cdot 2H_2O$ (2.2 g, 12.8 mmol) and $ZnCl_2$ (1.75 g, 12.8 mmol) respectively, to elicit metallation.

5.4.2 Preparation of PP-MOF film modified ITO electrodes.

1) Synthesis of Mn-PCN-222.

The Mn-PCN-222 nanoparticles were synthesized using a solvothermal reaction. $ZrOCl_2 \cdot 8H_2O$ (26 mg), MnTCPPCl (12 mg), benzoic acid (225 mg) were dissolved in 2 ml DMF in a vial and then the mixture was sonicated for 10 min. Then the reaction precursors were heated at 80 °C under stirring and kept for 1 day. After cooling down to room temperature, the obtained PCN-222 was collected, rinsed with fresh DMF and ethanol by centrifugation, and dried under vacuum.

Other M-PCN-222 (M = Fe, Co, Cu, and Zn) were synthesized similarly except for using 12 mg FeTCPPCl, CoTCPP, CuTCPP and ZnTCPP ligands respectively.

2) Preparation of Mn-PCN-222 film modified ITO electrode.

The films are fast integrated on ITO glass via the modular assembly method. The as-synthesized Mn-PCN-222 nanoparticles were dispersed in ethanol by ultrasonication to obtain a colloidal suspension (3.0 mg/cm^3); this suspension was

placed dropwise onto the surface of water in a beaker. Due to hydrophobicity of Mn-PCN-222, it spreads out to form a thin film. This thin film was easily transferred to a cleaned ITO glass within an exposed area of 1 cm x 1cm by stamping. The film was immersed in pure water to remove un-deposited Mn-PCN-222 and the water on the substrate was blown away. For the voltammetric detection, the modified ITO electrode with 1 stamping cycle Mn-PCN-222 film was used. The loading of the thin film is evaluated as 1.8 µg/cm^2 by the environmental-controlled quartz crystal microbalance (BEL-QCM), with a BET surface area of 3.62×10^{-3} m^2/cm^2 calculated based on the BET of MOF powder (2013 m^2/g).

Other M-PCN-222 (M = Fe, Co, Cu, and Zn) films were also prepared on ITO glasses via the modular assembly (by using the corresponding M-PCN-222 (M = Fe, Co, Cu, and Zn) nanoparticle precursor).

3) Synthesis of PCN-222.

The PCN-222 nanoparticles were synthesized using a solvothermal reaction. ZrOCl$_2$·8H$_2$O (26 mg), TCPP (12 mg), benzoic acid (225 mg) were dissolved in 2 ml DMF in a vial and then sonicated for 10 min. These reaction precursors were heated at 80 °C under stirring and kept for one day. After cooling down to room temperature, PCN-222 was collected by filtration, rinsed with fresh DMF and ethanol by centrifugation, and dried under vacuum.

4) Preparation of PCN-222 film modified ITO electrode.

The films are fast integrated on ITO glass via the modular assembly method. The as-synthesized PCN-222 nanoparticles were dispersed in ethanol by ultra-sonication to get a colloidal suspension (3.0 mg/cm^3); The suspension was placed dropwise onto the surface of water in a beaker, and due to the hydrophobic property of PCN-222, they spread out to form a thin film; The thin film was easily transferred to a cleaned ITO glass within an exposed area of 1 cm $\times$ 1cm by stamping. The film was immersed in pure water to remove the undeposited PCN-222 and residual water on the substrate was blown away. For the voltammetric detection, the modified ITO electrode with 1 stamping cycle PCN-222 film was used.

5.4.3 Preparation of Mn-TCPP modified ITO electrode.

1 mg MnTCPPCl was dissolved in 2 ml DMF and then the mixture was

sonicated for 10 min. To ensure equal loadings of the catalytially active Mn-TCPP on both the Mn-TCPP/ITO and Mn-PCN-222/ITO electrodes, the linear UV-Vis absorbance plot of Mn-TCPP at 465 nm was plotted as a function of loading amount (for the prepared 0.5 mg mL^{-1} Mn-TCPP solution) (**Figure 3.11** in Chapter 3). According to the average absorbance of 0.1421 a.u. found for Mn-PCN-222/ITO (**Figure 3.4** in Chapter 3), 10.7 μL of the Mn-TCPP solution was dropped on the ITO glass surface within an exposed area of 1 cm x 1 cm. After drying, the Mn-TCPP modified ITO electrode was obtained.

5.4.4 Electrochemical measurements and Limit of detection (LOD).

Electrochemical experiments were performed with a Metrohm Autolab PGSTAT302N. A standard three-electrode cell was used for the electrochemical experiments. The Mn-PCN-222 film modified ITO (1 cm x 1 cm) was used as the working electrode. A silver/silver chloride (Ag/AgCl) electrode and a platinum (Pt) electrode were used as the reference and the counter electrode, respectively. All potentials in this study are reported with respect to the Ag/AgCl electrode (3M KCl). In this study, all the sample solutions were purged with purified N$_2$ for 5 min each to remove oxygen prior to starting any series of experiments. The measurements were performed in 0.5 M NaCl solution containing nitrobenzene (NB) with a pH of 7.0 at room temperature after a 90 seconds immersion for NB accumulation. According to the definition of International Union of Pure and Applied Chemistry (IUPAC), the limit of detection (LOD) can be estimated according to the equation [2]:

$$LOD = K \times S_b/m$$

Where S$_b$ is the standard deviation (SD) of the responses on blank solutions (without analytes); m is the slope (analytical sensitivity) of the calibration plot on the linear analyte detection range; and K is a numerical factor chosen in accordance with the confidence level desired (K=3 is used, allowing a confidence level of 99.86%).

5.4.5 Part of supporting data.

Table S6. Comparison of analytical performances of previously reported sensors regarding electrochemical detection of NB.

Working Electrode	Linear range (μM)	Limit of detection (μM)	Ref.

Co-MOF-MPC-2/GCE	0.5-235	0.21	[3]
Au-MOF-5/GCE	20-500	15.3	[4]
JUC-62@pOMC-3/GCE	0.05-420	0.018	[5]
ZIF-67/PCF(1:1)/GCE	0.3-390	0.16	[6]
Ni-MOF-PVP/GC	0.2-1000	0.097	[7]
β-CD$_{1.2mg}$/GO/SPCE	0.5-100	0.184	[8]
GRGO-Ni-TPP/GCE	0.5-878	0.14	[9]
EDOT/MWCNT/CPE	0.25-43	0.083	[10]
OMCN-800/GCE	0.5-1000	0.18	[11]
ZSO-gCN/GCE	30-100	2.2	[12]
OMC/DDAB/GCE	20-2900	10	[13]
HCSs/GC	1.63-100	0.011	[14]
CMF-RGO	0.2–927.7	0.088	[15]
MMPCMs/GC	0.2-40	0.008	[16]
NPC-2/GCE	2-100	0.62	[17]
NHCPs-750–GCE	5–2610	2.29	[18]
MnFe-Na/GCE	50-300	4	[19]
[AgL$_{0.5}$(NO$_3$)]$_n$/GCE	1-2450	0.62	[20]
Ag/CS-G/GCE	8.13-894.3	4.88	[21]
PAA-AgNPs/GC	10-600	1.68	[22]
TPDT-Ag NPs/GC	1-7	1	[23]
ATP-Ag/GCE	3-30	1.1	[24]
β-CD–Au–TPDT/GC	10-80	-	[25]
Au-NPs/GCE	0.1-600	0.016	[26]
Au-MSM/GC	0.1-2500	0.015	[27]
Pd-GG-g-PAM-silica/GCE	1-1900	0.06	[28]
Pt-NPs-MPC/Nafion/GC	1-200	0.05	[29]
r-Al$_2$O$_3$/GCE	0.5-145.5	0.15	[30]
Mn-PCN-222/ITO	**0.08-700**	**0.03**	**This work**

Table S7. Comparison of analytical performances of previously reported sensors regarding electrochemical detection of 4-nitrobenzaldehyde.

Working Electrode	Linear range (μM)	Limit of detection (μM)	Ref.
Ru(bpy)$_3$$^{2+}$/OHA	20–800	1.09	[31]
BiFE	5-50	1.5	[32]
MWCNTs/GCE	0.007-2.32	0.002	[33]
Mn-PCN-222/ITO	**0.07-100**	**0.03**	**This work**

Table S8. Comparison of analytical performances of previously reported sensors regarding electrochemical detection of 4-Nitrophenol.

Working Electrode	Linear range (μM)	Limit of detection (μM)	Ref.
Nb$_2$CTx/ Zn-Co-NC/GC	1-500	0.07	[34]

AgPd@UiO-66- NH_2/GCE	100-370	0.032	[35]
AgNWs/GCE	0.6- 32	0.052	[36]
Nano-Au/GCE	10-1000	8	[37]
HA-NP/GCE	1-300	0.6	[38]
GC-UNFE	0.5−3000	0.23	[39]
FeOx/TiO_2@mC	5-310	0.183	[40]
Cu_2O-Pt RRDE	10-100	0.1	[41]
Mn-PCN-222/ITO	**0.5-100**	**0.106**	**This work**

Table S9. Comparison of analytical performances of previously reported sensors regarding electrochemical detection of 1,3-dinitrobenzene.

Working Electrode	Linear range (μM)	Limit of detection (μM)	Ref.
ER-GO/GCE	2.4-12	0.0096	[42]
HCSs/GC	0.06-100	0.005	[14]
CMK-3/GC	0.05-22	0.024	[43]
β-CDm/MWCNTs/GO/GCE	0.02–30	0.005	[44]
MIP/MWCNT/GCE	0.045–8.5	25.15	[45]
PBAcs/PC-800/GC	0.006-6	0.0007	[46]
FUNPANI-MIP/GC	8.8-317	2.9	[47]
Porphyrin/CNTs/GCE	0.008-0.5	0.002	[48]
Mn-PCN-222/ITO	**0.08-100**	**0.018**	**This work**

Table S10. Comparison of analytical performances of previously reported sensors regarding electrochemical detection of Catechol.

Working Electrode	Linear range (μM)	Limit of detection (μM)	Ref.
Cu-MOF-199/SWCNTs/GCE	0.1-1150	0.1	[49]
GR/GCE	1-50	0.01	[50]
PSA/PDDA-GN/GCE	1-400	0.22	[51]
PEDOT/GO/GCE	2-400	1.6	[52]
GR/MWCNTs/BMIMPF6/GCE	0.2-660	0.06	[53]
PTH/GCE	1-120	0.025	[54]
Graphene-chitosan/GCE	1-400	0.75	[55]
Pt/ZrO_2-RGO/GCE	1-400	0.4	[56]
Pt-MnO_2/GCE	15-447	0.018	[57]
CMK-3-Nafion/GCE	0.5-35	0.1	[58]
NH_2-SBA15/CPE	1-140	0.5	[59]
ECF-CPE	1-200	0.2	[60]

	Linear range	Limit of detection	Ref.
UT-CdSe/GCE	0.2-300	0.06	[61]
ER(GO-TT-CNT)/GCE	0.5-200	0.0049	[62]
alk-Ti$_3$C$_2$/N-PC/GCE	0.5-150	0.0031	[63]
MIL-101(Cr)-rGO-2	10-1400	4	[64]
E. *coli* BL21-C23O/NPG/GCE	1-500	0.24	[65]
Mn-PCN-222/ITO	**0.1-100**	**0.047**	**This work**

Table S11. Comparison of analytical performances of previously reported sensors regarding electrochemical detection of Cu^{2+}.

Working Electrode	Linear range (μM)	Limit of detection (μM)	Ref.
Chitosan-PCN-222/GC	0.4-13	0.05	[66]
BIA/SPE	0.39-1.97	0.03	[67]
Graphene/CeO2/GCE	0.2-2.5	1.64×10^{-4}	[68]
BTPSBA–MCPE	0.8-10	0.2	[69]
Ag-bipy-CP/PMB/GCE	0.02-0.1	0.01	[70]
L-cys-rGO/GCE	0.4-2	0.047	[71]
IDA-modified copolymer	1-10	0.06	[72]
Poly(2-amino-4-thiazoleacetic acid)/MWCNTs/GCE	0.7-50	5×10^{-4}	[73]
OPPy-GGH NW	0.02-0.3	-	[74]
Gly–Gly–His/PTAA	1-20	0.02	[75]
Mn-PCN-222/ITO	**0.06-100**	**0.013**	**This work**

Table S12. Comparison of analytical performances of previously reported sensors regarding electrochemical detection of Cr$_2$O$_7$$^{2-}$.

Working Electrode	Linear range (μM)	Limit of detection (μM)	Ref.
Phosphomolybdate/GCE	0.5-378	0.026	[76]
Polyoxometalate compounds/GCE	2-2610	0.174	[77]
Au NPs@SPE	0.38–3.8	0.1	[78]
AuNP/ITO	5-100	2	[79]
PZrS nanocomposite/GCE	0.55-39.5	0.0643	[80]
Graphite/SPE	3-10000	1	[81]
Au/GCE	0.38-38	0.085	[82]
SPCE/PH	0.1-15	0.05	[83]
Mn-PCN-222/ITO	**0.05-100**	**0.003**	**This work**

Table S13. Comparison of analytical performances of previously reported sensors regarding electrochemical detection of Cd^{2+}.

Working Electrode	Linear range (μM)	Limit of detection (μM)	Ref.
L-cys-rGO/GCE	0.4-2	0.03	[71]

PPCCE	0.05–3	0.03	[84]
PEDOT:PSS/CCE	0.102-4.06	0.03	[84]
Alk-Ti$_3$C$_2$/GCE	0.21-2.1	0.206	[85]
LB$_{TCA}$/GCE	0.2-50	0.02	[86]
Diacetyldioxime/CPE	0.25-25	0.04	[87]
Bi$_2$O$_3$/SPCE	0.18-0.89	0.01	[88]
G/PANI/PS/SPCE	0.09-4.46	0.04	[89]
Mn-PCN-222/ITO	**0.3-100**	**0.1**	**This work**

Table S14. Comparison of analytical performances of previously reported sensors regarding electrochemical detection of ascorbic acid.

Working Electrode	Linear range (μM)	Limit of detection (μM)	Ref.
GQDs/IL-SPCE	25-400	6.63	[90]
SPGNE	4-4500	0.96	[91]
MgO/Gr/Ta	5-350	0.03	[92]
Au/RGO/GCE	240-1500	51	[93]
ERGO/GCE	500-2000	0.3	[94]
Ni-sG/GCE	150-300	30	[95]
NG/GCE	5-1300	2.2	[96]
BN/GCE	30-1000	3.77	[97]
PG/GCE	9-2314	6.45	[98]
Pt@NP-AuSn/Ni/CFP	200-1200	13.4	[99]
Mn-PCN-222/ITO	**0.15-100**	**0.011**	**This work**

Table S15. Comparison of analytical performances of previously reported sensors regarding electrochemical detection of uric acid.

Working Electrode	Linear range (μM)	Limit of detection (μM)	Ref.
GQDs/IL-SPCE	0.5-20	0.03	[90]
SPGNE	0.8-2500	0.2	[91]
MgO/Gr/Ta	1-70	0.12	[92]
Au/RGO/GCE	8.8-53	1.8	[93]
ERGO/GCE	0.5-60	0.5	[94]
Ni-sG/GCE	2-15	0.46	[95]
NG/GCE	0.1-20	0.045	[96]
BN/GCE	1-300	0.15	[97]
PG/GCE	6-1330	4.82	[98]
Pt@NP-AuSn/Ni/CFP	25-500	0.76	[99]
Mn-PCN-222/ITO	**0.08-100**	**0.017**	**This work**

Table S16. Comparison of analytical performance of previously reported sensor regarding

electrochemical detection of Methyl orange.

Working Electrode	Linear range (μM)	Limit of detection (μM)	Ref.
Smectite-HDTMA/GCE	0.1-1.6	0.04	[100]
Mn-PCN-222/ITO	0.07-100	0.0094	**This work**

5.5 Experimental details of Chapter 4

Experiment contributions: Zhenyu Zhou designed and prepared the Ni-N-C catalysts, performed the experiments. Ms. Jing Zhang and Prof. Dr. Liujiang Zhou performed the DFT simulation for the MOR process on the 20% Ni-N-C catalyst. Prof. Dr. Roland A. Fischer and Dr. Weijin Li supervised the project.

5.5.1 Synthesis of Ni-TCPP ligands

The Ni-TCPP ligands used in Chapter 4 were synthesized according to process described in the 6.3.1 section, just change the metal salt to $NiCl_2 \cdot 6H_2O$ (3.1 g, 12.8 mmol) for porphyrin metalation.

Other metal-coordinated TCPP ligands (FeTCPPCl, CoTCPP, CuTCPP, MnTCPPCl and ZnTCPP) were also prepared by the same procedure except for the utilization of $FeCl_2 \cdot 4H_2O$ (2.5 g, 12.8 mmol), $CoCl_2 \cdot 6H_2O$ (3.1 g, 12.8 mmol), $CuCl_2 \cdot 2H_2O$ (2.2 g, 12.8 mmol), $MnCl_2 \cdot 4H_2O$ (2.5 g, 12.8 mmol) and $ZnCl_2$ (1.75 g, 12.8 mmol) respectively, to elicit metallation.

5.5.2 Synthesis of n% Ni-PCN-222 (n = 0%，20%，40% and 100%)

1) Synthesis of 20% Ni-PCN-222.

The 20% Ni-PCN-222 was synthesized using a solvothermal reaction. $ZrOCl_2 \cdot 8H_2O$ (109 mg), Ni-TCPP (7 mg), H_2TCPP (24 mg) CF_3COOH (0.45 mL) were dissolved in 10 mL DMF in a vial and then the mixture was sonicated for 10 min. Thereafter, the reaction precursors were heated at 120 °C and kept for 1 day. After cooling down to room temperature, the obtained 20% Ni-PCN-222 was collected, rinsed with fresh DMF and ethanol by centrifugation, and dried under vacuum.

Other 20% M-PCN-222 (M = Fe, Cu, Zn, Mn and Co) were synthesized similarly except for using 7 mg Fe-TCPPCl, Cu-TCPP, Zn-TCPP, Mn-TCPPCl and Co-TCPP ligands respectively instead of 7 mg Ni-TCPP .

2) Synthesis of 0% Ni-PCN-222.

The 0% Ni-PCN-222 was synthesized following the same process as 20% Ni-PCN-222, except for using H_2TCPP (30 mg) instead of the mixture of Ni-TCPP and H_2TCPP as organic ligands.

3) Synthesis of 40% Ni-PCN-222.

The 40% Ni-PCN-222 was synthesized following the same process as 20% Ni-PCN-222, except for using Ni-TCPP (13 mg) and H_2TCPP (18 mg) instead of the mixture of Ni-TCPP (7 mg) and H_2TCPP (24 mg) as organic ligands.

4) Synthesis of 100% Ni-PCN-222.

The 100% Ni-PCN-222 was synthesized following the same process as 20% Ni-PCN-222, except for using Ni-TCPP (30 mg) instead of the mixture of Ni-TCPP and H_2TCPP as organic ligands.

5.5.3 Synthesis of Ni-N-C catalysts

Synthesis of Ni-N-C catalysts

1) Synthesis of n% Ni-N-C.

The n% Ni-N-C were prepared upon the corresponding n% Ni-PCN-222. Specifically, n% Ni-PCN-222 were heated to 800 °C at a rate of 5 °C/min, and then maintained at this temperature for 2 h in N_2 atmosphere. After cooling to room temperature, n% Ni-N-C/ZrO_2 were obtained. Thereafter, the ZrO_2 in the n% Ni-N-C/ZrO_2 were removed by immersing the sample in the HF (20 wt%) solution at 60 °C for 10 h. The black sample was collected by centrifuging, washed several times with distilled water and ethanol, and dried at 60 °C under vacuum overnight.

2) Synthesis of mix-Ni-N-C.

The mix-Ni-N-C was obtained by the direct pyrolysis of the physical mixture of Ni-TCPP (7 mg) and H_2-TCPP (24 mg) at 800 °C for 2 h in N_2 atmosphere.

5.5.4 Electrochemical measurements

Electrochemical methanol oxidation was performed with a Metrohm Autolab PGSTAT302N. A standard three-electrode system was used for the electrochemical experiments. The glass carbon electrode (3 mm in diameter) was used as the

working electrode. A silver/silver chloride (Ag/AgCl) electrode and a platinum (Pt) electrode were used as the reference and the counter electrode, respectively. In this study, glassy carbon electrode was properly polished with alumina powders (size: 1.0 and 0.3 μm) before the catalyst deposition. The catalyst ink was prepared by dispersing 2 mg of catalyst into the mixture of 1.4 mL of ethanol, 0.5 mL water and 100 μL of 5 wt% Nafion. After sonicated for half hour, 2 μL of the catalyst ink was loaded on the polished glass carbon. Cyclic voltammetry (CV) was recorded at a scan rate of 50 mV s^{-1} in a N_2 saturated 1 M KOH with or without 1 M methanol. The chronoamperometry were performed in 1 M KOH + 1 M methanol solution to assess the MOR electrochemical stability of prepared Ni-based catalysts (at 1.46 V *vs.* RHE). The electrochemical impedance spectroscopy (EIS) of were determined under open circuit potential (OCP) at AC voltage with an amplitude of 10 mV in frequency range of 10 – 10^6 Hz in the 1 M KOH + 1 M methanol aqueous solution. The electrochemically active surface area (ECSA) was estimated by determining the double-layer capacitance of the system from CV curves in non-Faradaic potential region. CO poisoning experiment was estimated by chronoamperometry of MOR on 20% Ni-N-C in Ar saturated and CO saturated 1 M KOH + 1 M methanol.

All potentials in the chapter 4 were converted into the reversible hydrogen electrode (RHE) scale; the Ag/AgCl reference electrode was directly calibrated in H_2-saturated 1.0 M KOH solution, in which the Ag/AgCl electrode was used as the reference electrode, and two Pt wires were used as the working and counter electrodes. According to the calibration, the relationship between the potential of Ag/AgCl and RHE can be described as follows: E (*vs*. RHE) = E (*vs*. Ag/AgCl) + 1.013V.

5.5.5 DFT calculation

For MOR on 20% Ni-N-C SACs, all calculations were performed using the Vienna Ab initio Simulation Package (VASP) code programs, which were carried out using the density functional theory (DFT) with the generalized Perdew-Burke-Ernzerhof (PBE), and the projector augmented-wave (PAW) pseudopotential plane-wave method [5]. For the PAW pseudopotential, we included $3d^84s^2$, $2s^22p^4$ and $1s^1$ were treated as valence electrons for Ni, O, and H atoms, respectively. A Γ-centered 3×5×1 k-point grid was utilized. The plane-wave basis set cutoff energy was set to

500 eV. The maximal atomic force per atom of 0.02 eV Å^{-1} and the total energy change of 1×10^{-5} eV were used in the calculations of structural optimizations. The empirical DFT-D2 correction was adopted in all calculations. The unit cell of NiN_4C was optimized and the obtained lattice constants are, a = 17.04 Å, b = 12.30 Å, with a vacuum layer of 20 Å perpendicular to the surface. It should be noted that all energies reported here are corrected with the zero-point energy (ZPE).

The ideal reaction of MOR generally occurs following the following six-step reaction mechanism:

$* + CH_3OH \rightarrow CH_3OH*$	**(R0)**
$CH_3OH* \rightarrow CH_2OH* + (H^+ + e^-)$	**(R1)**
$CH_2OH* \rightarrow CH_3O* + (H^+ + e^-)$	**(R2)**
$CH_2O* \rightarrow CHO* + (H^+ + e^-)$	**(R3)**
$CHO* \rightarrow CO* + (H^+ + e^-)$	**(R4)**
$CO*+H_2O \rightarrow COOH* + (H^+ + e^-)$	**(R5)**
$COOH* \rightarrow CO_2* + (H^+ + e^-)$	**(R6)**
$CO_2* \rightarrow * + CO_2$	**(R7)**
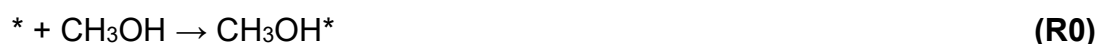
where * denotes the substrate. The R0 reaction is the adsorption of methanol molecules on the substrate surface, and R7 reaction is desorption of carbon dioxide from the substrate. While R1-R6 reactions are chemical dehydrogenation process, which means a hydrogen ion and an electron are popped out at each step.

To assess the MOR activities of 20% Ni-N-C, the Gibbs free energy change (ΔG_R) of each elementary step were calculated. All Gibbs free energies, including small molecule energies and adsorption energies, were corrected by vibration frequency calculation, combining zero point energy correction, entropy correction and enthalpy correction, processed via the VASPKIT. The temperature (T) was set to 298 K. ΔG is the final correction value, which is obtained through VASPKIT data processing. The formula is as follows.

$$G = E_{DFT} + \Delta G$$

In addition, the chemical potential of a pair of (H^++e^-) at 0 V vs. RHE ($G(H^++e^-)$) is referred to one half of the chemical potential of H_2 molecule based on the computational hydrogen electrode (CHE) approximation, which was proposed by

Nørskov and coworkers. Therefore, the reaction free energies can be calculated to be:

$$\Delta G_{R0} = G_{CH3OH^*} - G_* - G_{CH3OH}$$
$$\Delta G_{R1} = G_{CH2OH^*} + G_{(H^++e^-)} - G_{CH3OH^*}$$
$$\Delta G_{R2} = G_{CH3O^*} + G_{(H^++e^-)} - G_{CH2OH^*}$$
$$\Delta G_{R3} = G_{CHO^*} + G_{(H^++e^-)} - G_{CH2O^*}$$
$$\Delta G_{R4} = G_{CO^*} + G_{(H^++e^-)} - G_{CHO^*}$$
$$\Delta G_{R5} = G_{COOH^*} + G_{(H^++e^-)} - G_{CO} - G_{H2O}$$
$$\Delta G_{R6} = G_{CO2^*} + G_{(H^++e^-)} - G_{COOH^*}$$
$$\Delta G_{R7} = G_* + G_{CO2} - G_{CO2^*}$$

5.5.6 Part of supporting data

Table S17. Comparison of MOR performances of 20% Ni-N-C **and** previously reported non-noble metal electrocatalysts in alkaline media

Electrocatalyst	Electrolyte	Scan rate (mV s^{-1})	Activity		Durability [a]	Ref.
			mA mg^{-1}	Oxidation peak potential (V vs. RHE) [a]		
2Cu@CoO$_x$-CLS	1 M KOH + 1 M MeOH	50 mV s^{-1}	467.94	1.87 V	88 % activity retention after 10800 s at 1.57 V vs. RHE	[101]
KB&CTGU-15(1:2)	0.1 M KOH + 1 M MeOH	50 mV s^{-1}	527	1.67 V	65 % activity retention after 2400 s at 1.47 V vs. RHE	[102]
V$_O$-rich ultrathin NiO nanosheets	1 M KOH + 0.5 M MeOH	50 mV s^{-1}	299.3	1.73 V	Stable after 30000 at 1.53 V vs. RHE	[103]
Mesoporous Au-Ni film	0.5 M KOH + 3 M MeOH	50 mV s^{-1}	410	1.71 V	~13.3 % activity retention after 1200 s at 1.71 V vs. RHE	[104]
Ni/CN	1 M NaOH + 3 M MeOH	50 mV s^{-1}	57	1.61 V	~91 % activity retention after 9600 s at 1.53 V vs. RHE	[105]
Ni$_{0.75}$Cu$_{0.25}$	1 M NaOH + 0.5 M MeOH	50 mV s^{-1}	168	1.86 V	~91 % activity retention after 1200 s at 1.68 V vs. RHE	[106]
NiO	0.005 M KOH + 0.1 M MeOH	20 mV s^{-1}	50	~1.69 V	NA	[107]
NiP/rGO	1 M KOH + 0.5 M MeOH	10 mV s^{-1}	117	1.65 V	NA	[108]
Mn doped Ni(OH)$_2$	1 M KOH + 0.5 M MeOH	50 mV s^{-1}	16.4	~1.56 V	~90 % activity retention after 1000 cycles	[109]
Graphene/NiCo$_2$O$_4$	1 M KOH + 0.5 M MeOH	50 mV s^{-1}	239	1.45 V	60 % activity retention after 3600 s at 1.45 V vs.RHE	[110]

NiCo$_2$O$_4$/Ni foam	1 M KOH + 0.5 M MeOH	50 mV s^{-1}	40.9	1.53 V	~96 % activity retention after 1000 s at 1.53 V *vs.* RHE	[111]
Ni/N-C@500	1 M KOH + 0.5 M MeOH	50 mV s^{-1}	31.2	1.55 V	37 % activity retention after 12 h at 2.06 V *vs.*RHE	[112]
NiO/Ni-P composites (EP-M)	0.5 M KOH + 1 M MeOH	50 mV s^{-1}	467	1.55 V	Stable during 20000 s at 1.55 V *vs.* RHE	[113]
Ni-Co hydroxides	1 M KOH + 0.5 M MeOH	50 mV s^{-1}	200	~1.53 V	Stable during 800 s at 1.49 V *vs.* RHE	[114]
Microsphere-Co$_3$O$_4$ on Ni foam	1 M KOH + 0.5 M MeOH	10 mV s^{-1}	36.2	1.53 V	~96 % activity retention after 1000 cycles	[115]
NiMoO$_4$/C	1 M KOH + 2 M MeOH	50 mV s^{-1}	~16.3	~1.73 V	70 % activity retention after 500 cycles	[116]
ZnCo$_2$O$_4$/Ni foam	1 M KOH + 0.5 M MeOH	50 mV s^{-1}	149	1.63 V	17.1 % activity retention after 24 h at 1.63 V *vs.* RHE	[117]
Ni$_x$Co$_{3-x}$O$_{4-y}$	1 M KOH + 1 M MeOH	50 mV s^{-1}	200	1.48 V	~84 % activity retention after 1800 s at 1.43 V *vs.* RHE	[118]
Cu-Ni NWs/C	1 M NaOH + 0.5 M MeOH	50 mV s^{-1}	425	1.87 V	72 % activity retention after 18000 s at 1.87 V *vs.* RHE	[119]
Ni$_{0.5}$Cu$_{0.5}$Co$_2$O$_4$	1 M KOH + 0.5 M MeOH	50 mV s^{-1}	210	1.77 V	~98.9 % activity retention after 1000 cycles	[120]
NiO NS@NW/NF	1 M KOH + 0.5 M MeOH	10 mV s^{-1}	~60	1.62 V	81 % activity retention after 1000 cycles at 1.62 V *vs.*RHE	[121]
Urchin-like Ni$_1$Co$_2$O$_4$	0.1 M KOH + 0.5 M MeOH	50 mV s^{-1}	192.7	1.57 V	85 % activity retention after 1000 cycles at 1.57 V *vs.* RHE	[122]
NiCo$_2$O$_4$/GNF	1 M KOH + 0.5 M MeOH	5 mV s^{-1}	93.3	1.58 V	75.6 % activity retention after 9600 s at 1.58 V *vs.* RHE	[123]
Flower-like NiCo$_2$O$_4$	1 M KOH + 0.5 M MeOH	50 mV s^{-1}	217.6	1.53 V	~69.6 % activity retention after 1200 s at 1.53 V *vs.* RHE	[124]
Meso NiPO NT	0.5 M KOH + 0.5 M MeOH	50 mV s^{-1}	583	1.71 V	86.1 % activity retention after 1000 cycles at 1.66 V *vs.* RHE	[125]
Au/NiCo$_2$O$_4$	0.5 M KOH + 0.5 M MeOH	50 mV s^{-1}	95	1.65 V	55 % activity retention after 500 cycles at 1.65 V *vs.* RHE	[126]
Co(OH)$_2$ nanoflakes	1 M KOH + 0.5 M MeOH	10 mV s^{-1}	~150	1.57 V	84 % activity retention after 2000 s at 1.57 V *vs.* RHE	[127]
Co$_{0.2}$Ni$_{0.2}$-decorated graphene	1 M KOH + 3 M MeOH	50 mV s^{-1}	~176	1.83 V	~88 % activity retention after 60000 s at 1.43 V *vs.* RHE	[128]
NiCo$_2$O$_4$	0.1 M NaOH + 1 M MeOH	50 mV s^{-1}	~11	~1.62 V	NA	[129]
CeO$_2$/Nano-ZSM-5	0.5 M NaOH + 0.5 M MeOH	50 mV s^{-1}	52.6	~1.7 V	96 % activity retention after 1000 cycles at 1.51 V *vs.* RHE	[130]
Ni–Cu alloys	0.1 M NaOH + 0.2 M MeOH	50 mV s^{-1}	30	~1.81 V	NA	[131]
NiCo$_2$O$_4$/Ni(OH)$_2$	1 M KOH + 0.5 M	10 mV s^{-1}	92.3	1.63 V	~90 % activity retention after	[132]

Catalyst	Electrolyte	Scan rate	Value	Voltage	Stability	Ref.
	MeOH				1000 s at 1.63 V *vs.* RHE	
Core-shell PPy/Co₃O₄	1 M NaOH + 1 M MeOH	50 mV s⁻¹	~489.8	1.53 V	81.3 % activity retention after 16 h at 1.48 V *vs.* RHE	[133]
MWCNTs/MoS₂ QD	1 M NaOH + 1 M MeOH	50 mV s⁻¹	190	2.2 V	~94 % activity retention after 1800 s at 2.2 V vs. RHE	[134]
Co/NCNFs	1 M KOH + 3 M MeOH	50 mV s⁻¹	~75	1.73 V	~80 % activity retention after 1000 s at 1.43 V *vs.* RHE	[135]
Co₃(PO₄)₂ nanospheres	1 M KOH + 1 M MeOH	50 mV s⁻¹	556	1.65 V	Stable during 72000s at 1.53 V *vs.* RHE	[136]
ZnCo₂O₄/NF	1 M KOH + 0.5 M MeOH	10 mV s⁻¹	110	1.83 V	95.5 % activity retention after 2310 s at 1.83 V *vs.* RHE	[137]
MgCo₂O₄/NF	1 M KOH + 0.5 M MeOH	10 mV s⁻¹	98	1.68 V	Stable during 2400 s at 1.68 V *vs.* RHE	[138]
Ni-BTC-MOF-/4 wt % rGO	1 M NaOH + 2 M MeOH	50 mV s⁻¹	~189	1.63 V	83 % activity retention after 3600 s at 1.62 V *vs.* RHE	[139]
N-doped NiCNFs	1 M KOH + 3 M MeOH	50 mV s⁻¹	194.6	1.98 V	Stable during 1000 s at 1.43 V *vs.* RHE	[140]
MoS₂@CoNi-ZIF	1 M KOH + 0.5 M MeOH	50 mV s⁻¹	438.08	1.6 V	~88 % activity retention after 3000 s at 1.6 V *vs.* RHE	[141]
NiCo₂O₄/rGO	1 M KOH + 0.5 M MeOH	50 mV s⁻¹	~273	1.63 V	~19.2 % activity retention after 3000 s at 1.63 V *vs.* RHE	[142]
NiO NTs-400	1 M KOH + 0.5 M MeOH	50 mV s⁻¹	85.9	1.5 V	~67 % activity retention after 10000 s at 1.5 V *vs.* RHE	[143]
Ni/C-30	0.5 M KOH + 0.4 M MeOH	10 mV s⁻¹	~15	1.71 V	~54 % activity retention after 1800 s at 1.61 V *vs.* RHE	[144]
Hierarchical NiCo₂O₄	1 M KOH + 0.5 M MeOH	10 mV s⁻¹	51	1.58 V	Stable after 5000 s at 1.48 V *vs.* RHE	[145]
NiO/CNT	1 M KOH + 0.5 M MeOH	50 mV s⁻¹	498	~1.59 V	~89% activity retention after 3500 s at 1.48 V *vs.* RHE	[146]
20% Ni-N-C	**1 M KOH + 1 M MeOH**	**50 mV s⁻¹**	**634**	**1.55 V**	**90% activity retention after 25000 s at 1.46 V *vs.* RHE**	**This work**

[a] All potentials in table were evaluated and converted into reversible hydrogen electrode (RHE) according to following equations:

$E_{RHE} = E_{Ag/AgCl} + 0.199 + 0.0591 \times pH$;

$E_{RHE} = E_{Hg/HgO} + 0.098 + 0.0591 \times pH$;

$E_{RHE} = E_{SCE} + 0.241 + 0.0591 \times pH$;

Table S18. The calculated energies of the small molecules.

Species	E_{DFT}	E_{ZPE}	ΔG	G
CO_2	-22.96	0.307	-0.258	-23.22
$H_2O(aq)$	-14.22	0.569	0.001	-14.22
H_2	-6.75	0.266	-0.047	-6.80

CH$_3$OH(aq)	-30.21	1.355	0.709	-29.50	

Table 19. The adsorption energies of adsorbed intermediates in the optimized MOR pathway on 20% Ni-N-C.

Species	E$_{DFT}$	E$_{ZPE}$	ΔG	G	Bond length(Å)	Site
*	-724.68	-	-	-724.68	-	-
CH$_3$OH*	-755.14	1.384	1.213	-753.93	3.27	C
CH$_2$OH*	-750.33	1.103	0.991	-749.34	2.05	C
CH$_2$O*	-747.14	0.734	0.658	-746.48	2.77	C
CHO*	-742.76	0.351	0.368	-742.39	1.91	C
CO*	-739.62	0.156	0.012	-739.61	2.71	C
COOH*	-750.13	0.606	0.472	-749.65	1.95	C
CO$_2$*	-747.83	0.314	0.213	-747.61	3.19	C

Table S20. Comparison of energy barriers of rate-determining steps of previously reported electrocatalysts towards MOR.

Eletrocatalyst	Rate-determining steps (RDS)	RDS energy barrier (eV)	MOR activity	Ref.
NR-Ni(OH)$_2$	CH$_2$O* → CHO*	1.32	~180 mA cm^{-2} mg^{-1}	[147]
MoO$_3$(010)	CHO* → CO*	2.11	-	[148]
Co$_3$O$_4$(110)-B	CH$_3$O* → CH$_2$O*	1.78	-	[149]
Au$_3$Ag (111)	CH$_3$OH* → CH$_2$OH*	0.80	950 mA mg^{-1} (per Au loading)	[150]
Pt (111)	CO* → COOH*	1.06	591.9 mA mg^{-1} (per Pt loading)	[150]
Pd$_1$/ZnO	HCOO* → CO$_2$*	1.6	-	[151]
Fe-FeO/Pt	CH$_3$OH* → CH$_2$OH*	1.63	-	[152]
PdAu(1 0 0)	CH$_3$OH* → CH$_3$O*	1.67	-	[153]
PtRuNi	COOH* → CO$_2$*	1.08	1200 mA mg^{-1} (per Pt loading)	[154]
PtRu	COOH* → CO$_2$*	1.56	470 mA mg^{-1} (per Pt loading)	[154]
20% Ni-N-C	**CH$_3$OH* → CH$_2$OH***	**1.19**	**634 mA mg^{-1}**	**This work**

5.6 Reference

[1]   D. Feng, Z. Y. Gu, J. R. Li, H. L. Jiang, Z. Wei, H. C. Zhou, *Angew. Chem. Int. Ed.* **2012**, *51*, 10307-10310.

[2]   G. L. Long, J. D. Winefordner, *Anal. Chem.* 1983, 55, 712A-724A.

[3]   Y. Zhang, X. Bo, A. Nsabimana, C. Han, M. Li, L. Guo, *J. Mater. Chem. A* **2015**, *3*, 732-738.

[4]   D. K. Yadav, V. Ganesan, P. K. Sonkar, R. Gupta, P. K. Rastogi, *Electrochim. Acta* **2016**, *200*, 276-282.

[5]   C. Liu, X. Bo, L. Guo, *Sens. Actuators B Chem.* **2019**, *297*, 126741.

[6]   X. Feng, S. Lin, M. Li, X. Bo, L. Guo, *Anal. Chim. Acta* **2017**, *984*, 96-106.

[7]   P. Arul, S. A. John, *J. Electroanal. Chem.* **2018**, *829*, 168-176.

[8]   M. Velmurugan, N. Karikalan, S. M. Chen, Z. C. Dai, *J. Colloid Interface Sci.* **2017**, *490*, 365-371.

[9]   S. Kubendhiran, S. Sakthinathan, S. M. Chen, P. Tamizhdurai, K. Shanthi, C. Karuppiah, *J. Colloid Interface Sci.* **2017**, *497*, 207-216.

[10] G. Xu, B. Li, X. Wang, X. Luo, *Microchim. Acta* **2013**, *181*, 463-469.

[11] Y. Zhang, X. Bo, A. Nsabimana, C. Luhana, G. Wang, H. Wang, M. Li, L. Guo, *Biosens. Bioelectron.* **2014**, *53*, 250-256.

[12] S. Vinoth, P. M. Rajaitha, A. Pandikumar, *Compos. Sci. Technol.* **2020**, *195*, 108192.

[13] B. Qi, F. Lin, J. Bai, L. Liu, L. Guo, *Mater. Lett.* **2008**, *62*, 3670-3672.

[14] S. Pan, L. Wang, X. Chen, Y. Tang, Y. Chen, Y. Sun, X. Yang, P. Wan, *Electrochim. Acta* **2016**, *203*, 301-308.

[15] P. Balasubramanian, T. S. T. Balamurugan, S.-M. Chen, T.-W. Chen, T.-W. Tseng, B.-S. Lou, *Cellulose* **2018**, *25*, 2381-2391.

[16] J. Ma, Y. Zhang, X. Zhang, G. Zhu, B. Liu, J. Chen, *Talanta* **2012**, *88*, 696-700.

[17] L. Yan, X. Bo, Y. Zhang, L. Guo, *Electrochim. Acta* **2014**, *137*, 693-699.

[18] M. Liu, T. Zhang, H. Ren, L. Wang, T. Meng, J. Zhao, H. Wang, Y. Zhang, *Mater. Res. Bull.* **2018**, *104*, 15-19.

[19] Y. Sang, Y. Cui, Z. Li, W. Ye, H. Li, X. S. Zhao, P. Guo, *Sens. Actuators B Chem.* **2016**, *234*, 46-52.

[20] L. L. Liu, J. Chen, C. X. Yu, W. X. Lv, H. Y. Yu, X. Q. Cui, L. Liu, *Dalton Trans.* **2016**, *46*, 178-185.

[21] X. Lu, H. Qi, X. Zhang, Z. Xue, J. Jin, X. Zhou, X. Liu, *Chem. Commun.* **2011**, *47*, 12494-12496.

[22] V. M. Kariuki, S. A. Fasih-Ahmad, F. J. Osonga, O. A. Sadik, *Analyst* **2016**, *141*, 2259-2269.

[23] P. Rameshkumar, P. Viswanathan, R. Ramaraj, *Sens. Actuators B Chem.* **2014**, *202*, 1070-1077.

[24] F. Liang, B. Liu, Y. Deng, S. Yang, C. Sun, *Microchim. Acta* **2011**, *174*, 407.

[25] S. Manivannan, R. Ramaraj, *Chem. Eng. J.* **2012**, *210*, 195-202.

[26] R. Emmanuel, C. Karuppiah, S. M. Chen, S. Palanisamy, S. Padmavathy, P. Prakash, *J. Hazard. Mater.* **2014**, *279*, 117-124.

[27]   R. Gupta, P. K. Rastogi, V. Ganesan, D. K. Yadav, P. K. Sonkar, *Sens. Actuators B Chem.* **2017**, *239*, 970-978.

[28]   P. K. Rastogi, V. Ganesan, S. Krishnamoorthi, *Electrochim. Acta* **2014**, *147*, 442-450.

[29]   Y. Zhang, L. Zeng, X. Bo, H. Wang, L. Guo, *Anal. Chim. Acta* **2012**, *752*, 45-52.

[30]   B. Thirumalraj, S. Palanisamy, S. M. Chen, K. Thangavelu, P. Periakaruppan, X. H. Liu, *J. Colloid Interface Sci.* **2016**, *475*, 154-160.

[31]   F. Yuan, M. I. Halawa, X. Ma, A. Abdussalam, B. Lou, G. Xu, *ChemElectroChem* **2020**, 7, 4239-4244.

[32]   O. El Tall, D. Beh, N. Jaffrezic-Renault, O. Vittori, *Int. J. Environ. Anal. Chem.* **2009**, *90*, 40-48.

[33]   H. Ahmar, S. K. Shahvandi, *Electroanalysis* **2019**, *31*, 1238-1244.

[34]   R. Huang, D. Liao, Z. Liu, J. Yu, X. Jiang, *Sens. Actuators B Chem.* **2021**, *338*, 129828.

[35]   S. A. Hira, M. Nallal, K. H. Park, *Sens. Actuators B Chem.* **2019**, *298*, 126861.

[36]   C. Zhang, S. Govindaraju, K. Giribabu, Y. S. Huh, K. Yun, *Sens. Actuators B Chem.* **2017**, *252*, 616-623.

[37]   L. Chu, L. Han, X. Zhang, *J. Appl. Electrochem.* **2011**, *41*, 687-694.

[38]   H. Yin, Y. Zhou, S. Ai, X. Liu, L. Zhu, L. Lu, *Microchim. acta* **2010**, *169*, 87-92.

[39]   P. Wang, J. Xiao, A. Liao, P. Li, M. Guo, Y. Xia, Z. Li, X. Jiang, W. Huang, *Electrochim. Acta* **2015**, *176*, 448-455.

[40]   M. Wang, Y. Liu, L. Yang, K. Tian, L. He, Z. Zhang, Q. Jia, Y. Song, S. Fang, *Sens. Actuators B Chem.* **2019**, *281*, 1063-1072.

[41]   Y.-e. Gu, Y. Zhang, F. Zhang, J. Wei, C. Wang, Y. Du, W. Ye, *Electrochim. Acta* **2010**, *56*, 953-958.

[42]   T. W. Chen, Z. H. Sheng, K. Wang, F. B. Wang, X. H. Xia, *Chem. Asian J.* **2011**, *6*, 1210-1216.

[43]   D. Nie, P. Li, D. Zhang, T. Zhou, Y. Liang, G. Shi, *Electrophoresis* **2010**, *31*, 2981-2988.

[44]   J. Li, H. Feng, Y. Feng, J. Liu, Y. Liu, J. Jiang, D. Qian, *Microchim. Acta* **2014**, *181*, 1369-1377.

[45]   Y. Qu, Y. Liu, T. Zhou, G. Shi, L. Jin, *Chin. J. Chem.* **2009**, *27*, 2043-2048.

[46]   L. Wang, N. Wang, J. Wen, Y. Jia, S. Pan, H. Xiong, Y. Tang, J. Wang, X. Yang, Y. Sun, Y. Chen, P. Wan, *Chem. Eng. J.* **2020**, *397*, 125450.

[47]   Y. Liang, L. Gu, X. Liu, Q. Yang, H. Kajiura, Y. Li, T. Zhou, G. Shi, *Chemistry* **2011**, *17*, 5989-5997.

[48]   X. Lu, Y. Quan, Z. Xue, B. Wu, H. Qi, D. Liu, *Colloids Surf. B.* **2011**, *88*, 396-401.

[49]   J. Zhou, X. Li, L. Yang, S. Yan, M. Wang, D. Cheng, Q. Chen, Y. Dong, P. Liu, W. Cai, C. Zhang, *Anal. Chim. Acta* **2015**, *899*, 57-65.

[50]   H. Du, J. Ye, J. Zhang, X. Huang, C. Yu, *J. Electroanal. Chem.* **2011**, *650*, 209-213.

[51]   C. Li, W. Liu, Y. Gu, S. Hao, X. Yan, Z. Zhang, M. Yang, *J. Appl. Electrochem.* **2014**, *44*, 1059-1067.

[52]   W. Si, W. Lei, Y. Zhang, M. Xia, F. Wang, Q. Hao, *Electrochim. Acta* **2012**, *85*, 295-301.

[53]   X. Wang, M. Wu, H. Li, Q. Wang, P. He, Y. Fang, *Sens. Actuators B Chem.* **2014**, *192*, 452-458.

[54]   A. J. S. Ahammad, M. M. Rahman, G.-R. Xu, S. Kim, J.-J. Lee, *Electrochim. Acta* **2011**, *56*, 5266-5271.

[55] H. Yin, Q. Zhang, Y. Zhou, Q. Ma, T. liu, L. Zhu, S. Ai, *Electrochim. Acta* **2011**, *56*, 2748-2753.

[56] A. T. E. Vilian, S.-M. Chen, L.-H. Huang, M. A. Ali, F. M. A. Al-Hemaid, *Electrochim. Acta* **2014**, *125*, 503-509.

[57] B. Unnikrishnan, P.-L. Ru, S.-M. Chen, *Sens. Actuators B Chem.* **2012**, *169*, 235-242.

[58] J. Yu, W. Du, F. Zhao, B. Zeng, *Electrochim. Acta* **2009**, *54*, 984-988.

[59] X. Zhang, S. Duan, X. Xu, S. Xu, C. Zhou, *Electrochim. Acta* **2011**, *56*, 1981-1987.

[60] Q. Guo, J. Huang, P. Chen, Y. Liu, H. Hou, T. You, *Sens. Actuators B Chem.* **2012**, *163*, 179-185.

[61] X. Cao, X. Cai, Q. Feng, S. Jia, N. Wang, *Anal. Chim. Acta* **2012**, *752*, 101-105.

[62] H. S. Han, J.-M. You, H. Seol, H. Jeong, S. Jeon, *Sens. Actuators B Chem.* **2014**, *194*, 460-469.

[63] R. Huang, D. Liao, S. Chen, J. Yu, X. Jiang, *Sens. Actuators B Chem.* **2020**, *320*, 128386.

[64] H. Wang, Q. Hu, Y. Meng, Z. Jin, Z. Fang, Q. Fu, W. Gao, L. Xu, Y. Song, F. Lu, *J. Hazard. Mater.* **2018**, *353*, 151-157.

[65] Z. Liu, Y. Zhang, C. Bian, T. Xia, Y. Gao, X. Zhang, H. Wang, H. Ma, Y. Hu, X. Wang, *Biosens. Bioelectron.* **2019**, *126*, 51-58.

[66] Z. Xu, Q. Meng, Q. Cao, Y. Xiao, H. Liu, G. Han, S. Wei, J. Yan, L. Wu, *Anal. Chem.* **2020**, *92*, 10183.

[67] T. F. Tormin, R. R. Cunha, R. A. B. da Silva, R. A. A. Munoz, E. M. Richter, *Sens. Actuators B Chem.* **2014**, *202*, 93-98.

[68] Y.-L. Xie, S.-Q. Zhao, H.-L. Ye, J. Yuan, P. Song, S.-Q. Hu, *J. Electroanal. Chem.* **2015**, *757*, 235-242.

[69] I. Cesarino, G. Marino, R. Matos Jdo, E. T. Cavalheiro, *Talanta* **2008**, *75*, 15-21.

[70] A. Chira, B. Bucur, M. P. Bucur, G. L. Radu, *New J. Chem.* **2014**, *38*, 5641-5646.

[71] S. Muralikrishna, K. Sureshkumar, T. S. Varley, D. H. Nagaraju, T. Ramakrishnappa, *Anal. Methods* **2014**, *6*, 8698-8705.

[72] M. Lin, M. Cho, W.-S. Choe, Y. Son, Y. Lee, *Electrochim. Acta* **2009**, *54*, 7012-7017.

[73] H. Zhao, Y. Jiang, Y. Ma, Z. Wu, Q. Cao, Y. He, X. Li, Z. Yuan, *Electrochim. Acta* **2010**, *55*, 2518-2521.

[74] M. Lin, M. Cho, W. S. Choe, J. B. Yoo, Y. Lee, *Biosens. Bioelectron.* **2010**, *26*, 940-945.

[75] M. Lin, M. S. Cho, W. S. Choe, Y. Lee, *Biosens. Bioelectron.* **2009**, *25*, 28-33.

[76] Y. Wang, Y. Ma, Q. Zhao, L. Hou, Z. Han, *Sens. Actuators B Chem.* **2020**, *305*, 127469.

[77] X. Xin, N. Hu, Y. Ma, Y. Wang, L. Hou, H. Zhang, Z. Han, *Dalton Trans.* **2020**, *49*, 4570-4577.

[78] J. Tu, Y. Gan, T. Liang, H. Wan, P. Wang, *Sens. Actuators B Chem.* **2018**, *272*, 582-588.

[79] M. C. Tsai, P. Y. Chen, *Talanta* **2008**, *76*, 533-539.

[80] M. H. Motaghedifard, S. M. Pourmortazavi, S. Mirsadeghi, *Sens. Actuators B Chem.* **2021**, *327*, 128882.

[81] S. A. Miscoria, C. Jacq, T. Maeder, R. Martín Negri, *Sens. Actuators B Chem.* **2014**, *195*, 294-302.

[82] R. T. Kachoosangi, R. G. Compton, *Sens. Actuators B Chem.* **2013**, *178*, 555-562.

[83] M. F. Bergamini, D. P. dos Santos, M. V. B. Zanoni, *Sens. Actuators B Chem.* **2007**, *123*, 902-

908.

[84] H. Shi, F. Zhu, X. Zhou, H. Li, F. Yang, X. Zhang, J. Liu, *J. Electroanal. Chem.* **2019**, *840*, 328-337.

[85] X. Zhu, B. Liu, H. Hou, Z. Huang, K. M. Zeinu, L. Huang, X. Yuan, D. Guo, J. Hu, J. Yang, *Electrochim. Acta* **2017**, *248*, 46-57.

[86] H. Zheng, Z. Yan, H. Dong, B. Ye, *Sens. Actuators B Chem.* **2007**, *120*, 603-609.

[87] C. Hu, *Talanta* **2003**, *60*, 17-24.

[88] G.-H. Hwang, W.-K. Han, J.-S. Park, S.-G. Kang, *Sens. Actuators B Chem.* **2008**, *135*, 309-316.

[89] N. Promphet, P. Rattanarat, R. Rangkupan, O. Chailapakul, N. Rodthongkum, *Sens. Actuators B Chem.* **2015**, *207*, 526-534.

[90] K. Kunpatee, S. Traipop, O. Chailapakul, S. Chuanuwatanakul, *Sens. Actuators B Chem.* **2020**, *314*, 128059.

[91] J. Ping, J. Wu, Y. Wang, Y. Ying, *Biosens. Bioelectron.* **2012**, *34*, 70-76.

[92] L. Zhao, H. Li, S. Gao, M. Li, S. Xu, C. Li, W. Guo, C. Qu, B. Yang, *Electrochim. Acta* **2015**, *168*, 191-198.

[93] C. Wang, J. Du, H. Wang, C. e. Zou, F. Jiang, P. Yang, Y. Du, *Sens. Actuators B Chem.* **2014**, *204*, 302-309.

[94] L. Yang, D. Liu, J. Huang, T. You, *Sens. Actuators B Chem.* **2014**, *193*, 166-172.

[95] T. E. M. Nancy, V. A. Kumary, *Electrochim. Acta* **2014**, *133*, 233-240.

[96] Z. H. Sheng, X. Q. Zheng, J. Y. Xu, W. J. Bao, F. B. Wang, X. H. Xia, *Biosens. Bioelectron.* **2012**, *34*, 125-131.

[97] Q. Li, C. Huo, K. Yi, L. Zhou, L. Su, X. Hou, *Sens. Actuators B Chem.* **2018**, *260*, 346-356.

[98] S. Qi, B. Zhao, H. Tang, X. Jiang, *Electrochim. Acta* **2015**, *161*, 395-402.

[99] H. Yang, J. Zhao, M. Qiu, P. Sun, D. Han, L. Niu, G. Cui, *Biosens. Bioelectron.* **2019**, *124-125*, 191-198.

[100] H. L. Tcheumi, B. R. Babu, *Int. J. Environ. Anal. Chem.* **2017**, *97*, 1207-1222.

[101] Y. Sun, Y. Zhou, C. Zhu, W. Tu, H. Wang, H. Huang, Y. Liu, M. Shao, J. Zhong, S.-T. Lee, Z. Kang, *Appl. Catal. B* **2019**, *244*, 795-801.

[102] Y. P. Wu, J. W. Tian, S. Liu, B. Li, J. Zhao, L. F. Ma, D. S. Li, Y. Q. Lan, X. Bu, *Angew. Chem. Int. Ed.* **2019**, *58*, 12185-12189.

[103] W. Yang, X. Yang, J. Jia, C. Hou, H. Gao, Y. Mao, C. Wang, J. Lin, X. Luo, *Appl. Catal. B* **2019**, *244*, 1096-1102.

[104] A. S. Nugraha, J. Na, M. S. A. Hossain, J. Lin, Y. V. Kaneti, M. Iqbal, B. Jiang, Y. Bando, T. Asahi, Y. Yamauchi, *Appl. Mater. Today* **2020**, *18*, 100526.

[105] I. S. Pieta, A. Rathi, P. Pieta, R. Nowakowski, M. Hołdynski, M. Pisarek, A. Kaminska, M. B. Gawande, R. Zboril, *Appl. Catal. B* **2019**, *244*, 272-283.

[106] X. Cui, P. Xiao, J. Wang, M. Zhou, W. Guo, Y. Yang, Y. He, Z. Wang, Y. Yang, Y. Zhang, Z. Lin, *Angew. Chem. Int. Ed.* **2017**, *56*, 4488-4493.

[107] N. Spinner, W. E. Mustain, *Electrochim. Acta* **2011**, *56*, 5656-5666.

[108] H. Zhang, C.-D. Gu, M.-L. Huang, X.-L. Wang, J.-P. Tu, *Electrochem. Commun.* **2013**, *35*, 108-

111.

[109] B. Dong, W. Li, X. Huang, Z. Ali, T. Zhang, Z. Yang, Y. Hou, *Nano Energy* **2019**, *55*, 37-41.

[110] Z. Li, R. Yang, B. Li, M. Yu, D. Li, H. Wang, Q. Li, *Electrochim. Acta* **2017**, *252*, 180-191.

[111] L. Gu, L. Qian, Y. Lei, Y. Wang, J. Li, H. Yuan, D. Xiao, *J. Power Sources* **2014**, *261*, 317-323.

[112] N. Wu, M. Zhai, F. Chen, X. Zhang, R. Guo, T. Hu, M. Ma, *Nanoscale* **2020**, *12*, 21687-21694.

[113] Y. Y. Tong, C. D. Gu, J. L. Zhang, H. Tang, X. L. Wang, J. P. Tu, *Int. J. Hydrog. Energy* **2016**, *41*, 6342-6352.

[114] S. Sun, Z. J. Xu, *Electrochim. Acta* **2015**, *165*, 56-66.

[115] G. Rajeshkhanna, G. Ranga Rao, *Int. J. Hydrog. Energy* **2018**, *43*, 4706-4715.

[116] P. R. Jothi, S. Kannan, V. G, *J. Power Sources* **2015**, *277*, 350-359.

[117] R. Shi, Y. Zhang, Z. Wang, *J. Alloys Compd.* **2019**, *810*, 151879.

[118] R. P. Antony, A. K. Satpati, B. N. Jagatap, *ChemElectroChem* **2017**, *4*, 2989-2996.

[119] W. Tong, Q. Shao, P. Wang, X. Huang, *Chemistry* **2019**, *25*, 7218-7224.

[120] S. Samanta, K. Bhunia, D. Pradhan, B. Satpati, R. Srivastava, *ACS Sustain. Chem. Eng.* **2018**, *6*, 2023-2036.

[121] Q. Luo, M. Peng, X. Sun, A. M. Asiri, *Catal. Sci. Technol.* **2016**, *6*, 1157-1161.

[122] P. Manivasakan, P. Ramasamy, J. Kim, *Nanoscale* **2014**, *6*, 9665-9672.

[123] M. Yu, J. Chen, J. Liu, S. Li, Y. Ma, J. Zhang, J. An, *Electrochim. Acta* **2015**, *151*, 99-108.

[124] Y. Yu, B. Yang, Y. Wang, X. Shen, X. Hu, *ACS Appl. Energy Mater.* **2020**, *3*, 9076-9082.

[125] X. Song, Q. Sun, L. Gao, W. Chen, Y. Wu, Y. Li, L. Mao, J.-H. Yang, *Int. J. Hydrog. Energy* **2018**, *43*, 12091-12102.

[126] H. Gao, Y. Cao, Y. Chen, X. Lai, S. Ding, J. Tu, J. Qi, *J. Alloys Compd.* **2018**, *732*, 460-469.

[127] A. Roy, H. S. Jadhav, G. M. Thorat, J. G. Seo, *New J. Chem.* **2017**, *41*, 9546-9553.

[128] N. A. M. Barakat, M. Motlak, *Appl. Catal. B* **2014**, *154-155*, 221-231.

[129] M. U. Anu Prathap, R. Srivastava, *Nano Energy* **2013**, *2*, 1046-1053.

[130] B. Kaur, R. Srivastava, B. Satpati, *ACS Catal.* **2016**, *6*, 2654-2663.

[131] R. Ding, J. Liu, J. Jiang, F. Wu, J. Zhu, X. Huang, *Catal. Sci. Technol.* **2011**, *1*, 1406.

[132] B. Wang, Y. Cao, Y. Chen, R. Wang, X. Wang, X. Lai, C. Xiao, J. Tu, S. Ding, *Inorg. Chem. Front.* **2018**, *5*, 172-182.

[133] D. Khalafallah, O. Y. Alothman, H. Fouad, K. Abdelrazek Khalil, *Int. J. Hydrog. Energy* **2018**, *43*, 2742-2753.

[134] X. Yang, Q. Jia, F. Duan, B. Hu, M. Wang, L. He, Y. Song, Z. Zhang, *Appl. Surf. Sci.* **2019**, *464*, 78-87.

[135] B. M. Thamer, M. H. El-Newehy, N. A. M. Barakat, S. S. Al-Deyab, H. Y. Kim, *Fibers Polym.* **2017**, *18*, 696-705.

[136]   P. Arunachalam, M. Shaddad, A. Alamoudi, M. Ghanem, A. Al-Mayouf, *Catalysts* **2017**, *7*, 119.

[137] H. S. Jadhav, A. Roy, W.-J. Chung, J. G. Seo, *Electrochim. Acta* **2017**, *246*, 941-950.

[138] H. S. Jadhav, A. Roy, G. M. Thorat, J. G. Seo, *Inorg. Chem. Front.* **2018**, *5*, 1115-1120.

[139] L. Yaqoob, T. Noor, N. Iqbal, H. Nasir, N. Zaman, *Catalysts* **2019**, *9*, 856.

[140] B. M. Thamer, M. H. El-Newehy, N. A. M. Barakat, M. A. Abdelkareem, S. S. Al-Deyab, H. Y.

Kim, *Electrochim. Acta* **2014**, *142*, 228-239.

[141] Y. Liu, B. Hu, S. Wu, M. Wang, Z. Zhang, B. Cui, L. He, M. Du, *Appl. Catal. B* **2019**, *258*, 117970.

[142] N. Narayanan, N. Bernaurdshaw, *ChemCatChem* **2019**, *12*, 771-780.

[143] T. J. Wang, H. Huang, X. R. Wu, H. C. Yao, F. M. Li, P. Chen, P. J. Jin, Z. W. Deng, Y. Chen, *Nanoscale* **2019**, *11*, 19783-19790.

[144] R. M. Abdel Hameed, R. M. El-Sherif, *Appl. Catal. B* **2015**, *162*, 217-226.

[145] L. Zhang, D. Zhang, Z. Ren, M. Huo, G. Dang, F. Min, Q. Zhang, J. Xie, *ChemElectroChem* **2017**, *4*, 441-449.

[146] X. Tong, Y. Qin, X. Guo, O. Moutanabbir, X. Ao, E. Pippel, L. Zhang, M. Knez, *Small* **2012**, *8*, 3390-3395.

[147] X. Wang, S. Xi, W. S. V. Lee, P. Huang, P. Cui, L. Zhao, W. Hao, X. Zhao, Z. Wang, H. Wu, H. Wang, C. Diao, A. Borgna, Y. Du, Z. G. Yu, S. Pennycook, J. Xue, *Nat. Commun.* **2020**, *11*, 4647.

[148] T. Choksi, J. Greeley, *ACS Catal.* **2016**, *6*, 7260-7277.

[149] C.-Q. Lv, C. Liu, G.-C. Wang, *Catal. Commun.* **2014**, *45*, 83-90.

[150] L. Xiong, Z. Sun, X. Zhang, L. Zhao, P. Huang, X. Chen, H. Jin, H. Sun, Y. Lian, Z. Deng, M. H. Rummerli, W. Yin, D. Zhang, S. Wang, Y. Peng, *Nat. Commun.* **2019**, *10*, 3782.

[151] T. B. Rawal, S. R. Acharya, S. Hong, D. Le, Y. Tang, F. F. Tao, T. S. Rahman, *ACS Catal.* **2018**, *8*, 5553-5569.

[152] Z. Chen, Y. Mao, J. Chen, H. Wang, Y. Li, P. Hu, *ACS Catal.* **2017**, *7*, 4281-4290.

[153] M. Zhang, Y. Wu, Y. Yu, *Appl. Surf. Sci.* **2020**, *510*, 145434.

[154] H. Li, Y. Pan, D. Zhang, Y. Han, Z. Wang, Y. Qin, S. Lin, X. Wu, H. Zhao, J. Lai, B. Huang, L. Wang, *J. Mater. Chem. A* **2020**, *8*, 2323-2330.

Chapter 6

Conclusion and outlook

Combined the merits of functional porphyrins (*e.g.,* strong aromaticity, optical/electrical properties, rich metal coordination chemistry) and MOFs platform (well-defined, periodic and porous structure), porphyrinic MOFs (PP-MOFs) afford promising applications in various specific applications, including separations, sensing, energy production, electronic devices and optical applications. Some of these applications, such as sensing, optics, integration of PP-MOFs onto solid surfaces as thin-film forms is a prerequisite. Thus, facile and versatile thin film fabrication strategies are desired to prepare specific high-quality PP-MOF thin films. Besides, porphyrinic MOFs are recently proposed as suitable precursors for derived M-N-C PCs, showing great potential in electrocatalysis. However, how to optimize the M-N-C materials with desired functionalities and enhanced specific catalytic properties remains a great challenge. Herein, this thesis aims at facile and efficient preparation of high-quality PP-MOFs thin films and exploiting its practical applications in electrochemical sensing; moreover, highly attractive M-N-C with atomically dispersed metal centres was achieved and further utilized for electrocatalytic applications.

Firstly, a facile and versatile method, so-called vapor-assisted conversion (VAC) was introduced and developed to grow crystalline, oriented and homogeneous PP-MOF thin films on various substrates. To further understand the nucleation and growth mechanism of PP-MOF films, several other useful methods (*viz.*, solvothermal, modular assembly, LPE-LBL) also were adopted to prepare thin films of PP-MOFs varying dimensionalities: 2D and 3D. It was revealed that different strategies undergo different nucleation and growth processes, which lead to films with distinctive features. Among these techniques, VAC achieved preparation of crystalline, oriented and homogeneous thin films of both 2D and 3D PP-MOFs, manifesting its high versatility and efficiency. Encouraged by the first successful example of VAC in high-quality PP-MOF thin films, this inclusive study also provides an additional perspective toward other related PP-MOF films preparation and their controlled growth.

Besides the VAC technique, the merits of modular assembly are also highlighted in this inclusive study due to its fast and facile film fabrication process. Thus, further exploration of PP-MOF film based on this strategy and their sensing application is encouraged. Herein, typical PP-MOF, Mn-PCN-222, was integrated as

a thin film on the conductive indium tin oxide (ITO) surface. The resulting Mn-PCN-222/ITO demonstrates multifaceted voltammetric sensing of several inorganic ions, organic hazardous substances and pollutants, *viz.*, nitroaromatics, phenolic and quinone-hydroquinone toxins, heavy metal ions, biological species, as well as azo dyes. Sensitive detections with wide linear ranges and low LODs are obtained with Mn-PCN-222/ITO. The electrode shows high efficiency not only towards single substrates, but also retains its high performance in binary and ternary systems of increased complexity. The excellent sensing performance is attributed to synergetic effect of periodic and porous Mn-PCN-222 platform and incorporated ordered metalloporphyrin units as catalytic centres.

At last, in addition to the film fabrication of original PP-MOFs and their superb performance in sensing, PP-MOFs derived M-N-C materials are recognized as superior catalysts for many electrochemical reactions. Herein, a series of isostructural n% Ni-PCN-222 were synthesized by a mixed ligand strategy with different Ni-TCPP loading ratios (n% = 0%, 20%, 40% and 100%). With low loading at 20%, the Ni-TCPP ligands in 20% Ni-PCN-222 network feature an expanded distance, effectively inhibiting Ni atom aggregation, thereby leading to the formation of single-atom Ni sites in porous N-doped carbon after pyrolysis. The proposed Ni-based single atom catalysts (SACs), defined as 20% Ni-N-C. Compared to their counterparts, 20% Ni-N-C SACs features a superior performance towards electrochemical methanol oxidation: a low onset potential with superb mass activity as 634 mA mg^{-1} at low peak potential of 1.55 V versus RHE and impressive durability with 90% retention of initial activity after 25000s of MOR test. This is ascribed to its abundant single-atom Ni active sites, hierarchical porosity with highly oriented mesochannels, excellent conductivity and stable Ni-N$_4$ moieties.

The development of PP-MOF based sensors is still in its infancy and tremendous possibilities are yet to be explored. Building upon the compositional modularity of M-PP-MOFs, varying intrinsic properties such as, pore environments, redox-potentials/windows for each (*e.g.*, by choosing M properly or combining different M-PPMOFs in one sensor device) paves the way for a number of related approaches, *e.g.,* redox-potentials/windows are tuneable by an *à la carte* catalogue of metal nodes and this is likely to offer another dimension to the control of electrochemical properties of M-PP-MOF based voltammetric sensors. Similarly, by

regulating the PP-MOF precursors (*e.g.,* changing the Chemical configuration) and pyrolysis conditions (*e.g.,* different temperature or atmosphere), the PP-MOFs derived M-N-C catalysts also can be turned with specific properties and thus manifest huge potential for a range of electrocatalysis.

Appendix

List of scientific publications

1) **<u>Zhenyu Zhou</u>**, Soumya Mukherjee, Julien Warnan, Weijin Li, Suttipong Wannapaiboon, Shujin Hou, Katia Rodewald, Bernhard Rieger, Peter G Weidler, Christof Wöll and Roland A. Fischer," Porphyrin based metal–organic framework films: nucleation and growth", *J. Mater. Chem. A*, 2020,**8**, 25941-25950.

2) Anna Lisa Semrau, **<u>Zhenyu Zhou</u>**, Soumya Mukherjee, Min Tu, Weijin Li and Roland A. Fischer, "Surface-mounted metal-organic frameworks: past, present, and future perspectives", *Langmuir*, 2021, **37**, 6847–6863. (**Equal first authors**)

3) **<u>Zhenyu Zhou</u>**, Soumya Mukherjee, Shujin Hou, Weijin Li, Martin Elsner, and Roland A. Fischer, "Porphyrinic MOF Film for Multifaceted Electrochemical Sensing", *Angew. Chem. Int. Ed.*, 2021, **60**, 20551-20557.

4) **<u>Zhenyu Zhou</u>**, Jing Zhang, Soumya Mukherjee, Shujin Hou, Rachit Khare, Markus Döblinger, Ondřej Tomanec, Michal Otyepka, Liujiang Zhou, Weijin Li, and Roland A. Fischer, "Porphyrinic MOF Derived Single-atom Electrocatalyst Enables Methanol Oxidation", 2021, manuscript in preparation.

Scientific poster presentation

"Liquid Phase Epitaxy of Surface-mounted Porphyrin Metal-Organic Frameworks via Coordination Modulation strategy" 6th International Conference on Metal-Organic Frameworks (MOF 2018), (9th-13th December 2018, Auckland, New Zealand).

Author contributions

Chapter 1: This chapter was written by Zhenyu Zhou. Dr. Soumya Mukherjee helped in revision and polishement of the drafts.

Chapter 2: The results of this chapter are reproduced by Zhenyu Zhou according to the published paper: "Z. Zhou, S. Mukherjee, J. Warnan, W. Li,* S. Wannapaiboon, S. Hou, K. Rodewald, B. Rieger, P. G. Weidler, C. Wöll, R. A. Fischer,* *J. Mater. Chem. A* 2020, 8, 25941-25950." Zhenyu Zhou designed and prepared all the porphyrinic MOF films, performed the experiments, wrote the draft paper. Dr. Soumya Mukherjee helped in simulation of structure of $Zn_2(ZnTCPP)$. Dr. Soumya Mukherjee, Dr. Julien Warnan and Dr. Suttipong Wannapaiboon help in data curation, analysis and revision of the drafts. Mr. Shujin Hou help in the graphic for Table of Contents (TOC). Data of SEM were collected by Katia Rodewald, Prof. Dr. Bernhard Rieger and Zhenyu Zhou. Ms. Shanshan Yin and Prof. Dr. Peter Müller Buschbaum help Zhenyu Zhou to collect the surface profile analysis data. Prof. Dr. Roland A. Fischer and Dr. Weijin Li supervised the project.

Chapter 3: The results of this chapter are reproduced by Zhenyu Zhou according to the published paper: "Z. Zhou, S. Mukherjee, S. Hou, W. Li,* M. Elsner, R. A. Fischer,* *Angew. Chem. Int. Ed.* 2021, 60, 20551-20557." Zhenyu Zhou Zhenyu Zhou designed and prepared the porphyrinic MOF films as sensors, performed all the electrochemical sensing experiments, wrote the draft paper. Mr. Shujin Hou and Dr. Weijin Li helped Zhenyu Zhou to develop the electrocatalytic system. Prof. Dr. Martin Elsner and Dr. Soumya Mukherjee helped in data curation, analysis and revision of the drafts. Raman were measured by Mr. Shujin Hou. Data of SEM were collected by Katia Rodewald, Prof. Dr. Bernhard Rieger and Zhenyu Zhou. Prof. Dr. Roland A. Fischer and Dr. Weijin Li supervised the project.

Chapter 4: The results of this chapter are reproduced by Zhenyu Zhou according to the prepared manuscript: "Zhenyu Zhou, Jing Zhang, Soumya Mukherjee, Shujin Hou, Rachit Khare, Markus Döblinger, Ondřej Tomanec, Michal Otyepka, Max Koch, Liujiang Zhou,* Weijin Li,* Roland A. Fischer*, 2021." Zhenyu Zhou designed and prepared the Ni-N-C catalysts, performed all the experiments and wrote the draft paper. Mr. Shujin Hou helped Zhenyu Zhou to develop the

electrocatalytic system. Dr. Soumya Mukherjee helped in data curation, analysis and revision of the drafts. Ms. Jing Zhang and Prof. Dr. Liujiang Zhou performed the DFT simulation for the MOR process on the 20% Ni-N-C catalyst. Data of XAS were collected and analyzed by Dr. Rachit Khare. Dr. Markus Döblinger, Dr. Ondřej Tomanec and Prof. Dr. Michal Otyepka provided the TEM images. Data of XPS were collected by Dr. Christian Jandl. Data of Raman were collected by Mr. Shujin Hou and analyzed by Zhenyu Zhou. ICP were measured by Mr. Max Koch. Prof. Dr. Roland A. Fischer and Dr. Weijin Li supervised the project.

Chapters 5 and 6: These two chapters are written by Zhenyu Zhou.

Mr. Zhenyu Zhou

Date of record: 28.09.2021

Munich, Germany